Thermally Responsive Peptide Coated Superparamagnetic Iron Oxide Nanoparticles for Drug Delivery

By

Abdul Majid

A thesis submitted in partial fulfilment for the requirements for the degree of

Doctor of Philosophy at the University of Central Lancashire

August 2017

STUDENT DECLARATION FORM

Concurrent registration for two or more academic awards

*I declare that while registered as a candidate for the research degree, I have not been a registered candidate or enrolled student for another award of the University or other academic or professional institution

Material submitted for another award

*****I declare that no material contained in the thesis has been used in any other submission for an academic award and is solely my own work

Signature of Candidate: Abdul Majid

Type of Award: Doctor of Philosophy

School: Physical Sciences and Computing

Abstract

Target specific delivery of anticancer drugs to the effected site without showing systematic toxicity to normal tissues is important. Multifunctional biodegradable delivery systems reduce systematic toxicity in an efficient manner. These drug carriers should provide controlled release, be directed towards desired site, track payloads *via* contrast imaging, heat the effected sites and trigger drug release. In this context, superparamagnetic iron oxide nanoparticles based drug delivery systems are highly desirable. Superparamagnetic iron oxide nanoparticles upon exposure of alternate magnetic field could be directed and provide heat to localised areas. Moreover, superparamagnetic iron oxide nanoparticles also have image contrast ability for magnetic resonance imaging.

This study aimed to develop biocompatible superparamagnetic iron oxide nanoparticles. These nanoparticles were coated by bioinspired materials such as peptides (diphenylalanine) to achieve monodispersed dual efficient such as drug carriers and hyperthermia. Thermally responsive core-shell materials with tubular and spherical morphologies without compromising the inner cores properties such as superparamagnetism is highly desirable.

Two shapes of iron oxide (spherical and tubular) were prepared using co-precipitation of iron (II) and (III) ion and oxidative hydrolysis of ferrous sulphate in alkaline solutions, respectively. Spherical peptide shells were synthesised using tert-Butyloxycarbonyl modified diphenylalanine peptide in ethanol-water (1:1) mixture. Tubular peptide shells were prepared using similar diphenylalanine non-modified peptide. The iron oxide nanoparticles (spherical and tubular) were encapsulated *via* template-mediated synthesis using ultra-sonication and vortex-mixing methods.

These materials were characterised using variety of techniques such as, zetasizer, Scanning Electron Microscopy (SEM), Energy Dispersive X-ray Spectroscopy (EDAX), Fourier Transform Infrared Spectroscopy (FTIR), Brunauer–Emmett–Teller (BET) analysis, Transmission Electron Microscopy (TEM), X-ray Diffraction (XRD), Thermogravimetric Analysis (TGA), Vibrating Sample Magnetometer (VSM) and magnetic field induced hyperthermia. The diameter of spherical superparamagnetic iron oxide nanoparticles were measured to be ranges from 10 to 35 nm and rod-shaped core materials showed nearly 10 nm width and several hundred nanometres in length. Spherical peptide were approximately 1 µm in diameter. Tubular-shaped peptide were between 100-300 nm in width and several micrometres in length. These peptides were used as shells for the preparation of core-shell composites. Both spherical and rod-shaped core-shell composites were similar in dimensions to the pure peptide particles. Observational analysis confirmed the presence core-shell composition. Spherical iron oxide core materials were crystalline magnetite (Fe_3O_4) structures confirmed by powder XRD. These magnetite

nanocrystals were further modified with a biocompatible silica shell. Brunauer–Emmett–Teller (BET) analysis revealed a mesoporous shell structure. Spherical peptide shells were found to be amorphous and tubular peptide shells were crystalline in nature. VSM of core-shell composite materials depicted superparamagnetic nature, hence these materials have ability to heat over the exposure of applied external magnetic field for hyperthermia ablation.

Anticancer drug (doxorubicin, DOX) loading and release profile of bare spherical and rod-shaped iron oxide nanoparticle and peptide, silica and peptide-capped silica coated spheres were studied for potential therapeutic application. The doxorubicin loading efficiency was observed to be ranging from 12 % to 90 % depending on the type materials. The *in vitro* drug release profiles were measured at 37 °C without the exposure of magnetic field in incubation and with applied magnetic field. Time-dependent studies showed sustained release of DOX in silica coated and peptide- capped silica coated spherical superparamagnetic iron oxide nanoparticles were ranging from 0 to 30 % over 72 hours of incubation. Concentration dependent studies revealed that the ratio of 1:100 (doxorubicin:superparamagnetic iron oxide nanoparticles) had the maximum loading efficiency with minimum release capability. Exposure to Alternate Current (AC) magnetic field (200 G; 406 kHz) the spherical materials generated hyperthermia in a time dependent manner reaching 50 °C in 3 minutes. Tubular peptide coated iron oxide materials did not induce heat even after 25 minutes of exposure indicating weak superparamagnetism. Magnetic field triggered drug release was seen only in spherical core-shell nanocomposites with 6X higher compared at 37 °C without exposure.

Table of Contents

List of Figures

List of Tables

Acknowledgement

All praises, thanks and admirations are for Allah (SWT), the most merciful and beneficent, Who is source of knowledge and wisdom. He blessed me ideas, nice and expert guides, cheering friends, health and a wonderful opportunity to complete this level of education. I would like to extend my sincere and greatest appreciation to my Director of Studies, Dr Tapas Sen for all his support, expertise guidance, invaluable advices and productive feedback for the successful completion of this project.

I would particularly like to thank Dr Yogita Patil-Sen for being co-advisor and guide for setting up this project and leading to completion on time. Her productive comments has pushed me to expand the depth of knowledge specifically in drug loading and release experiments. Thanks to my second supervisor Professor Waqar Ahmed, for his guidance for completing my thesis and belief in my abilities, which motivated me to stretch my limits and expand my research excellence.

I am also thankful to Dr Abdelbarry Elhissi and Professor Jaipaul Singh for their support and help in those moments, when I was really disappointed and confused, gave me the reason to continue. Thanks must be extended to Dr Abdullah Isreb for his help and support for TGA and Dr Jennifer Readman for XRD analysis. Many thanks to technicians James Donnelly and Tamar Garcia for their help with handling instrumentation and reagents. I am also grateful to Dr Karl Dawson, University of Liverpool for providing TEM facility.

Thanks to everyone, I have met during my time in Preston for their infinite trips to local desi shops for Pizza and coffee. Sometimes sudden trips to the Manchester for dinner at Nawaab and Trafford Centre that is memorable. I would like to extend thanks to all the administrative staff and research colleagues in School of Physical Sciences and Computing.

Most importantly, I owe the deepest gratitude to my loving parents, my brothers, sisters and my Grandmother for their unconditional love and prayer; no words can convey my gratitude toward them.

In last, I would like to extend my special thanks to Higher Education Commission (HEC) of Pakistan and Shah Abdul Latif University (SALU) Pakistan for providing me scholarship to do MSc and PhD. I appreciate my employer SALU for their sincere efforts to support its project “Strengthening the Infra-Structure of Shah Abdul Latif University Khairpur” for the benefit of institution and the education.

List of Abbreviations

AC	Alternate Current
BET	Brauner-Emmett Teller
BOC	Butoxycarbonyl
BOC-FF	Butoxycarbonyl diphenylalanine
BOC-SPION-SS	Butoxycarbonyl Coated Superparamagnetic Iron Oxide nanoparticles Spherical- Shaped
BOC-Si-SPION-SS	Butoxycarbonyl-capped Silica-coated Superparamagnetic Iron Oxide nanoparticles Spherical- Shaped
B-SPION-SS	Bare Superparamagnetic Iron Oxide Nanoparticles Spherical-Shaped
FM-ION-RS	Ferromagnetic Iron Oxide Nanoparticles Rod-Shaped
CD	Circular Dichroism
CTAB	Cetyltrimethylammonium Bromide
DLS	Dynamic Light Scattering
DMSO	Dimethyl Sulfoxide
DOX	Doxorubicin
EDAX	Energy Dispersive X-Ray Spectroscopy
EDP	Electron Diffraction Pattern
EPR	Enhanced Permeability and Retention
FDA	Food and Drug Administration
FF	Phenylalanine (two amino acids)
FF-FM-ION-RS	Diphenylalanine coated Ferromagnetic iron Oxide Nanocomposites Rod-shaped
FTIR	Fourier Transform Infrared Spectroscopy
HFIP	Hexafluoroisopropanol
HT	Hyperthermia
MNPs	Magnetic nanoparticles
MPS	Mononuclear Phagocytosis System
MRI	Magnetic Resonance Imaging
NIR	Near Infrared (wavelength)
NNI	National Nanotechnology Initiative
OD	Optical Density

PBS	Phosphate Buffered Saline
PEG	Polyethylene Glycol
Phe-Phe	Phenylalanine (two amino acids)
PMMA	Polymethylmethacrylate
PNTs	Peptide Nanotubes
RES	Reticuloendothelial System
ROS	Reactive Oxygen Species
RT	Room Temperature
SEM	Scanning Electron Microscopy
SPA	Specific Power Absorbance
SPIONs	Superparamagnetic Iron Oxide Nanoparticles
Si-SPION-SS	Silica-coated Superparamagnetic Iron Oxide Nanoparticles Spherical-Shaped
TEM	Transmission Electron Microscopy
TEOS	Tetraethyl Orthosilicate
TGA	Thermogravimetric Analysis
UV	Ultraviolet
VSM	Vibrating Sample Magnetometry
XRD	X-Ray Diffraction

List of Symbols

B	Magnetic field
C_s	Specific heat of sample
$\varnothing$	Particles diameter
kHz	Kilohertz (frequency of magnetic field)
H	Field intensity amplitude
I	Current
M	Magnetic moment of particles
M_s	Saturation magnetisation of nanoparticles
M_{np}	Mass of nanoparticles
t_B	Brownian rotation time
t_N	Nėel relaxation time
M_r	Remnant magnetisation
$emu.g^{-1}$	Electromagnetic unit per gram (saturation magnetisation)
T	Temperature
λ	Wavelength
$g.mL^{-1}$	Grams per millilitre
$mg.mL^{-1}$	Milligrams per millilitre
$\mu g.mL^{-1}$	Micrograms per millilitre
kDa	Kilo Daltons
mmol	Millimolar
$kW.m^{-2}$	Kilowatt per square metre
G	Gauss (magnetic field strength)
kOe	Kilo-oersted

Publications

Abstract:

Majid, A., Patil-Sen, Y., Ahmed, W., & Sen, T. (2016). Self-Assembling Peptide Tunable Structure: A Novel Approach for Designing of Dual Biologically Active Agents. In Functional Nanomaterials in Industrial Applications: Academic-Industry Meet (p. 63) 29th to 31st March 2016, UCLan, Preston, UK.

Publications:

Majid, A., Patil-Sen, Y., Ahmed, W., & Sen, T (2017). Tunable Self-Assembled Peptide Structure: A Novel Approach to Design Dual-Use Biological Agents. Materials Today: Proceedings, 4(1), pp.32–40.

Majid, Abdul, Waqar Ahmed, Yogita Patil-Sen, and Tapas Sen. (2017). Applications of Magnetic Nanoparticles in Medicine. In Waqar Ahmed and Mark Jackson. Ed. Micro & Nanomanufacturing. Springer New York (accepted).

CHAPTER ONE

INTRODUCTION

1.1 Introduction and Background

Magnetic nanoparticles have attracted considerable attention in recent years for a range of applications including magnetic storage, drug delivery and medical diagnostics. They are highly attractive due to their tunable size, shape, surface chemistry and the propensity to direct them to selected target sites. For example, nanoparticles of magnetite materials display excellent magnetic properties, non–toxicity and biocompatibility. The nanosize characteristics induce favourable surface chemistry due to the large surface area making them highly suitable for a range of applications. Despite extensive studies, there is still need to obtain a better understanding of the various characteristics of nanoparticles and their properties such as the relationships of shape, surface chemistry, polydispersity, and in particular the magnetic properties of magnetite. An attractive feature of magnetite is the ability to tune the synthesis protocol in order to achieve well-defined structures. Current research focuses on the magnetic materials with superparamagnetic properties and magnetic susceptibility. These are single domain structures with randomly oriented magnetic moments, which rotate rapidly towards the direction of applied magnetic field hence increasing the magnetic flux. Once the applied external magnetic field is turned off, the particle again become randomly oriented with no magnetic remanence due to the Brownian motion (Arruebo et al. 2007). These materials have advantages, if they could be designed as seeds with biocompatible materials as a shell. They can be useful in magnetic field guided target specific drug carriers, tumour hyperthermia, MRI contrast agents for tracking and delivery of a drug (Kumar & Mohammad 2011; Dobson 2006; Sun et al. 2008; Arruebo et al. 2007; Brusentsov et al. 2001).

1.2 Aims and objectives

This study will be focused on the synthesis of Superparamagnetic iron Oxide Nanoparticles (SPIONs) of two different morphologies. The motivation was to develop, characterise and test them as drug delivery systems. The first step will be to develop a simple, robust, quick and low cost method for rod-shaped SPIONs. In next step, these materials could be coated with mesoporous silica to achieve control release drug delivery system. In the final step of synthesis, all materials will be coated with bioinspired naturally occurring dipeptide (diphenylalanine) as its native and modified forms with tert-butyloxycarbonyl (boc) group to tune the desired shape of peptide shells for corresponding SPIONs cores. All synthesised materials will be characterised using variety of physicochemical techniques. In final step, all materials will be investigated for their hyperthermia efficiency, drug loading and release and magnetic field triggered drug release.

The aim of this study is to design and synthesise the peptide shells and use them for coating of iron oxide nanoparticles as core-shell structures. Hence, the resultant core-shell composites can be used as a magnetic field guided localised drug delivery system.

Consequently, higher doses of drugs can be delivered magnetically to a tumour site, hence reducing the toxicity to healthy tissues compared to non-targets specific cancer therapies. In these core–shell structures, peptide shells will separate the structures from biological system ensuring biocompatibility in biological fluids. This will prolong sustainability of magnetic particles in the blood stream.

The specific objectives of this research include the following:

- To synthesise and characterise monodisperse peptide coated surface stabilised iron oxide (Fe_3O_4) nanoparticles with tunable size and shape while retaining magnetic behaviour.
- To incorporate the model drug within this magnetic core *via* adsorption or attached to the inner layer of the peptide.
- To study the implication of nanoparticles shapes in the drug delivery system by exploiting two different shapes (rod-shaped and spherical core-shell) of peptide coated iron oxide particles.
- To investigate spherical and tubular structural effects on hyperthermia triggered drug release profiles.

1.3 Thesis outlines

This thesis is contributed into nine chapters.

Chapter 1 introduces to magnetic nanoparticles within the context of guided drug delivery systems. The research aims and specific objectives of this study are given along with an outline of the thesis.

Chapter 2 presents a detailed literature review of the nanomaterials as drug delivery systems and pharmaceutical vehicles. The different types of polymers and their advantages and disadvantages are discussed. Background of self-assembling peptides structures in biomedical applications is explained.

Chapter 3 describes the preparation and characterisation of the (iron oxide nanoparticles), peptide particles of spherical and tubular morphologies and corresponding

core-shell structures. Characterisation methods include SEM-EDAX. TEM, VSM FTIR, TGA, DLS, XRD, BET and hyperthermia are also explained.

Chapter 4 presents and discusses the results of the investigation on spherical cores of iron oxide nanoparticles and boc-diphenylalanine peptide shells. The influence of the two synthesis approaches on the coating of the peptide to magnetite will be discussed using data from characterisation techniques including, Scanning Electron Microscopy (SEM), Energy Dispersive X-ray Spectroscopy (EDAX), Fourier Transform Infrared Spectroscopy (FTIR), Brunauer–Emmett–Teller (BET) analysis, Transmission Electron Microscopy (TEM), X-ray Diffraction (XRD), Thermogravimetric Analysis (TGA), Vibrating Sample Magnetometer (VSM) and magnetic field induced hyperthermia.

Chapter 5 describes the results obtained from rod-shaped iron oxide nanoparticles, diphenylalanine peptide-based tubes and the corresponding core-shell structures. The implication of shape on their physicochemical properties and magnetic moment and hyperthermia are discussed.

Chapter 6 presents and discusses the drug loading and release profile of core and core-shell spherical nanoparticles and nanocomposites. A detailed study of concentration and time-dependent loading and release profiles is also presented.

Chapter 7 similarly discusses the drug loading and release profile of core and core-shell rod-shaped nanoparticles and nanocomposites. The effects of loading and release profiles of anticancer drug on parameters such as concentration and time have been presented.

Chapter 8 discusses the hyperthermia ability of core nanoparticles and core-shell nanocomposites of spherical and rod-shaped morphologies. In addition, this chapter will

also reveal the comparative analysis of magnetic field triggered drug release profile of both spherical and rod-shaped morphologies.

Chapter 9 gives a summary of the main conclusions and future work suggested for further studies.

CHAPTER TWO

Nanotechnology-based drug delivery systems: a review

2.1 Introduction

This chapter gives a review of the current literature on nanoparticles based drug delivery tools. It highlights the relevant factors that may affect the biocompatibility, immunogenicity, self-aggregation of nanoparticles. The physicochemical properties of multifunctional drug delivery systems will also be reviewed. The major obstacles of the nanoparticles arise in drug delivery system have been considered.

The peptide self-assemblies, especially those classed as amylogenic dipeptide will be described in detail along with the possible effects of solvents on the structure and properties. An attractive proposition is a possibility of coating the metallic structures with self-assembling peptides in drug delivery systems will be considered. Finally, the core-shell formation of peptides shells and superparamagnetic iron oxide nanoparticles core materials will be summarised.

The review also provides an insight into ways of overcoming the biocompatibility, aggregation related drawbacks in magnetically triggered hyperthermia and drug delivery systems.

2.2 Nanotechnology

Nanotechnology has numerous applications aimed to improve the quality of life and the environment. The advantages of nanotechnology include tunable physical and chemical properties such as a high surface to volume ratio, and can be surface functionalised with ligands, coatings, charge and other alternative tools. Recent studies focus on the oncology

based applications of nanoscience (Ahmad et al. 2010). National Nanotechnology Initiative terms the “nanotechnology as the engineering of materials conducted at the nanoscale (1-100 nm) in any one dimension” (Kim 2008). However, this has been broadened by research in different fields referring to materials with average feature size in the range 1 to 1000 nm. Engineering nanoscale structures exhibit a multitude of functional properties in contrast to the individual molecular behaviour of the nanostructure constituents or the behaviour of bulk materials (Alexis et al. 2008).

The use of nanomaterials in nanomedicine is an exciting prospect. For example, in drug delivery, it is possible to alter the properties of the encapsulated drug by tuning physicochemical properties such as ionic strength, solubility and reactivity (Strebhardt & Ullrich 2008). The commercialisation of variety of nanotherapeutics has made nanoparticles based drug delivery a reality. Many nanoparticle-based drug delivery systems are biodegradable, have a low immune response, target specificity and provide controlled release of the drug. Nanocarriers encapsulate poorly bio-available drugs and increase their half-life (Alexis et al. 2008).

In cancer treatments, the majority of therapeutics are toxic to normal cells and can be readily excreted. Consequently. Kipp (2004) studied that 40 % of all compounds are hydrophobic and due to their lower solubility and associated poor bioavailability. They did not reach to clinical trials. Recently, a variety of hydrophobic drugs have been formulated with nanocarriers such as Food and Drug Administration approved Doxil® (a doxorubicin formulation with liposomes shown reduced cardiac cytotoxicity (O’Brien et al. 2004). Abraxane also an FDA approved formulation, which consists of paclitaxel with albumin with an average diameter of 100 nm has been used commercially. The

encapsulation process omits the use an organic solvent thus reducing the risk of inflammation or hypersensitivity (Cortes & Saura 2010).

The ideal anti-cancer formulation should have two properties:

i) Ensure effective penetration in affected sites with minimal loss of drug for a longer period.

ii) Have the ability to recognise and kill the cancerous cells without affecting normal tissues.

By increasing the intracellular therapeutic level, this reduces dose limiting drug toxicities, which in turn increases the patient`s survival rate and the quality of life.

2.2.1 Diagnosis and imaging of cancer

Early stage diagnosis is an essential step towards effective treatment of cancers. If cancer is diagnosed in early staged can be treated effectively. It is a big challenge; as clinical symptoms often are not expressed until a fatal stage is reached. Minimally invasive, cost effective and accurate with have enhanced imaging for cancer diagnostics are still in their infancy (Misra et al. 2010). Over the last decade, a plethora of nanotechnological tools has been investigated for the detection and imaging of various cancer types (Wang et al. 2008; Li 2014). Specifically, iron oxide nanoparticles with magnetic resonance imaging (MRI) have been used in prostate cancer diagnosis (Farokhzad & Langer 2006). Gold and quantum fluorescence quantum dots were in clinical trials for the detection of cancer cells (Craig et al. 2010; Sukhanova et al. 2016). Gold nanoparticles modified with RNA aptamer have also been used for the detection of prostate and circulating cancer cells (Kim et al. 2010; Dickey & Giangrande 2016).

Engineering nanoparticle based delivery systems will not be effective until an adequate drug delivery at a subcellular level are achieved. These properties can be achieved by exploiting a strategy called “theragnostic” combining both therapeutics and diagnostics (Ilaria Parisi et al. 2016).

2.2.2 Targeted drug delivery systems

Nanocarriers encapsulating drug remain in the target tissue for a longer time than the free drug thus enhancing its efficiency in normal tissue and yielding reduced cytotoxicity in normal cells (Ulbrich et al. 2016). There are two natural ways to target the desired tissues; passive targeting and active targeting.

Nanoparticles with stealth ability can protect themselves from the mononuclear phagocytosis system (MPS), therefore allowing their retention in the bloodstream for a prolonged period to achieve the best drug efficiency. This can be done by adjusting the ionic properties, including size, charge, surface and pH of drug-encapsulated nanoparticles. The nanoparticle size should be in the range of 10 to 100 nm for penetration into the leaky vasculature of cancer, where the pore cut-off size is approximately 100 - 700 nm (Cho et al. 2008). The administered nanoparticles should have the size larger than 10 nm to avoid clearance *via* renal filtration and leakage from the capillaries (Danhier et al. 2010).

In addition to particle size, the surface properties are also important in the assessment the fate of injected nanoparticles. Once nanoparticles reach plasma, opsonisation (adsorption of proteins on nanoparticles) occurs. MPS of spleen, liver or bone marrow recognises the nanoparticles, where opsonin interact with phagocytes (Petros & DeSimone 2010). To

avoid opsonisation of nanoparticles, hydrophilic clouds are designed on the surface on nanoparticles.

2.2.3 Passive targeting

Accumulation of macromolecules polystyrene-co-maleic acid-neocarzinostatin in cancerous tissue has been reported for the first time by (Matsumura & Maeda 1986). An albumin-bound anti-cancer drug was utilised, which remained for a longer period in the cancer interstitium, where it showed poor lymphatic passage and improper vasculature system (figure 2-1). By exploiting this phenomenon enhanced permeability and retention can be achieved (Egusquiaguirre et al. 2012).

In tumours, when uncontrolled cell growth begins, the normal body system is not able to supply enough oxygen and nutrients to the newly proliferated cells. The cells do not receive sufficient nutrients and oxygen and begin to excrete growth factors. These form a different anatomical structure “angiogenesis” resulting in defective, irregular and leaky vessels. Poor lymphatic drainage retains molecules levels up to 50 times higher in a tumour environment compared to normal vasculature (Iyer et al. 2006).

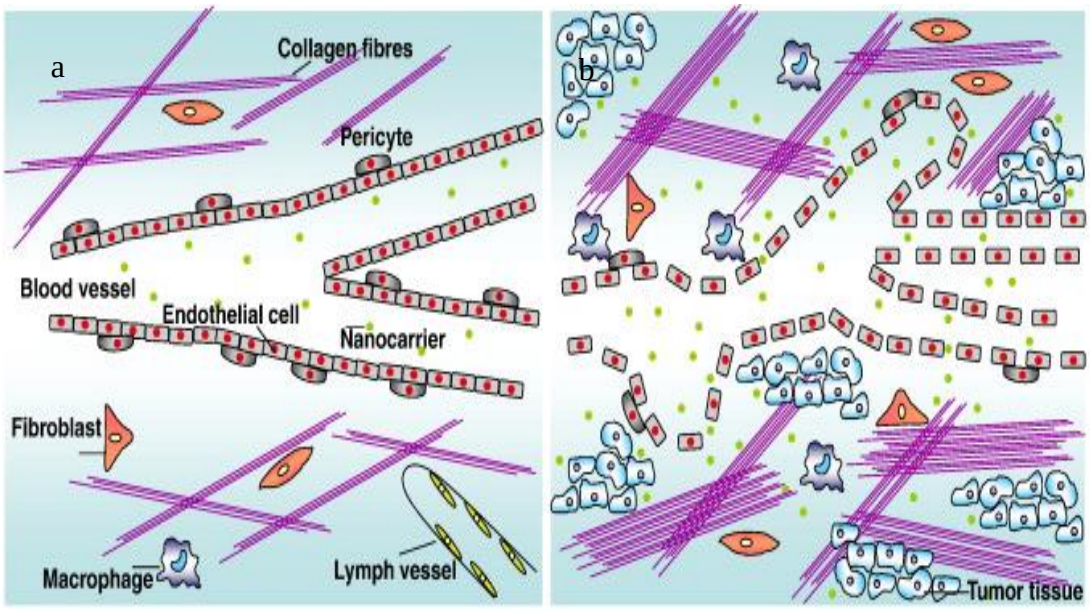

Figure 2-1 Schematic diagram depicts the passive targeting mechanism (a) normal tissues and (b) tumour tissues (adopted from Danhier et al. 2010)

The tumour microenvironment differs in terms of oxygenation, pH and metabolic conditions from a normal microenvironment in the defective vascular system, (Cho et al. 2008). The high proliferation rate of cancer cells leads to insufficient supply of nutrients. They are dependent on glycolysis, which produces an acidic environment. The intra-cellular pH of cancer cells is lower (6 to 7) while in normal cells, it is 7.4 (Danhier et al. 2010). The pH-sensitive liposomes are stable at pH 7.4 and below pH 7.4 destabilisation occurs which triggers to release the cargo (Yatvin et al. 1980).

2.2.4 Active targeting

In the active targeting, nanocarriers are functionalised with ligands, such as small peptides, proteins, nucleotide base pairs, sugars and vitamins. These molecules can recognise the receptors specifically to target sites, which are expressed on the targeted cells. Target receptors may also be proteins, sugars or lipids (Saha et al. 2010). In the initial stages of active targeting experiments, antibodies attach directly to drug molecules, however these were unable to increase the drug efficiency due to rapid clearance by MPS

(Tolcher et al. 1999). Shortly after, various types of vehicle systems were designed and synthesised, possessing the ability to prevent MPS and selectively targets the cells. These nanocarriers are comprised of ternary structures i.e. drug molecule, carrier and targeting molecule (Wu et al. 2011). Nanocarriers should have two key properties; ability to bind to the ligand and have a delivery capacity. The selection of ligands is critical. The receptor should be expressed uniformly and on targeted cells only, nanocarrier and ligand should not be detached during blood circulation. The schematic diagram of active targeting nanocarrier is depicted in figure 2.2.

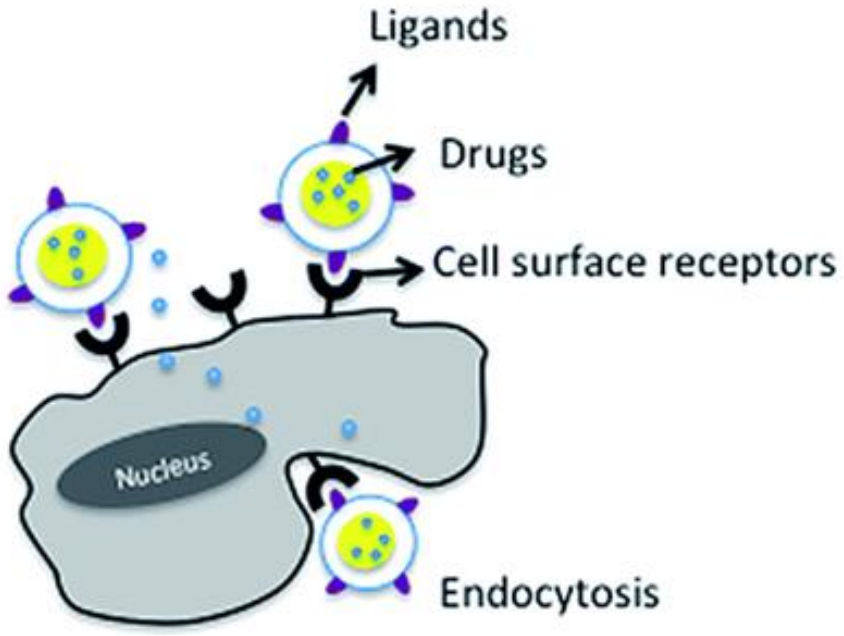

Figure 2-2 Schematic depiction of receptor mediated active targeting nanocarrier (adopted from Salim et al. 2014)

2.3 Nanoscale drug delivery tools

Nanotechnology is being studied extensively for controlled drug release such as in cardiovascular diseases (Guzman et al. 1996), orthopaedics (Holland & Mikos 2006), diabetics (Eerikäinen & Kauppinen 2003) and optometry (Le Bourlais et al. 1998). The worldwide market of nanomaterials has expanded significantly over the last decade and

is around 60 billion per year, and over 100 million people are using these materials (Karim 2015). Some of the most commonly used nanomaterials are discussed.

2.3.1 Polymeric Micelles

Studies on biodegradable materials have increased exponentially, especially in the field of oncology. Nanomaterials carry drugs by encapsulation, trapping, solubilising, ionic interactions and covalent attachment. The resulting structures are different such as nanospheres, nanotubes and nanocapsule depending on the composition of polymers, drug attachment and method of preparation. Polymeric nanoparticles are biocompatible and surface tuneable. The method of preparation is simple and cost effective. Polymeric nanoparticles increase the pharmacokinetic of the drug by adjusting the release of environmentally sensitive drugs (Putnam & Kopeček 1995). Biodegradable cationic polymeric nanoparticles have already been used in drug delivery for example, polylactic acid (PLA), polyglycolic acid (PGA), proteins, sugars and synthetic materials such as polymethyl methacrylate (PMMA), Polyethene glycol (PEG) and poly-glutamic acid (Cho et al. 2008).

Naturally, occurring polymers such as albumin and chitosan have been studied for the delivery of protein, DNA and drug. Some of the formulations are in clinical trial in different types of cancers such as lung and-and non-blood tumours (Green et al. 2006; Nyman et al. 2005), and oral delivery (Gan & Wang 2007). Dendrimers have been extensively studied as a delivery vehicle and in diagnostic applications. These macromolecules provide globular structures composed of branches (hydrophilic) attached to the core (hydrophobic unit) and surface groups. An individual dendrimer can carry three agents such as a therapeutic drug, a diagnostic agent and targeting element (Gillies & Fréchet 2005). The release of loaded molecules depends upon the length and rigidity

of branches. Gillies et al. (2004) studied the pH and enzymatic stimuli-responsive dendrimers to release the cargo at targeted sites. Half-life and clearance from kidney are adjustable with the length of branches. The dendrimers with a molecular weight around 40 kDa showed an increased half-life in the blood stream (van der Poll et al. 2010). The conjugated dendrimer with doxorubicin showed tenfold decreased toxicity in mice compared to free drug. The half-life of doxorubicin conjugated dendrimers was 16 hours when administered intravenously. The uptake of cells for conjugated dendrimers was ninefold higher than that at free doxorubicin (Lee et al. 2006).

Biodegradable polyamide amine (PAMAM) is dendrimer and studied for DNA encapsulation delivery. Encapsulation protects the DNA from enzymatic breakdown and increases the cell uptake by crossing from cell membrane barriers. A huge variety of dendrimers has reported from the core materials to surface groups of alcohol, amine, and carboxylic acid. The dendrimer theragnostic nanoformulation was obtained by combining the imaging probe, drug and folic acid (Majoros et al. 2006). PEGylated dendrimers also have a half-life (increased accumulation at tumour vascular system). PEGylating was achieved by attaching PEG molecules to dendrimer surface groups. PEGylated dendrimer conjugated with 5-fluorouracil showed no haemolytic toxicity (Guillaudeu et al. 2008).

2.3.2 Carbon nanotubes

Carbon nanotubes possess a variety of properties that includes electrical conductivity, thermal ablation and have high surface area. Carbon nanotubes are classified in two categories single wall carbon nanotubes and multi-wall carbon nanotubes. The single wall carbon nanotubes size ranges from 0.5 nm to 2.0 nm in width while 20 nm to approximately 1 μm in length and multi-wall carbon nanotubes size ranges from 1.4 nm

to approximately 100 nm in width and 1μm to several μm in length (Bianco, Kostarelos, Partidos et al. 2005).

Carbon nanotubes have been studied from field emission displays (Bianco, Kostarelos, Partidos et al. 2005) to biological applications. Biological applications include detection and separation of DNA and proteins and as drug, proteins and DNA carriers (Bianco, Kostarelos & Prato 2005). Applications of carbon nanotubes in cancer treatment include thermal ablation and delivery of anticancer drug to the cells. Carbon nanotubes have successfully delivered the short length nucleotides to the cells (Kam et al. 2005). Thermal ablation therapy of carbon nanotubes has been studied in biological systems. Where carbon nanotubes at the near infrared (NIR) region (700 nm–1400 nm) absorb light, hence this strong absorbance is used deliver their cargo in a cell by rupturing the membrane using NIR energy (Bianco, Kostarelos & Prato 2005). NIR energy creates excessive heat that causes the cell damages. Thus, by attaching targeting moieties on the surface of carbon nanotubes selectively kill the cells, reducing the toxic effect to normal cells. Temperature dependent studies showed that cellular uptake of targeted carbon nanotubes was lower, which suggest the energy dependent cellular uptake of carbon nanotubes (Kam et al. 2005). Constant exposure of NIR (800 nm laser at 14 $kW.m^{-2}$) carbon nanotubes 25 $mg.L^{-1}$ up to 3 minutes can increases the temperature up to 70 °C if exposure remained for a longer time this can reach to boiling of the solution. The folate receptors are overexpressed on the surface of cancer cells. Folate functionalised carbon nanotubes have shown the maximum cell damage with the NIR exposure, however, the normal cells, folate are not expressed did not damage. In addition, carbon nanotubes were localised into the cells, when labelled fluorescence tag and showed receptor-mediated endocytosis pathway of cellular uptake.

Carbon nanotubes have successfully delivered the small interfering RNA (siRNA) to the target cells. This successful delivery of siRNA was confirmed *via* the proliferation of tumour cells in a mouse model (Bhirde et al. 2009).

The biocompatibility of carbon nanotubes has been assessed with human cells. Carbon nanotubes have inhibited the cells growth, which was related to time and dose dependent manner (Cui et al. 2005). The cells, when treated with carbon nanotubes, released the proteins up to 40 kDa. These proteins then interwoven with carbon nanotubes causes the cells and carbon nanotubes aggregations. Amphotericin B covalently attached with carbon nanotubes containing a fluorescent dye. This complex structure of drug fluorescence dye and carbon nanotubes was taken by three fungi species (Candida paraphimosis, Cryptococcus neoformans and Candida albicans) (Wu et al. 2005). This amphotericin B functionalised carbon nanotubes showed more antifungal activity then event amphotericin B as alone. The anticancer drug (methotrexate) was also delivered with fluorescence functionalised carbon nanotubes. This delivery system showed time and dose dependent uptake of drug into cancer cells. Methotrexate also found to have more cellular uptake when delivered with the carbon nanotubes.

Carbon nanotubes lack solubility in biocompatible solvent systems. Functionalisation improves the carbon nanotubes solubility. In addition, it also decreases the polydispersity and aggregation. However, some limitations still need to be overcome such as cost effectiveness, reproducibility, large scale production possible minimal impurities (Baughman et al. 2002). Ecological and environmental hazards such as lungs and pulmonary toxicity. Carbon nanotubes, when treated to lung cell, showed dose and time dependent inflammation (Lam et al. 2004). There is still a long way to overcome the chronic inhalation based serious occupational health hazards of carbon nanotubes.

2.3.3 Liposomes

Liposomes are amphiphilic lipid-based vesicles, resembles with the cell membrane. The membranous vesicles are of either one layer or multiple layers also called unilamellar or multilamellar respectively. The membranes lipids are encapsulated in bilayers of hydrophilic and hydrophobic moieties (figure 2-3). Liposome-based drug delivery system reported since 1970s. However their nanoscale size distribution was focused since early 1990s (Kim 2007). Liposomes, do not fit within the core of nanotechnology due to the nanoscale definition of National Nanotechnology Initiative (NNI) as their size >100 nm. In contrast, the redefinition of materials up to 1 μm enables liposome to be studied in nanotechnology discipline.

The difference in head groups and a variety of fatty acids length alter their transition temperature, leading them as an ideal candidate for the tuneable structural configuration and control release of drugs to the sites (Simões et al. 2004). The temperature sensitive liposomes released the drug at 40 °C. These temperature-sensitive liposomes were made from the dipalmitoylphosphatidylcholine and mono palmitoyl phosphatidylcholine. The lipid transition temperature liquefies the membrane that releases the encapsulated drug. The phase transition temperature can be altered by modifying the fatty acid chain length and incorporation of cholesterol.

The liposomes rapidly cleared in blood circulation *via* Reticuloendothelial System (RES), which is a major drawback. A variety of strategies has been suggested to increase their half-life. PEG coating is a key approach for making them hydrophilic and biocompatible vesicles. The PEG form a cloudy layer on the surface, which prevents the attachment of opsonin and prevents the uptake by MPS (Karanth & Murthy 2007). PEG attached liposomes reached successfully in the clinical trials (Gabizon et al. 2004). One of the

drawbacks of these stealth liposomes is the release of cargo. Recent studies show that liposome once reaches at target site *via* EPR effect (Maeda et al. 2009) the PEG can be removed *via* acidic environment of the tumour. Other polymers have also been studied for coating such as poly meth acrylamide (PMAM) (Whiteman et al. 2001), polyvinyl pyrrolidone (PVP) (Torchilin et al. 2001; Takeuchi et al. 2001), amino acids such as asparagine and glutamine (Metselaar et al. 2003).

The liposomes can be functionalised with the ligands that recognise the target cell to avoid the drug contract with normal cells. Folate and Ig fragment are used as targeting moieties attached covalently to the liposomes. If liposomes could not have sufficient time to reach the target cell, they can accumulate in the liver.

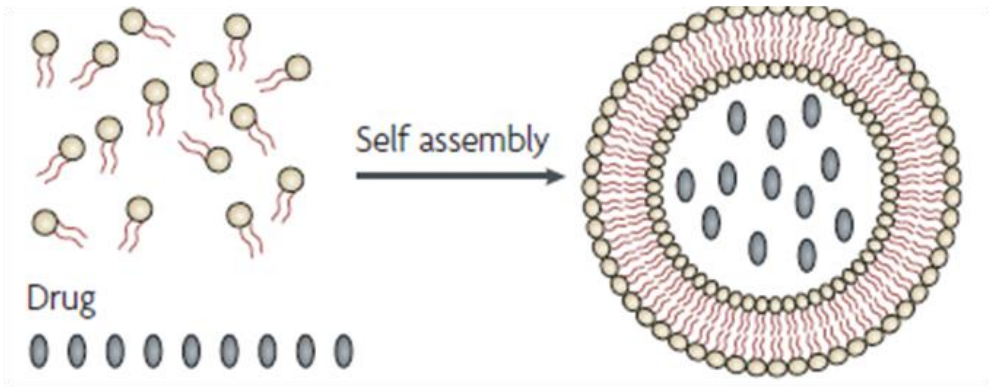

Figure 2-3 Self-assembly of phospholipids and drug molecules (left) into a liposome containing drug molecules (right) (Adapted from Davis et al. 2008)

The ligand and PEG-functionalised liposomes still do not overcome limitations arising immune system, attachment of proper ligand with compromising the integrity of structure and aggregation. Agglomerated liposomes again rapidly cleared by MPS. Meanwhile, if the ligand is covered with PEG coat, then the ligands receptor proteins interaction will be compromised.

2.3.4 Self-assembling peptides

Self-assembly of macromolecules is an attractive approach for nanostructures synthesis. This approach has been found useful in a variety of fields such as; bioelectronics to sensor devices, drug delivery systems to tissue regeneration. The idea of self-assembling the molecules was suggested by (Feynman 1960). It is a common strategy to obtain nanoscale structures, which is a "top-down" approach to achieving two-dimensional structures. Nanomaterials up to the size of 50 nm have been successfully achieved with lithography. The self-assembly at the molecular level is a promising approach to build the nanoscale functional materials.

The self-assembly is referred to the spontaneous diffusion or aggregation of individual molecules. The hydrophilic, non-covalent van der Waals and hydrophobic interactions govern this process of self-assemblies. The variety of bimolecular self-assemblies has been reported such as including; proteins (Ringler & Schulz 2003), peptides (Riley et al. 2009) and aromatic compounds (Bushey et al. 2003; Petitjean et al. 2002).

Peptides are sequences of proteins or their *de novo* designed analogues which can be self-assembled leading to a variety of structures, spheres, tubes, rods and gels. The majority of peptides are analogical sequences of the segments of naturally occurring proteins, such as amyloid peptides of amylogenic proteins which have formed aggregates in aqueous solutions (Ray et al. 2006). Besides the naturally occurring peptides, these can be designed for desired sequences for the aggregation. A variety of synthetic amphiphilic peptides has been used to form micro/nanostructures (Aggeli et al. 2001).

i) Diphenylalanine peptide nanotubes

Diphenylalanine (FF) peptide monomers are commercially available with a molecular weight of 312.37 $g.mol^{-1}$. The FF readily formed nanotubes. These self-assembling structures are normally referred to as Phe-Phe or FF class, occasionally including other hydrophobic amino acids (leucine, isoleucine and tryptophan) along with phenylalanine (Görbitz 2007).

The self-assembly of FF-based Peptide Nanotubes (PNTs) is the simplest way to obtain nanostructures (Reches & Gazit 2003). The hydrophobic interactions of the side groups of amino acids move to same side groups of peptide backbone forming tubular structures with the water molecules interacts with the hydrophilic amino and carboxylic groups. Song et al. (2004) Showed that they formed PNTs by dissolving the FF in the HFIP. However, the data suggested that FF monomers shared different nanotube properties such as straightness, stiffness and number of branches. Various studies have been performed on the modification on the amino terminal of FF (Table 2-1).

Table 2-1 Modified analogues of FF peptide and their nanostructure pattern

Structure	Self-assembling pattern	References
BOC-Phe-Phe-OH	Nanotubes, spheres	(Reches & Gazit 2003; Song et al. 2004)
Fmoc-Phe-Phe-OH	Hydrogel	(Mahler et al. 2006)
Ac-Phe-Phe-OH	Nanotubes	(Reches & Gazit 2005)
H_2N-Phe-Phe-OH	Nanotubes	
Z-Phe-Phe-OH	Amyloid	

FF, when modified with BOC group at the amino terminal, resulting two types of nanostructures which are reported as nanotubes and nanospheres (Adler-Abramovich & Gazit 2008). In both cases, FF was dissolved in HFIP at a concentration of 100 $mg.ml^{-1}$. Further dilution was performed using water as a solvent for the native structures

(nanotubes). However, when these peptides were dissolved in ethanol-water (50 %) mixtures after dissolving in HFIP, they showed a spherical structure with average size 500 nm to 2 μm (Reches & Gazit 2003). Another analogue of FF modified with fluorenyl methoxycarbonyl (Fmoc) group. Fmoc-Phe-Phe-OH exhibited a gel-like structure in an acidic environment (Johnson et al. 2011). These hydrogels can be potentially used in tissue culture scaffolding, biosensing, drug delivery carrier and in batteries (Reches & Gazit 2005). Initially, the structural organisation was proposed, similar to that of amyloid formation of individual monomers arranged in β-sheets confirmations. The confirmation method used in addition to experimental data analysed with FTIR and amyloid disease testing methods such as Congo red staining (Reches & Gazit 2003). The FF contains two phenylalanine amino acids, which is hydrophobic with amino and carboxylate as hydrophilic groups backbone (figure 2-4).

2.3.1 Doxorubicin

The cytotoxic drug doxorubicin (DOX) was chosen as a model drug. It intercalates and inhibits the DNA and RNA synthesis. It restricts the catalytic cycle of Topoisomerase II by stabilising it in cleavable complex and subsequently it breakage the DNA strands (Holmgren et al. 2015). DOX can form the reactive oxygen species, which damages the cells. DOX can inhibit the nitric oxide synthase activity, which is the result of significant damage in tumours (Świerniak et al. 2016). However, the dose-limiting toxicity, chemotherapy-induced myelosuppression, rapid elimination from the body and acute renal failures restricted its use in clinical applications. Hence, the importance of designing new strategies for safe and multifunctional carriers for DOX increased exponentially (Liu & Auguste 2015). Loading of the DOX into the peptide coated magnetite nanoparticles

was carried out with the combination of two different methods including ultrasonication and incubation

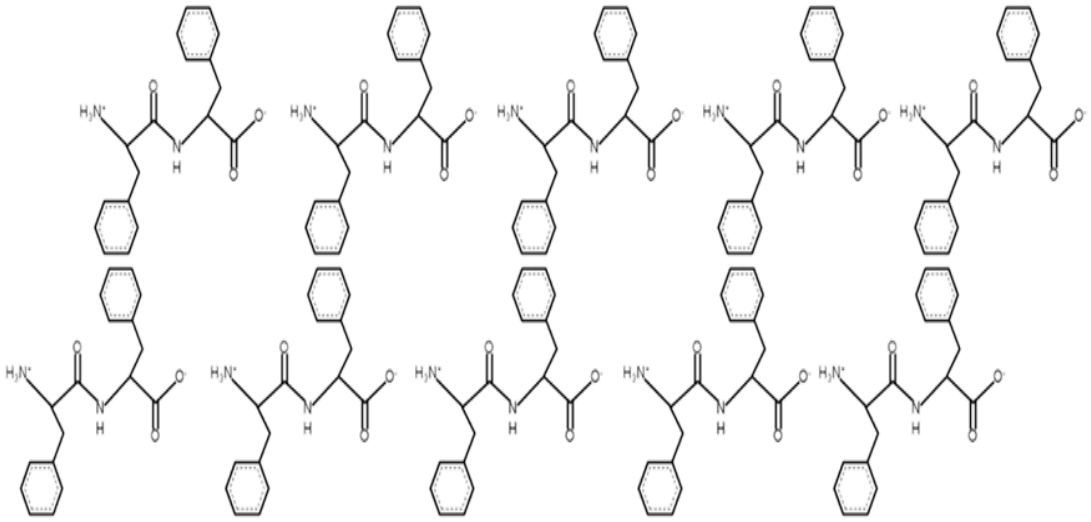

Figure 2-4 Proposed model of non-modified FF peptide as linear tubes (where hydrophobic and ionic interaction assumed to play role)

2.3.2 Iron oxide nanoparticles

Superparamagnetic iron oxide nanoparticles (SPIONs) also have received significant attention (figure 2-5), including superparamagnetic features and tunable physicochemical properties such as size, shape and constituent of materials. Additionally, iron oxide is known as biocompatible iron ions with biological systems. Size may be controlled from several to hundreds of nanometres, smaller than living cells (10-100 μm) being more comparable to viruses (20 – 450 nm) or proteins (5 – 50 nm). Proteins, lipids, smaller peptides and polymers coated by magnetic nanoparticles can be a useful tool in biochemical applications (Bruce et al. 2004a; Mahmoudi et al. 2011; Sen & Bruce 2009; Zheng et al. 2013; Elhissi et al. 2012).

i) Magnetite (Fe_3O_4)

Magnetite is naturally occurring minerals black in colour with strong magnetic properties. Magnetite **(Fe_3O_4)** crystal has been seen in certain bacterial, birds and human brain (Šafařík & Šafaříková 2002). Magnetite are inverse spinal in cubic structural configuration, which closely packed with oxygen and iron in both tetra and octahedral fashion. Thus, magnetite possesses interesting magnetic properties from iron spins in both tetra and octahedral interaction sites. In bulk form, magnetite possesses higher Curie temperature and are ferromagnetic at room temperature (Lowrie 1990). However, due to their nanoscale size distribution possess superparamagnetic behaviour. The arrangement of ferric and ferrous ions in both sites creates electron transfer *via* applied magnetic field. If the particle size is > 50 nm, the individual particle has a single randomly oriented domain that caused superparamagnetism. Thus, the size and shape influence the coercivity and remanence effect (Hergt et al. 1998). The nanomagnetite have a high surface-to-volume ratio. Therefore, they tend to aggregate, while decreasing their surface energy. During synthesis or storage, magnetite oxidises to maghemite. One of the important roles of coating materials is to prevent aggregation and oxidation of magnetite. The superparamagnetic behaviour, when modified with biomaterials can be an ideal candidate for biomedical applications. Alongside the above applications, the nanomagnetite have been used in other applications, such as magnetic seals, contrast agents, bio-separation, catalysis, hyperthermia and applied external field directed targeting (figure 2-5) (Santhosh & Ulrih 2013; Mahmoudi et al. 2011).

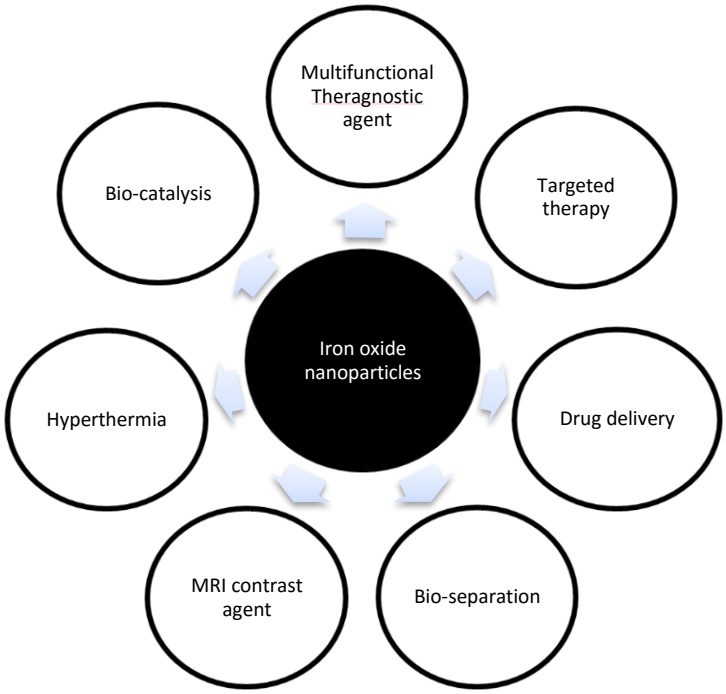

Figure 2-5 Biomedical applications of iron oxide nanoparticles

ii) Synthesis routes of magnetite nanoparticles

In this section, a different preparation method for magnetite iron oxide proposed so far will be discussed.

a) Co-precipitation: this method is comparably simple, quick and cost-effective for the preparation of magnetite and maghemite nanomaterials. This method is involved in mixing of ferric and ferrous ions (usually 1:2 or 1:1.5 respectively) in alkaline medium. However, the acidic medium can also be used. Ideally, the solution is heated below 80 °C (or at room temperature). To avoid the oxidation of magnetite to maghemite inert gas environment is used. The parameters such as temperature, pH and molar ratio affects the size, shape and type (magnetite or maghemite) of resulting products.

Though this is the easiest method for the iron oxide nanoparticles synthesis in aqueous solution, some researchers also have used the surfactant to the solution to avoid the

aggregation and obtaining of narrow size distributed nanoparticles (Mahmoudi et al. 2011).

b) Thermal decomposition method: This method involves in thermal decomposition of iron (III) (dodecacarbonyl) or iron (III) (acetylacetonate) source in absolute ethanol using temperature up to 280 °C. This method though bit complicated but yields monodispersed nanoparticles. The nanoparticles cannot be dispersed in aqueous medium but only be dissolved in organic solvent along the use of surfactant (Maity et al. 2009; Amara et al. 2009).

c) Microemulsion method: This method involves more complex system comprising of three main components; polar, nonpolar and amphiphilic mediums. The amphiphilic substances (surfactants) reduces the surface tension of both immiscible mediums and produces the transparent medium. The water nanodroplets in bulk oily medium provide the "nanoreactors" for the synthesis of resulting iron oxide nanoparticles. The shape of water nanodroplets are spherical so provide spherical nanoparticle, meanwhile size of these nanodroplets influences the size of resulting nanoparticles. Thus, the size and shape of nanoparticles can be tuned according to size and shape of water nanodroplets (Laurent et al. 2017).

d) Hydrothermal method: This method involves the high pressure and temperature to hydrolyse the dehydrated salt resulting in the supersaturation of metal salts. The high temperature and pressure are used to achieve increased dehydration with good diffusivity of salts in water. In this approach, higher supersaturation can be obtained fine grains having good crystallinity. The reaction parameters such as time, temperature, pressure and iron source can be tuned to obtained desired size and shape of nanoparticles. This process does not involve the use organic solvent or surfactant (Cai et al. 2013).

e) Sonochemical method: this method involves the use of ultrasound waves arise from acoustic cavitation. The formation, growth and implosive collapse of bubble occur in the aqueous medium. The implosive collapse creates a confined hotspot through shock wave within the bubbles. This hotspot creates extreme conditions in which nanoparticles are formed. The nanoparticle formed with this method usually have undefined shapes and sizes.

2.3.3 Hyperthermia and magnetic field triggered drug release from core-shell materials

The term hyperthermia indicates the increased temperature based precise therapy of body tissues. In cancer applications, hyperthermia is the treatment of cancer exploiting the increased temperature. According to initial studies, increased precise heating can cook the cancer cells (Hahn 1974; Quinto et al. 2015). The hyperthermia-based treatment could be divided in three categories based on the temperature utilisations.

a) Diathermia: in this type of hyperthermia treatment temperature usually be kept lower than 41 °C. This type of treatment is used for physical and occupational therapies. The heat is induced from ultrasound, microwave and shortwave.

b) Moderated hyperthermia: This applies to the treatment with temperature ranges from 40 °C-45 °C. This range of temperature is ideal of killing of cancer (Nikam et al. 2014).

c) Thermal ablation: In this hyperthermia-based treatment, the temperature reaches up to 55 °C. This temperature causes the necrosis of cells, coagulation of body proteins and other biomolecules. The hyperthermia can be used into localised area, regional or organ based or even for whole body (Majeed et al. 2014).

Different techniques can induce the hyperthermia-localised temperatures, including IR radiation, ultrasound, microwave, magnetic based materials, and administration of heated liquids or direct heating from chamber. The hyperthermia based treatments of cancers, however proved effective in initial clinical trials (Cihoric et al. 2015). The molecular mechanism behind the cells killing is still not fully understood. Several studies have revealed the intracellular mechanism of heat induced cell damages. The hyperthermia activate the energy for proteins coagulation (Kampinga 2006). The proteins in nucleus are more sensitive to hypothermia induced coagulation compared to other intracellular biomolecules (Lepock 2004). Moreover, the nucleus is more efficient place for heat-induced protein denaturation (Nishita et al. 1998). Meanwhile, studies have revealed the good correlation of heat-induced cell damaging and nuclear proteins denaturation (Kampinga & Dikomey 2001; Kampinga 2006).

The relation between immune system and hyperthermia was studied (Shen et al. 1994). According to these studies, hyperthermia was assumed to have increased the whole body temperature after applying the localised hyperthermia. However, it promotes the defence system by inducing the immune system. The killing of cells starts at 40 °C. *In vivo* studies confirmed the accumulation of dead cells in cancer sites after localised hyperthermia (Burd et al. 1998). Another important application of magnetic field triggered drug release and targeted region (localised hyperthermia), which also triggers the drug release to specific sites.

i) Methods for induction of Hyperthermia

a) Heated water circulations: this is the oldest techniques used for induction of hyperthermia, in which whole body is kept in insulated chamber where circulating warm water increases the heat inside the body. This technique was initially used in replacement

of chemotherapy or radiotherapy. To achieve the hyperthermia different instruments were design in a systematic way, where patient whole body is kept inside chamber except its head (Pettigrew et al. 1974). This type of hyperthermia approach is recommended to high-risk patients after surgery. This technique has a drawback of the non-uniform distribution of heat inside the body, which causes the lesions and surface burning. This approach could not reach to the patients because of its side effects such as on cardiac arrest, red blood cells and platelets deficiency and biomolecules coagulations. In general, this approach has led to the investigation of localised hyperthermia.

b) Non-invasive wireless induced hyperthermia: In this approach, localised regions are targeted *via* applying waves; these waves cause heat generation over targeted region. The various applicators are studied and commercially available for treatment of localised cancers. Such heat inducing applicators include; high energy focused ultrasound waves, non-invasive electromagnetic radiofrequency waves, infrared frequency based microwave, electromagnetic frequency waves based on inserting the antennas to avoid the un-even distribution of heating in localised hyperthermia, macroscopic radiofrequencies electrodes induced heating for localised hyperthermia, few centimetres ferromagnetic materials implantation in a magnetic field and nanoparticles (Varon & Acosta 2008; Vaupel et al. 1989; Wust et al. 2002; Lele 1990).

c) Nanoparticles induced hyperthermia: In nanoparticles induced hyperthermia, heat is produced from loss of hysteresis or relaxation over applied Alternate Current (AC) magnetic field. This approach of hyperthermia-based treatment is more precise, where nanoparticles are systematically administered to body and can be targeted *via* magnetic field or attachment of selective moieties or by exploiting enhanced permeability and

retention effect. Nanoparticles upon systematic administration in body can be directed and excited *via* applying external magnetic field. In comparison other studied approaches such as radiofrequency electromagnetic waves, microwaves and high energy focused ultrasound could not be directed by any means to the desired sites (Jordan et al. 1999). Magnetic nanoparticles also are MRI contrast materials, hence can be tracked and visualised for their localised distribution inside the targeted sites before starting the hyperthermia treatment (Mornet et al. 2004).

A systematic hyperthermia triggered controlled release drug systems were designed, where magnetic nanoparticles were coated with certain thermo-sensitive polymers and drug molecules. For this purpose, gels were used to coat the magnetic materials. These gels have shown morphological alteration when exposed to different temperatures (Ang et al. 2007). In addition, gels also work as sponge material for controlled release of payloads. In a drug delivery application, magnetic nanoparticles *via* thrust force can be propelled to targeted sites, where they can increase the temperature of hydrogel, thereby releasing the cargo molecules inside.

d) Heat induction from magnetic nanoparticles in alternating magnetic field:

The heat induction from magnetic nanoparticles is caused by either hysteresis loss, Nėel relaxation or Brownian relaxations phenomenon. The relative strength of these mechanism depends on the different factors such as; size, shape, chemical composition and strength of the nanoparticles.

e) Magnetic domains

Large size particle contains more than one domain to reduce the magnetostatic energy. This energy comes up from magnets own field. The magnetostatic energy (ME) is defined in following terms:

$$ME = \left(\frac{1}{2}\right) f H^2 \, dv \qquad \text{Equation 2.1}$$

where *dv* denotes the volume, *H* defines the applied magnetic field

Figure 2-6 explains the materials of numerous domains reducing the magnetic field *H*. The magnetostatic energy of particles reduces as domain volume increase. The domains are separated with a domain wall. A huge amount of magnetic movement *m* is produced from each domain.

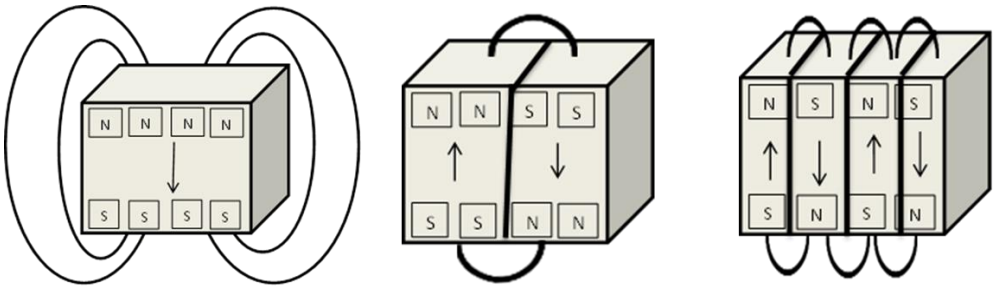

Figure 2-6 Schematic diagram of magnetostatic energy reduction as number of domains increases

The magnetic materials then can be classifies such as ferrimagnetic, ferromagnetic, antiferromagnetic and paramagnetic according to the orientation of their magnetic moment. The theory and mechanism for formation of these magnetic materials could not be possible to explain in this section; however, figure 2-7 displays the magnetic moment orientation of different magnetic materials. The magnetic moment orientation of ferrimagnetism, ferromagnetism and antiferromagnetism is aligned in one direction under

the Curie temperature. Magnetic moment orientation varies from domain to domain; however, the domains are aligned in one orientation, when external field is not applied, this orientation is called “easy axis”.

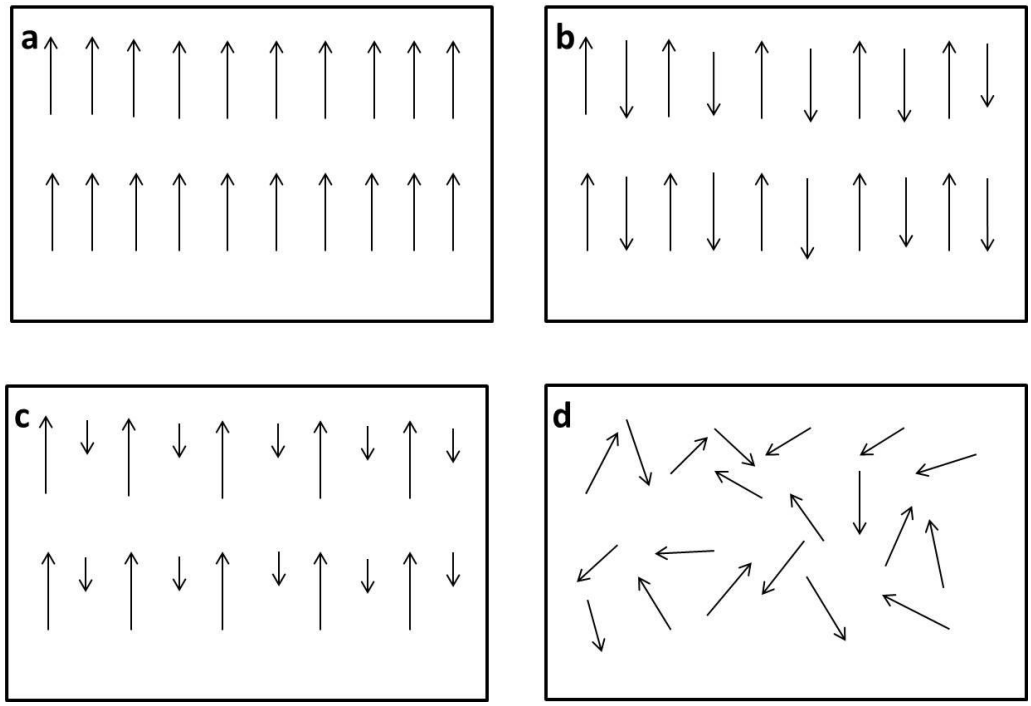

Figure 2-7 Schematic diagram of magnetic moment orientation of different magnetic materials (a) ferromagnetic, (b) antiferromagnetic, (c) ferrimagnetic and (d) paramagnetic materials

ii) Hysteresis

The application of moderate magnetic field *H*, magnetic moment of particle energy control over the anisotropy energy (Harris 2002). This change is energy reciprocally rotate the magnetic moment of domains into the new orientation, these orientation are moving with exposure of applied external magnetic field. The changes in magnetic moment of domain walls are somewhat comparable to the anisotropy energy. Thereafter, as applied external magnetic field modify the balance of energies causing the moment’s re-orientation. Increased magnetic field led to achieve saturation magnetisation (*Ms*) of magnetic materials (figure 2-8). The magnetic moment reversed and slowly aligned with

applied magnetic field amplitude direction causes the hysteresis of sample of single domain (Jiles 2015). Hence, *Ms* value for microsize materials is different compared to nanosize materials. The observed experiment *Ms* values for nanosize magnetic materials were in range of 30-60 emu.g^{-1}, compared to bulk magnetic materials, where *Ms* value were 90 emu.g^{-1} (Harris 2002). The nanosize magnetic particles containing single domain of less than 50 nm approximately called superparamagnetic iron oxide nanoparticles (SPIONs). In SPIONs, the higher magnetic moment and lower potential energy in volume is significantly smaller compared to their thermal energy. Therefore, thermal energy itself creates the magnetic moment of nanoparticles with applying magnetic field (Brown Jr 1963). This behaviour of iron oxide materials causes the lack of hysteresis losses. Where coercive fields do not reaches to zero, lacking hysteresis loss creating the heat release within nanosize magnetic materials.

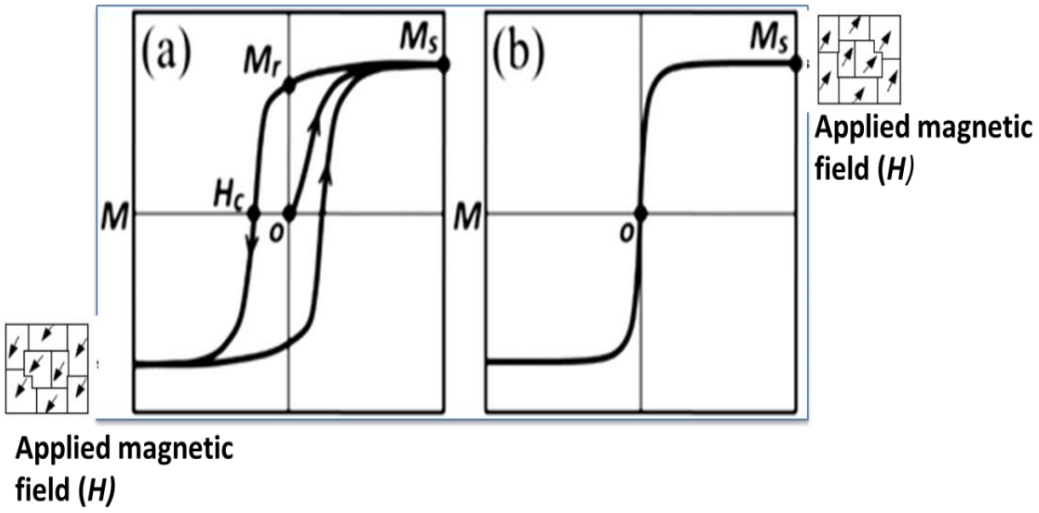

Figure 2-8 Hysteresis curves of (a) several domain bulk magnetic materials and (b) single domain superparamagnetic nanoparticles (adopted from Frey et al. 2009)

Figure 2-8 (a) shows zero magnetisation (M=0) of non-magnetised ferri or ferromagnetic materials. When external field applied (arrows), these materials aligned with magnetic

field until they reach to *Ms* (saturation magnetisation) plateau. The *Ms* is defined as in following equation:

$$Ms = \frac{M}{p} \quad \left[\frac{emu}{g}\right] \qquad \text{equation 2.2}$$

where, p is the density of magnetised materials *M* is applied magnetic field

2.3.4 Core-shell nanocomposites

Iron oxide nanoparticles have been used as Magnetic Resonance Imaging (MRI) agents due to their slower excretion from glomeruli filtration compared to other contrast agents. SPIONs can also be used as drug delivery vehicles. Drug loaded SPIONs (drug being bound irreversibly or co-attached with coating), can be targeted using external magnetic fields to specific regions and tracked using imaging (Neuberger et al. 2005).

To attain magnetic based target, specific drug delivery SPIONs should be biocompatible, have a long half-life in blood circulation, high dispersion rate and stability against enzymes of serum and immune system. Coating of SPIONs also reduces the van der Waals attractions based aggregation (Deng et al. 2014). Aggregates of SPIONs are cleared from blood rapidly after systematic administration by macrophages reticuloendothelial system (RES) (Jain et al. 2008). SPIONs may be coated with biocompatible molecules such as cyclo(Arg-Gly-Asp-D-Phe-Cys) peptide (cRGD) to give them “stealth property” and targeted specificity (Richard et al. 2017). Proline-rich peptide coated SPIONs also showed improved MRI capability (Ozdemir et al. 2016). Coating with hydrophilic polymers such as dextran or starch and targeted to peptide for the better colloidal stability and longer circulation kinetics, have already been reported (Kim et al. 2003). However, limited drug loading and release efficiency was observed. In

addition, polylactide and dendrimer-based coating for SPIONs have been reported (Strable et al. 2001), however suffer from associated loss of magnetisation.

Lipids have also been reported as potential coating materials for SPIONs (Zhang et al. 2006), for example oleic acid coated SPIONs have shown excellent colloidal stability. However, the poor aqueous solubility is still a challenge to overcome. A thermally responsive polymer such as; poly-ethyleneimine-modified poly-ethylene oxide poly-propylene oxide poly-ethylene oxide (PEO−PPO−PEO) a block copolymer based coated magnetic nanoparticles have been reported (Chen et al. 2007). They have limitation related to their biocompatibility and biodegradability. Easy preparation method with high SPIONs, drug loading and controlled release of the drug is a highly challenging problem that needs to be overcome.

This literature review shows a summary of various nanoscale based drug delivery tools, which can be used once the aggregation and biocompatibility related issues addressed, thus it is not far that these will be in use in the future and have an impact on society.

2.4 Conclusions

This review has covered various ways in which nanoscale carriers can be used for targeted drug delivery. To overcome the limitations of the common materials currently employed, core-shell structures have been considered in detail. The researchers are studying the different core-shell structures and shapes *via* different synthesis routes. Template mediated synthesis is a useful approach for the organic shell and SPIONs core (core-shell) materials. However, all methods have shown some limitations such as loss in particle`s functional properties, difficult to separate, high cost and reaction step are complicated.

SPIONs as core material are useful for their hyperthermia response; magnetic field triggered and targeted drug delivery system. The advantage of peptide shells over other organic polymers is the ability to control the shape and structure by alternating in primary sequence or by modification to any terminal of amino acids.

CHAPTER THREE

Materials and Methods

3.1 Introduction

This chapter describes materials and methods employed in this study. It also gives the basic principles of the characterisation techniques used. It is divided into two sections: Section A and Section B.

Section A describes the type of materials used in this work. It also briefly explains the protocols performed for the synthesis of peptide self-assemblies, SPIONs of different shapes and the coating of self-assembled peptide to core-shells nanocomposites. This approach will aid the understanding of self-assemblies of short derivative peptides into nanoscale to microscale structures in an aqueous medium.

Section B describes the instrumental techniques used to characterise the stability, and conformity of synthesised structures at chemical, molecular and elemental level, quantitatively or qualitatively. These approaches will provide the base of their functional properties in targeted drug delivery applications.

3.2 Materials

All chemicals used in this project were of high purity and analytical grade and commercially available. They were used without further modification unless otherwise stated.

3.2.1 Diphenylalanine peptide analogues

Two synthetic analogues of butyloxycarbonyl-diphenylalanine (BOC-FF) with a molecular weight of 412.49 and FF molecular weight of 312.37 were purchased from Bachem (Bubendorf, Switzerland) purity > 95 %.

3.2.2 All other chemicals

HPLC grade absolute ethanol, Iron (II) chloride, hexadecyltrimethyl ammonium bromide (CTAB), tetraethyl orthosilicate (TEOS), ferrous sulphate heptahydrate and doxorubicin hydrochloride were purchased from Sigma-Aldrich (Poole, UK). 1,1,1,3,3,3-hexafluoro-iso-propanol (HFIP), Dimethyl sulfoxide (DMSO) and Iron (III) chloride were purchased from Alpha-aeser (Lancashire, UK). Aluminium stub, carbon tabs and carbon coated copper grids for SEM and TEM, respectively were from Agar Scientific (Essex, UK). Ammonium hydroxide was purchased from VWR (Leicestershire, UK). Phosphate buffer saline tablets, methanol and potassium hydroxide were purchased from Fisher Scientific (Loughborough, UK). Milli-Q water was used in all the experiments with 18 MΩ·cm resistances or otherwise discussed.

3.3 Methodology

3.3.1 Preparation of analogues of diphenylalanine based peptide into various structures in different environmental conditions

i) Synthesis of peptide nanotubes in hexafluoro-iso-propanol -water mixture

Lyophilised peptide boc-diphenylalanine (BOC-FF) and non-modified diphenylalanine (FF) powder were dissolved in HFIP at the concentration of 100 $mg.ml^{-1}$ as a stock solution. For each set of experiments, fresh stock solutions were prepared to avoid pre-aggregation as reported (Jeon et al. 2013). The stock solutions were subsequently diluted

in Milli-Q water with 18 MΩ·cm resistances to a final concentration of 2 mg.ml^{-1} and vortex mixed. The flow chart gives an indication of peptide nanotubes (PNTs) preparation (figure 3-1).

Scheme 3-1 Shows the chemical structure of (a) BOC-FF and (b) FF (adopted from Bachem 2016)

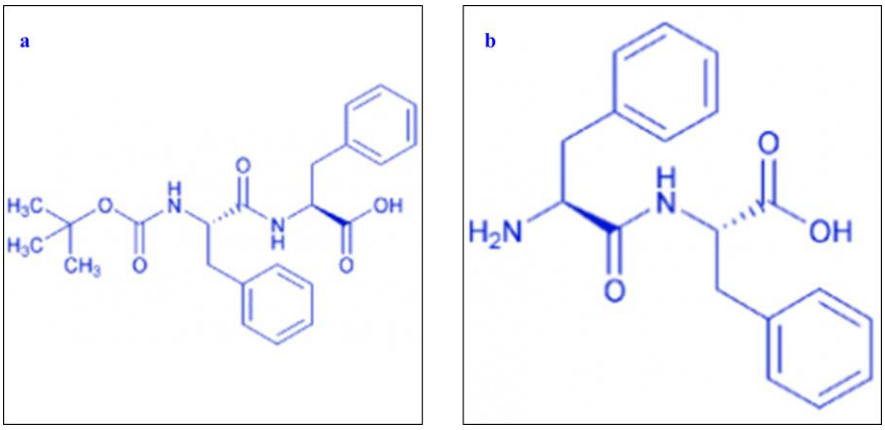

ii) Synthesis of spherical boc-diphenylalanine peptide in ethanol-water mixture

Boc-diphenylalanine was dissolved in 10 mg.ml^{-1} of absolute ethanol and then diluted to 2 mg.ml^{-1} in ethanol-water (1:1). After dilution, the sample was kept in an ultrasonic bath for 15 minutes. The solution was then left at room temperature for 15 minutes then further characterisation was performed.

iii) Synthesis of diphenylalanine peptide nanotubes in water and ethanol-water

Initially, diphenylalanine peptide was dissolved in absolute ethanol at the concentration of 10 mg.ml^{-1} (stock solution). The stock solution was further diluted to 5 mg.ml^{-1} with ethanol-water (1:1) mixtures. Experiment were performed using various concentration ranges from 2, 6, 8, and 10 mg.ml^{-1} with ethanol-water ratios of 25 %, 50 %, 75 % and in 100 % ethanol. The experiment was repeated by diluting into the water after dissolving in HFIP keeping similar condition to those discussed for BOC-FF peptides.

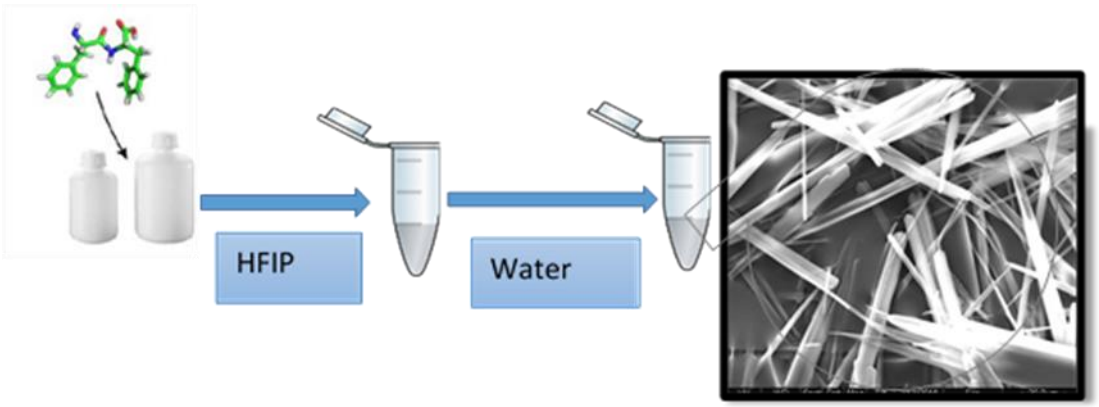

Figure 3-1 Proposed methodological diagram for obtaining peptide self-assemblies

3.3.2 Preparation of iron oxide nanoparticles involving oxidative alkaline hydrolysis of ferrous ions

Rod-shaped iron oxide (FM-ION-RS) nanoparticles were prepared by oxidative hydrolysis of ferrous sulphate ($FeSO_4.7H_2O$) in an alkaline medium. Briefly, ferrous sulphate heptahydrate ($FeSO_4.7H_2O$, 17.71 g) was dissolved in 400 ml of deionised water degassed with nitrogen in three-neck round bottom flask with a magnetic stirrer, nitrogen gas flow and condenser. The solution was heated in an oil bath connected to 90 °C with continuous nitrogen flow while stirring. Once the temperature reached 90 °C, 100 ml of 150 mM potassium hydroxide (13.8 g) and 50 ml of 5 mM potassium nitrate (oxidising agent) prepared separately were added to a flask containing ferrous sulphate solution under continuous stirring (pH 13). The temperature (90 °C) was maintained for a further two hours in nitrogen flow until a jet-black precipitate appeared. The solution was left to cool at room temperature under nitrogen. Afterwards, the solution was transferred to 2L conical flask. This material was initially washed twice with 2 L of deionised water, then once with 2 L of diluted nitric acid and again several times with deionised water until the pH value reached to 7.0. The whole washing process was performed through magnetic separation using slab magnet, and the supernatant was aspirated using the water pump.

The final product obtained from this method was jet black, and the supernatant was clear. The final volume was adjusted to 1 L with deionised degassed water. For the density measurement, three empty Eppendorf tubes were weighed and labelled. 1 mL of well-mixed FM-ION-RS was added to each tube. Water was removed through magnetic separation and left at 60 °C for overnight. The final mass of FM-ION-RS was expressed in $mg.ml^{-1}$ for further characterisation. This method yielded 25 grams. The reaction scheme for this synthesis of maghemite is illustrated in Scheme 3-2

Scheme 3-2 showing oxidative hydrolysis of ferrous sulphate into FM-ION-RS (adopted from Ketebu et al. 2015)

$$6KOH + 3FeSO_4 \rightarrow 3Fe(OH)_2 + 3K_2SO_4$$

$$3Fe(OH)_2 + NO^-_3 \rightarrow Fe_3O_4 + NO^-_2 + 3H_2O$$

$$2\ Fe(OH)_2 + 2NO^-_2 \rightarrow Fe_3O_4 + 2NO + 2H_2O + 2OH^-$$

$$15Fe(OH)_2 + 2NO \rightarrow Fe_3O_4 + 2NH_3 + 2H_2O$$

$$2Fe_3O_4 + \frac{1}{2}O_2 \rightarrow 3Fe_2O_3$$

3.3.3 Synthesis of iron oxide nanoparticles involving precipitation of ferrous and ferric chloride in alkaline medium

Ferrous and ferric chlorides (in hydrates) were precipitated as iron precursors in a molar ratio of 1:2, respectively. The precipitation was carried out using ammonium hydroxide (Bruce et al. 2004b). Briefly, iron (II) chloride tetrahydrate (3.9762 g, 0.02 mol) dissolved in 10 mL HCl (2 M). To this solution, Iron (III) chloride hexahydrate ($FeCl_3$. 6H2O, 10.8120 g, 0.04mol) was added (dissolved in 40 ml of deionised water, degassed with nitrogen whilst stirring). The solution was heated to 80 ^oC with continuous nitrogen purging to remove the oxygen from the solution to avoid oxidation of magnetite. This

solution was continuously stirred. A small amount of HCl was used to increase the chloride ions dissolution whilst heating the solution. When iron precursor solution was reached at 80 °C, 25 ml of 28 % of ammonium hydroxide solution was added dropwise over a period of 45 minutes. The solution colour became reddish brown to black, due to the nucleation of magnetite nanoparticles. The reaction was left for additional one hour under the same conditions, then the heating was turned off, and the solution was left to reach the room temperature. The solution was then transferred to 1L conical flask on slab magnet to sediment the particles. The sediment product was washed several times with deionised water to remove unreacted material and impurities. The washing process was repeated until it reached to pH 7.0. The method has produced ultra-small spherical nanoparticle with an average size around 15 nm to 25 nm. The product was labelled as B-SPION-SS. The mechanism of precipitation of iron oxide with ammonia is depicted in scheme 3-3

Scheme 3-3 Co-precipitation of iron (II) and (III) ions in alkaline medium for synthesis of spherical nanoparticles

$$2FeCl_3 + FeCl_2 + 8NH_3 + 4H_2O \rightarrow Fe_3O_4 + 8NH_4Cl$$

3.3.4 Synthesis of mesoporous silica-coated superparamagnetic iron oxide nanoparticles

Mesoporous silica-coated SPIONs were made according to the method (Sharifabad et al. 2014a; Bruce et al. 2004b; Sen & Bruce 2009; Sen et al. 2006). Briefly, 1 g of FM-ION-RS was dispersed in ethanol-water (1:1). 30 mL of 28 % ammonium hydroxide was added to the solution and stirred for 10 minutes. Subsequently, 2 g of hexadecyl-trimethyl ammonium bromide (CTAB) powder was added to the mixture. It was stirred for a further 5 minutes and sonicated in an ultrasonic bath for 15 minutes, and the solution was heated

to 60 °C in a nitrogen flow. 12 mL of silica precursor tetraethyl orthosilicate (TEOS) was added drop-wise under continuous stirring for 24 hours. The black product obtained was transferred to the 1 L conical flask. The material was then washed initially with 500 mL of deionised water (two cycles) using slab magnet, two cycles of acidic ethanol using ultrasonic bath and then several cycles of water until the pH of the mixture was reached to pH 7.0. The product was then labelled as Si-SPION-RS. A schematic depiction of mesoporous Si-SPIPN-SS is given in figure 3-2.

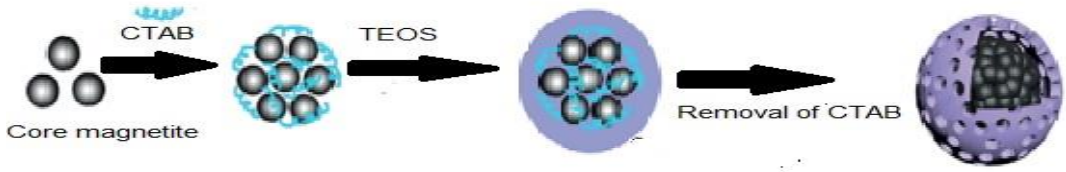

Figure 3-2 Silica coating on bare SPIONs (modified from Barbosa et al. 2016)

3.3.5 Coating of rod-shaped iron oxide nanoparticles and spherical iron oxide nanoparticles

BOC-SPION-SS were achieved in a mixture of ethanol-water (1:1) using the combination of ultrasonication and vortex mixing techniques, according to method published by Dalton et al. 2004; Talelli et al. 2009. Briefly, solutions of 20 mg, 50 mg, 100 mg and 200 mg of peptide were prepared in HFIP at the concentration of 100 $mg.mL^{-1}$. Then, iron oxide nanoparticles were taken from the stock solution, and water was removed *via* magnetic separation. The final iron oxide to peptide ratio was made 1:1, 1:5, 1:10 and 1:20 with ethanol-water mixture (1:1). The mixture was vortex mixed for 5 minutes. The samples were sonicated using ultrasonic bath for 30 minutes, yielding the dense black solution. The sonicated samples were then magnetically separated from the supernatant containing unutilised peptide was removed. The magnetically separated material was then

re-suspended in the ethanol-water mixture (1:1) and transferred into clean vials for further studies.

The BOC-FF coating to B-SPION-SS was also performed as previously described *via* template-mediated polymerisation (Wu et al. 2008). Briefly, 200 mg of BOC-FF was dissolved in 20 mL of ethanol and added to a 3-neck round bottom equipped with a magnetic stirrer. The solution pH was then raised to a pH of 7.5 using 1 M sodium hydroxide, to get negatively charged carboxyl groups on peptide structures, to increase the incorporation of positively charged Fe ions into the peptide. In another beaker, Fe (III) and (II) chlorides were dissolved in 25 mL ethanol-water mixture (1:1) and mixed for 30 minutes. The peptide solution was heated to 60 $^{\circ}$C and Fe solution was added dropwise under continuous nitrogen purging and vigorous stirring where ferrous ions were bound to the carboxyl groups of BOC-FF resulting in the formation of a dark green suspension. Magnetic nanoparticles were separated using slab magnet and supernatant containing free peptide was removed.

3.3.6 Doxorubicin loading to nanomaterials

i) Preparation of standard calibration curves for doxorubicin loaded in nanomaterials

Accurate amount 5 mg of DOX was weighed and dissolved in 50 ml of DMSO-water (1:1) to obtain a stock solution of 100 µg.mL^{-1}. The standard solutions were prepared by taking 2, 4, 6, 8, 10 ml into the 10 ml volumetric flask. Volume of volumetric flask was made with either DMSO-water (1:1) for loading or with PBS for release experiments to achieve final DOX concentration of 20, 40, 60, 80, 100 µg.mL^{-1}, respectively.

ii) Drug loading in bare spherical and rod-shaped iron oxide nanoparticles

The DOX loading was performed by dispersing different ratios (1:25, 1:50, 1:75 and 1:100 drug:carrier ratio). Briefly, 2.5, 5, 7.5 and 10 mg of FM-ION-RS and B-SPION-SS were added in 1 mL of aqueous DOX solution (drug concentration 100 $\mu g.mL^{-1}$). Following the experimental procedure described by (Unsoy et al. 2014; Byeon et al. 2016). The mixture of iron oxide nanoparticles in DOX was then mixed with rotator for 5 minutes. The solution was then sonicated for a further 5 minutes in the ultrasonic bath to facilitate DOX uptake. At this point, the UV- absorbance of free drug was taken as 0 hours. The DOX and iron oxide nanoparticles solution was kept in an incubator at 18 °C for 48 hours. During this period of incubation, at fixed time intervals, the iron oxide nanoparticles were separated from the liquid using the magnetic stand and the optical density of DOX in the supernatant was measured at λ_{485} nm by UV–vis spectrophotometer. After each measurement, iron oxide nanoparticles were re-dispersed in supernatant containg DOX solution for further adsorption. After 48 hours of adsorption time, there were no further changes in the measurement of DOX. At this point, the loading capacity of the iron oxide nanoparticles had reached to saturation. DOX-loaded nanoparticles were magnetically separated and washed with deionized water prior to use in the drug release experiments. The drug loading efficiency (DE), denotes to the percentage of drug loaded into the iron oxide nanoparticles relating to the total drug in added initially and drug loading capacity (LC), denotes to the drug content in the system were calculated using the following formulae:

$$\text{DE } \% = \frac{\text{TD}-\text{FD}}{\text{TDvol}} \times 100 \qquad \text{(Equation 3-1)}$$

$$\text{LC } \% = \frac{\text{TD}-\text{FD}}{\text{TDwt}} \times 100 \qquad \text{(Equation 3-2)}$$

where TDvol refers to the total DOX added initially to nanoparticles, FD refers to the DOX content in the supernatant and TDwt refers to the weight of nanoparticles.

iii) Doxorubicin loading in mesoporous silica-coated iron oxide nanoparticles

The density of Si-SPION-SS were measured by drying 3×1 mL of suspension at 60 °C overnight. Four different ratios were taken (1:25, 1:50, 1:75 and 1:100) for DOX and Si-SPION-SS. Briefly, 2.5, 5, 7.5 and 10 mg of SiSPION-SS were taken in Eppendorf tube. The suspensions were mixed using vortex for 5 minutes and sonicated in an ultrasonic bath for 5 minutes. The mixture was then separated using magnet and absorbance of free DOX was measured at λ_{485} nm using UV-vis spectrophotometer. The mixture was then left at 18 °C in the end-over-end rotator for further 48 hours. The samples were magnetically collected and stored at – 4 °C for DOX release studies.

iv) Doxorubicin loading in peptide coated spherical and rod-shaped iron oxide nanoparticles

The mesopores of Si-SPION-SS were capped with BOC-FF to improve the controlled release profile. In actual process, Si-SPION-SS, 10 mg were weighed and dispersed in DOX solution (1 mL of 100 $\mu g.mL^{-1}$). This solution was then left at 18 °C in the end-over-end rotation for further 48 hours. After 48 hours, peptide solution was added to the drug and Si-SPION-SS mixture and ultrasonicated to achieve a homogeneous solution. The DOX loading profile was assessed at different time intervals using UV-vis absorption at λ_{485} nm. The DOX-loaded nanoparticles were then collected and stored for DOX release studies. A schematic process of DOX loading to mesoporous Si-SPION-SS along with peptide capping is depicted in figure 3-3.

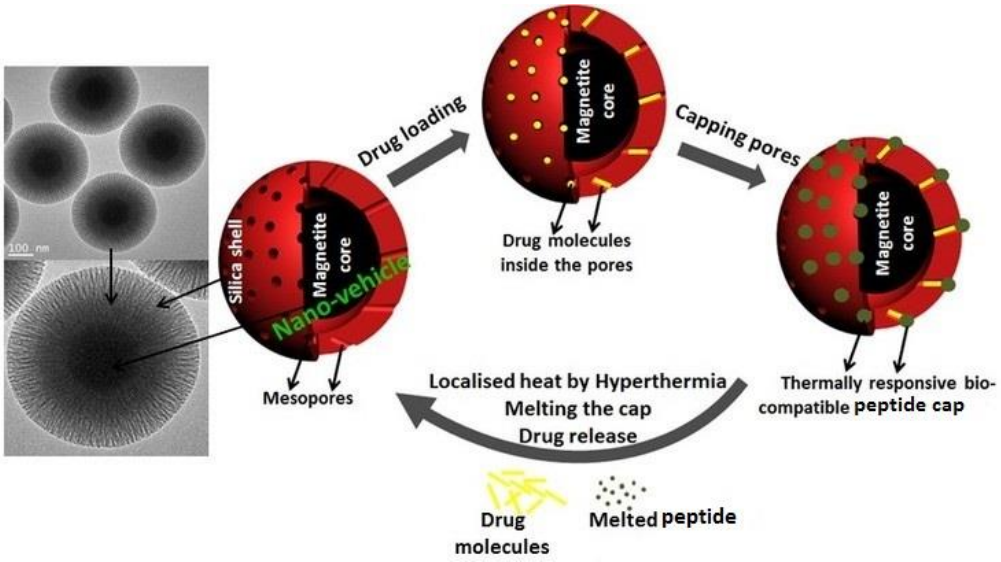

Figure 3-3 Schematic diagram of different coating on SPIONs for drug loading (adopted from Sen 2016)

3.3.7 Doxorubicin release profile of iron oxide nanomaterials

DOX release profile was assessed in PBS buffer (pH 7.4) under continuous end-over-end rotation at 37 °C in incubation and under the influence of an AC magnetic field.

i) Doxorubicin release from superparamagnetic iron oxide nanoparticles at 37 °C

The DOX release from B-SPION-SS and FM-ION-RS were assessed in 1 mL PBS buffer (pH 7.4) at 37 °C (body temperature). The DOX-loaded nanoparticles of the various ratios (1:25, 1:50, 1:75 and 1:100 DOX: B-SPION-SS or FM-ION-RS) were kept in an incubator at 37 °C temperature on an end-over-end rotator (40 rpm) for 48 hours. During this period, 200 µL of supernatant (free DOX) were withdrawn *via* magnetic separation at defined time intervals. The supernatant volume was replaced with an equal volume of fresh buffer, and the absorbance was noted at λ_{485} nm. The DOX released from B-SPION-SS and FM-ION-RS was calculated using the pre-established standard curve of DOX in PBS. The results were plotted as percentage total DOX released as a function of time.

ii) Doxorubicin release in the presence of an AC magnetic field

DOX release profile was also generated under an AC magnetic field (DM100, nB nanoscale Biomagnetics, Spain) to investigate the temperature triggered DOX release. DOX-loaded iron oxide nanoparticles (1 mL of PBS buffer) were kept in an AC field applicator using a frequency of 406 KHz and magnetic field strength 200 G for 15 minutes. A schematic diagram is depicted in figure 3-4. The DOX release profile was obtained by measuring UV absorbance at λ_{485} nm of supernatant *via* magnetic separation. DOX content was measured using the standard curve in PBS. The results have been plotted as percentage DOX release over time and temperature (see section 8.3.1 and 8.3.2).

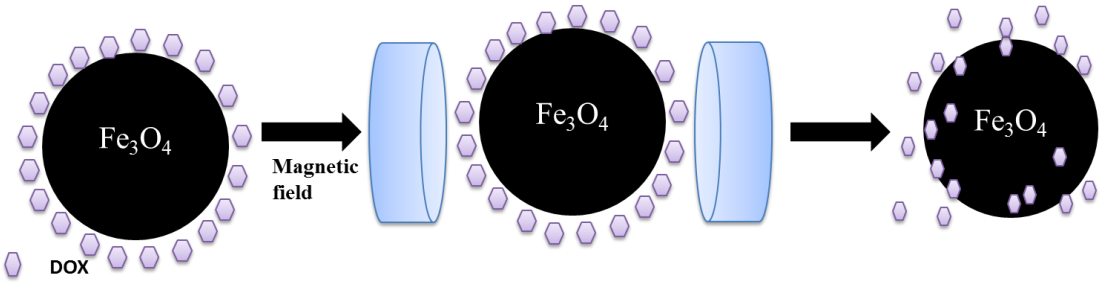

Figure 3-4 Schematic diagram of DOX release after exposure to magnetic field

iii) Doxorubicin release from silica-coated iron oxide nanoparticles at 37 °C

DOX release from silica-coated iron oxide nanoparticles (Si-SPION-SS) was performed in PBS buffer (pH 7.4). After the removal of the free DOX from loaded nanoparticles, 1 mL of PBS buffer was added, and the solution was vortex mixed and sonicated for 5 minutes in an ultrasonic bath. The initial absorbance of free DOX was taken using magnetic separation. The solution was then kept in an incubator at 37 °C on an end-over-end rotation for 48 hours. 200 µl of supernatant from magnetic separation was withdrawn at various time intervals, and DOX content released into the solution was calculated. The

calculation of DOX in the solution was carried out using the standard curve of DOX in PBS buffer (Giri et al. 2005).

iv) Doxorubicin release from the core-shell magnetic nanocomposites

DOX release profile of core-shell (peptide-capped mesoporous silica-coated iron oxide nanoparticles and peptide coated nanocomposites was evaluated in PBS buffer (pH 7.4) at 37 °C in incubation and under the exposure of magnetic field. DOX-loaded nanocomposites were dispersed in 1 mL PBS buffer (pH 7.4) by vortex mixing and ultrasonication for 5 minutes and initial OD at λ_{485} was taken. The dispersion was then kept at 37°C in an incubator with end-over-end rotation for 48 hours. At each time interval (0, 6, 12, 24, and 48 hours), 200 µl of the supernatant was taken after the separation of nanocomposites *via* magnetic separation for UV-vis absorption measurement at λ_{485} nm. The DOX content was calculated using the standard curve of DOX in PBS.

Similarly, DOX release profile under AC magnetic field was studied. Briefly, DOX-loaded nanoparticles in PBS buffer solution were placed in an AC magnetic applicator using a frequency of 406 kHz, and magnetic field strength was 200 G over 15 minutes. The concentration of the free DOX was calculated by magnetic separation, and UV-vis absorption was measured at λ_{485} nm.

3.4 Characterisation techniques

A variety of physicochemical properties were investigated using different instruments such as Zeta-sizer, Scanning Electron Microscopy (SEM), Energy Dispersive X-Ray Spectroscopy (EDAX), Transmission Electron Microscopy (TEM), Fourier Transform Infrared Spectroscopy (FTIR), X-Ray Diffraction (XRD), Thermogravimetric Analysis (TGA), Brunauer–Emmett–Teller (BET) analysis, Vibrating Sample Magnetometer

(VSM) and magnetic field induced hyperthermia. This section describes the principles behind the instruments and parameters used for corresponding sample analysis.

3.4.1 Scanning Electron Microscope

Scanning Electron Microscope (SEM) is a high-resolution technique used to study the surface characteristics of specimens. The electrons, instead of light, are used to give much higher magnification and resolution. The incident electron energy can be varied from 100 eV to 30 keV. The incident electrons travelled from condenser lenses in the column and focused into beams, forming a spot size on the sample. At the end of column scanning coils direct the focused beam in a raster fashion on the surface of sample (figure 3-5 a). The emitted secondary electrons are collected *via* a detector and the intensity is displayed as an image. Vacuum is used in this process. The images produce the morphology of sample surfaces. Non-conducting materials are coated with gold or platinum using sputtering system. Similarly, Energy Dispersive Analysis using X-rays (EDAX) was performed for elemental analysis. As electron beam shines on the sample surface, this leading to the excitation of an electron to a higher level where the gap is filled by an electron of higher energy level. The number and energy as X-ray are measured with a detector (figure 3-5 b).

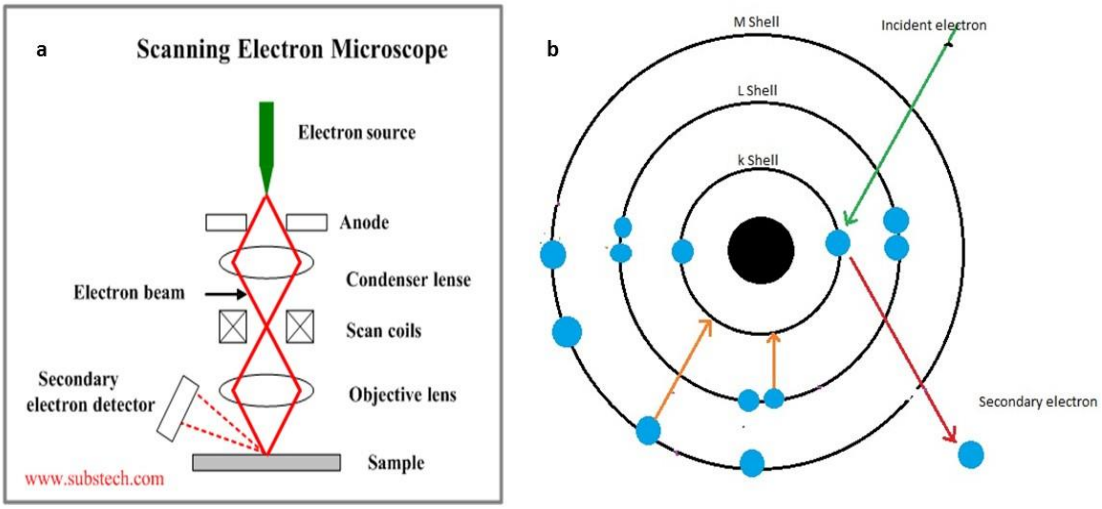

Figure 3-5 Schematic diagram of (a) SEM instrument set up (b) and energy dispersive X-ray spectroscopy. In EDAX, radiant X-ray ejects an inner shell electron; an outer shell electron, releasing a characteristics photon fills vacancy (SubsTech 2016).

The sample size, morphology and elemental composition were obtained by drying 10 µl of the sample on carbon tape on aluminium stub at room temperature. Dried sample was then coated using low vacuum fine coater at an ionic current of 25 mA for 30 seconds in each cycle in two cycles (JFC-1200, JEOL, Japan). The images were taken using Quanta-200, (FEI, UK) at different magnifications (50x to 50000x) operating at 20 kV.

3.4.2 Transmission electron microscopy

Transmission electron microscopy (TEM) was used to study the detailed structure and crystallinity of materials at the nanoscale with enhanced contrast and resolution. The electron gun at the top of instrument emits the electron flows travelling through a vacuumed column. Electromagnetic lenses condense the emitted electrons into an electron beam. This beam transmits through the sample; some of electron diffracts from sample, depending on samples electron density. Detector located at the bottom of instrument, collects the transmitted electrons from the sample. Depending on electron

density of sample, different shadow images appear reflecting the various shadow morphologies of sample contrast shadow of each shell.

TEM images of synthesised materials were taken using a JEOL JEM2000FX (JEOL, Japan) instrument at 200 kV. The images were taken using Gatan digital camera. Samples were prepared with diluted solution, a tiny drop of sample was placed on 200 mesh carbon coated copper grid (Agar, Scientific) and left to dry at room temperature.

3.4.3 X-ray diffraction

X-ray diffraction is useful technique to identify the atomic or molecular level structure of regular organised (crystalline) sample. X-rays wavelength falls in the range of interatomic distances, when X-rays are bombarded on the crystalline sample; the atoms of that sample diffract the X-rays into constructive interferences. The measurement of diffracted incident beams angle is detected from rotating sample. The intensity of diffracted X-ray angles is collected.

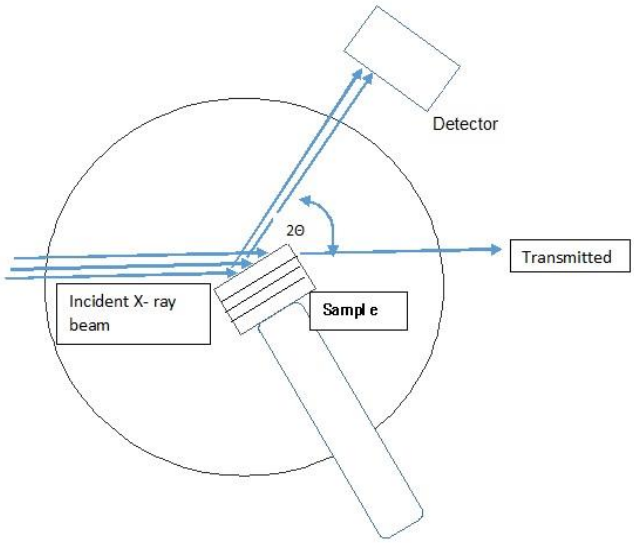

Figure 3-6 Schematic diagram of X-ray powder diffractometer

Bruker D2 diffractometer (Bruker AXS, Cambridge, UK) has been used to scan the materials. The characteristic X-ray source was CuKα radiation with a wavelength of 0.154 nm. The voltage of 30 kV and the filament current was 10 mA. The sample was either packed into glass sample holders with proper distribution and flat surface in hollow space or spray dried on a flat Si surface sample holder. All samples were scanned from 5° to 80° (2Θ), whereas Si-SPION-SS were scanned from 1.5° to 10° (2Θ). Step width was 0.01 and 0.45-second time count.

3.4.4 Dynamic light scattering and laser diffraction

Dynamic light scattering (DLS) is a rapid and non-destructive technique for obtaining the size of particles size ranging from 1 nm to 1 μm. The technique involves a colloidal suspension, where light beam targets the sample and is scattered in various directions. It relies on the hydrodynamic radius of nanoparticle. The incidence beam fluctuates over time due to the Brownian motion. A photon detector at set scattering angle detects the fluctuations of the beam providing information on the particle size. This information is useful for the nanoparticle size determination, where nanoparticles are stable in buffers or solvent systems.

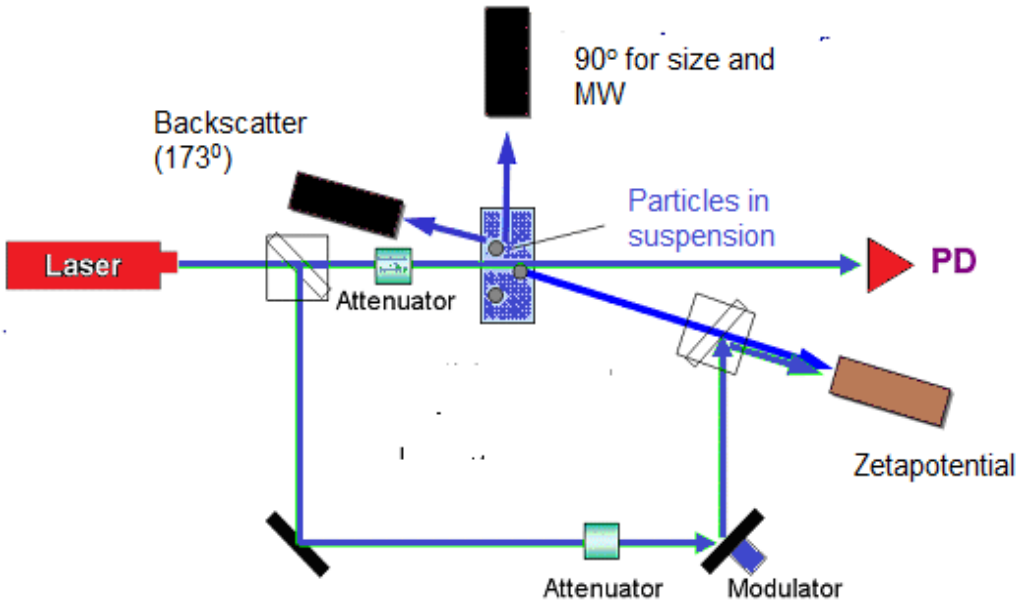

Figure 3-7 Experimental setups of DLS instrument (modified from Horiba Scientific Horiba 2017)

The size of structures greater than 1 micron was measured by laser diffraction (LD), where a laser beam is focused on material which in turns scattered to certain angles. The smaller the size, the higher the diffraction angles which is detected by series of photodetectors. The data was obtained from the Dispersion Technology Software (DTS) provided by (Malvern Mastersizer 2000 Instruments, Worcestershire, U.K.). The equipment was cleaned with distilled water after each measurement to avoid the cross-contamination. Zeta potential of FF was measured with Zetasizer Nano ZS (Malvern Instruments, Worcestershire, UK). 1 ml of (2 $mg.mL^{-1}$) each of the peptide solutions (water, ethanol and water/ethanol mixtures) were used for each measurement. Peptide solutions were transferred in zeta potential folded capillary cuvette (Malvern, Worcestershire, UK). Zeta potential was measured by applying the constant voltage supplied from the electrodes of the instrument sample chamber. Zeta potential was measured from electrophoretic mobility of the charged particles using Smoluchowski formula (Rutgers & De Smet 1947). The results are shown in mV from an average of

three independent samples. For each sample, three measurements were performed with 20 scans at 25 °C. The acquisition time was set 120 seconds. The temperature was set at 25 °C and acquisition time was 120 seconds. Ten runs were performed with an average of three measurements.

3.4.5 Fourier transform infrared spectroscopy

Fourier Transform Infrared Spectroscopy (FTIR) technique deals in the infrared region of incident beams. In this region, high energy electromagnetic radiation excites the vibrational mode of an individual atom in the molecule by identifying these energies provides molecular fingerprints of materials.

FTIR spectra were measured on IR 200 (Thermo Scientific, USA) spectrometer. FTIR spectra were processed and analysed using the software package Omnic (8.0 software). FTIR system measures the infrared radiation of sample against wavelength. The infrared bands give the molecular structure and their bonding positions. A simple FTIR instrument consists of the interferometer, source, sample compartment, detector and amplifier. An interferometer modulates the wavelength and detector measure the transmitted or reflected light.

3.4.6 Magnetic field induced hyperthermia

Magnetic hyperthermia involves the transformation of magnetic energy into heat generated from the thermal fluctuation of magnetic nanoparticles in an AC magnetic field. The heat may be utilised both for the destruction of tumour cell directly (thermal ablation) or in combination with chemotherapy (figure 3-8).

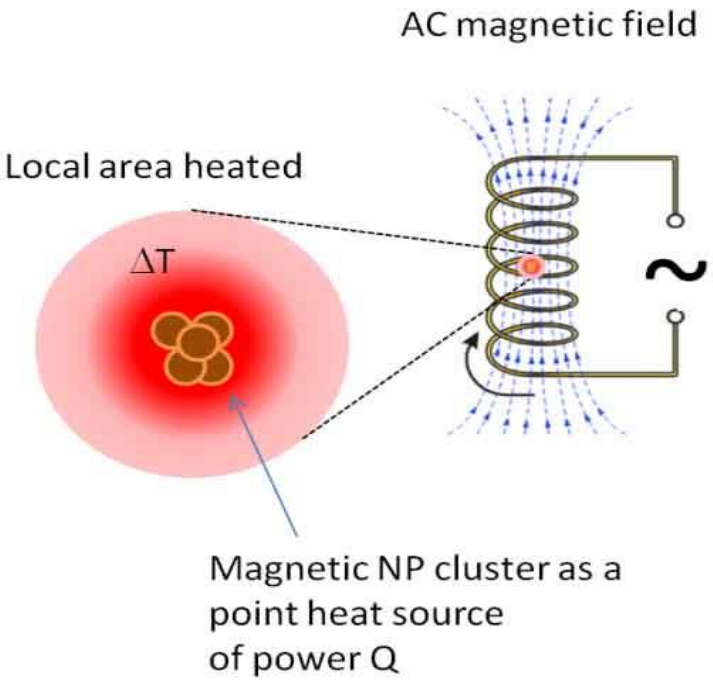

Figure 3-8 Schematic diagram of magnetic hyperthermia based treatment (adapted from Malekigorji 2014)

Specific Power Absorption (SPA) of B-SPION-SS, Si-SPION-SS, BOC-SPION-SS and BOC-Si-SPION-SS was determined in a commercial AC field applicator (DM100, nB nanoscale Biomagnetics, Spain, see figure 3-8). The frequency and magnetic field strength were set as f = 418.5 kHz and 200 G, respectively. All measurements were performed within a thermally insulated working space of about 1 cm^3, using a closed capped vials of 1.0 mL volume.

3.4.7 Vibrating sample magnetometer

Vibrating Sample Magnetometer (VSM) was used to analyse the magnetic behaviour of magnetite and coated hybrid materials at room temperature. A typical magnetisation hysteresis loop was obtained which depicts the magnetic behaviour of a sample corresponding to the applied external magnetic field. There are various factors which can alter the hysteresis loop of magnetic materials. These includes; size, shape, interaction

and chemical structure of sample also the orientation of the magnetising field (Simeonidis et al. 2013; Jiles 2015). The parameters used to express the magnetic capacity of materials includes the saturate magnetisation (Ms), the saturation field (Hsat). These are needed to obtain saturation magnetisation, the remnant magnetisation (Mr) the magnetisation amount of material, when applied field is removed and the coercivity (Hc) the magnetic field at the zero magnetisation. Another parameter for magnetisation is the moving field (Hs) of magnetisation hysteresis loop.

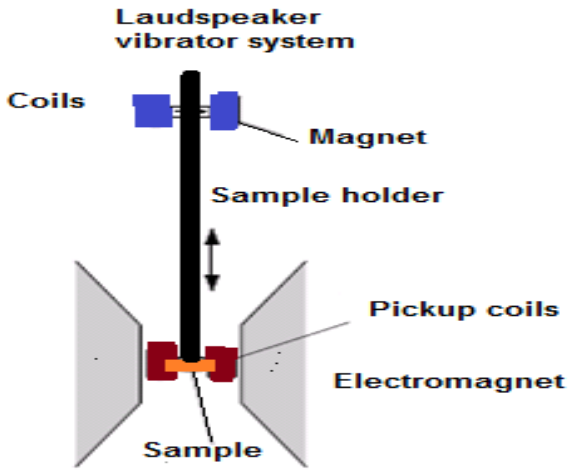

Figure 3-9 Instrument setup of VSM

In this research, the saturation magnetisation of magnetite and core-shell material was performed on; in-house UCLan built VSM as shown in figure 3-9. This instrument is based on the Faraday's Law of Induction. According to this law, changes in the magnetic field produce the electric field. The electric field is then measured, this provides the information regarding the magnetic behaviour of magnetic particles. Measurements were performed at room temperature using 7 kOe magnetic field. All samples were dried and ground into a fine powder then packed into plastic tubes of length ~10 mm and internal diameter ~1.9 mm. For each measurement ~ 150 mg of magnetite materials were used.

The saturation magnetisation values were expressed as Electro Magnetic Unit per Gram ($emu.g^{-1}$).

3.4.8 Surface area measurement using Brunauer, Emmet and Teller

Silica-based materials have an open porous framework, which led them as an ideal candidate for drug delivery applications. In these materials, gases or liquids can penetrate *via* the interconnected open pores framework. The physisorption isotherms are classified according to IUPAC in six types. In this work, type four (like hysteresis loop) isotherm was used. This type four is the characteristic isotherm for materials of mesoporous size. Hysteresis loop also reveals capillary condensation in the mesopores where the first fragment of the curve depicts the monolayer adsorption (Marsh 1987; S. Li et al. 2016).

The pores size distribution in any porous materials is classified corresponding to mean pore diameter (Table 3-1). According to this classification, silica layered materials are primarily mesoporous and microporous.

Table 3-1 The pore size distribution based on IUPAC classification

Type of pore	*Micropor*	*Mesopore*	*Macropore*
Pore size (nm)	*< 2*	*2-50*	*> 50*

The methods used for the characterisation of porous matter are mainly based on adsorption phenomena. There are two adsorption processes, chemisorption and physisorption. In chemisorption, chemical bonding is involved, wherein physisorption, an adsorbate and adsorbent interact directly through chemical linkage. Hence, chemisorption can only be performed in a monolayer at saturation pressure. In the physisorption (physical adsorption), the pores are filled by the adsorbate saturation, where multilayers are produced.

In 1938 Brunauer, Emmett and Teller (BET) established an equation based method for the specific surface area measurement (Brunauer et al. 1938). BET equation helps the measurement of adsorption of gas on a sample surface. The BET gas adsorption technique is used as a routine procedure for the measurement of the surface area of most of the porous materials. In 1951, Barret, Joyne and Halenda (BJH) had extended the Kelvin equation and proposed a new model for the determination of pore size corrected for multilayer adsorption (Barrett et al. 1951). BJH is commonly used for the mesopore size calculations and partly for macropore range.

In this work, BET method of the nitrogen adsorption-desorption isotherms to silica coated materials is used to calculate the surface area, pore volume and pore size. The mesoporous area is calculated from BJH method. The pore diameter is calculated from pore volume and surface area values taken after the saturation pressure.

The surface area of bare SPIONs and silica coated SPIONs ~ 200 mg were weighed (up to four decimal places) and kept in the sample vial. All samples were dried overnight at 50 °C and degassed at 80 °C, prior to measurement. The materials were vacuumed and then kept at 270 °C for 4 hours. All experiments were performed in a Micromeritics Accelerated Surface Area and Porosimetry System (ASAP 2010, USA). BET analysis and BJH calculation were performed using built-in Micromeritics ASAP 2010 software.

3.4.9 Thermogravimetric analysis

The principle behind Thermogravimetric Analysis (TGA) is heating of mixture to a higher level temperature so that one or some of the elements degraded into a gas. During the whole process of combustion, the changes in mass of sample relative to the temperature are measured under the controlled environment. The resulting thermogram depicts loss in

mass of a sample in relation to the increased temperature. As this technique involves the changes in weight and temperature, it is obvious to have a good precision in both parameters; weight and temperature. Hence, prior to analysis the instrument was calibrated for both parameters weight and temperature. Initially, the temperature was calibrated with nickel at the cure point (350 °C). This was the reference for calibrating the temperature scale. In the next step, two reference weights of 5 mg and 25 mg were calibrated with software connected balance of TGA. The thermal profile of sample materials was tared the TGA with provided software (TGA/SDTA-85).

TGA is a useful technique for determining the composition and purity of a sample. This technique uses heat and stoichiometry ratios to determine the percent mass of different compounds in a mixture. Thermal stability of BOC-FF, SPIONs and composites were characterised with Mettler-Toledo equipment (TGA/SDTA-851, Mettler-Toledo Ltd., Leicester, UK). A schematic diagram is depicted (figure 3-10). Prior to the sample analysis, the empty aluminium pan was run on a whole range of temperature, and this was set as blank.

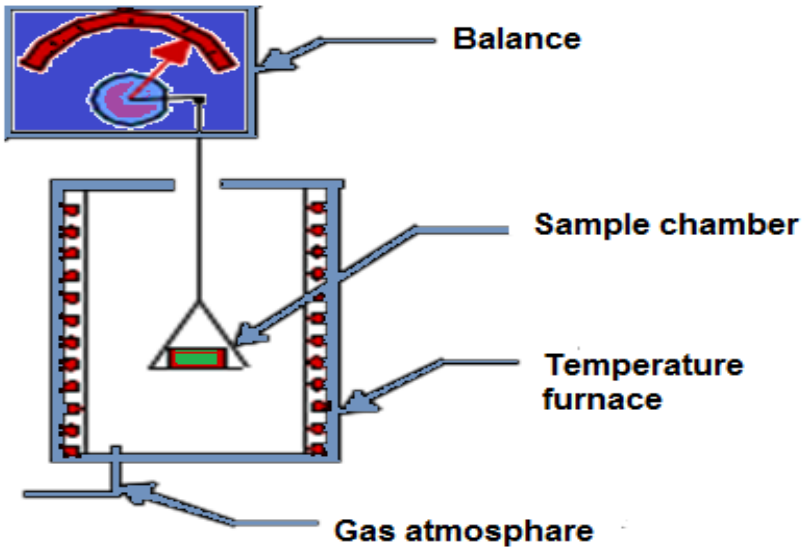

Figure 3-10 Schematic diagram of TGA (adopted from Radcham 2016)

The sample was then measured approximately 5 mg in the same aluminium pan. The pan was kept carefully on the balance arm in a closed chamber of the furnace. The chamber was filled with nitrogen gas. The heating temperature was set at a rate of 10 °C per minute, starting from 25 °C to 500 °C. The weight of the sample was recorded by software connected balance. The exact output of analysis was plotted with a loss in weight percentage over the range of temperature analysed.

CHAPTER FOUR

Characterization of core-shell structures of spherical peptide shell and SPIONs core

4.1 Introduction

The physicochemical characterisation of the core-shell nanocomposites of spherical morphologies of bare SPION, silica coated SPION, boc-diphenylalanine coated SPION and boc-diphenylalanine-capped silica-coated SPION (B-SPION-SS, Si-SPION-SS, BOC-SPION-SS and BOC-Si-SPION-SS, respectively) synthesised in this research will be discussed in this chapter. Various characterisation techniques including zeta-sizer, SEM, EDAX, FTIR, BET analysis, TEM, XRD, TGA, VSM and magnetic field induced hyperthermia have been used to understand and confirm the desired nanomaterials. The characterization techniques used for each material synthesised have been summarised in Table 4-1.

Table 4-1 Summary of the characterisation techniques used for spherical materials

	Characterisation					
Sample	**SEM/EDAX**	**FTIR**	**XRD**	**DLS**	**TGA**	**VSM**
B-SPION-SS	√	√	√	√	√	√
Si-SPION-SS	√	√	√	√	√	√
BOC-FF	√	√	√	√	√	
BOC-SPION-SS	√	√	√	√	√	√
BOC-Si-SPION-SS	√	√	√	√	√	√

4.2 Iron oxide nanoparticles core materials

4.2.1 Morphological analysis of spherical superparamagnetic iron oxide using scanning electron microscopy

SEM analysis of B-SPION-SS shows the spherical shapes with a mean diameter in the range of ~ 20 - 35 nm (figure 4-1).

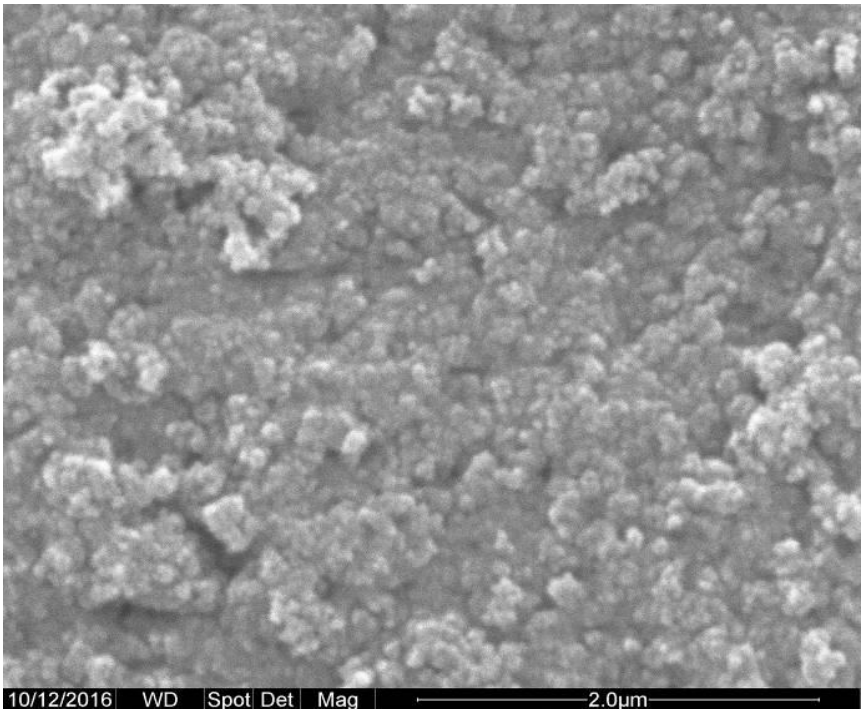

Figure 4-1 SEM image of bare spherical Superparamagnetic Iron Oxide Nanoparticles SPIONs (image is representative of three independent samples)

The shape and size distribution is narrow for B-SPION-SS. These images are taken after sonication for 15-30 minutes in ultrasonic bath, B-SPION-SS showed good stability and reduced aggregation. After observing SEM images of bare SPIONs synthesised *via* co-precipitation method using iron (II and II) chloride, a decision was made to use these nanoparticles to be coated with silica due to their narrow size distribution and ordered spherical shape. B-SPION-SS after coating with mesoporous silica further hybridised with BOC-FF, were well-separated and stable in 50 % ethanol water mixtures. Bare SPIONs were coated with a thin layer nonporous silica on individual magnetite particle

seeds, forming the Fe_3O_4 composites with core-shell pattern spheres. This nonporous layer was important for further coating of mesoporous silica. Briefly, it facilitates the interaction between CTAB and silicate materials. Hence, it favours the deposition of CTAB and then SiO_2. In addition, it reduces the chances of Fe_3O_4 core from being rapidly etched under acidic environment. It protects the Fe_3O_4 magnetite cores to oxidise as maghemite by retaining its magnetic property in the final step of the removal of CTAB templates. After removal of CTAB, discrete mesoporous core-shell structured nanospheres with size ~ 500 nm were obtained (figure 4-2).

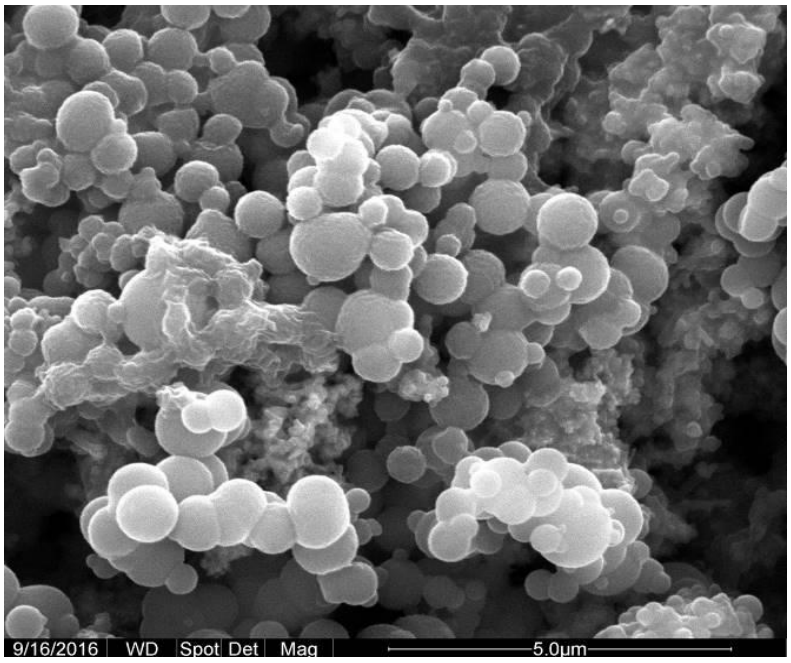

Figure 4-2 Mesoporous silica-coated iron oxide (Si-SPION-SS) core-shell nanocomposites (image is representative of three independent samples)

Elemental analysis using Energy Dispersive X-ray Spectroscopy (EDAX) confirmed the presence of constituent elements. Figure 4-3 (a-b) show the elemental analysis of bare SPIONs and mesoporous silica coated core-shell nanoparticles, respectively. As expected iron and oxygen peaks were observed on the collected spectrum along with a carbon and

gold peaks, eliminating from the carbon tape and gold coating respectively. Similarly, mesoporous silica coated nanoparticle showed the silica peak in the spectrum.

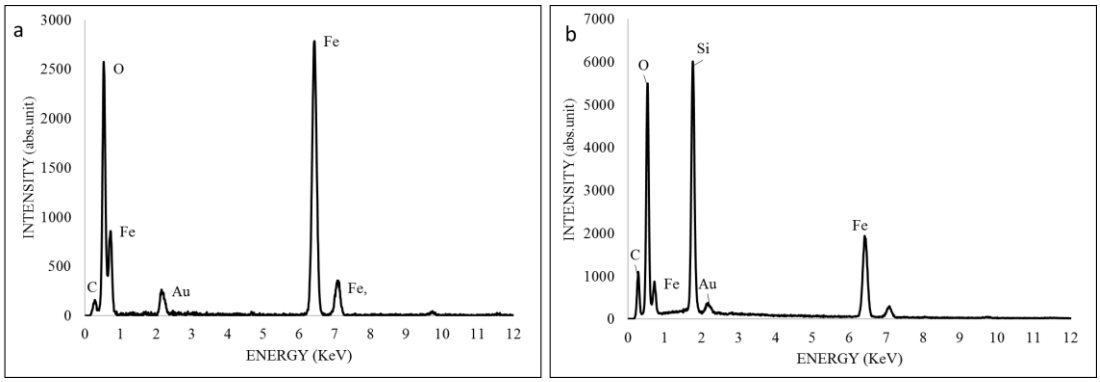

Figure 4-3 EDAX analysis of (a) B-SPION-SS (b) Si-SPION-SS (graphs are representative of three independent samples)

For each sample, EDAX spectra from three representative areas were recorded and the results were averaged for each element identified. Tables 4-2 shows the detected elemental compositions and mass percent, however these result could not reflect the stoichiometry of formulated elements.

Table 4-2 EDAX data of bare SPIONs and mesoporous silica coated core-shell nanoparticles (constituents in mass percentage)

	B-SPION-SS		**Si-SPION-SS**	
Elements	Weight (%)	Atomic (%)	Weight (%)	Atomic (%)
C	7.78	18.91	24.7	38.98
O	26.76	48.85	35.78	42.38
Au	5.31	0.79	5.57	0.54
Fe	60.15	31.45	14.29	4.85
Si			19.64	13.25

Gold and carbon were present as shown in the Table 4-2 and figure 4-3, in the sample from coating and carbon tab of the aluminium stub. Table 4-2 shows the bare magnetite,

where, it did not reflected the predicted iron and oxygen contents, this might be due to the interference atmospheric oxygen.

i) Transmission electron microscopy

Figure 4-4 reveals the spherical shape of B-SPION-SS. TEM images showed size distribution of these core nanoparticles approximately 10-35 nm in diameter with average size if 35 nm in diameter. The SPION size distribution and shape obtained were in good agreement with already published data (Sharifabad et al. 2014b; Sen et al. 2006; Sen et al. 2012). The nanoparticles showed relatively narrow uniform spherical shape and size distribution. Hence, these materials were further used for the coating with mesoporous silica and peptide spherical shells.

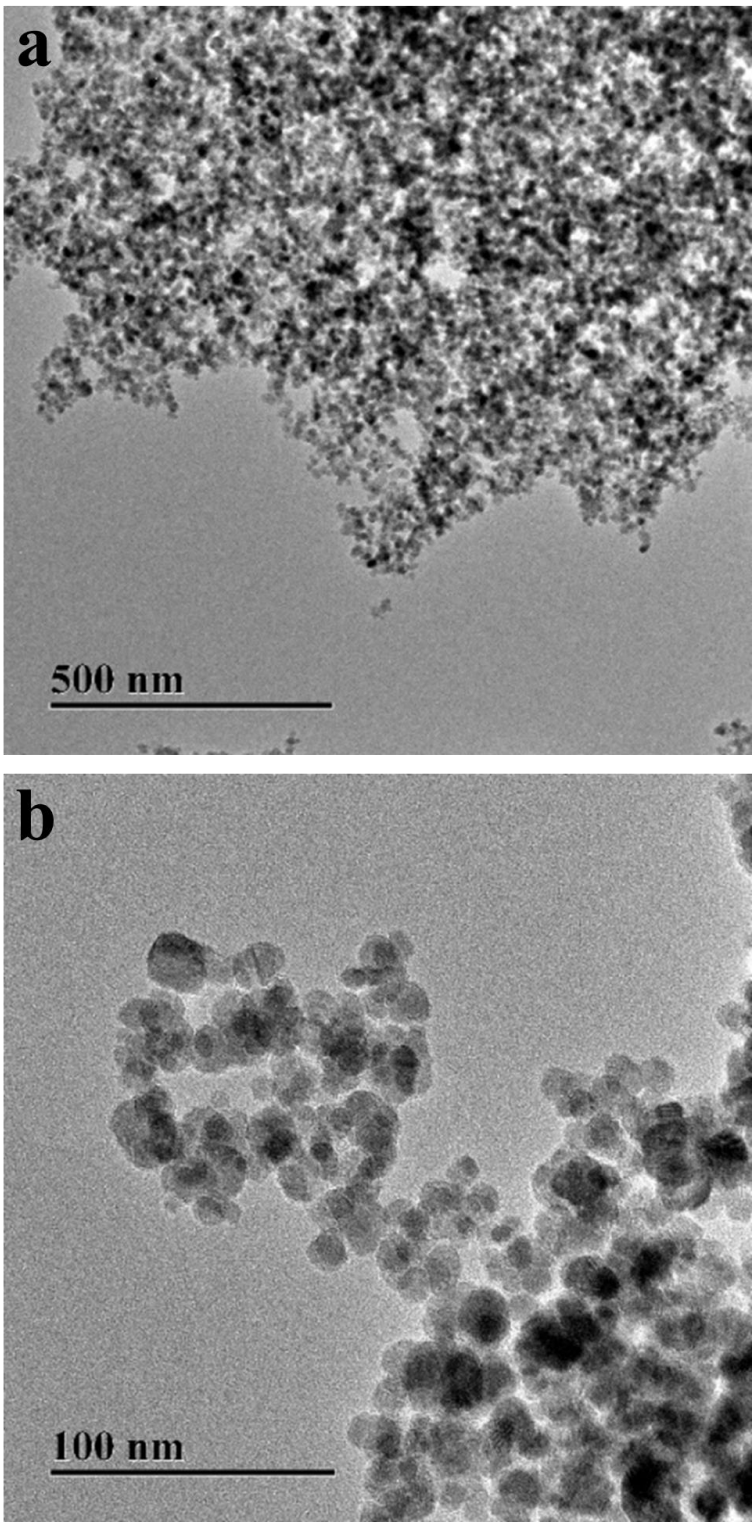

Figure 4-4 TEM images of spherical B-SPION-SS synthesised *via* co-precipitation of iron (II) and (III) ions in alkaline medium (these images were taken at Liverpool university)

The Si-SPION-SS showed nearly 200 nm size in diameter as shown in figure 4-5. Figure 4-5 depicts the TEM images, showing the core-shell structure. The core-shell structure

comprises of multiple small SPIONs cores and a layer of mesoporous silica with average diameter of approximately 150-200 nm. Mesoporous nature of silica layer has been further confirmed by BET. The size and shape of synthesised materials are in good agreement with published studies (Sen et al. 2012; Bruce et al. 2004b; Bruce & Sen 2005).

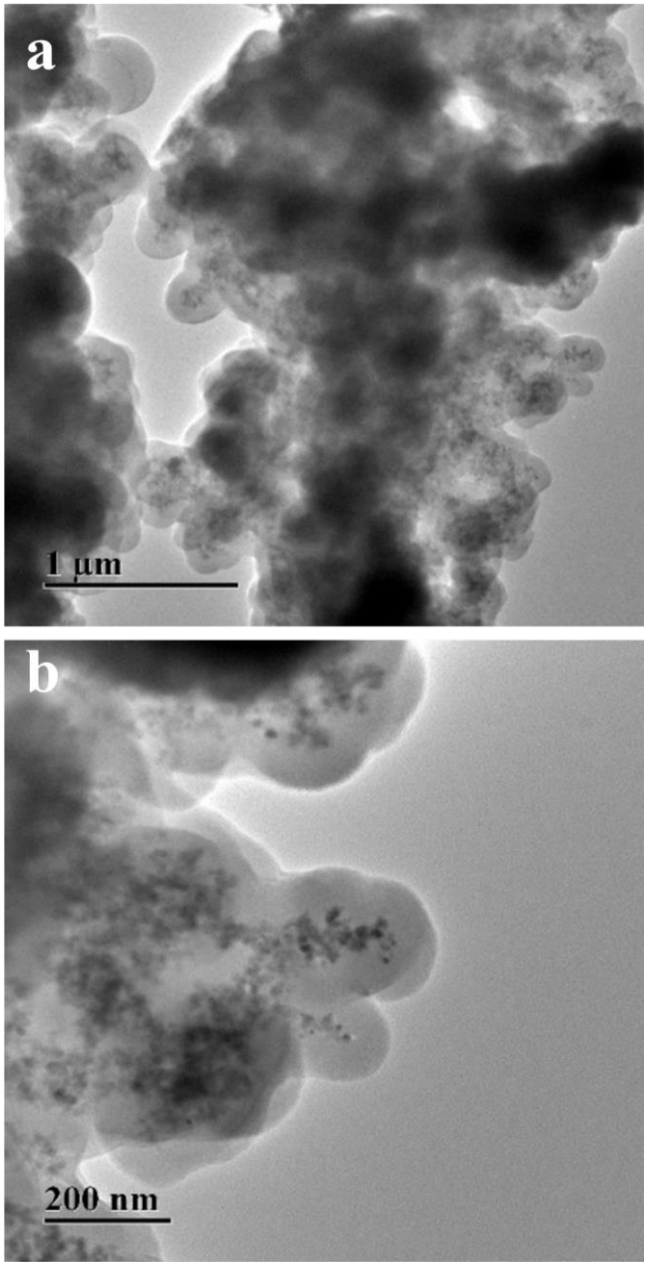

Figure 4-5 TEM images of mesoporous Si-SPION-SS (these images were taken at Liverpool university)

ii) Size measurement using dynamic light scattering

Size measurement using Dynamic Light Scattering (DLS) was performed to measure the hydrodynamic size of synthesised nanoparticles. Hydrodynamic size significantly differs from SEM measured size due to aggregation particularly for B-SPION-SS and functionalized with mesoporous Si-SPION-SS.

A mean hydrodynamic size value for B-SPION-SS is 115.2 nm ± 19.1 nm. It can be concluded that due to its aggregation and a significant amount of solvent adsorb on the surface of SPIONs and possibly some irregular shaped nanoparticles may also contribute to the increased hydrodynamic diameter of B-SPIOPN-SS.

An average hydrodynamic size for mesoporous Si-SPION-SS core-shell nanocomposites is 449 ± 52.4 nm, which is different to calculated sizes from the SEM images. This possibly due to the aggregation of nanocomposites. The average size significantly differs from dispersed bare SPIONs size. It is almost 5 times larger. Core-shell materials with hydrodynamic diameter greater than 1 μm are not considered in average size calculations, probably because of the possible aggregation. The hydrodynamic size distribution is larger than the SEM calculated value. Possibly, silica interacts with water in a different way compared to bare magnetite.

iii) Chemical conformational analysis Fourier transform infrared spectroscopy

B-SPION-SS and Si-SPION-SS were also characterised using FTIR to confirm the bonding of FeO. The FTIR spectrum of both core and core-shell materials is depicted in figure 4-6.

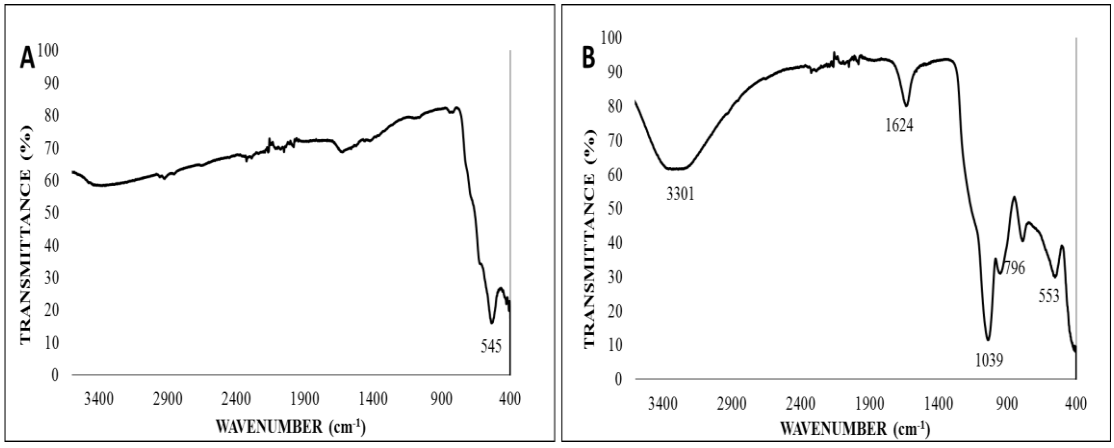

Figure 4-6 FTIR spectrum of (a) B-SPION-SS nanoparticles and (b) Si-SPION-SS nanocomposites (graphs are representative of three independent experiments)

In Figure 4-7 (a), the peaks at 545 cm^{-1} and 553 cm^{-1} are assigned to the Fe-O bond of Fe_3O_4. However, the characteristic bands for a Fe-O bond of bulk Fe_3O_4 are stated as 570 cm^{-1}, a shift in the bands of the Fe-O were around 545 and 553 cm^{-1}, respectively, as reported for the Fe_3O_4 nanoparticles (Bordbar et al. 2014). This shift is probably due to the nanosize of materials, where certain bonds of surface atoms are broken and causing the rearrangement of electrons on the particle surface. The successful deposition of silica on the bare magnetite material, namely mesoporous silica-coated iron oxide nanoparticles (Si-SPION-SS) was also confirmed by FTIR analysis. The silica-coated material was compared to bare magnetite nanoparticles. From the literature findings the FTIR spectrum of silica coated magnetic nanoparticles are shown in figure 4-7 (b), and the assignment of the bands shown in Table 4-3. The characteristic bands nearly at 1085, 800 and 553 cm^{-1} are corresponding to the stretching and bending of Si-O and Fe-O bonds, respectively. The main sharp peak of the Si-O vibrational band at 1085 cm^{-1} shows a stoichiometric arrangement of the silicon dioxide structure. Some impurity vibrational bands are also seen in the FTIR spectrum shown in Table 4-3. These are small compared to the main peaks. The peaks at 1624 cm^{-1} are corresponding to vibrations of carbon impurity atoms. The FTIR spectrum (figure 4-7) for the deposited silica also showed a wide peak of OH

groups at around of 3200 cm^{-1} to 3400 cm^{-1}. These results reveal the presence of OH molecules on the surface of the mesoporous silica-coated iron oxide nanoparticles.

Table 4-3 Band assignment in FTIR spectrum of iron oxide nanoparticles

Wavenumber (cm^{-1})	**Possible assignment**
550	Fe-O-Fe bending
800, 802	Si-O bending
939, 932	Si-OH stretching
1083, 1089	Si-O-Si stretching
1630, 1628	C-O bending
3200 - 3400	…-OH stretching

iv) Crystalline structure magnetite confirmation using X – ray diffraction analysis

X-ray diffraction (XRD) pattern of the B-SPION-SS is shown in figure 4-7. XRD analysis was performed, and the lattice constant values (a) were obtained, and spectra were matched with International Centre for Diffraction Data (ICDD) database to predict the type of the nanoparticles.

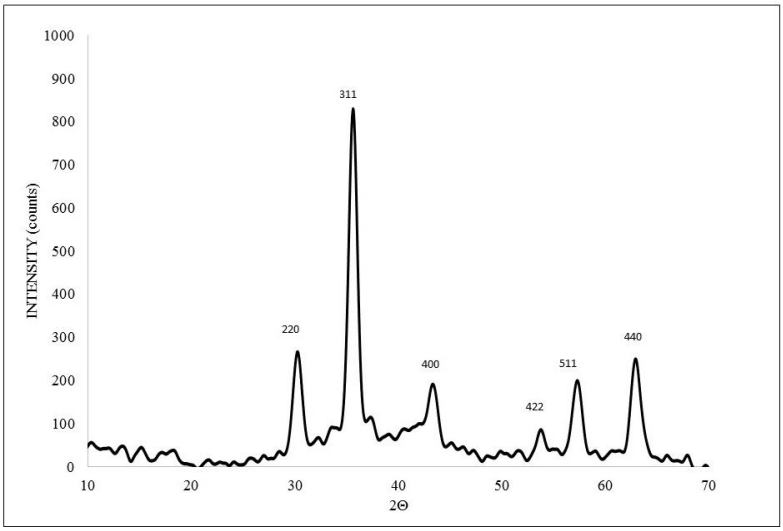

Figure 4-7 XRD pattern of spherical B-SPIONs-SS (graph is representative of three independent experiments)

The data from figure 4-7 were used for interplanar spacing (d) calculation in the atomic lattice, and the lattice constant (a) calculations for the identification of crystal structure using software (DIFFRAC.EVA, Bruker, UK).

The lattice constant value (a) is used to identify the magnetic type of the iron oxide nanoparticles. For maghemite, this value is 0.833 nm, and for magnetite, it is 0.839 nm (Mineralogy Database accessible from Bruker software). From the data of figure 4-8, the calculated value of B-SPION-SS was 0.839 nm. The resulting core magnetic nanoparticles were magnetite (Fe_3O_4) possessing cubic spinal structures. The bare magnetite produced multiple peaks with *hkl* value of 220, 311, 400, 422, 511, and 440 in the 2θ (PDF04 005-4319, 01-086-1362), showing good agreement with published data (Sen et al. 2006; Bruce et al. 2004a; Sen & Bruce 2009; Sharifabad et al. 2014a; Sen et al. 2012). Meanwhile, there was no evidence of impurities observed in the XRD pattern.

XRD pattern of B-SPION-SS shows the low intensity corresponding to very small size of magnetite nanoparticles. The average particle diameter was calculated from the XRD

pattern of the wide intense peak (3 1 1). Scherer equation was used to measure the size of the nanoparticle. The equation as presented in equation 4-1 (Holzwarth & Gibson 2011; Monshi et al. 2012; Burton et al. 2009).

$$D = \frac{K\lambda}{(B\cos\Theta)} \qquad \text{(Equation 4-1)}$$

Where, factor K is 0.9 (as spherical), B structural = B observed – B standard (where B is the Full Width at Half Maximum in radians), θ is half of the Bragg angle (in radians), and λ is, the wavelength of the X-rays (1.5418 Å) used. The calculated diameter of magnetite was about 24 nm in agreement with SEM images (figure 4-1).

Figure 4-8 shows the XRD patterns where six diffraction peaks (220, 311, 400, 442, 511 and 440) are seen in the wide-angle region. The peaks are indexed to the crystalline structure of pure magnetite nanoparticles along with the wide, intense peak (25° 2Θ) of amorphous silica. The XRD pattern confirms mesoporosity of spheres with a similar diffraction pattern. The major diffraction peak at 35.5°(311), along with others at 30.5°(220), 43.5°(400), 57.5°(511), and minor at 63°(440) confirm the presence of magnetic core in silica matrix (El Mendili et al. 2016).

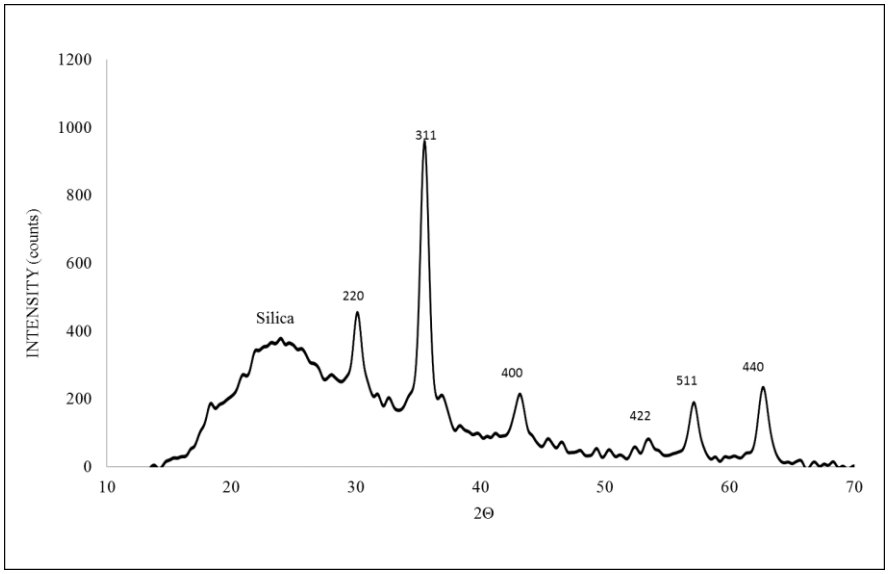

Figure 4-8 XRD pattern of Si-SPION-SS nanocomposites (graph is representative of three independent experiments)

XRD pattern of mesoporous silica magnetite materials at low angles indicates the ordering of the mesopores within the nanocomposite. Low angle XRD was taken at 1.2 to 40° 2Θ. Mesopores size was determined using the Bragg's equation:

$$n\lambda = 2d\sin\theta \qquad \text{Equation 4-2}$$

where n is an order, λ is the wavelength of the X-ray radiation (0.154 nm), and θ is the angle of diffraction.

Low angle XRD patterns for Si-SPION-SS is shown in figure 4-9. The peak index (1 0 0) at 2.2° 2θ corresponding to the mesoporous structures, these are in agreement with published data (Li et al. 2016; Egodawatte et al. 2015). However, for shell mesoporous silica material, the characteristic (1 0 0) peak was noticed at 1.9° 2Θ. In case of magnetite material present in the cores, the peak is shifted slightly, as observed in previous publications (Datt et al. 2012).

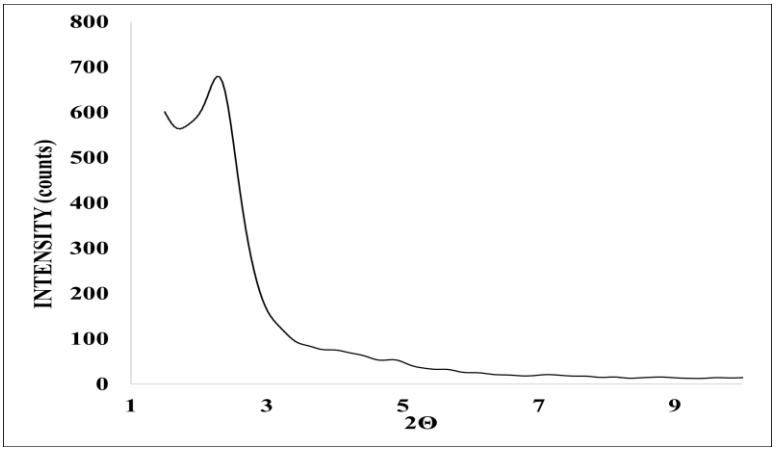

Figure 4-9 Low angle XRD pattern of mesoporous Si-SPION-SS nanocomposites (graph is representative of three independent experiments)

v) Saturation magnetisation measurement using vibrating sample magnetometer

The magnetisation properties of B-SPION-SS nanoparticles and Si-SPION-SS nanocomposites were measured at room temperature using the 7 kOe magnetic field. The saturation magnetisation (*Ms*) of B-SPION-SS is 64 emu.g^{-1} (figure 4-10), and Si-SPION-SS (of around 40 emu.g^{-1}). Bare magnetite nanoparticles saturation magnetisation values are in good agreement with the literature (Feng et al. 2008; Banaei et al. 2015; Greene et al. 2014). However, the saturation magnetisation was significantly lower compared to bulk materials 92 emu.g^{-1} for bare magnetite crystals (Qu & Tie 2009). The lower value of saturation magnetisation possibly because of the size distribution of the nanoparticles (Chatterjee et al. 2003; Maaz et al. 2016). A decrease in saturation magnetisation was noticed due to coating mesoporous silica.

In both materials B-SPION-SS and Si-SPION-SS, the 0 coercivity and remanence was observed in the hysteresis loops, confirming the SPIONs made *via* co-precipitation methods are superparamagnetic. Size is an important factor for magnetic properties (Martinez-Boubeta et al. 2013; Nakamura et al. 2013; Simeonidis et al. 2013).

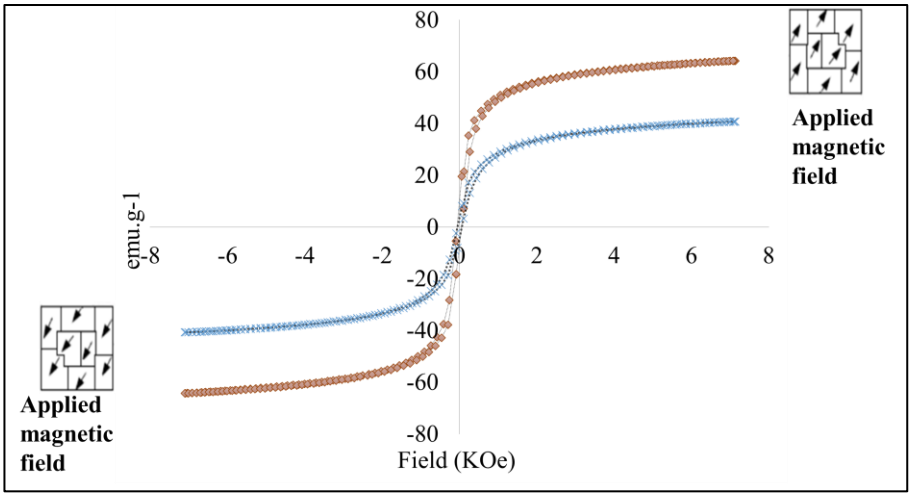

Figure 4-10 hysteresis loops of B-SPION-SS (red-square) and Si-SPION-SS (blue-crossed) (graph is representative of three independent experiments)

Zero remanence value indicated superparamagnetic nature of B-SPION-SS and Si-SPION-SS, they become magnetised when external magnetic field applied and nonmagnetic once the field is removed. Hysteresis loop pattern of Si-SPION-SS is similar to the core magnetite indicating the magnetic properties are retained during the procedure of silica coating and precipitation. This desired behaviour SPIONs are making them an ideal candidate for biomedical applications (Graczyk et al. 2015; Ling et al. 2015; Karimzadeh et al. 2016; Kandasamy et al. 2016). As observed from the hysteresis curves for bare SPIONs and silica coated SPIONs, both materials reached magnetisation saturation at around 2 kOe of applied field.

vi) Surface area analysis using Brunauer-Emmett-Teller

Surface area analyses were obtained using nitrogen gas adsorption techniques using surface area analysis *via* BET. The mesoporous silica coated magnetite silica nanoparticles exhibited very high specific surface area 791.3154 m^2. g^{-1} compared to bare magnetite 85.8505 $m^2.g^{-1}$ (figure 4-11 and 4-12).

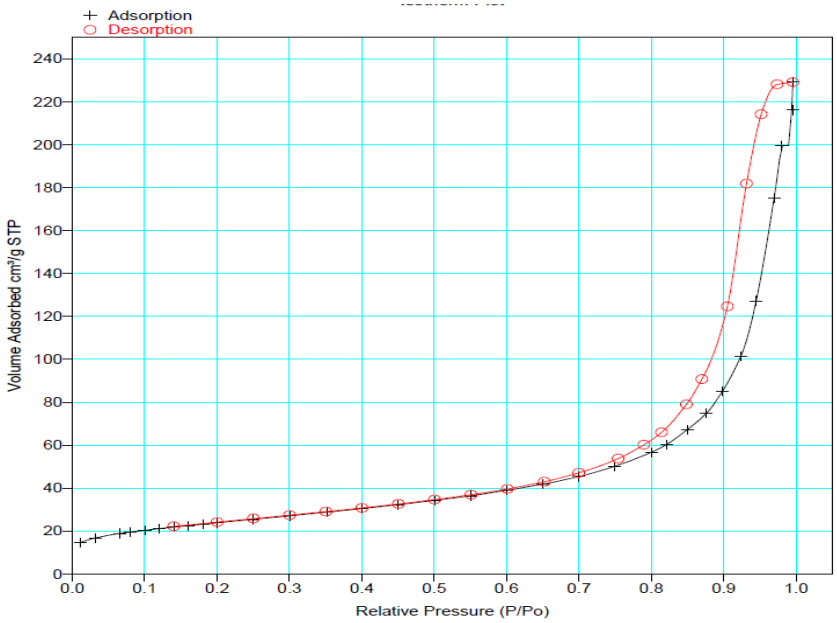

Figure 4-11 Nitrogen adsorption-desorption of B-SPION-SS with spherical shape (graph is representative of three independent experiments)

The adsorption-desorption isotherm for the silica-coated iron oxide nanoparticles shows hysteresis curve, which is IUPAC 4 isotherm. This hysteresis isotherm is characteristic of the behaviour of mesoporous materials. No such hysteresis was seen in the adsorption-desorption isotherms of bare SPIONs (figure 4-11). Hysteresis behaviour only occurs in porous materials, where pores cause the adsorption and desorption of gas which reveals the type of isotherms to have different path (figure 4-12).

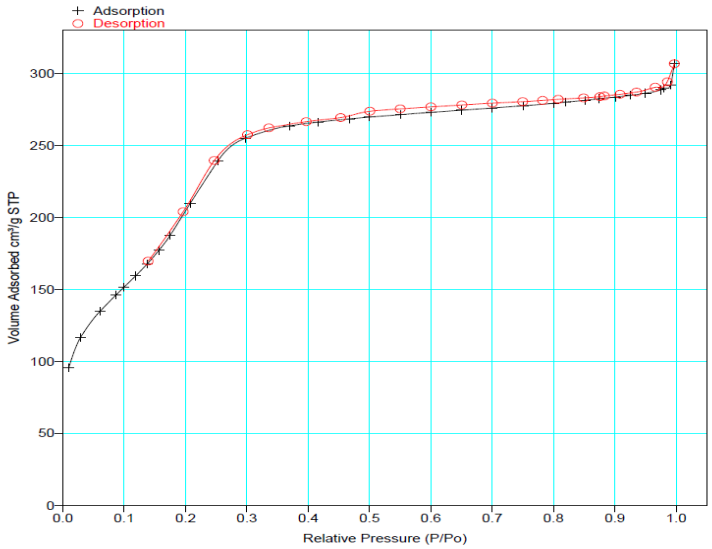

Figure 4-12 Nitrogen adsorption-desorption of Si-SPION-SS of spherical shape (graph is representative of three independent experiments)

vii) Thermal stability measurements using thermal gravimetric analysis

TGA analysis of B-SPION-SS and Si-SPION-SS is useful for qualitative and quantitative purposes of volatile elements of the nanocomposite. The TGA curve (Figure 4-13) depicts the weight loss of bare magnetite over the temperature range from 25 °C to 500 °C is ~ 3.5 %, possibly, due to the loss of residual water from the sample. TGA was also performed to measure the relative mass proportion of the silica coated materials. It is worth knowing the amount of water adsorbed, which can be useful in the design of drug carriers.

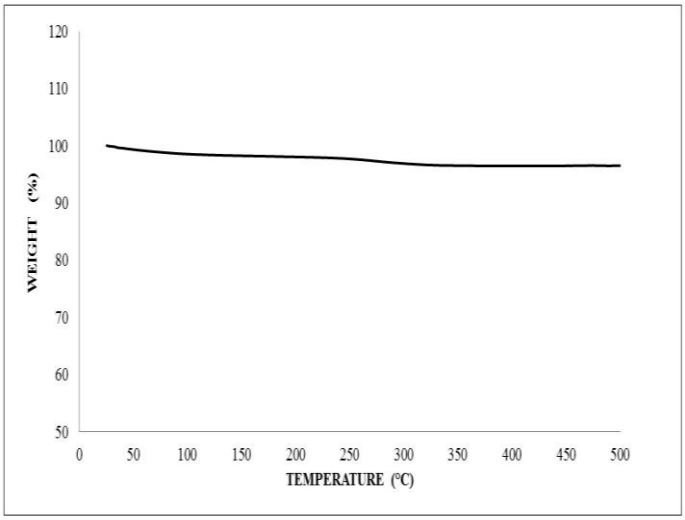

Figure 4-13 Thermogravimetric analysis of bare SPIONs (graph is representative of three independent experiments)

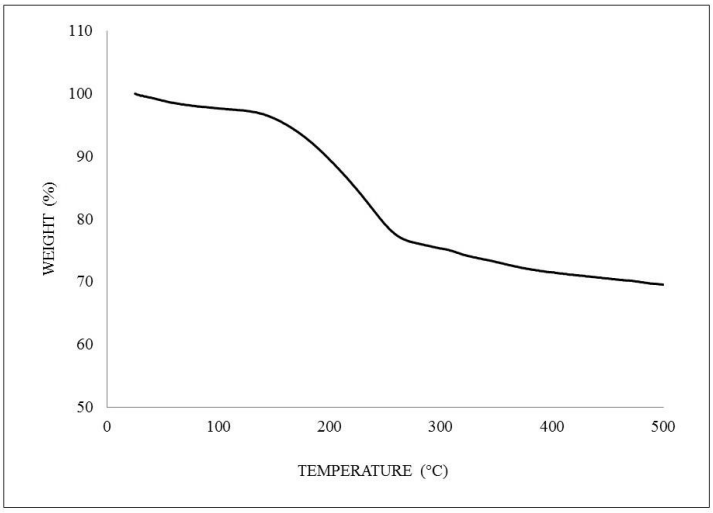

Figure 4-14 Thermogravimetric analysis of silica coated spherical SPIONs (graph is representative of three independent experiments)

The removal of water from silica material was accomplished at 120 °C and remained the losing of CTAB molecules till 250 °C from porous silica materials. CTAB weight loss appeared at 30-500 °C *via* decomposition (figure 4-14). Thermal profile of CTAB as alone showed complete degradation at 400 °C (Wang et al. 2007). Hence, it could be possible that CTAB degradation happened gradually by shifting to higher temperature up to 500 °C.

viii) Chemical confirmation analysis after heating at high temperatures

TGA and FTIR reveals that most of the CTAB layer was removed at high temperatures. The peaks at 3400 - 3200 cm^{-1} and 1600 cm^{-1} were assigned to CH groups of Br-OH (Boccuzzi et al. 1999; Ping et al. 2001). The percentage weight loss in the TGA curve also reveals the amount silica layers on magnetite. The average mass content of silica layers on magnetite is about 30 % (figure 4-15).

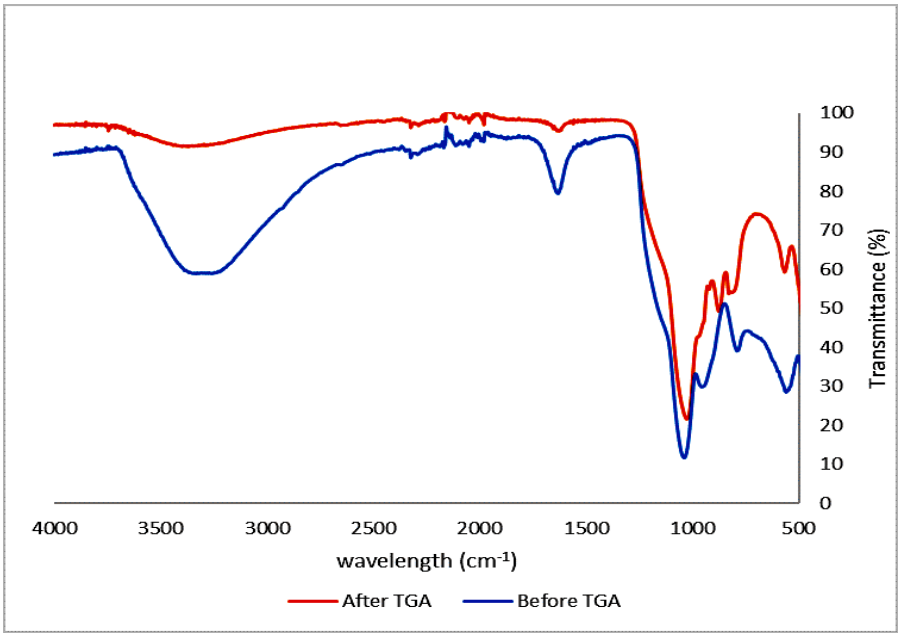

Figure 4-15 FTIR of Si-SPION-SS (blue line) before and (red line) after the TGA experiments (graphs are representative of three independent experiments)

TGA measurements were also performed to check the atmospheric effect over the temperature range 25 °C to 500 °C at 10 °C/min under an air atmosphere. The TGA profiles, the weight loss of bare and the silica-coated magnetite are depicted in figure 4-15. It worth noting that the silica-coated materials revealed a certain amount of absorbed water and OH groups, bare magnetite did not show significant weight loss (5 wt%). These results have concluded that Si-SPION-SS nanocomposites created the hydration compared to the B-SPION-SS nanoparticles.

4.3 Boc-diphenylalanine spherical particles

4.3.1 Characterisations

i) Morphological analysis using scanning electron microscopy

Figure 4-17 shows the SEM images of the boc-diphenylalanine indicating spherical morphologies. Studies were performed on the self-assembly of boc-modified aromatic dipeptides (boc-diphenylalanine). The SEM shows that the boc-diphenylalanine peptide forms spherical nanostructures in an aqueous environment (figure 4-16). Under similar conditions, a non-modified analogue of this peptide, FF which also self-assembled into tubular structures, (figure 4-17) which is confirmed by looking at the edge (cross section).

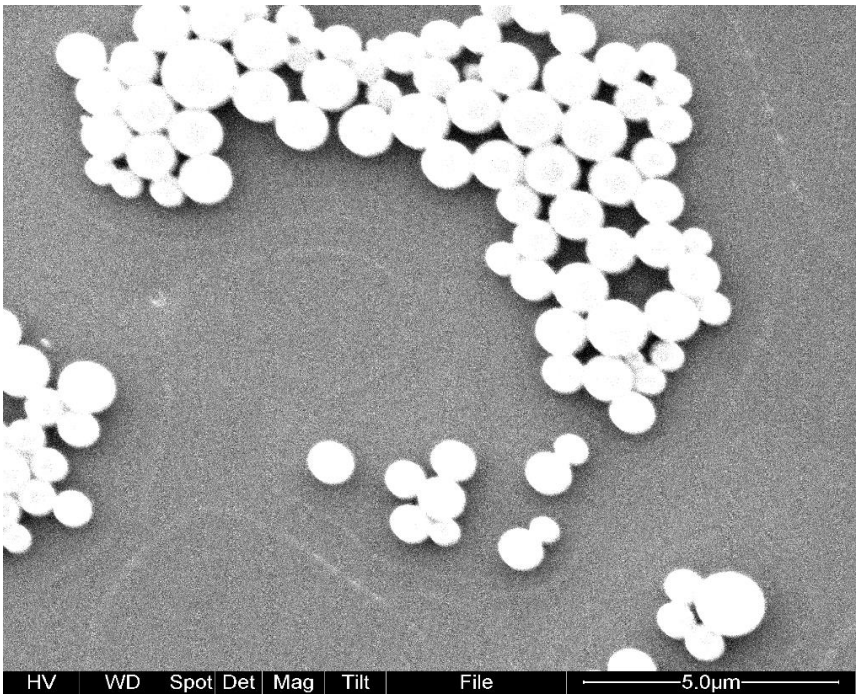

Figure 4-16 SEM image of spherical BOC-FF particles prepared in ethanol-water mixture (1:1) (image is representative of three independent experiments)

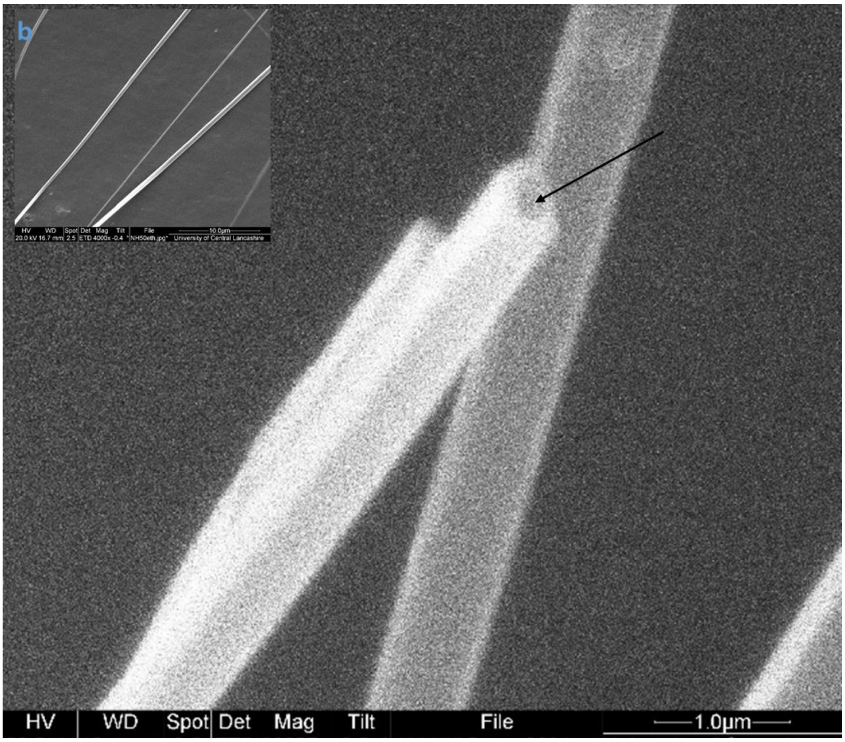

Figure 4-17 SEM image of tubular FF prepared in ethanol-water (1:1) (image is representative of three independent experiments)

Another important finding is the remarkable modulation effect of peptide concentration on the aggregated final morphology of the peptides. In previous studies (Huang et al. 2011; Li et al. 2015; Yan, Zhu & Li 2010a; Maity et al. 2014), HFIP was used as a highly volatile crystalline solvent to dissolve peptide, where peptide concentration was not kept in attention as stock solvent beforehand. In this study, considerable attention was paid to the role of peptide concentration in the aggregation or self-assembly without using HFIP. Initially, the peptide was dissolved in absolute ethanol, and further dilution was performed in 50 % ethanol in water. The concentration of peptide was set as 1, 2, 4, 6, 8 and 10 mg.mL^{-1}. SEM images of the self-assembled morphologies of BOC-FF at various concentration are shown in Figure 4-18.

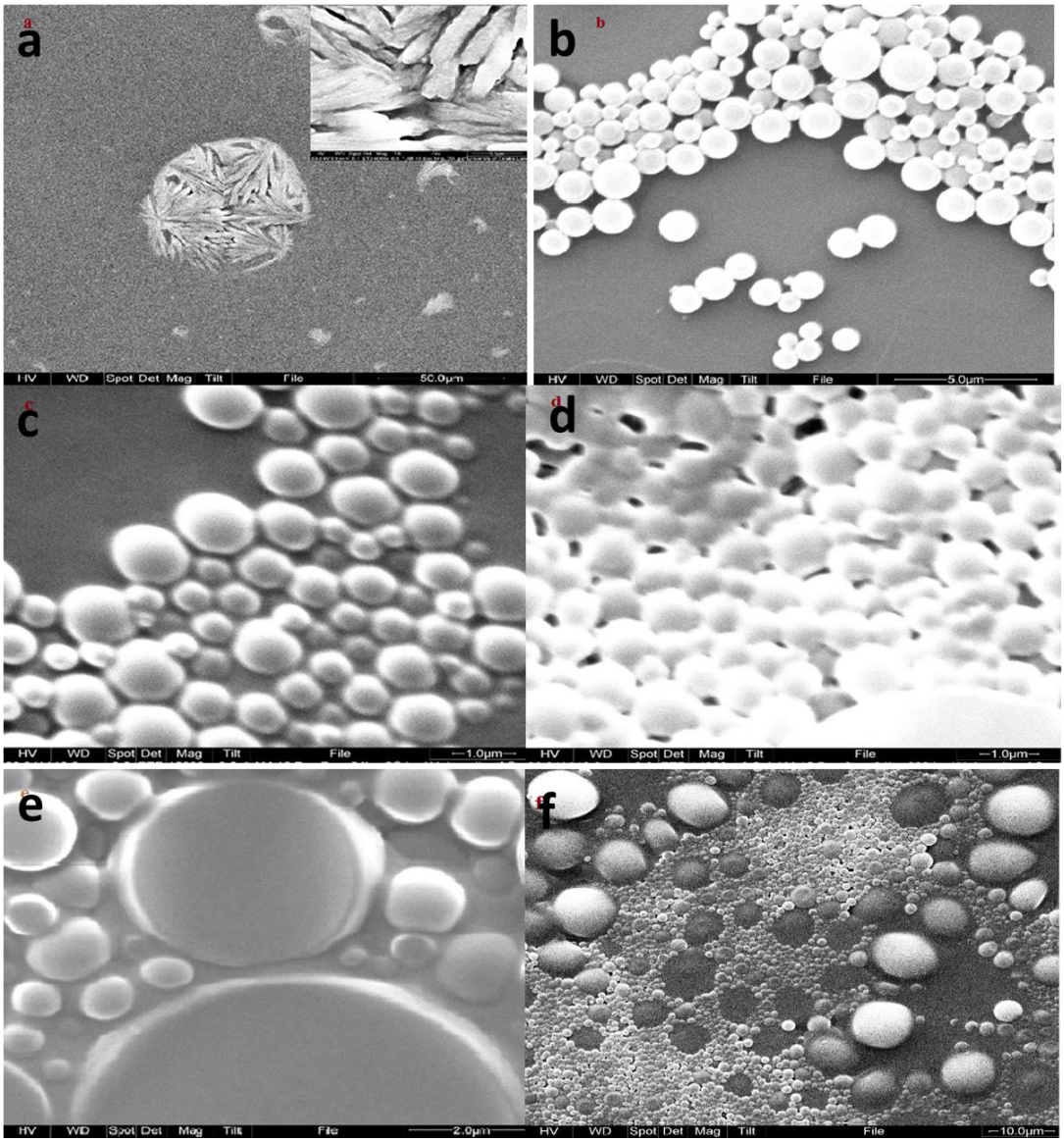

Figure 4-18 SEM images show the variation of BOC-FF morphologies at various concentration (a) 1 mg.mL^{-1}, (b) 2 mg.mL^{-1}, c) 4 mg.mL^{-1}, (d) 6 mg.mL^{-1}, (e) 8 mg.mL^{-1}, (f) 10 mg.mL^{-1}, (images are representative of three independent experiments)

Figure 4-18 (b-f) exhibited spherical morphologies, whereas figure 4-18 (a) showed needle-shaped nanoparticles to larger spherical morphology. SEM showed these types of structures were obtained when a drop of peptide solution was vaporised at room temperature on carbon tab of the aluminium stub of SEM. This revealed that the homogenous dispersion and initial saturation is important for the assessment of self-

assembled architectures. Further studies showed the morphological growth of these hierarchical structures were concentration dependent.

SEM images of BOC-FF of 4 mg.mL^{-1} showed smooth surface spheres (figure 4-18 (c)). However, self-assembly pattern of peptide is concentration driven hence the transition from tubular to spherical structures appeared from 2 mg.mL^{-1} and remained spherical up to 10 mg.mL^{-1}. The spheres have varying size distribution ~ 300 nm to 10 µm nm in diameter, which is in good agreement with (Adler-Abramovich et al. 2010). BOC-FF spheres transform gradually into large spheres when the conentration of the solution was increased. Yan et al. (2007) confirmed the spherical structures using 3D atomic force microscopy.

For comparison, another analogue of zwitterion FF was chosen. Experiments were performed under the similar conditions, where FF self-assembled into tubular morphologies (figure 4-17). This self-assembly pattern was similar to that previously reported data (Yan, Zhu & Li 2010a; Huang et al. 2014; Görbitz & Gorbitz 2006; Huang et al. 2011; Dinesh et al. 2015; Andersen 2013; Levin et al. 2014). Circular dichroism spectra of BOC-FF showed a shift in the secondary structure during the peptide self-assembling process.

Fabrication of porous flower-like ordered structures was obtained, when solvent system was changed to methanol:water (1:1) mixture (figure 4-19) using BOC-FF concentration of 2 mg.mL^{-1}. Similar structures were reported for tyrosine amino acid and phenylalanine amino acid combination by Koley et al. (2015); Sakurai et al. (2014) using controlled applied voltages. Figure 4-20 shows the porous structure of self-assembled BOC-FF (average diameter 20 µm), prepared in methanol-water (1:1) without the application of a

voltage different from previously reported by Koley et al. (2015); Sakurai et al. (2014), where they found multifarious arrangements of the sheet-like petals (thickness of around 30 – 60 nm). In their study, they used combination of tyrosine and phenylalanine using a complex methodology.

It was reported that sself-assembly driven structures were only somewhat dependent on the electric field, electric current and temperature (Sakurai et al. 2014). In this study, multifarious structures were found for samples in alcoholic solution after drying on a glass substrate (without using any voltage).

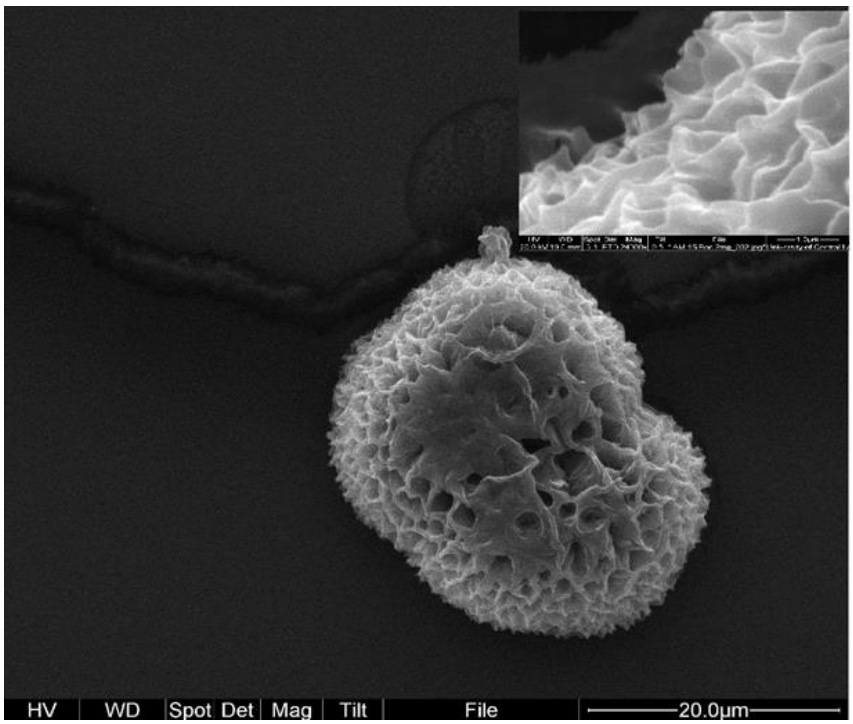

Figure 4-19 Figure 4 20 Figure 4 20 SEM images showing the formation of hierarchical structures and high-magnification showing the surface morphology from the methanol-water solution (1:1) (image is representative of three independent experiments)

ii) Chemical confirmation of self-assembled spherical peptide using Fourier transform infrared spectroscopy

Fourier Transform Infrared Spectroscopy (FTIR) was used to further study the self-assembling pattern of BOC-FF. The dried samples of the spherical peptide in ethanol-

water mixture (1:1) and commercially available lyophilised powder were investigated. The N-H stretching vibrations were observed at 3317 cm^{-1}. These confirmed the backbone of the peptide (Hopkins et al. 1991). 1700-1600 cm^{-1} is a characteristic region for Amide–I, which was used to confirm the peptide backbone. This did not have significance on the length or sequence of amino acid residues. In this region peaks positions were depicted; β-sheets at 1637-1615 cm^{-1} and 1696-1685 cm^{-1} (Chirgadze et al. 1976). While, β-turns can be observed at 1680 cm^{-1}. Similarly α – helix can be differentiated at 1665-1650 cm^{-1}. The region 1580-1510 cm^{-1} depicted the Amide-II bond, which is characteristic of the plane N-H bending (Kong & Yu 2007) (Table 4-4).

Table 4-4 FTIR spectral peak position and their possible reflection to bonding positions

Wavenumber (cm^{-1})	**Possible assignment**
3280	H-bonded OH groups, NH_2 stretching
2960–2920	Aliphatic C–H stretching (fatty acids)
1715 C=O stretching (carbonic acid)	C=O stretching (carbonic acid)
1600–1700	NH_2 bending, C=O, C=N stretching (amides I and II)
1624-1648	B-sheets
1650-1665	A-helix
1670-1695	B-turns
1450	C–H deformations in aliphatic
1400	C=O stretching (symmetric) of COO–
1390–1398	C–H bending, –CH3 stretching (fatty acids)
1240–1310	C–N stretching (amide III)
1000–1200	C–O, –, C–C stretching, C–O–H, C–O–C deformation (boc-modification)

In the BOC-FF samples; the Amide - I (associated with the – N - H stretching vibrations) was observed in water at 3280 cm^{-1}, confirming the hydrogen bonding in NH groups. BOC-FF in spherical self-assemblies (ethanol-water mixture) showed band at 3320 cm^{-1}. In Amide-I region (also showing the existence of C=O stretching vibrations) showed peaks at 1666 and 1658 cm^{-1} for lyophilised peptide. The Amide-I peak of the peptide in

the ethanol-water mixture was observed at 1685-1606 cm^{-1}, while in water Amide–I peaks were found at 1629-1655 cm^{-1}, The splitting of the some peaks appeared, due probably to the interactions of self-assembling monomers (Doyle et al. 1975).

The FTIR data (figure 4-20) reveal the presence of Amide–I region 1700-1600 cm^{-1} (Table 4-4). Amide-I peaks in the region of 1648-1624 cm^{-1} and 1665-1650 cm^{-1} of peptide sample can be assigned to β-sheet and α-helix secondary structures, respectively. The peak from 3300-3200 cm^{-1} reveals the NH stretching. Amide III band can be seen from1300-1200 cm^{-1}.

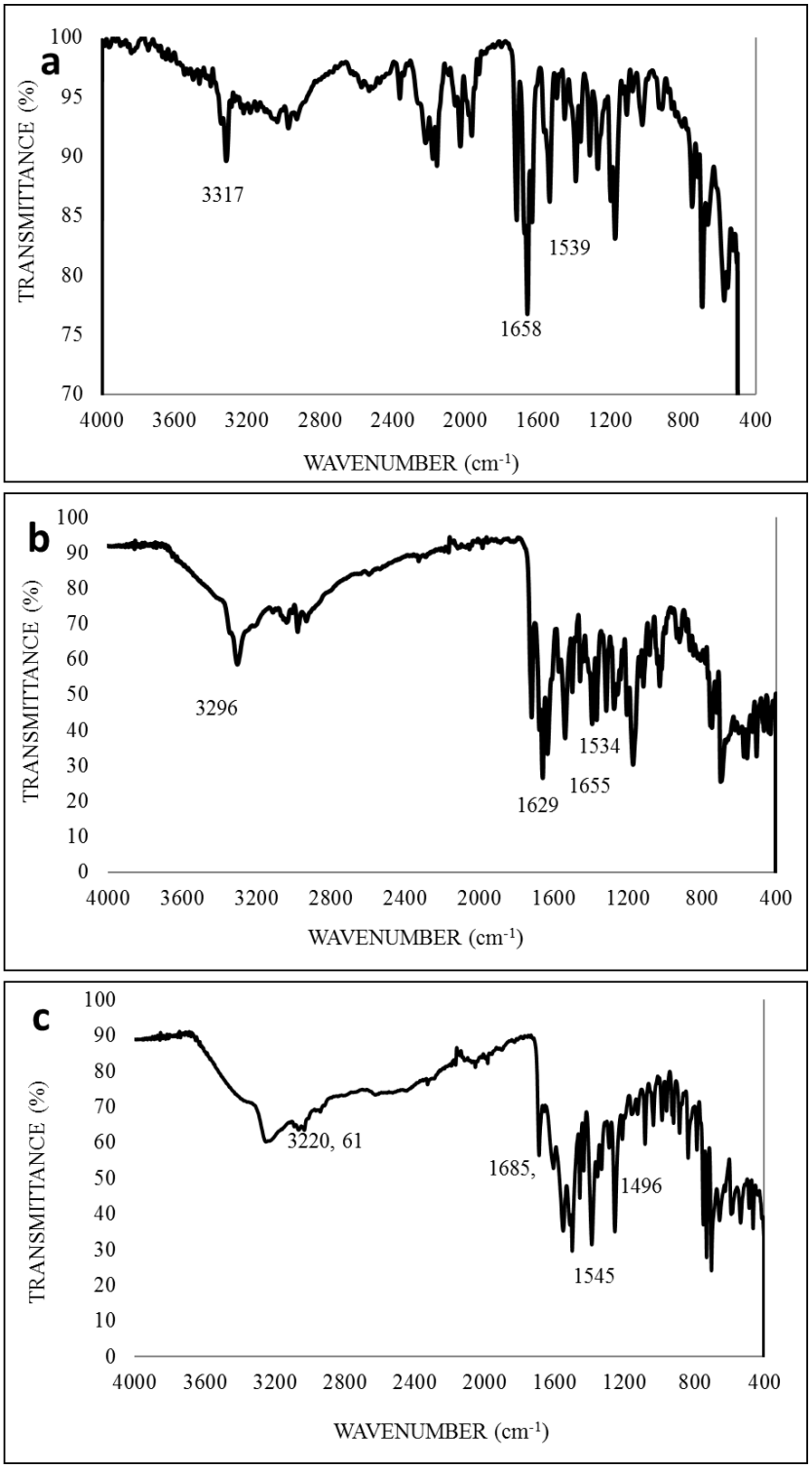

Figure 4-20 FTIR spectra of BOC-FF; (a) lyophilised powder (commercially available), (b) water alone and (c) ethanol-water mixture (1:1) (graphs are representative of three independent experiments)

In spherical morphologies, however the peaks around 1685 cm^{-1} were attributed to β-sheets secondary structures but the presence of other frequencies could be due to a

mixture of different secondary structures configurations (figure 4-20). The circular dichroism technique may be helpful to confirm the quantitative secondary structure compositions.

iii) Crystalline confirmation studies using X-ray diffraction analysis

X-ray Diffraction (XRD) was performed to study the crystallinity of BOC-FF particles along with their secondary structure. The presence of amino acids in self-assembled peptide structures in an ordered repeating distance can diffract X-ray beam. Self-assembling alignment of the peptide in different solvents may reveal structural information. For example, β-sheet showed two main diffraction peaks at ~4.7 Å and ~ 10 Å (Makin et al. 2006). The broad peak at 18 2Θ is the characteristic distance (4.7 Å) of the hydrogen bonding between β-sheets in ordered nanostructures, while the peak at (2Θ) value of 8.5 corresponds to the distance (10 Å) showing the distance between two separate β-sheet layers stacking on top of each other. Figure 4-22 shows the schematic depiction of β-sheet layers.

Figure 4-21 shows the XRD patterns of spherical BOC-FF. Along with the all characteristics peaks of the BOC-FF, a sharp peak also appeared at 11.3° (2θ), which can be attributed to the colloidal spheres (Li et al. 2013).

Figure 4-21 displayed the helical arrangement of residues. Each residue possibly be extended to some extent curved as α - helix attracted to carboxyl terminal in the core. In similar order, many helical residues interact each other to form the curved structures (Yan, Zhu, Fei et al. 2010; Maity et al. 2011; Li et al. 2013). These types of self-assemblies have been reported alongside α-helices and β-sheets. The spherical assemblies displayed XRD pattern of α-helices (5 A° = 17.7° (2Θ)) characteristic. The typical XRD patterns

arise from stacking of α-helical in a coiled-coil configurations, where they contribute to the spherical axis.

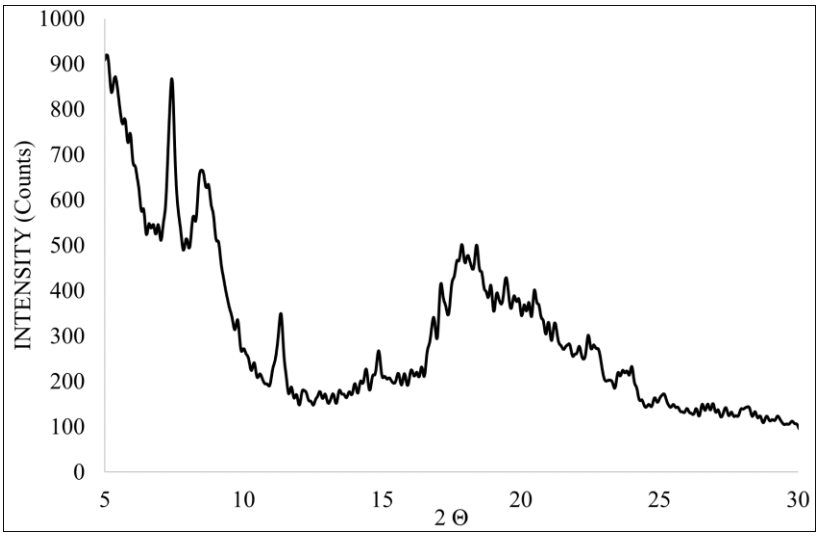

Figure 4-21 XRD pattern of BOC-FF in ethanol-water (1:1) mixture (graph is representative of three independent experiments)

Figure 4-22 schematic diagram of typical distances. Aligned layers of β - sheets are perpendicular to each other. The inter-residue space of π–π interaction is 4.7 A°, while layer-to-layer space is approximately 10 A°.

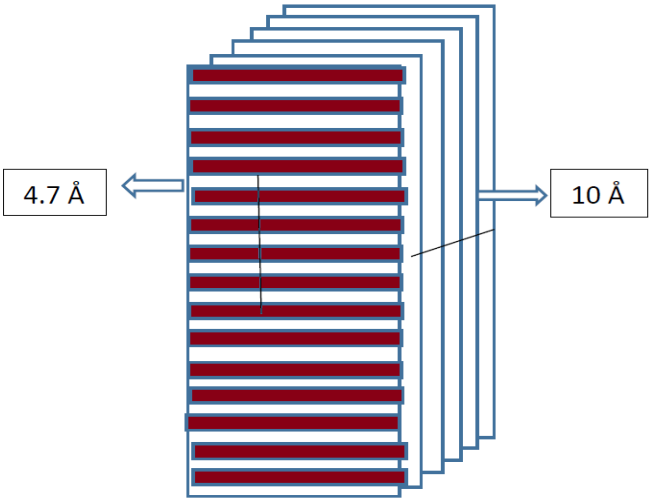

Figure 4-22 Schematic diagram of repeat unites of β-sheets

Figure 4-22 displayed the oriented arc at 18 (2Θ), corresponding to the distance of 4.72 Å, (characteristics β-sheet hydrogen bonding distance). Another arc characteristic to the interlayer spacing is seen at 8 (2Θ), where distance is 10 Å. Similar XRD peaks were also found in tubular structures. The peak, at 20 (2Θ) 4.4 Å, corresponds to the β-sheet. The slight shift in the position of the peak from 4.72 Å revealed the increased β-sheet spacing. This also correlates with a shift in peak position in FTIR (figure 4-20) indicating the changes occurred in the tubular structure. The typical distance (~10 Å) was observed for phenylalanine, glutamate and lysine based peptide self-assemblies (Wang et al. 2005). The substitutions of the nonpolar amino acid altered the distance of interlayer sheets to ~11 Å. The studies proved that the phenylalanine amino acid possibly involving in the formation of stacked sheets. This was usually proposed in a self-assembling mechanism for number of peptides residues. The molecular dynamic simulations on the BOC-FF also showed that π–π stacking and bulky nature of phenylalanine rings, which facilitate the self-assembling process (Yan, Zhu & Li 2010b). This would prevent the twisting of the fibril, as in case of spherical structures.

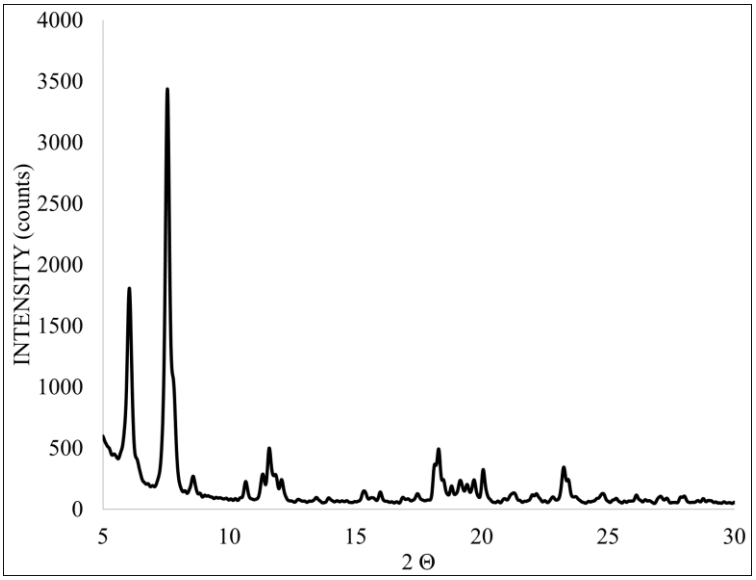

Figure 4-23 XRD pattern of BOC-diphenylalanine tubular structures in water (graph is representative of three independent experiments)

XRD data from the peptides showed a huge difference in the molecular arrangement when they self-assemble into different morphologies. For spherical BOC-FF peptide, the major peaks appeared at 2θ 8.7 and 18.04, and some minor peaks also appeared at 11, 14 and 23, whereas for BOC-FF in water showed major peaks at 6°, 7.5°, 8.8°, 18.8°, 20° and 23.2° (figure 4-23).

4.4 Peptide-coated spherical core – shell composites

Superparamagnetic iron oxide nanoparticles with different surface modifications have been studied in various applications; such as MRI contrast agent, in tissue repair, immunoassay, fluid separation, hyperthermia triggered drug delivery and in cell separation and identifications, etc. (Cai et al. 2013; Mahdavi et al. 2013; Ling & Hyeon 2013; Mahmoudi et al. 2011). These diverse applications required high saturation magnetisation values of smaller and uniformed particles size.

Ideal nanoparticles should have good dispersion in an aqueous environment to achieve desired results. These applications of magnetic nanoparticles require coatings with

minimal toxicity during targeting and tracking in the desired area. To achieve nanoparticle dispersions, numerous studies have been performed with water-soluble polymers (polysaccharide), (Guardia et al. 2012) dendritic stabilisers (poly amidoamine), (Nordmeyer et al. 2014) thiols (siloxanes), (Rajabi et al. 2013) and proteins (Sakulkhu et al. 2014). Among all these polymers, proteins got great attention as stabilisers due to their range of desired properties, such as stimuli responsiveness against pH or temperature and specified nanoparticle surface for effective cellular communications. Therefore, proteins nanoparticles are considered as biomimetic type of functional materials. However, due to high cost, complicated synthesis and further modifications processes and commercial scale productions have limited their applications.

Peptides are studied as simple alternatives of proteins. They possess different versions, based on sequences of amino acid (acidic, basic, polar, or nonpolar). Compared to proteins, peptides are commercially available leading them an attractive material for advanced materials science (Rad-Malekshahi et al. 2015).

Peptide-based spheres also showed stimuli-responsive to pH and temperature and a novel adaptive encapsulation property for functional inorganic materials (Yan, Zhu & Li 2010b). Based on the adaptability to hybrid materials, the self-assembling peptides had opened new horizons for a variety of guest materials. These hybrid materials include; charged or uncharged, hydrophilic to hydrophobic inorganic materials. This approach has been exploited in this work and can be extended to variety of bioactive molecules and functional inorganic materials to design multifunctional biomaterials. The adaptation of functional materials as core materials in the hybrid structures possibly will lead to the new avenues for encapsulation of functional inorganic materials into bioactive and biocompatible self-assemblies. The flexible biocompatible organic–inorganic hybrid

materials with novel functionalities will help in solving problems associated with biocompatibility, aggregation, solubility and bioavailability in drug delivery system.

Peptides have promising properties; a little is known for the functional properties of peptide - inorganic materials. Self-assembling peptides usually are based on tryptophan, tyrosine, phenylalanine and lysine (Chavarria et al. 2015). The mechanism to control the self-assemblies of the peptide is still needed to be explored. However, fabrication and self-assemblies on stabilised metal nanoparticles have been well studied (Sakulkhu et al. 2014; Rajabi et al. 2013; Nordmeyer et al. 2014; Guardia et al. 2012; Cai et al. 2013; Mahdavi et al. 2013; Ling & Hyeon 2013). Similarly, this needs to be explored that how these peptides transform into properties of the functional hybrid materials. It is crucial to understand how to control and regulates the self-assemblies of hybrid materials.

4.4.1 Characterisations

i) Morphological study using scanning electron microscope

The iron oxide and peptide based core–shell materials were prepared using two different methods. BOC-FF self-assemblies were achieved in ethanol-water mixture; hence, the solvent was kept idintical in both methods. The aim of using two approaches for coating of bare magnetite is to study whether the pre-established peptide self-assemblies influence on the coating of magnetite nanoparticles. Finally, optimisation of the best method to coat magnetite cores with the peptide. These two different approaches were i) one – pot synthesis of both core-shell materials and ii) a template-mediated method, where peptide was added dropwise to synthesised magnetite nanoparticles. After addition of peptide, materials were sonicated (power 40 W) for 10 minutes using probe sonicator. The ratio of magnetite nanoparticle to peptide was kept identical in both methods.

Figure 4-24 shows the core–shell morphology of nanocomposites produced by one-pot fabrication method. The size of core–shell structures was found approximately 400 nm in diameter. These were the smaller compared to core–shell structures prepared using template mediated method (figure 4-25).

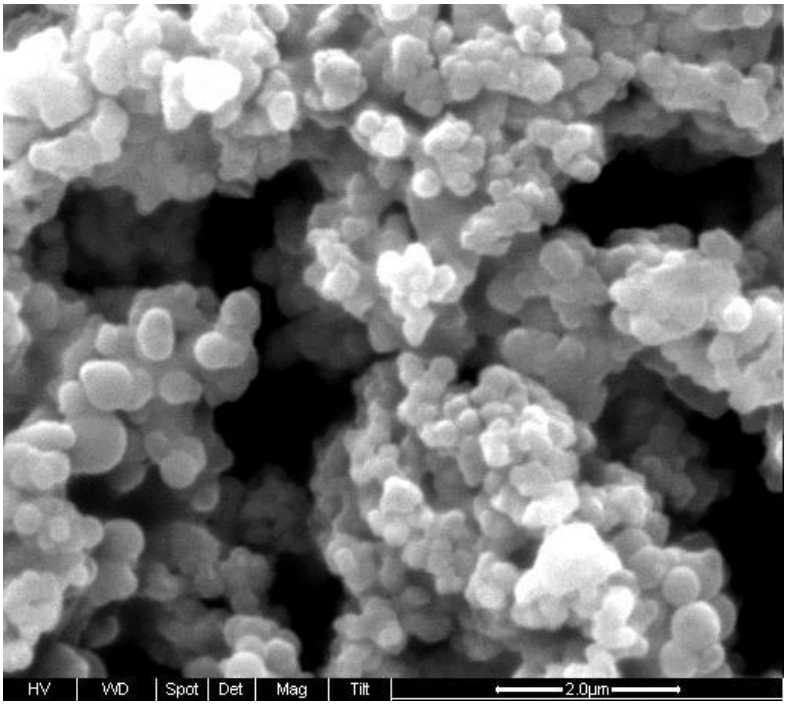

Figure 4-24 SEM image of peptide coated iron xide nanoparticles by using one pot fabrication method (Image is representative of three independent experiments)

In template mediated synthesis approach, the resulting BOC-SPION-SS were spherical, with size distribution ranging from 400 to 800 nm (figure 4-24). The core–shell materials were different in size from the bare iron oxide nanoparticles.The change in size distribution indicates the presence of peptide shell on iron oxide nanoparticles while retaining the magnetic properties. However, SEM could not differentiate the core-shell structure to confirm the number of B-SPIOPN-SS encapsulated. The core–shell structure could not be differentiated with SEM images, hence Energy Dispersive X–Ray Spectroscopy (EDAX) was used to confirm their chemical composition.

The SEM image (figure 4-25) showed a bi-phasic mixture of peptide particles and magnetite (Fe_3O_4) crystals. It is clear that wrinkled spheres are the attachment of iron oxide nanoparticles on the surface of the peptide. The images (figure 4-25 and 4-26) were taken from different places of same experiment (one-pot fabrication method). Hence, once the peptide assemblies formed it could not coat the SPIONs efficiently leaving a bi-phasic mixture of both individual components.

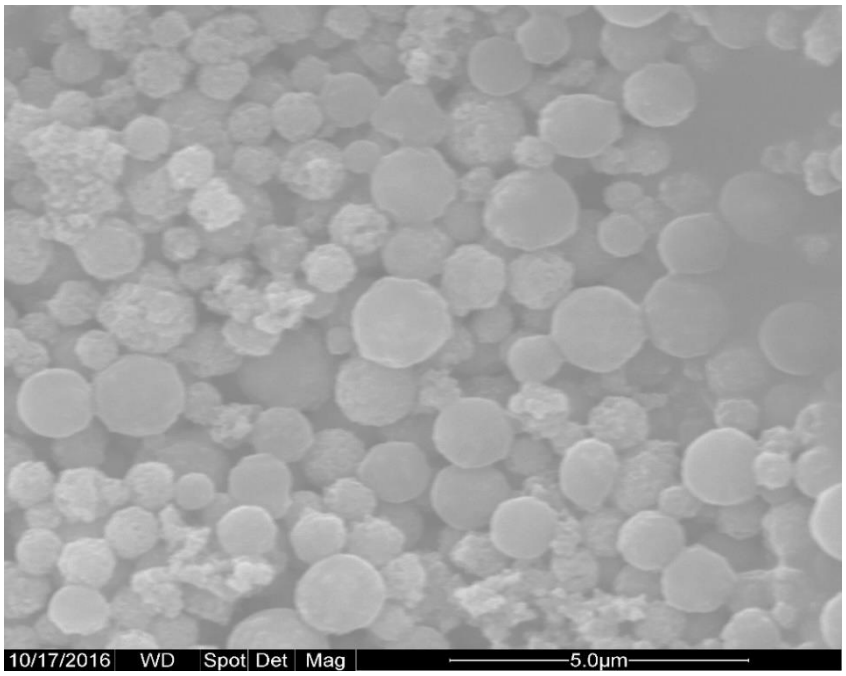

Figure 4-25 SEM image of SPIONs coated the peptide spheres using one-pot fabrication method (image is representative of three independent experiments)

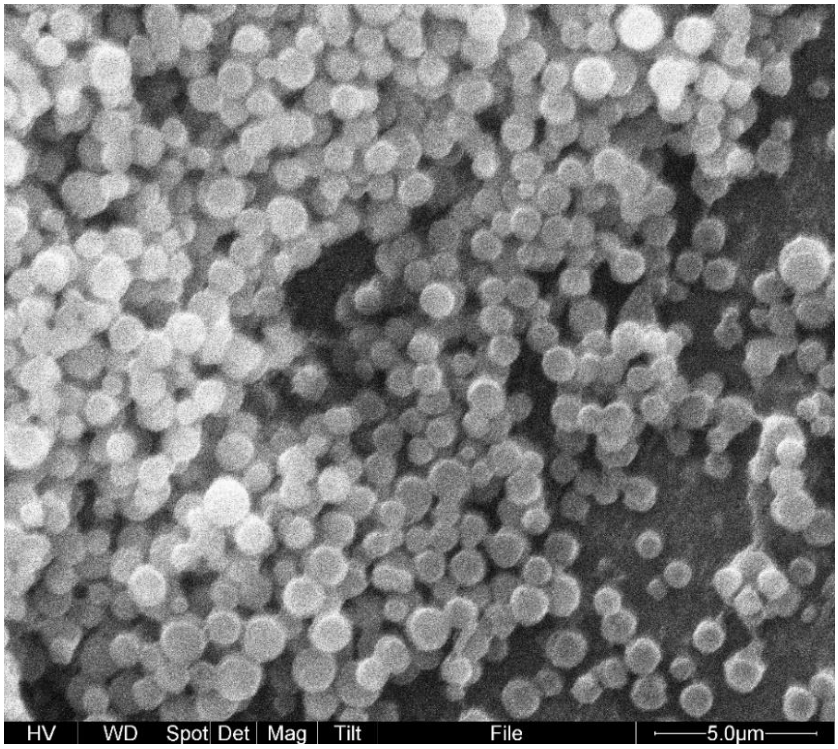

Figure 4-26 SEM image of BOC-SPION-SS by using template-mediated method (image is representative of three independent experiments)

Energy dispersive X-ray (EDAX) spectra were recorded from various places of the materials of both one-pot fabrication and template mediated synthesis method. The K lines are strongly energetic consisting of $K\alpha_1$, $K\alpha_2$, $K\beta_1$, and $K\beta_2$ radiations. Santra et al. (2001); Z. Z. Xu et al. (2004) have reported a similar pattern of EDAX spectrum for polymer coated magnetic nanoparticles.

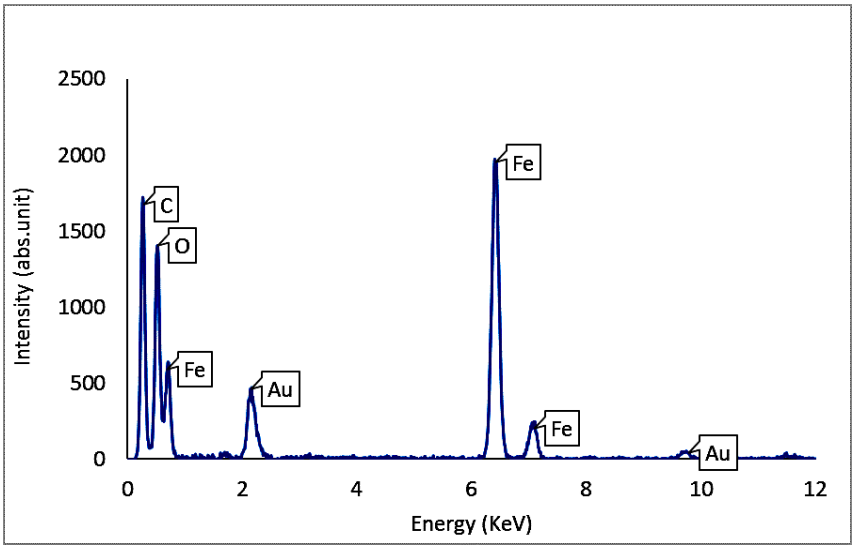

Figure 4-27 EDAX representative spectrum from BOC-SPION-SS nanocomposites (graph is representative of three independent experiments)

Peak intensities corresponding to C, O, Fe and Au were observed similar in both methods (figure 4-27). In both cases, as predicted, the peaks corresponding to Au have been found because of the coating to get clear visuals in SEM. Generally, for quantification of oxygen based materials, oxygen values would not be considered accurate due to the presence of carbon dioxide and adsorbed water molecules on the surface of materials. Thus, the quantification was obviated for core – shell materials, focusing only on identification.

ii) Size analysis using dynamic light scattering

The zetaiszer size distribution of core–shell materials BOC-SPION-SS synthesised *via* one-pot fabrication method measured to be in the range of 50 nm to 2 µm in diameter with high polydispersity. The iron oxide nanoparticles, when coated with peptide using template mediated synthesis method, the size distribution was predominantly uniform in diameter (400 nm). The difference between the two methods with zeta sizer is not comparable as to certain extent both materials showed aggregation (figure 4-28). However, ultrasonication could narrow down the material size distribution.

Figures 4-24 to 4-26 showed the effect of the both approaches of core–shell magnetite coated with peptide shells. The size distribution, for bare magnetic nanoparticles where core size even after aggregation, is 114 nm. The zeta sizer results of core–shell particles show different size distributions with an average size is, however greater than core materials.

iii) Chemical composition confirmation using Fourier transform infrared spectroscopy

FTIR studies performed for peptide-coated magnetite. The characteristic bands of the analysed materials including; OCO, CO, NH, FeO, CC were shown in Table 4-4. Figure 4-28, displays the FTIR spectra of bare iron oxide in the basic form Fe_3O_4 and peptide carbonyl capped iron oxide nanoparticles.

FTIR spectra of iron oxide skeleton show strong bands at 600-450 cm^{-1}. However, below 1000 cm^{-1}, the iron oxide has a weak band. The spectrum of bare magnetite (Fe_3O_4) displayed the corresponding signals at 550 and 450 cm^{-1} (Bruce & Sen 2005). The peptide characteristic vibrations include the NH bending and OCO. These stretching vibrations were seen at 1700-1400 cm^{-1}. Comparing bare and peptide coated magnetite, the peaks at 1637, and 1413 cm^{-1} can be observed confirming peptide coating. Peaks found in region 1637 and 1020 cm^{-1} corresponded to the CCO and CO stretching of the peptide. Bands at 2965 and 1000 cm^{-1} were referred to CH_2 stretching and CH out-of-plane bending vibrations, respectively. These peaks of functional groups peptides revealed that iron oxide is covered with the peptide.

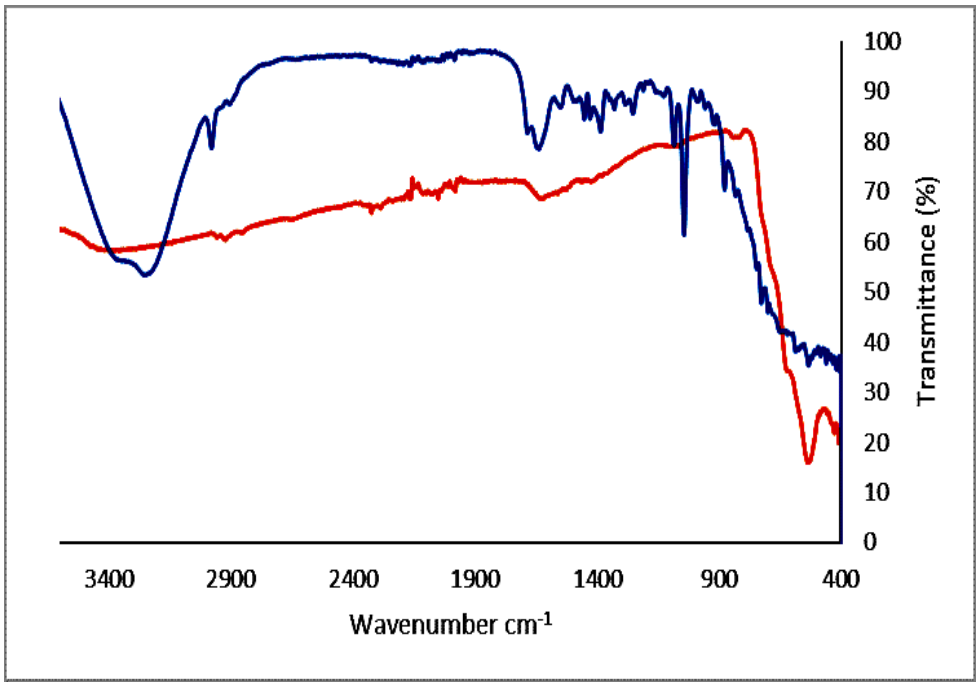

Figure 4-28 Infrared spectra of B-SPION-SS (red) and BOC-SPION-SS (blue) (graphs are representative of three independent experiments)

From FTIR data, it can be assumed that the presence of peptide surface will translate into a coating to iron oxide. FTIR peaks at 1465 cm^{-1} and 1700 cm^{-1} backing the assumption that the magnetic core interacts with to the carboxylate groups.

iv) Crystalline confirmation studies using X-ray diffraction of core–shell structures

Figure 4-31 shows the X-ray diffraction (XRD) patterns for the peptide coated SPIONs. The characteristic peaks of magnetite in coated materials could not be observed at 2θ, confirming the peptide after coating has amorphous structures. Hence, the functionalisation has altered the arrangement of the lattice which led to the disordering of the crystalline nature of bare magnetite. The spherical peptide shells overshadow the intensity of crystalline magnetite diffraction peaks (figure 4-29).

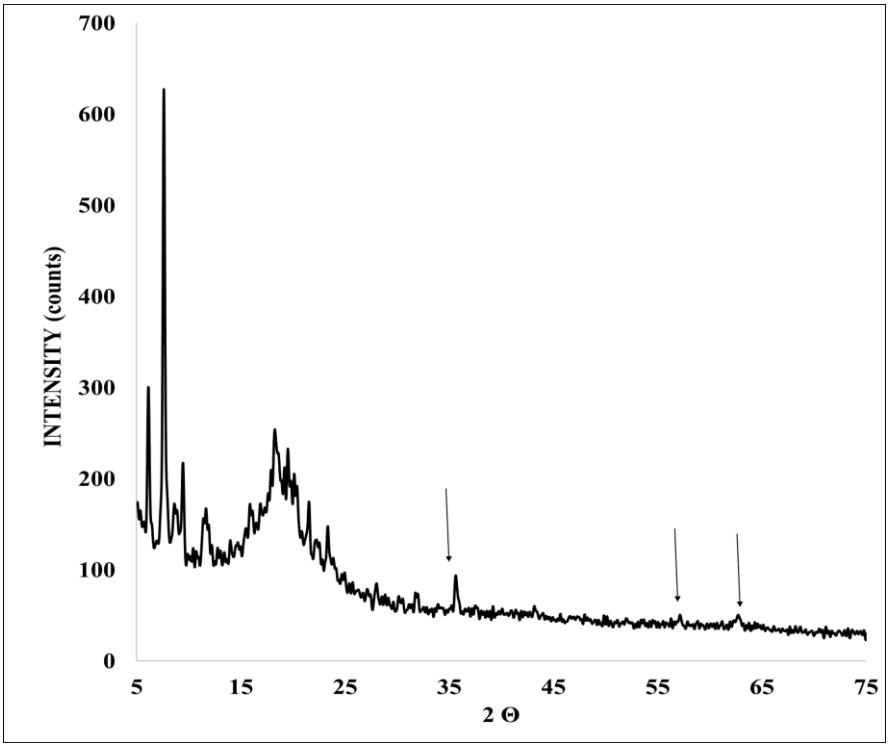

Figure 4-29 XRD pattern of BOC-SPION-SS (graph is representative of three independent experiments)

v) Saturation magnetisation measurement of core–shell nanocomposites using vibrating sample magnetometer

The magnetic behaviour of peptide coated iron oxide nanoparticles was assessed using field-dependent VSM. The hysteresis curves of core-shell nanocomposites were compared to B-SPION-SS. When the applied field was zero, basic magnetic domains are aligned irregularly with overall magnetisation value of zero. In this study, a reasonable high magnetic field (7 kOe) was used. There is evidence of saturation magnetisation in the peptide coated iron oxide nanoparticles compared to bare magnetite, showing the magnetic domains again aligned randomly when the magnetic field is removed. The dependence of peptide coated iron oxide materials` magnetisation on the applied magnetic field and lower magnetisation values compared to bare magnetite confirming that core – shell domains were aligned with the applied field.

Figure 4-30 shows the saturation magnetisation curves of B-SPION-SS, and BOC-SPION-SS. The saturation magnetisation values of B-SPION-SS, and BOC-SPION-SS were found to be 65 emu.g^{-1} and 18 emu.g^{-1} respectively. A reduction in saturation magnetisation values is due to presence of nonmagnetic peptide shell with Fe_3O_4 nanoparticles. The ideal saturation magnetisation value that applies to biological applications should be in the range of 7 – 22 emu.g^{-1} (Brusentsov et al. 2001; C. Xu et al. 2004). The saturation magnetisation achieved for peptide coated iron oxide nanoparticles (18 emu.g^{-1}) was reasonable for biological applications. VSM data also proved lack of hysteresis loss as both eminence and coercivity being zero, confirming the coating did not have any effect on the superparamagnetic behaiviour (figure 4-30). Due to this saturation magnetisation ability, the core–shell materials possibly have high enough contrast to be used in magnetic resonance imaging (MRI).

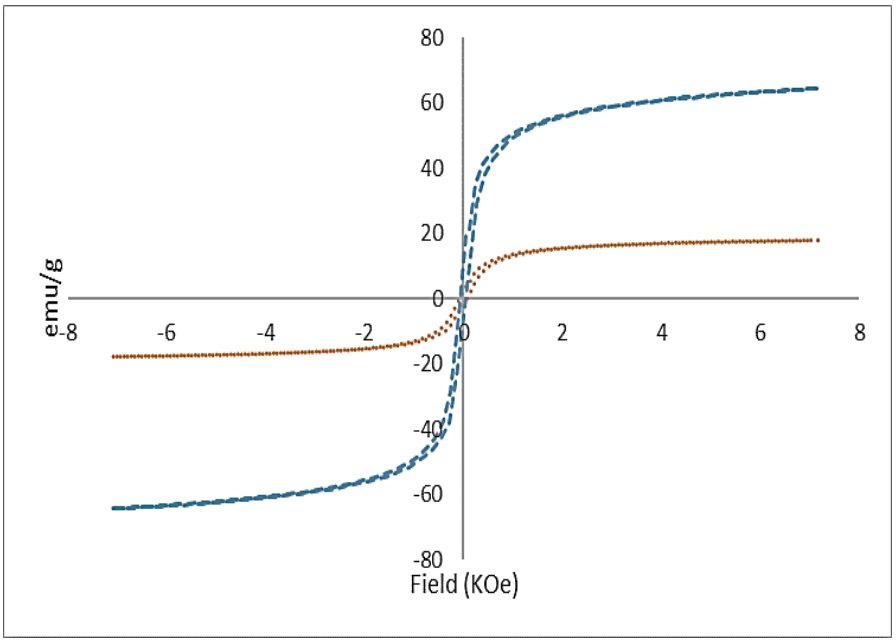

Figure 4-30 Magnetisation saturation curves of B-SPION-SS (blue dash line) and BOC-SPION-SS (orange dotted line) (graphs are representative of three independent experiments)

vi) Thermal stability measurements of core – shell structures using Thermogravimetric analysis

TGA curves of B-SPION-SS and BOC-SPION-SS nanocomposites were were obtained using TGA instrument under nitrogen atmosphere with heating rate of 10 °C.minute^{-1}. Figure 4-31 shows the variations in the residual masses of the materials over a range of temperatures. The peptide was completely burnt into gas products without any residual mass. The BOC-SPION-SS composites were burnt into magnetite at after 320 °C, respectively. The amount of remained magnetite can be quantified from the composite residual mass, where pure B-SPION-SS nanoparticles (figure 4-31) had a total weight loss less than 10 % over the temperature range analysed. This loss of weight is possibly due to the adsorbed water. The peptide started to burn above 150 °C. It can be estimated that the weight loss of total peptide coated on the iron oxide nanoparticles is nearly 55 % (figure 4-31 dashed line). The TGA curves for BOC-SPION-SS and pure peptide and B-SPION-SS are similar (figure 4-31). The first weight loss step is less than 130 °C, this can be attributed to the evaporation of water from peptide matrix, while second step beginning at from 158 °C, due to the burning of the peptide. TGA curve of peptide coated iron oxide nanoparticles estimated that the iron oxide amount at be around 45 %.

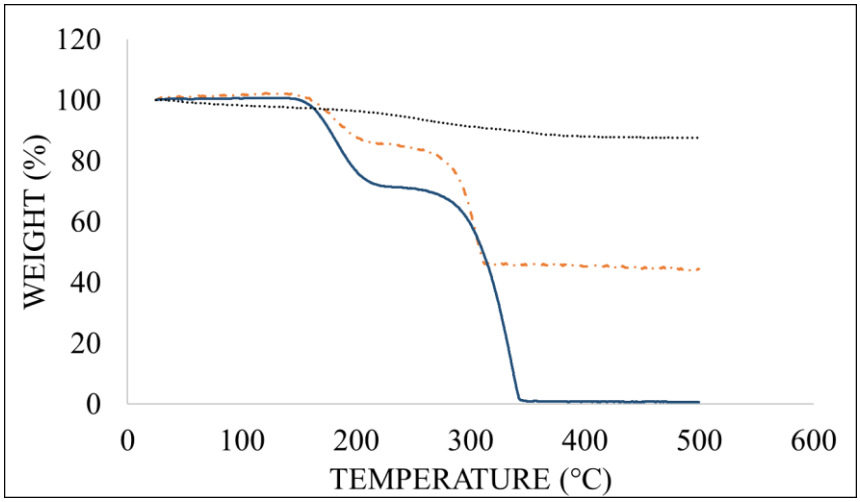

Figure 4-31 TGA curves of B-SPION-SS (black dotted line), BOC-FF peptide (solid blue line) and BOC-SPION-SS (orange dashed line) (graphs are representative of three independent experiments)

4.5 Peptide-capped mesoporous silica-coated iron oxide core-shell composites

Mesoporous silica-coated iron oxide nanoparticles have been studied as a potential drug delivery carrier. The mesoporous silica coated iron oxides have a high surface area to volume ratio with internal porosity can be used to achieve controlled drug delivery system. Controlled drug delivery system provides efficiency to restrict and permit the release of drugs. The synthesis of mesoporous silica-coated iron oxide nanoparticles capped with peptide were characterised and discussed for potential use in drug delivery system. The system consisted of a BOC-FF capping the mesoporous entrance of mesoporous silica-coated iron oxide with an average of particle size ranges of 400 nm. The average pore size is around 2.7 nm. By inserting the dry mesoporous silica coated particles to an aqueous solution of peptides, the mesopores were capped with self-assembling process of peptide.

i) Morphological studies of peptide-capped silica-coated iron oxide materials using scanning electron microscopy

SEM image of mesoporous silica-magnetite core-shell nanocomposites before and after peptide capping are shown in figure 4-32. Both materials have the spherical morphology of almost 1 µm in diameter. The SEM image of the peptide-capped silica-coated iron oxide displayed excellent dispersibility due to peptide-capped layer.

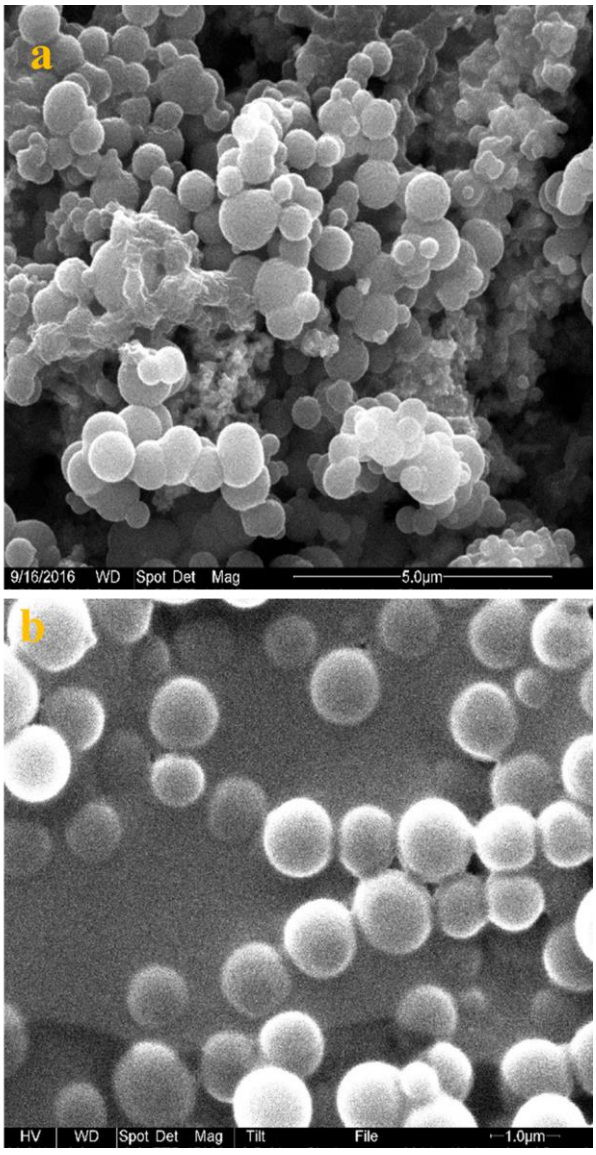

Figure 4-32 SEM images of (a) mesoporous Si-SPION-SS and (b) BOC-Si-SPIONs-SS structures (Images are representative of three independent experiments)

EDAX analyses were also performed to confirm the elemental composition of mesoporous silica-coated iron oxide nanoparticles. Figure 4-33 displays the EDAX spectra of silica coated core-shell with peptide capped materials. The EDAX peaks to the corresponding elements Si, O and Fe are labelled, confirming the composition associated with core Fe_3O_4 and mesoporous SiO_2 shell.

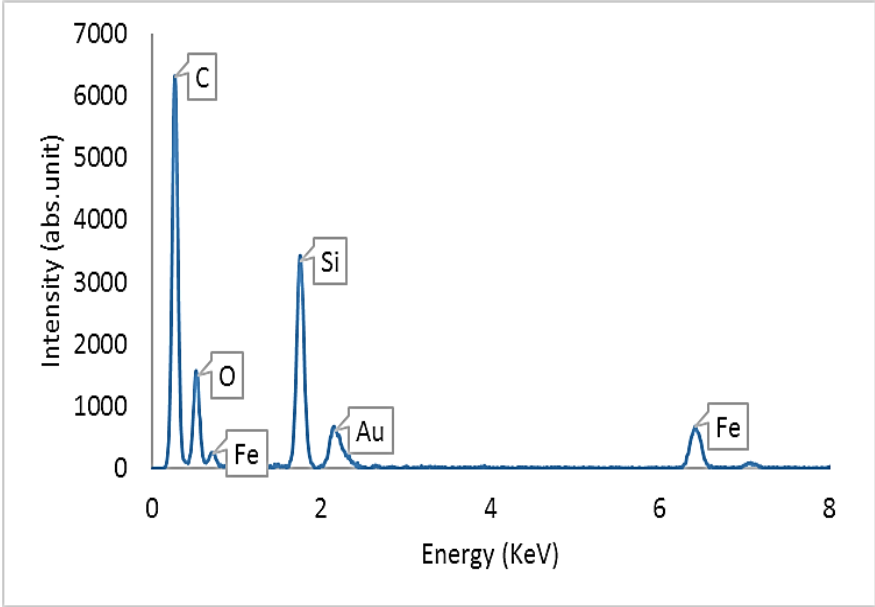

Figure 4-33 EDAX spectra of BOC-SPION-SS compositions (graph is representative of three independent experiments)

ii) Chemical composition confirmation of peptide-capped silica-coated iron oxide particles using Fourier transform infrared spectroscopy

Figure 4-36 showed the FTIR spectra of the Si-SPION-SS nanoparticles and the BOC-Si-SPION-SS composites. Vibration bands in the region of 1200 -1000 cm^{-1} and 800 cm^{-1} are characteristic of the Si-O and O-Si-O groups respectively. The band at 650 cm^{-1} could be due to the symmetric SiOSi stretching of four membered siloxane ring on the surface of iron oxide while 950 cm^{-1} band reveals the existence of the Si-O-H group. In mesoporous silica, the OH bands were found at 3600-3100 cm^{-1}, due to the presence of adsorbed water in siloxane rings. The intensity of the SiOH band at 950 cm^{-1} is reduced

in peptide capped core-shell structures. This indicates that SiOH contributes to the interaction with the peptide. The bands at 1180-1040 cm^{-1} correspond to stretching vibrations of the CO and CC groups of carboxyl and phenyl ring of the peptide, confirming the presence of peptide. In general, FTIR spectra of peptide capped materials were characteristics of carboxyl, amide and with a high concentration of siloxane groups. FTIR results of silica without peptide but with another organic polymers also looks similar to Yang et al. (2008) due to symmetrical and asymmetrical stretching of CC and NC of the polymers (figure 4-34).

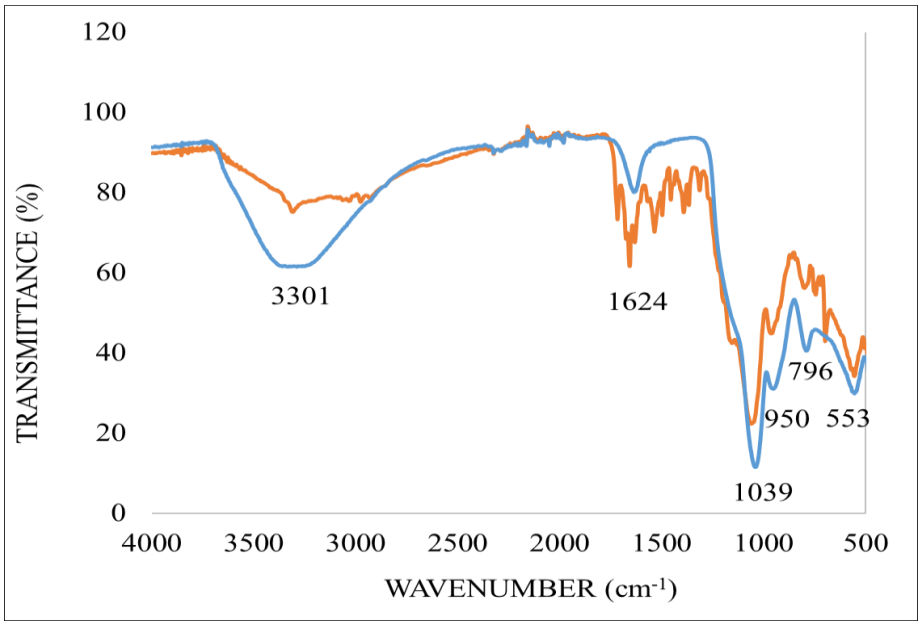

Figure 4-34 FTIR spectrum of Si-SPION-SS (blue line) BOC-Si-SPION-SS nanocomposites (orange line) (graphs are representative of three independent experiments)

iii) Thermal stability measurement using thermogravimetric analysis

Figure 4-37 shows the TGA curves of Si-SPSION-SS (black line), pure peptide (blue line) and BOC-Si-SPION-SS composites (red line) are shown in figure 4-35. Step-1 is the removal of adsorbed water below 150 °C. In this step, initial weight loss is approximately 10 weight %. From 150-500 °C, the total weight loss of peptide capped silica-coated iron oxide nanoparticles is 23 %. BOC-FF decomposes between 160 and 358 °C. Peptide-

capped core-shell composites decomposes with similar profile characteristics as the combination of pure peptide and uncapped core-shell composites. The total weight loss is around 55 % due to the peptide cappinhg around core-shell composites between ~ 180 and 330 °C (figure 4-35).

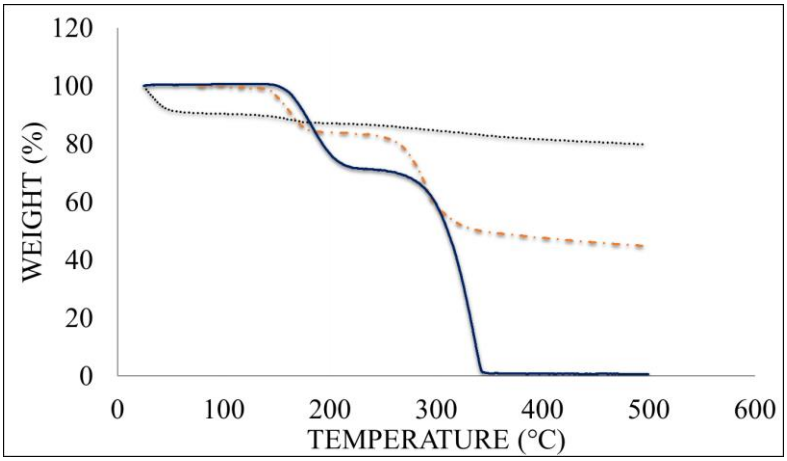

Figure 4-35 TGA curves of peptide (blue solid line), Si-SPION-SS (black dotted line) and BOC-Si-SPION-SS (dashed red line) composites (graph are representative of three independent experiments)

iv) Saturation magnetisation measurement using vibrating sample magnetometer

The magnetic properties of Si-SPION-SS core-shell and BOC-Si-SPION-SS composites were performed on vibrating sample magnetometer (VSM). Figure 4-36 displayed the characteristic hysteresis curves showing the zero coercivity and remanence confirming the superparamagnetism. The saturation magnetisation value of Si-SPION-SS was 45 emu.g^{-1}. However, the bare magnetite gives a value of 65 emu.g^{-1} (figure 4-36). The saturation magnetisation of BOC-Si-SPION-SS core-shell composites was approximately 10 emu.g^{-1}. The presence of both silica and peptide is responsible for the lowering of saturation magnetisation values due to non-magnetic property. However, the morphology and the magnetic properties in the context of coercivity and remanence were not altered.

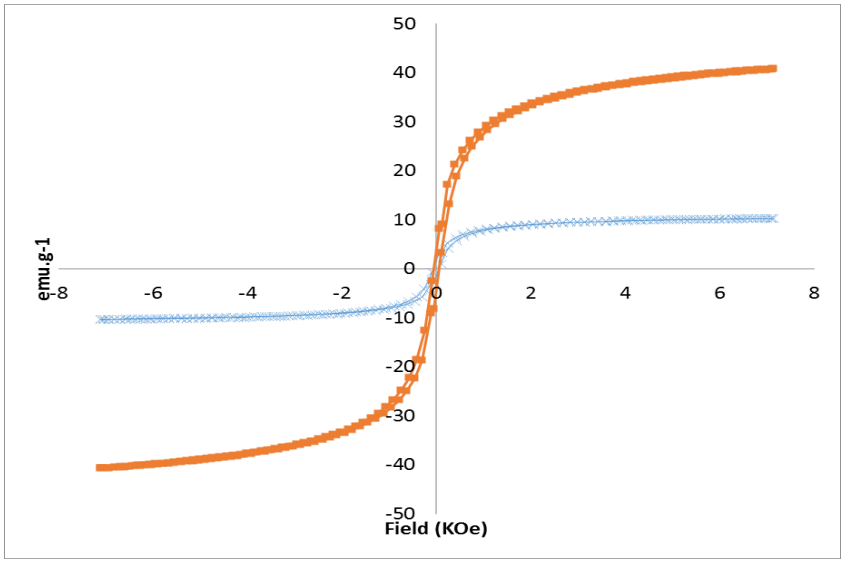

Figure 4-36 VSM saturation magnetisation curves of Si-SPION-SS (square) and (cross) BOC-Si-SPION-SS nanocomposites (graph are representative of three independent experiments)

4.6 Conclusions

Novel spherical superparamagnetic core-shell composites were prepared with magnetite (Fe_3O_4) core and peptide shells. All materials synthesised retained the superparamagnetic property. The objective was to encapsulate the magnetite core with high surface area mesoporous silica and peptide shells *via* template-mediated coating and to stabilise the spheres as core-shell materials. FTIR, XRD and EDAX have confirmed the presence of magnetite (Fe_3O_4) nanoparticles. Meanwhile, morphology and size were analysed using SEM and DLS respectively. The size distribution of spherical iron oxide cores was 20-35 nm in diameter, while coated materials were of almost 1 μm. TGA Thermal profile of individual and composite materials have confirmed the peptide coating on SPIONs and silica-coated SPIONs. The presence of characteristics FTIR bands for NH, OCO and FeO also confirmed the peptide coating on magnetite nanoparticles surface. Saturation magnetisation values for bare SPIONs, peptide coated SPIONs, mesoporous silica coated SPIONs and peptide-capped silica-coated SPIONs were 65, 18, 45 and 10 $emu.g^{-1}$ respectively. The core-shell composites have shown to be superparamagnetic in nature. The saturation magnetisation values were measured to be lower than core (Fe_3O_4) due to organic shells without affecting the superparamagnetism.

CHAPTER FIVE

Characterization of core-shell tubes peptide as shell and SPIONs as core material

5.1 Introduction

The shapes of nanoparticles play a key role in changing their physicochemical properties, which ultimately drives their functionality. The nanoscale iron oxide particles are the key in developing low-cost, functional materials for a variety of applications. The magnetic property of these materials make them ideal candidates for a variety of technological applications (Xie et al. 2009; Hutchings et al. 2013). Low cost and simple protocols are needed to engineer tuneable iron oxide nanoparticles to achieve most of their healthcare benefits. A number of protocols have been suggested for the synthesis of controlled shape nanoparticles including sol-gel, reverse micelle, co-precipitation and solvothermal methods. (Wilcoxon & Provencio 1999; Seip & O'Connor 1999; Jiang et al. 2004; Hyeon et al. 2001; Vayssieres et al. 2005). The co-precipitation method was used to synthesise both rod-shaped rod and spherical-shaped iron oxide nanoparticles.

Currently, it is challenging task to have a concise protocol to achieve controlled size and shapes of prepared nanoparticles. This work also aided in the better understanding of the synthesis of rod-shaped iron oxide nanoparticles. Iron oxide nanorods have already been synthesis by different protocols (Woo et al. 2003; Huang et al. 2011; Vayssieres et al. 2005; Sarawade et al. 2014; Polshettiwar et al. 2009; Fihri et al. 2012). This method is relatively simple, quick and does not require microwave or other sophisticated techniques. The spherical and rod-shaped iron oxide nanoparticles were synthesised with similar protocol simply by changing iron oxide salts. This new synesthetic approach to achieve different shapes of iron oxide nanoparticles is unique and not found in the

available literature. The size, shape, thermal degradability, magnetic susceptibilities and crystallinity of the iron oxide nanoparticles were characterised.

This chapter focuses on the physicochemical characterisation of the tubular peptide, rod-shaped iron oxide and iron-shaped core-shell nanocomposites. A variety of characterisation techniques including; SEM, EDAX, TGA, XRD, FTIR and VSM were performed. These techniques were carefully chosen to study best materials for drug delivery applications.

Sample preparation for each experiment and the equipment settings and parameters were described in section 3.4. Table 5-1 shows the concise list of the characterisation techniques used for each synthesised material.

Table 5-1 Characterisation techniques used for spherical materials

Sample	SEM/EDAX	FTIR	XRD	DLS	TGA	VSM
FM-ION-RS	√	√	√	√	√	√
FF	√	√	√		√	
FF-FM-ION-RS	√	√	√		√	√

5.2 Iron oxide as core materials

5.2.1 Characterisation

i) Morphology of the core materials nanoparticles using scanning electron microscopy

Figure 5-1 showed the morphology of rod-shaped iron oxide nanoparticles. The rod-shaped nanoparticles showed lower aggregation and uniform size in both length and width. They were approximately 500 and in length and 10 nm in width, respectively (figure 5-1). The tiny rods have a high aspect ratio hence it was difficult to focus in SEM.

XRD data showed the clear lattice fringes, confirming the crystalline structure of the rod-shaped iron oxide nanoparticles (figure 5-7).

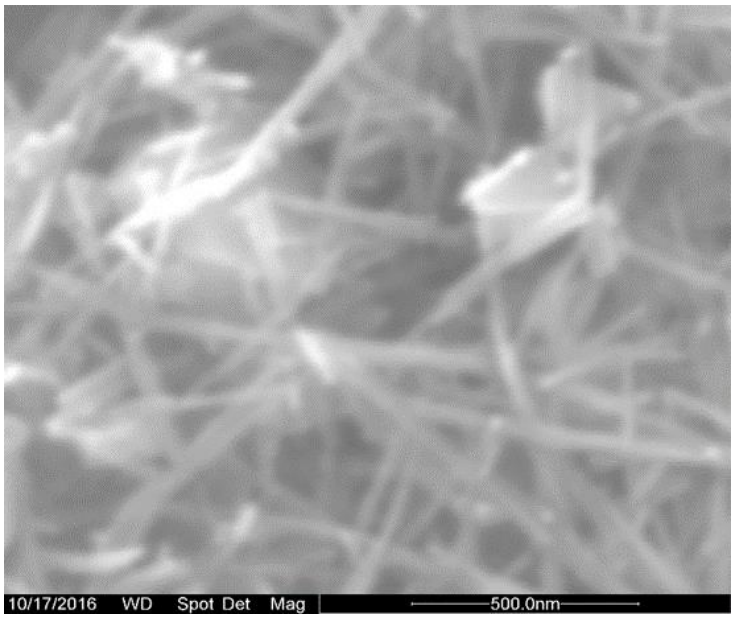

Figure 5-1 SEM images of Ferromagnetic Iron Oxide Nanoparticles Rod Saped (FM-ION-RS) synthesised *via* co-precipitation of ferrous sulphate route (Image is representative of three independent experiments)

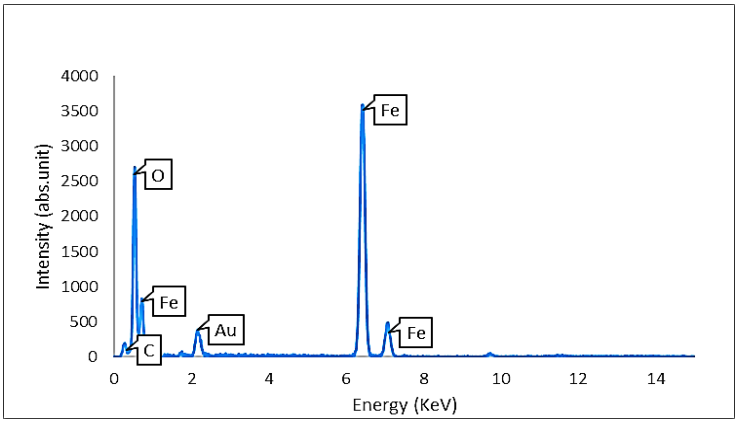

Figure 5-2 Energy dispersive spectroscopy of FM-ION-RS nanoparticles (graph is representative of three independent experiments)

Elemental analysis was performed on rod-shaped iron oxide nanoparticles using Energy Dispersive X-ray Spectroscopy (EDAX) to confirm the presence of iron and oxygen. Figure 5-2 shows the elemental analysis of bare rod-shaped iron oxide nanoparticles. As

expected, iron and oxygen peaks were observed due to the core iron oxide along with carbon and gold peaks due to carbon tape and gold coatings, respectively from sample holder. For each sample, EDAX spectra were recorded from three representative areas and the results were averaged for each element identified. Tables 5-2 showed EDAX elemental compositions and mass percent. The data showed the bare iron oxide magnetite was composed of iron and oxygen.

Table 5-2 Energy dispersive spectroscopy of rod-shaped iron oxide nanoparticles

	FM-ION-RS	
Elements	Weight (%)	Atomic (%)
C	7	19
O	23	44
Au	5	1
Fe	65	66

ii) Transmission electron microscopy

The method used to achieve rod-shaped iron oxide nanoparticles is novel, however ferrous sulphate based iron oxide have been published (Sayed & Polshettiwar 2015) but the method was fairly complicated. They used urea, CTAB and process involved microwave radiation. The method used in this study was relatively simple and quick. Synthesised rod-shaped magnetic materials showed a narrow size distribution. Figure 5-3 shows the TEM images of FM-ION-RS nanoparticles. The brief preparation method is described in section 3.4. Size distribution of rod-shaped iron oxide nanoparticles is nearly 10 nm in width and several hundred nanometres in length. Detailed analysis of the rod-shaped nanoparticles with higher magnifications has been presented in figure 5-3 (a-b). A nice crystalline structure with atomic resolution indicating well-ordered structure, which has been confirmed further *via* XRD analysis.

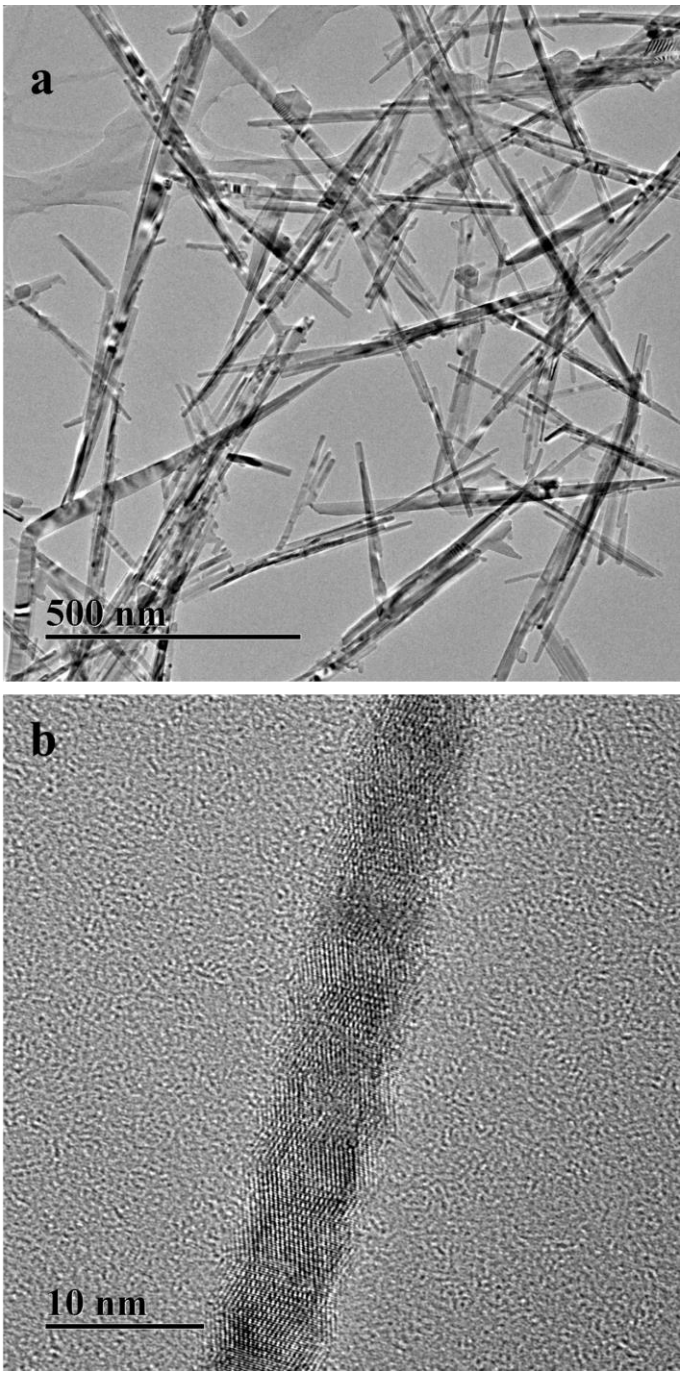

Figure 5-3 (a-b) TEM images of FM-ION-RS nanoparticles at different magnifications (Image is representative of three independent experiments and these images are taken in Liverpool University)

iii) Chemical confirmation of core materials using Fourier transform infrared spectroscopy

FTIR was used to characterise the iron oxide nanoparticles, to confirm the iron oxide bonding. FTIR spectrum of the bare core material is shown in figure 5-4. In figure 5-4,

the peaks at 550 cm^{-1} assigned to the Fe-O bond of iron oxide. However, the characteristic bands for a Fe-O bond of bulk Fe_3O_4 are stated as 570 cm^{-1}. A shift of Fe-O vibration band to to 550 cm^{-1} has been reported for the Fe_2O_3 nanoparticles (Bordbar et al. 2014). Hence, XRD analysis has been carried out for further confirmation.

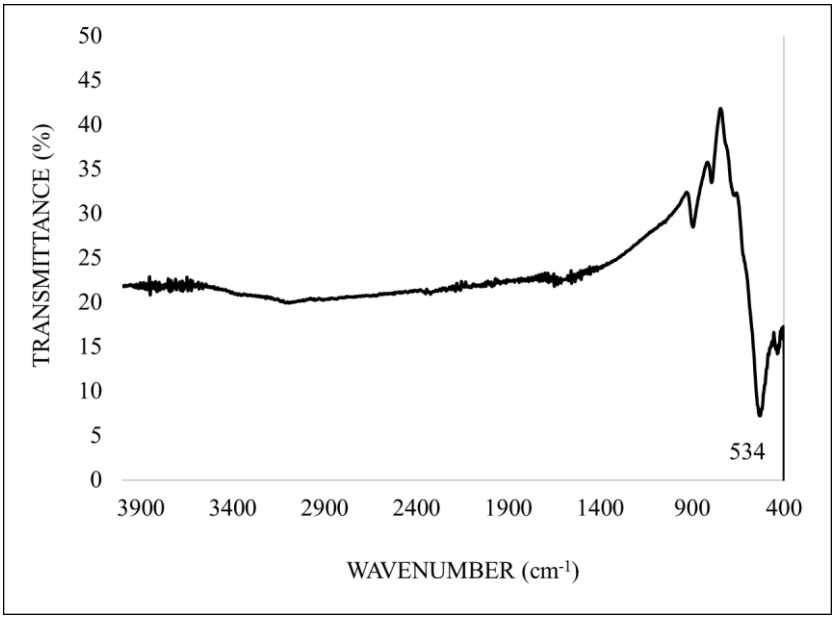

Figure 5-4 Fourier transform infrared spectrum of FM-ION-RS (graph is representative of three independent experiments)

FTIR (figure 5-4) confirmed the presence of FeO vibration band at 534 cm^{-1}. The peaks at 530 cm^{-1} and 440 cm^{-1} are assigned to the Fe-O bond. However, the characteristic bands for a Fe-O bond of bulk Fe_3O_4 are stated as 570 and 400 cm^{-1}, a shift in the bands of the Fe-O were around 545 and 440 cm^{-1}, respectively, as reported for the Fe_3O_4 nanoparticles (Bordbar et al. 2014). This shift is probably due to the nanosize of materials, where certain bonds of surface atoms are broken and causing the rearrangement of electrons on the particle surface. The successful deposition of silica on the bare magnetite material, namely mesoporous silica-coated iron oxide nanoparticles (Si-SPION-SS) was also confirmed by FTIR analysis.

iv) Crystalline analysis of core materials using X–ray diffraction

XRD pattern of the bare iron oxide nanoparticles is shown in figure 5-5. XRD pattern of FM-ION-RS materials have multiple diffraction lines corresponding to crytal phase of maghemite (Fe_2O_3) (figure 5-5). Figure 5-5 shows the characteristic peaks of Fe_2O_3 could be seen indicating a high degree of purity of bare iron oxide. Supporting the atomic scale resolution of TEM data

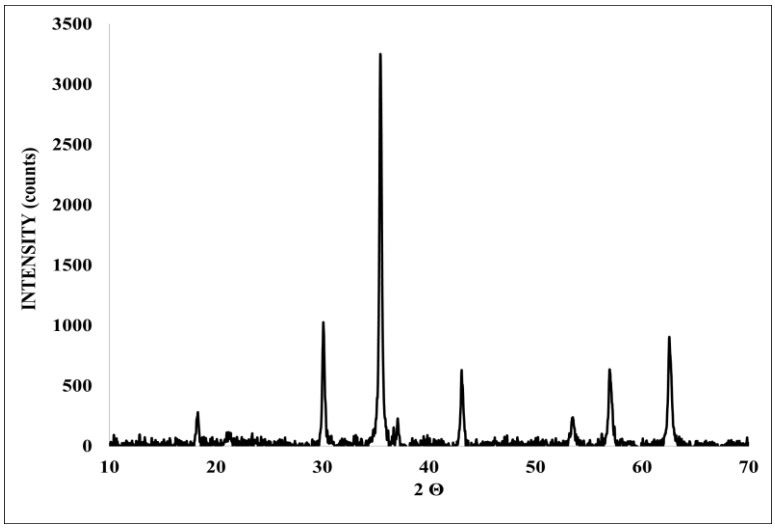

Figure 5-5 XRD plots of FM-ION-RS (graph is representative of three independent experiments)

v) Saturation magnetisation measurement using vibrating sample magnetometer

The magnetic properties of iron oxide nanoparticles may be affected by various factors such as; size, shape, crystallinity, preparation conditions, the cations substitution and surface modifications (Sarawade et al. 2014; Hyeon et al. 2001; Jiang et al. 2004; J. Huang et al. 2011). Figure 5-6 showed the VSM hysteresis curves indicating small ferromagnetic behaviour.

The magnetisation properties of core rod-shaped material of magnetic nanoparticles were measured at room temperature using the 7 kOe magnetic field. The saturation magnetisation (Ms) of core rod-shaped materials was 45 emu.g^{-1}, and silica hybrid iron

oxide was measured to be 19 emu.g^{-1} (figure 5-6). The coercivity was 0.05 emu.g^{-1}. The coercivity was largely influenced by different factors such as size, shape and surface modification. The previous study showed that coercivity in one-dimensional nanostructures is increasing, due to shape anisotropy of materials (Jain & Jothi 2015). Spherical nanoparticles as already discussed (figure 4-10) showed zero coercivity compared to the rod-shaped iron oxide nanoparticles. This may be due to the one-dimensional structure. In rod-shaped structures, the magnetic spins aligned with long axis, while in reversing to their opposite directions at reverse applied field, they require higher energy compared to spheres. The ferromagnetic behaviour of rod-shaped nanoparticles might be due to large size of particles as well as one dimension at over domain size.

As discussed earlier, spherical nanoparticles are superparamagnetic with no hysteresis, while the rod-shaped iron oxide nanoparticles are, ferromagnetic in nature.

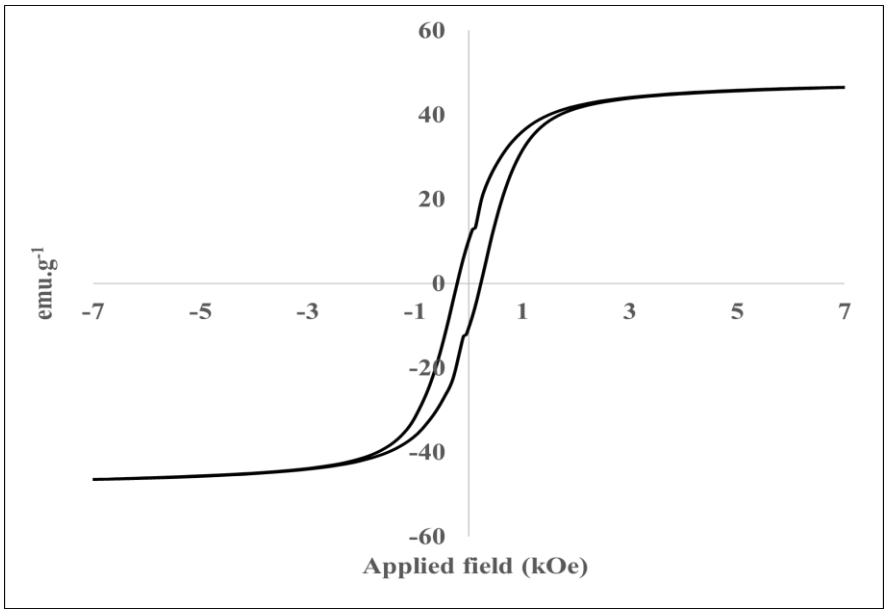

Figure 5-6 Hysteresis curve of FM-ION-RS nanoparticles (graph is representative of three independent experiments)

vi) Thermal stability measurements using Thermogravimetric analysis

Thermogravimetric analysis (TGA) of FM-ION-RS was performed for the identification of degradable elements of the nanocomposites. TGA experiments performed on the rod-shaped iron oxide over the temperature range from 25 °C to 500 °C. The total weight loss detected was approximately 11 % (figure 5-7). The loss in weight might be due to the loss of residual water in the sample.

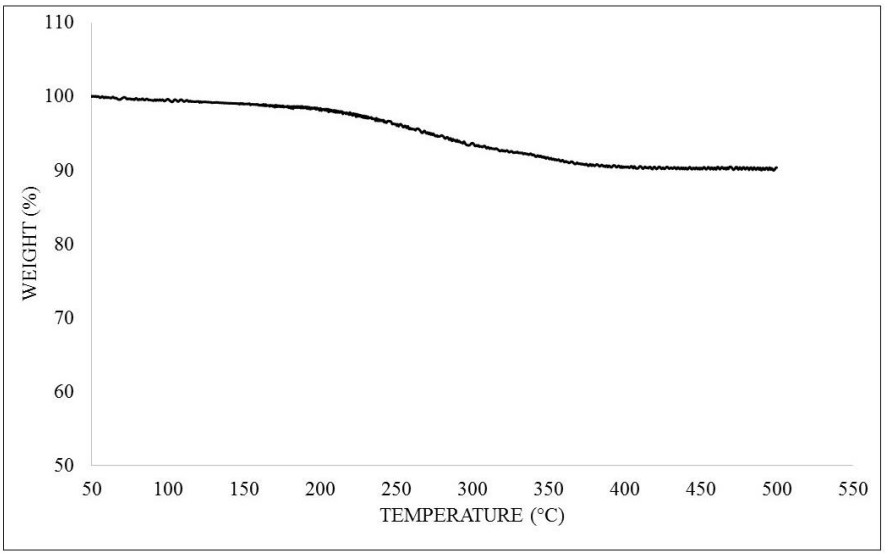

Figure 5-7 Thermogravimetric analysis of FM-ION-RS (graph is representative of three independent experiments)

5.3 Diphenylalanine as shell materials

5.3.1 Characterisation of tubular diphenylalanine self-assemblies

Peptide nanotubes are promised biocompatible, thermally and mechanically stable materials, which can be used in bionanotechnological applications (Kol et al., 2005; Lihi Adler-Abramovich et al., 2006). The hydrophobic peptides self-assemble into nanotubes *via* non-covalent interactions of repeating units of amino acid (Adler-Abramovich et al., 2009). The peptide-based nanotubes can be used as electrochemical biosensors, energy storage devices and various other applications (Matos & Alves, 2011). The self-

assembling pattern of FF peptide with the iron oxide nanoparticles into tubular morphology was studied.

i) Morphological analysis using scanning electron microscopy

Two analogues of FF (H-Phe-Phe-OH and BOC-Phe-Phe-OH) were used in this study. The H-Phe-Phe-OH and BOC-Phe-Phe-OH analogues used were abbreviated as FF (non-modified) and BOC-FF (boc-modified). Both self-assembled into long, stable bundles of tubes and fibres (Diaz & Çağin 2010). The self-assembly of both peptides was carried by dissolving in hexafluoroisopropanol (HFIP) and further diluting in either pure water or ethanol-water (1:1). Formation of fibrillar and discrete tube bundles proceeded over at room temperature. SEM images showed the diversity of elongated structures with a range of dimensions.

BOC-FF in ethanol-water mixture showed spheres (discussed in detail in chapter 4). The same material in water, showed aggregated fibres (figure 5-8). This sample was prepared in HFIP-water mixture (initially, 100mg.ml^{-1} in HFIP then 2 mg.ml^{-1} in water). The nanofibers were closely interconnected having lengths up to several microns. SEM images showed fibre bundles intertwined rather than thick discrete sheets of each fibre.

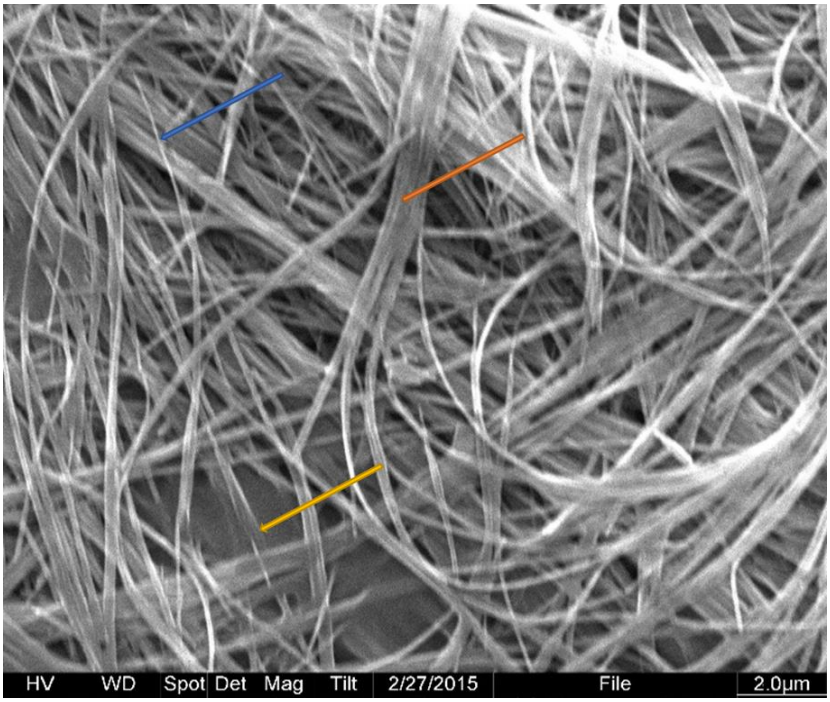

Figure 5-8 SEM micrograph of Boc Modified Diphenylalanine (BOC-FF) nanofibers prepared in an HFIP/water mixture (Image is representative of three independent experiments)

Figure 5-8 showed SEM images of dried sample of BOC-FF nanofibers. The length of nanofibers was up to several micrometres. Some individual nanofibers of up to 100 nm in width also appeared (figure 5-8 green arrow). However, the majority of these nanofibers were interconnected (orange arrow) forming long nanotubes with open ends (yellow arrow). The elongation of a fibre possibly results in peptide additions at one end. The SEM confirmed that microscale fibres are made of several short nanofibers assembling edgewise. The hydrogen bonding network may be involved *via* a shift in the Amide I band predictable with FTIR, corresponding to the β-sheets (figure 5-12) (Keten et al. 2010). It is difficult to confirm whether this addition is monomeric or polymeric.

SEM images also showed that BOC-FF fibres assembled structures are of two distinct types. Some structures were not bundled having the diameters of up to 100 nm while some were bundled showing diameters of up to several microns. The bundles composed of several ~100 nm (diameter) assemblies. In bundles, the gaps in between of fibres can

be seen, (highlighted in figure 5-8 orange arrow), confirming the attachment of individual fibres in the bundle. This bundling may have occurred *via* hydrophobic interaction of peptide assemblies, or it might be the function of evaporation of solvent during the synthesis process. This data is in good agreement with the suggested pattern of peptide stacking of β-sheets with TEM of individual fibres of 2 nm in diameter (Mart et al. 2006). This data confirm that the BOC-FF fibres are composed of individual nanofibers. From above evidence, it can be concluded to that large structures have three level assemblies; from the individual fibres of approximately 2 nm in diameter, stacking into the fibre of approximately 100 nm in diameter and then bundled fibre of approximately 1μm in diameter (figure 5-8). Even though in this study, it was not be possible to confirm the first stage of fibre formation in solution however the second level fibre transition to bundled fibres can be clearly seen. The previous study showed stable individual fibres during modification of peptide with polymers (Xu et al. 2011). It can be concluded that without protecting with polymers, first level fibres continue to stack into larger fibres.

Figure 5-9 showed the low magnification SEM image of a FF nanotube in HFIP-water (100 $mg.ml^{-1}$ in HFIP then diluted to 2 $mg.ml^{-1}$ in water). The nanotubes are stacked closely up to hundreds of microns in lengths. The results are comparable to published work on FF nanotubes (Adler-Abramovich et al. 2006).

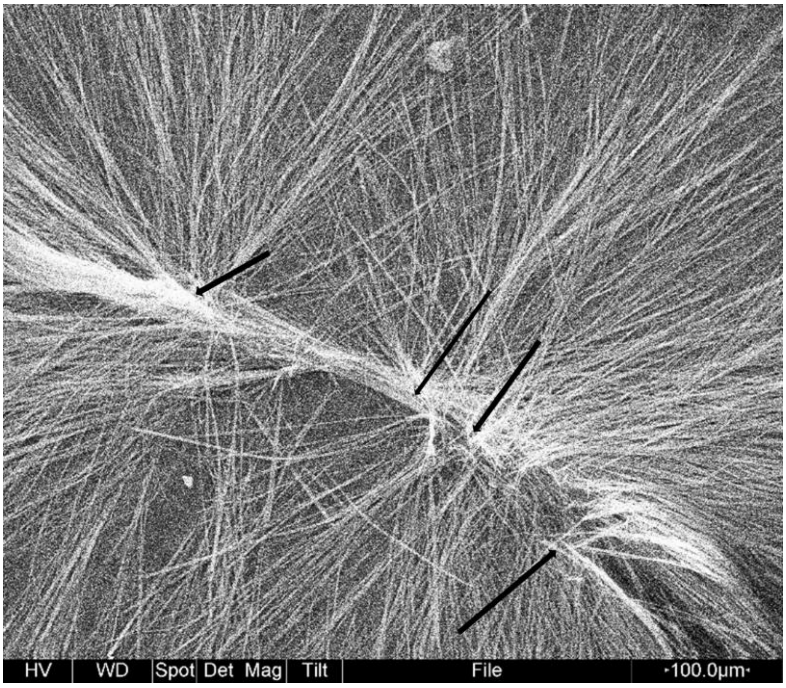

Figure 5-9 Image of Diphenylalanine (FF) nanotubes prepared in an HFIP-water mixture (Image is representative of three independent experiments)

Figure 5-10 shows the 'crystal-like' features stacked into bundles. This is a pattern of tubes initiation from a nucleating point and extending outwards. Red arrows depict the nucleation points in figure 5-10. Image were consistent with the data obtained by (XU 2011). Tubes initiating from nucleating points showed variations at the end. Some tubes are straight, others have curved morphology ending and some tubes merge within the surface of the substrate (figure 5-10).

In addition, when FF was dissolved directly in water at 1 $mg.ml^{-1}$ showed a 'feather-like' morphology with number of small tubular structures (figure 5-11 (a) and (b)). Figure 5-11 b showed some rod-shaped structures with lengths from 5 μm to 50 μm besides the feather-like morphologies. The end of these both branches was needle-like, (annotated with red arrows). The small round shape morphologies with diameters up to 10 μm are also found, a representative of which is annotated with blue arrows.

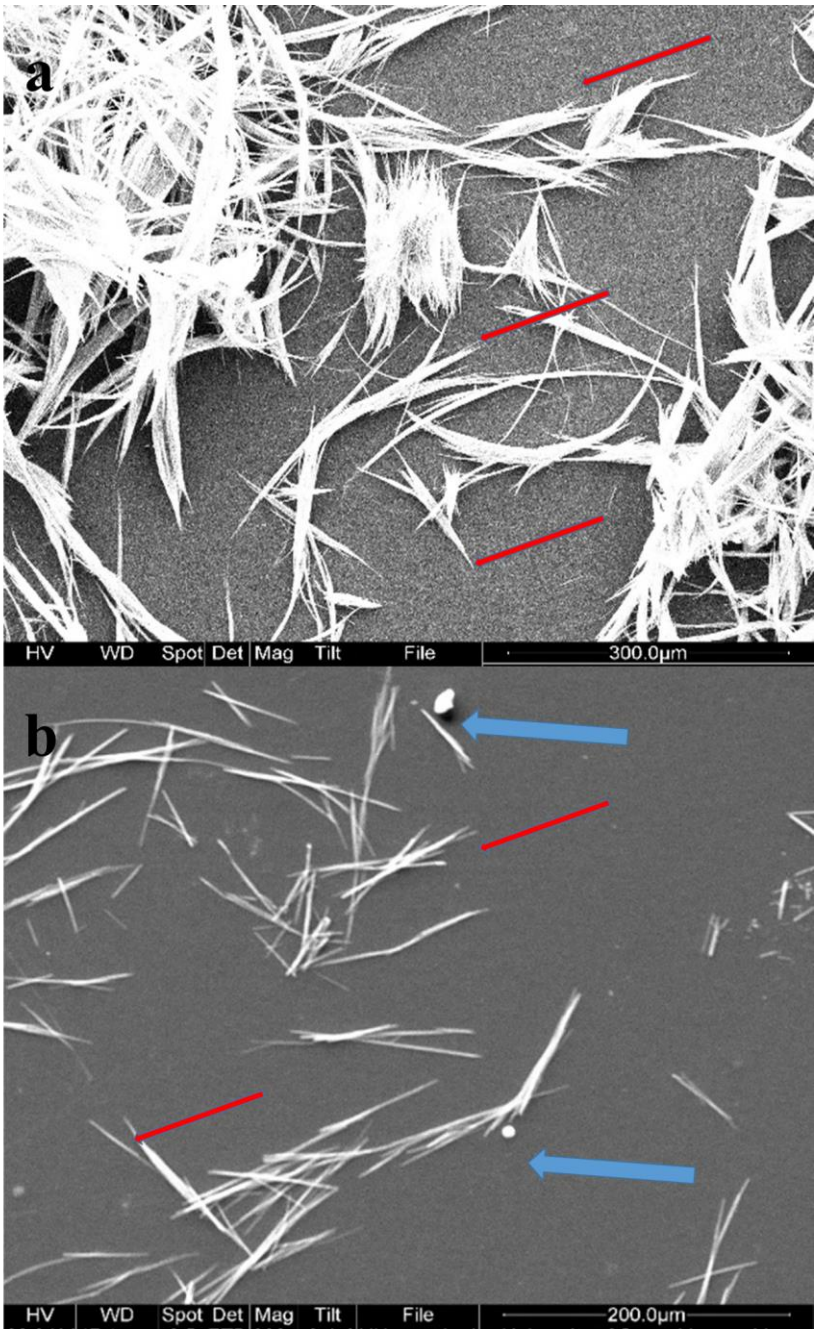

Figure 5-10 SEM images of FF dissolved in water alone from two representative area (a and b) (Images are representative of three independent experiments)

SEM images of FF in ethanol-water (1:1) showed the presence of nanotubes with hollow structures (figure 5-11). The length of nanotubes was up to several micrometres. In contrast to FF in water formed nanofibers, FF assembled into discrete nanotubes. Shao & Parquette (2009) found, using tapping-mode AFM, a cross-sectional space of 20 nm with average lengths of several micrometres. The AFM revealed that the long axis of the tubes

was smooth and consistant. These findings were consistent with the nanotube formed in this work. The average diameter (6 nm) of the peptide nanotubes were reported as smallest β-sheet based nanotubes of octapeptide (Valéry et al. 2003).

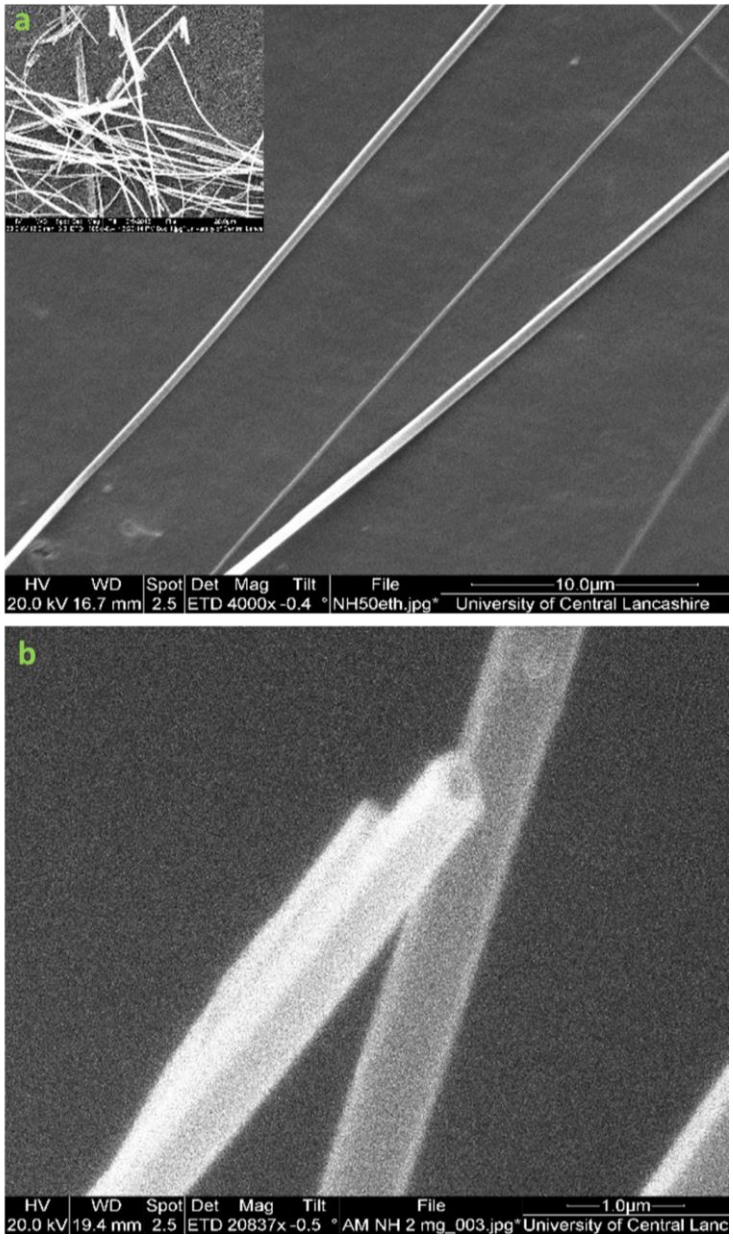

Figure 5-11 SEM images of FF in ethanol water (1:1) mixture (a) long discrete nanotubes (b) end of nanotubes with hollow space(Images are representative of three independent experiments)

Figure 5-11 showed SEM image of the FF nanotubes in ethanol-water (1:1) mixture . Nanotubes formed with ethanol-water mixture showed well-defined nature and were loosely packed and well scattered on the substrate. The nanotubes were not stacked on each other without nucleation point of growth. A low-magnification image of the nanotubes (as shown in a small rectangle in figure 5-11(a)) revealed the range of tubes of several hundred nanometres in diameter and up to hundreds of microns in length. The results are consistent with previously published work, where researchers found tubes diameter ranging from 10 nm to 100 nm and an extended length of up to 100 μm (Song et al. 2004). The hollow ends of each FF nanotubes can be seen clearly (figure 5-11 (b)).

ii) Chemical confirmation analysis using Fourier transform infrared spectroscopy

Figure 5-12 shows the Fourier transform infrared spectroscopy (FTIR) spectra of dried FF in water and ethanol-water (1:1) mixtures. FF confirmed the CO stretching (amid band) at 1512 – 1494 cm^{-1}, characteristics bands of β-sheets. In addition, nanotubes showed broad bands at 1660 - 1512 cm^{-1} and a sharp peaks at around 1674 cm^{-1} (figure 5-12). FTIR spectra of both structures showed mixture of β-turns and β-sheets secondary structure configuration. While FF in water only showed a peak at 1685 cm^{-1}, which is characteristic to antiparallel β-sheets (Martinez & Millhauser 1995). Considering both, peptide nanotubes self-assembled as results of π-β conformation (Baldassarre et al. 2016; Aggeli et al. 1997)**.** Remarkably, the band at 1685 cm^{-1} found in FF in water reported to be stacked fibres (Gallagher 1997). Thus, the lack in the antiparallel β-sheet characteristic band for FF in ethanol-water revealed stacking and discrete structure, which is governed by hydrophobic π-π interactions. The difference in morphology of both structures of FF in water and ethanol-water mixtures was clearly visible in the SEM (figure 5-11).

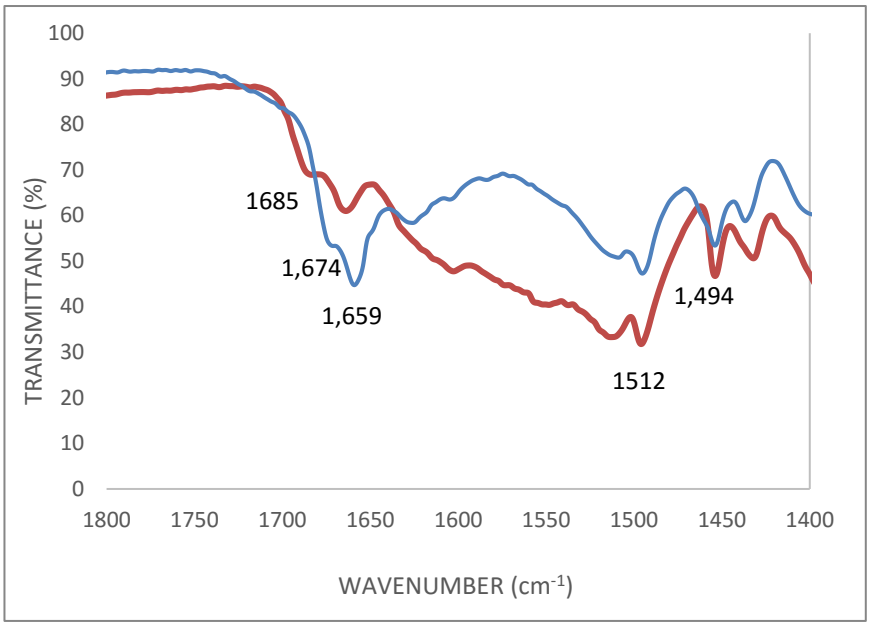

Figure 5-12 FTIR spectra of FF in water (red line) and ethanol-water (1:1) mixture (blue line) (graphs are representative of three independent experiments)

iii) Crystalline analysis using X-ray diffraction

X-ray diffraction (XRD) was used to characterise the dried tubular morphologies of FF prepared in both solvents systems (water and ethanol-water mixture) to study the difference in the crystalline structure. Figure 5-13 shows the XRD patterns of the nanotubes prepared by two different conditions. Both conditions provided nanotubes, which are crystalline in nature. However, there is a distinct difference in their crystalline structure.

The results obtained in this study were compared with published work (Görbitz & Gorbitz 2006). The diffraction pattern of peptide nanotubes was compared to simulated diffraction pattern of tubular structures where XRD pattern showed the curves were similar to the single crystal simulated curves. This pattern is in good agreement with published XRD data on FF nanotubes (Görbitz & Gorbitz 2006).

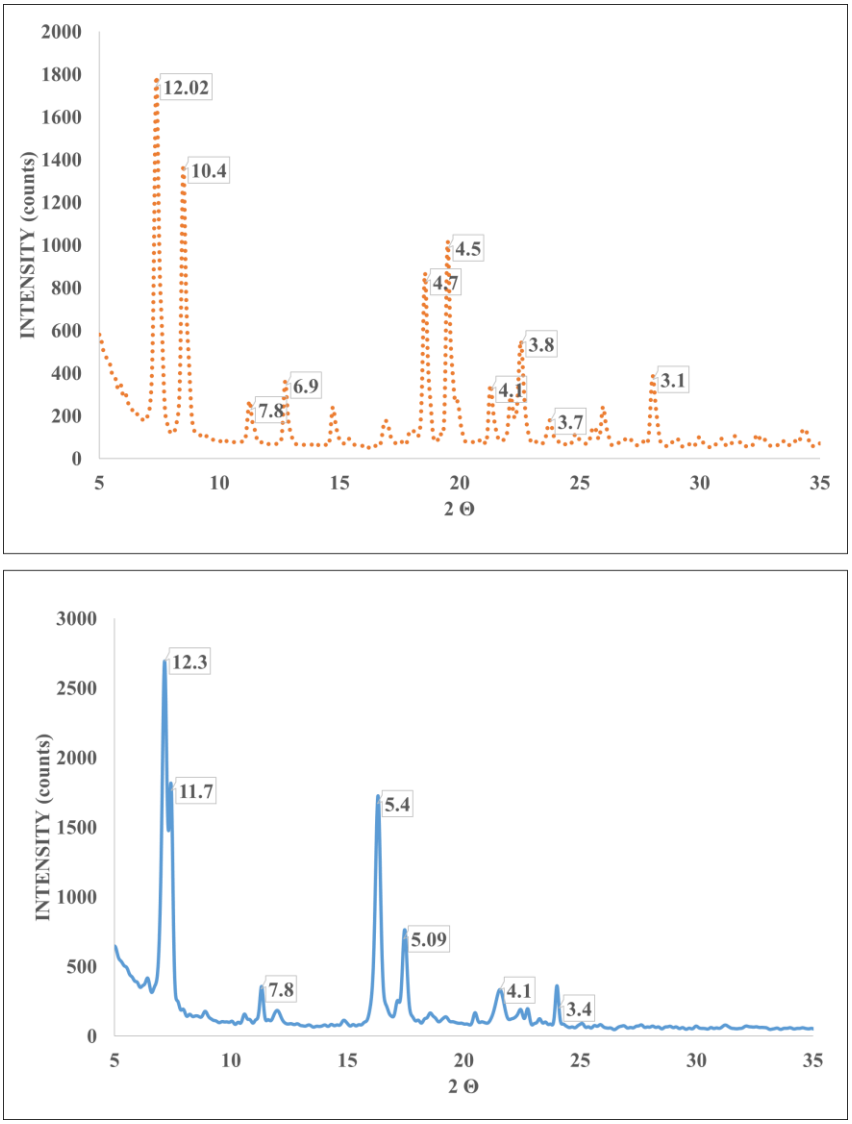

Figure 5-13 XRD pattern of (orange dotted) FF in ethanol water and (blue solid) in water alone showing d spacing in (Å) (graphs are representative of three independent experiments)

XRD patterns of FF in ethanol-water mixture and water alone revealed the presence of ordered β-sheets within the nanotubes (figure. 5-13). XRD data was further investigated to extend the understanding of the supramolecular order of FF nanostructures. As a backbone of similar material, characteristic amyloid peaks confirmed the peptides self-assemblies of elongated structures (Görbitz & Gorbitz 2006). The characteristic peaks at 4.1 Å, and 3.4 Å showed the self-assemblies of phenylalanine monomers interacting *via* π–π stacking. The peaks at 4.7 Å and 5.09 Å are characteristic of inter-sheet distances. 12.02 Å and 12.5 Å, which can be assigned to peptide lengths, as confirmed by computer

simulation (Görbitz & Gorbitz 2006). The intense peak at 12.5 Å, and a weak peak at 12.02 Å for discrete and bundle-like structures suggesting the typical space between individual structure (Marchesan et al. 2015). X-ray diffraction pattern with d-spacing was found to be 4.5 Å (a) and 5.09 Å (b), both were the typical inter-strand spacing of "cross-β" patterns, while the typical spaces in the helical structures were 3.4 Å and 3.1 Å. The discrete nanotubes in ethanol-water mixture were tightly packed with antiparallel β-sheets in a higher supramolecular order compared to stacked bundles in water. Anti-parallel β-sheets have a more intense XRD signature compared to the peptide displayed disorder secondary structure configuration. This revealed that stacked bundled structures are not only composed of disordered β-sheets, but may have peptide folding with other secondary level configuration.

iv) Thermal stability analysis using Thermogravimetric analysis

Thermal stability of self-assembled FF in water and ethanol-water was measured using TGA. TGA provided the information of changes in mass of peptide during thermal degradation. These studies confirmed the onset degradation is similar in both structures (stacked bundles to discrete tubes) of FF in water and ethanol-water (1:1) mixtures, respectively. Figure 5-14 shows TGA profile of both materials, where initial weight loss corresponded to the possible removal of adsorbed water below 130 °C. This weight loss of almost 12 % was consistent with the hollow structures of both materials. These results also confirmed that the framework remained stable up to 270 °C, before it can be fully decompose at 350 °C.

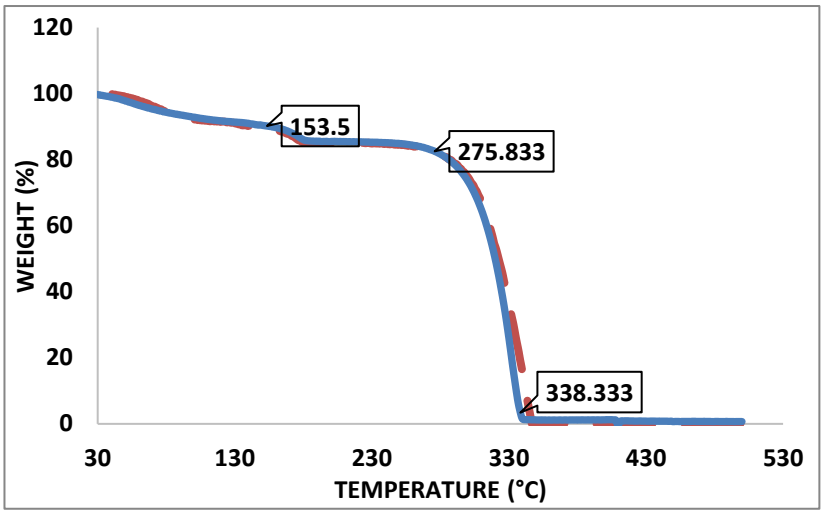

Figure 5-14 TGA profile of FF in ethanol-water (orange dashed line) and FF in water (solid blue line) (graphs are representative of three independent experiments)

5.4 Peptide-coated core-shell magnetic nanorods

5.4.1 Characterisations

The rod-shaped iron oxide cores were coated with tubular FF in order to achieve core-shell nanorods. The concentration ratio of iron oxide cores to peptide was (1:5). The bare rod-shaped iron oxide cores tend to aggregate and settles in bottom. The stable iron oxides were obtained after coating with the FF nanotubes in uniform dispersion in ethanol-water system. The coated product was then obtained *via* magnetic separation. The magnetic materials then re-suspended again in ethanol-water. Physical observations confirmed the dispersions and the ability to separate out by magnet. The success in achieving the core-shell structure can be due to the self-assembly of FF on iron oxides cores. The resulting modification achieved *via* non-covalent interactions of peptide and the surface of the nanorods of iron oxide cores. The biologically derived peptide sequence was used gave a positive reinforcement to this approach for designing core-shell materials. However, there are some specific sequences designed to interact with specific metallic cores (Wang

et al. 2003). In addition, the phenylalanine amino acid side may interact with the iron oxide surface due to stronger π-π interaction.

i) Morphological analysis using scanning electron microscopy

Figure 5-15 showed the SEM images of coated rod-shaped iron oxide nanoparticles. Images of dried sample of core-shell materials were taken on carbon tape at room temperature. Figure 5-15 revealed that the most of the coated iron oxide nanorods were separated into short length rod-shaped structures. they were closely packed possibly due to hydrophobic force on the surfaces. This effect can be reduced by optimising the hydrophobicity by modifying their side chain or by replacing with another amino acid of different polarity. Figure 5-15 exhibits the FM-ION-RS was around 7 nm in width coating thickness of around 3.5 nm clearly seen from the contrast different shown in figure 5-16 (b). The atomic scale of fine crystal pattern of core FM-ION-RS are not visible due to peptide coating.

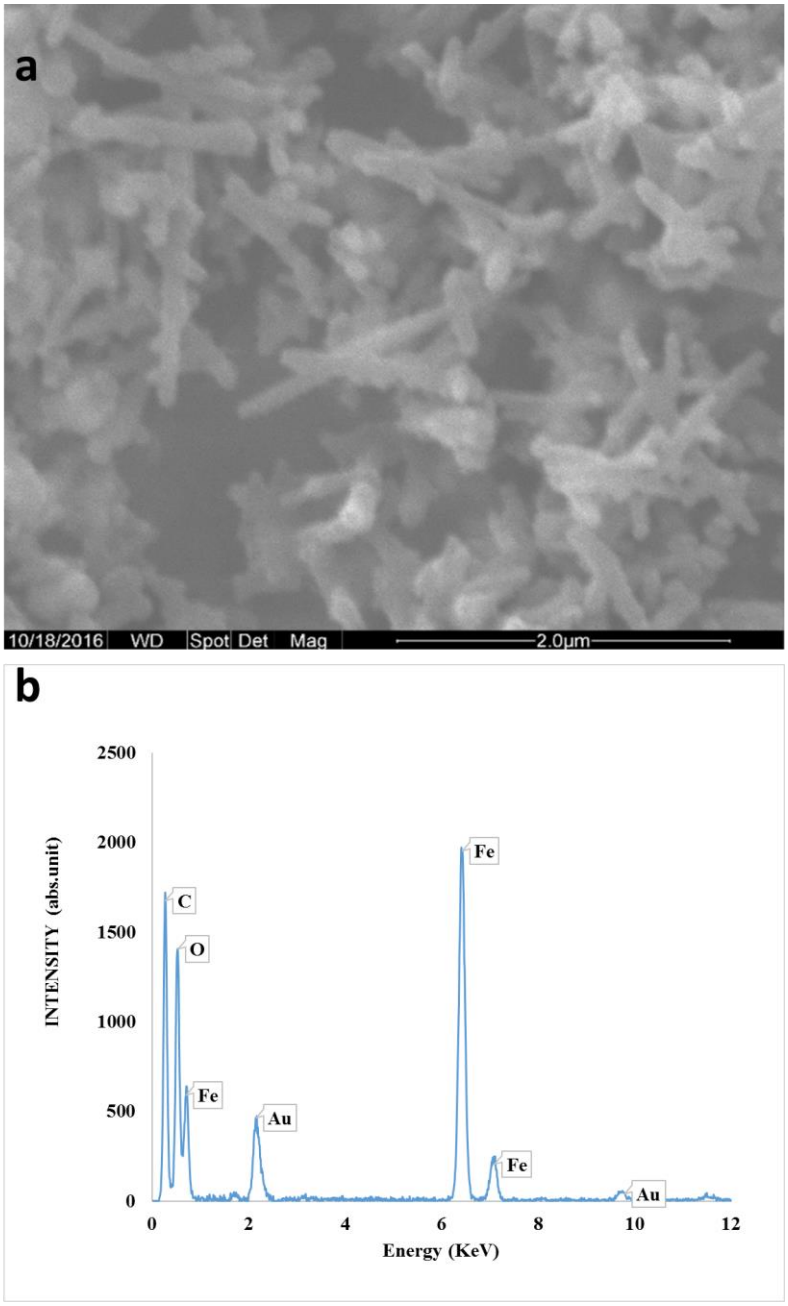

Figure 5-15 SEM image of the (a) FF-FM-ION-RS and (b) EDAX analysis of FF-FM-ION-RS (graph and image is representative of three independent experiments)

Energy Dispersive Spectroscopy (EDAX) studies of the FF-FM-ION-RS confirmed the presence of iron and oxygen, gold peaks appearing from the gold coating via sputtering (figure 5-15 (b)).

ii) Transmission electron microscopy

Figure 5-16 revealed the peptide coated rod-shaped iron oxide nanocomposites (FF-FMION-RS). Peptide shell has have successfully encapsulated the rod-shaped iron oxide. Figure 5-17 showed the difference in thickness of coated and uncoated rod-shaped iron oxide nanoparticles along with their fine structure. FM-ION-RS exhibited a well-ordered structure in atomic length scale (Å) with a rod width of approximately 7 nm. The size of nanocomposite was also large (approximately 25 nm in width) compared to bare iron oxide rods (10 nm in width). In low and high magnification peptide coated iron oxide materials showed different surface morphologies.

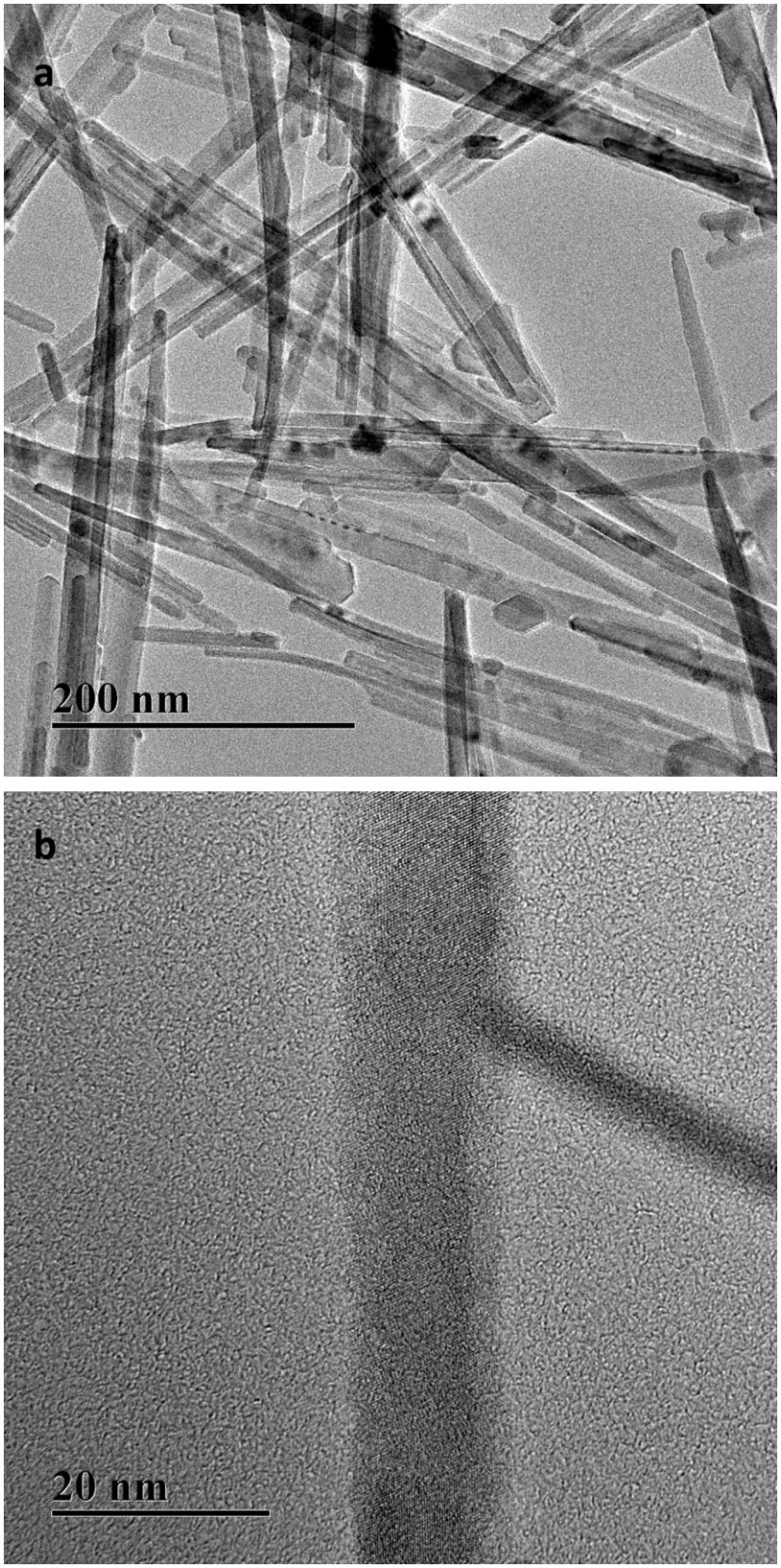

Figure 5-16 (a-b) TEM images of FF-FM-ION-RS core-shell nanocomposites at different magnification (Images arerepresentative of three independent experiments and these images are taken at Liverpool university)

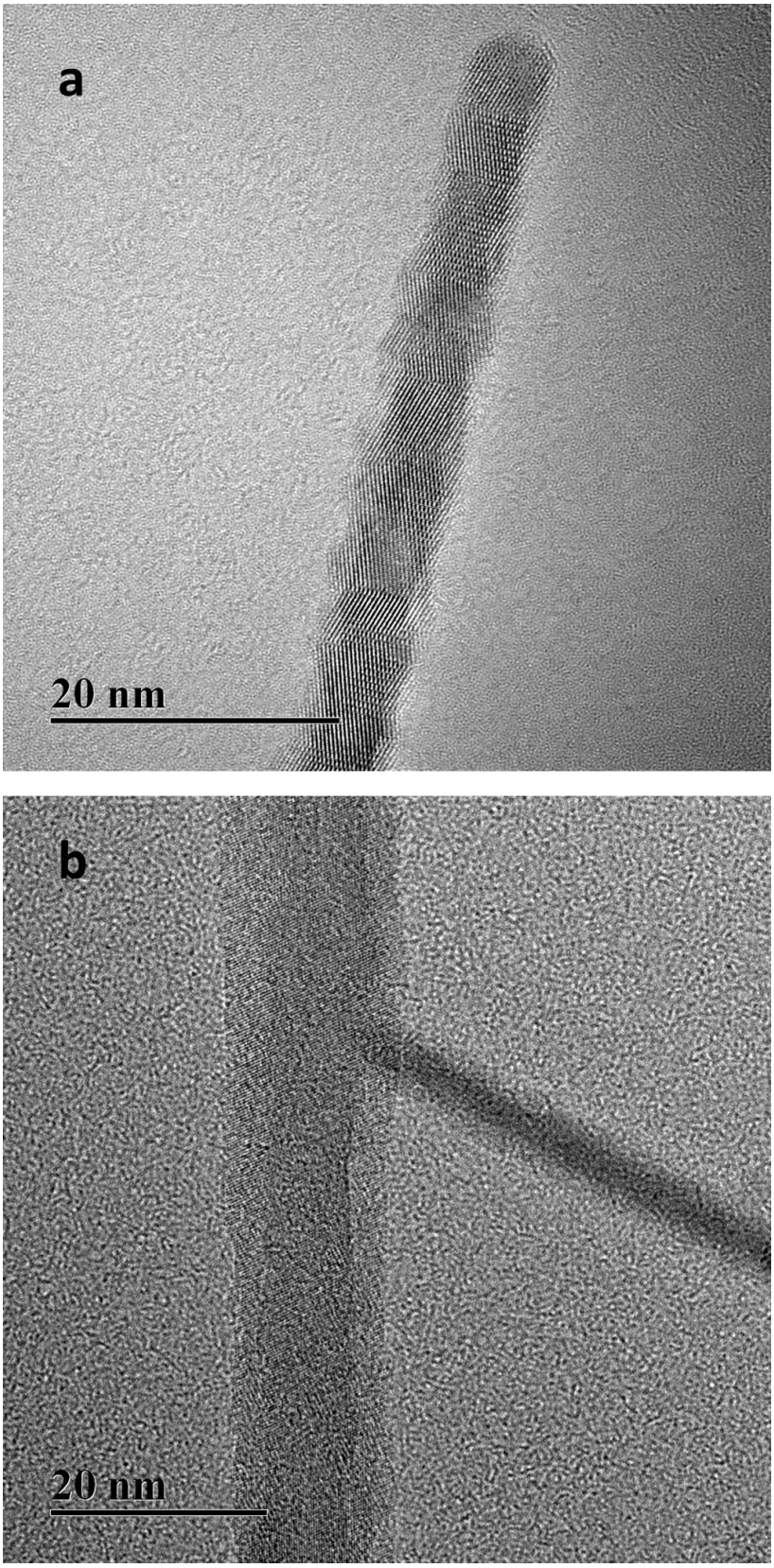

Figure 5-17 TEM images of (a) bare rod-shaped iron oxide nanoparticles and (b) peptide coated tubular iron oxide nanoparticles (Images are representative of three independent experiments and these images are taken at Liverpool university)

iii) Chemical confirmation analysis using Fourier Transform Infrared spectroscopy

Figure 5-18 revealed the infrared spectrum of dried FM-ION-RS, peptide and FF-FM-ION-RS nanocomposites. The infrared spectrum of the iron oxide skeleton showed strong bands at 791 to 528 cm^{-1}. In addition, iron oxides have a weak band below 900 cm^{-1}. Bruce & Sen 2005 reported the iron oxide show signal at 410 and 550 cm^{-1}. The peptide has characteristic vibrations, the NH and OCO bending, these bending vibration were seen at around 1700 to 1400 cm^{-1}. The peptide are composed of FF residues, the phenol and aromatic hydrocarbon also have intense peaks below 1000 cm^{-1}. Comparing bare iron oxide and peptide coated iron oxide, the vibrations at 530, and 730 cm^{-1} were characteristics of iron oxide along aromatic hydrocarbon, confirming peptide coating. Characteristics peaks at 1637 and 1020 cm^{-1} were also found for the CCO and CO stretching. The bands at 2965 and 1000 cm^{-1} were referred to $–CH_2$ stretching and –CH out-of-plane bending vibrations, respectively. The presence of characteristics peaks of peptide functional groups revealed that the peptide is covering the iron oxide.

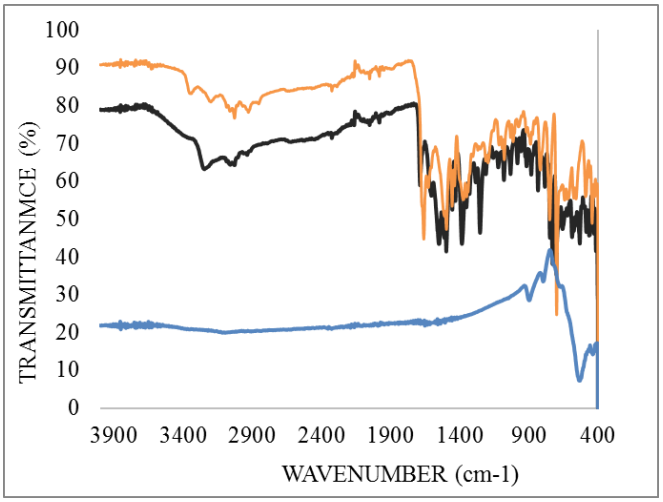

Figure 5-18 Shows the FTIR spectra of FM-ION-RS (blue) FF (black) FF-FM-ION-RS (orange) (graph are representative of three independent experiments)

FTIR data confirmed the presence of both iron oxide and peptide characteristics bonds for the product obtained after coating. The infrared spectrum of carboxylate group *via* symmetric stretching at 1465 cm^{-1} supporting the assumption that iron oxide core interact with hydrophilic carboxylate groups of the peptide. However, the presence of a peak at 1700 cm^{-1} indicated the presence of free carboxylic acid groups possibly located on the outer surface of the particles.

iv) Crystalline analysis using X-ray diffraction

X-ray Diffraction (XRD) pattrens of FM-ION-RS, pure FF and FF-FM-ION-RS core-shell nanocomposites are presented figure 5-19. The characteristic peaks of FM-ION-RS were at 2 Θ = 31°, 37°, 43°, 55.3°, 58.9° and 64.4°, which is characteristic pattern of maghemite as described earlier. Pure peptide nanotubes also exhibited multiple peaks due to crystalline structure (figure 5-22 a). FF-FM-ION-RS exhibited multiple peaks which are in combination with FM-ION-RS and pure peptide indicating that FF-FM-ION-RS is a hybrid nanorods with crystalline structure.

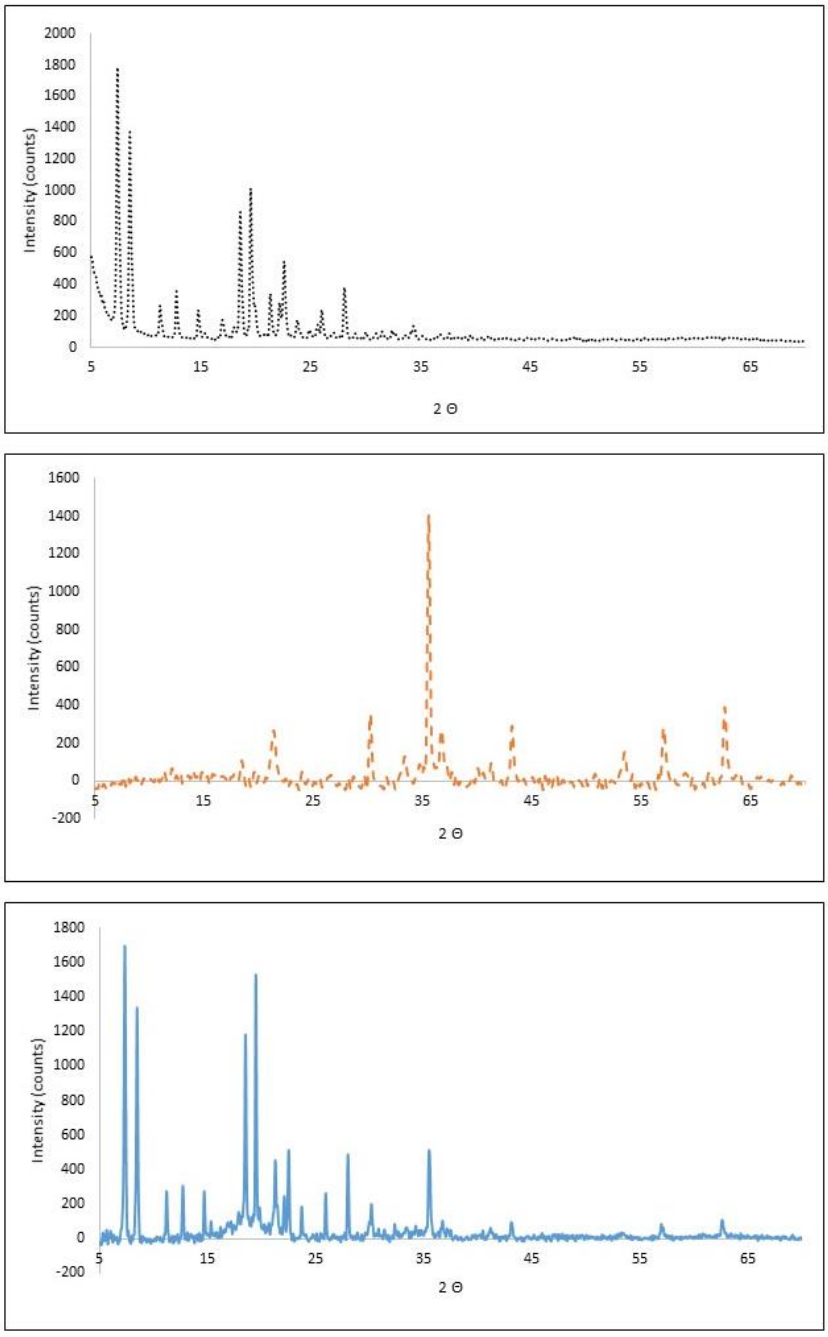

Figure 5-19 XRD pattern of pure FF (black dots), FM-ION-RS (orange dashes) and FF-FM-ION-RS (solid blue line) (graph are representative of three independent experiments)

v) Saturation magnetisation measurement using vibrating sample magnetometer

It is well-known that magnetic properties of iron oxide nanoparticles can be influenced by coating of organic polymers (Sarawade et al. 2014; Hyeon et al. 2001; Jiang et al. 2004; Huang et al. 2011). Figure 5-20 presents the VSM hysteresis loops when 7 kOe

magnetic field was applied. Both of the materials showed a small ferromagnetic behaviour possibly due to a slight disarrangement of the spin axis of rod-shaped domains from exact anti-parallelism.

The magnetic properties of core-shell tubular nanoparticles were measured at room temperature in UCLan custom-built VSM. The saturation magnetisation (Ms) of FM-ION-RS was measured to be 45 emu.g^{-1} and FF-FM-ION-RS was 16 emu.g^{-1} (see figure 5-20). Studies showed that the coercivity of one-dimensional nanostructure can be influenced by crystallinity and shape anisotropy (Jain & Jothi 2015). Spherical nanoparticles showed zero coercivity compared to rod-shaped nanoparticles.

As discussed earlier, spherical nanoparticles were superparamagnetic in nature with no hysteresis observed, while in the case of rod-shaped iron oxide nanoparticles, the ferromagnetic behaviour (hysteresis) was found clearly. Notably, a small but noticeable saturation magnetisation appeared in FF-FM-ION-RS due to diamagnetic peptide.

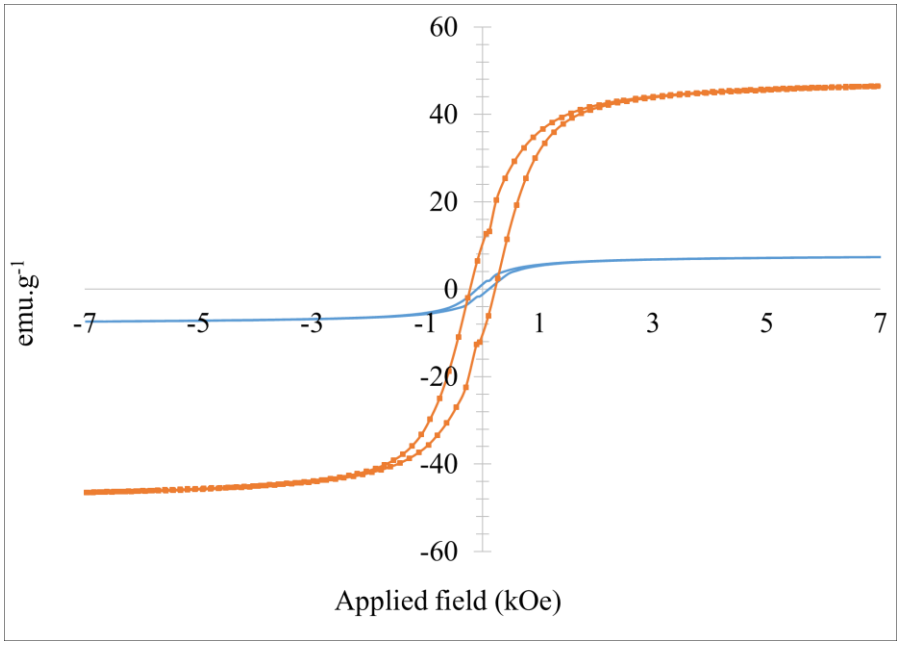

Figure 5-20 Magnetisation saturation of FM-ION-RS (blue line) FF-FM-ION-RS (orange cross) (graphs are representative of three independent experiments)

vi) Thermal tability measurement using Thermogravimetric analysis

Thermogravimetric analysis (TGA) curves of Ferromagnetic Rod-Shaped Iron Oxide Nanoparticles (FM-ION-RS) and Non-modified Ferromagnetic Rod-Shaped Iron Oxide Nanoparticles (FF-FM-ION-RS) composites are shown in figure 5-21. The core-shell composite showed the removal of adsorbed water below 150 °C. In this step, initial weight loss was approximately 10 %. From 150-500 °C, the total weight loss of peptide coated iron oxide nanoparticles was almost 50 % due to decomposition of peptide. FF decomposed completely at 350 °C, where the maximum slope was appeared at 300 °C. FF-FM-ION-RS decomposed with similar profile as individually decomposed materials and showed 80 % weight loss between ~ 350 to onwards 500 °C (figure 5-21).

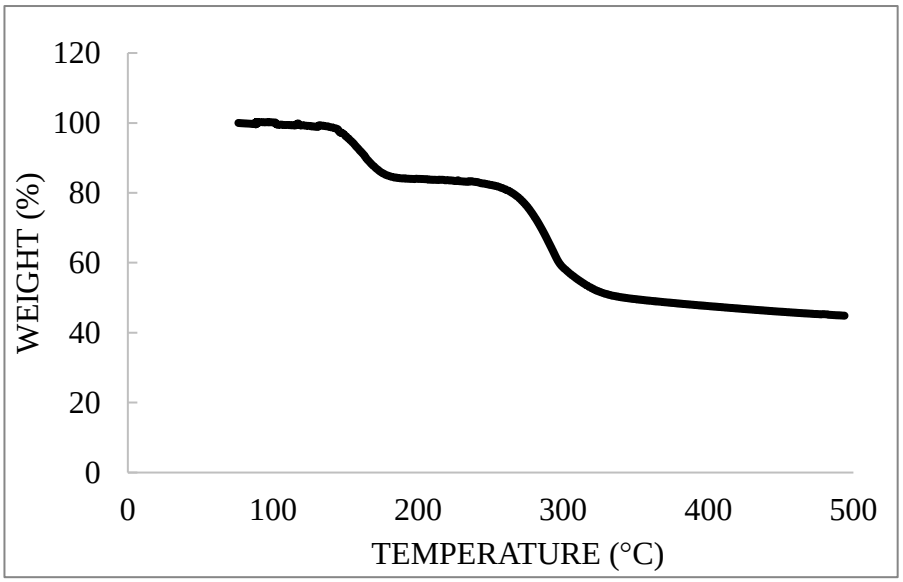

Figure 5-21 Thermal degradation profile of FF-FM-ION-RS (graph is representative of three independent experiments)

5.5 Conclusions

This chapter focused on developing the rod-shaped iron oxide nanoparticles (FM-ION-RS) using novel ferrous sulphate as iron source *via* co-precipitation method. The synthesis of rod-shaped iron oxide nanoparticles has opened new way to synthesise iron oxide based materials of different shapes. The shape of iron oxide nanoparticles has clearly influenced on the superparamagnetic behaviour of the nanoparticles. The saturation magnetisation values were 45 and17 $emu.g^{-1}$ for bare rod-shaped iron oxide nanoparticle and peptide-coeated iron oxide nanoparticles, respectively. Thus the physicochemical properties can be modified. For the first time, FF peptide self-assemblies demonstrated that they could wrap the rod-shaped iron oxide cores in a tubular core-shell morphology.

SEM-EDAX analysis of coated iron oxide and individual materials provided evidence that FF nanotubes can wrap around iron oxide rods. The size of bare rod-shaped iron oxide and peptide-coated iron oxide was approximately 10 nm 20 nm in width. The novel materials with magnetic properties and crystalline structures can be used in a variety of applications including; drug delivery, thermal ablation, magnetic field targeting and bio-separation. The novel materials had magnetic response, hence can be separated *via* slab magnate. The presence of characteristics FTIR bands for OCO, NH and FeO confirmed the peptide coating on iron oxide. TGA profile of core-shell composites showed comparable pattern to individual materials. These techniques have successfully identified the iron oxide from self-assembled FF tubes. By adjusting the solvent and modifying the amino terminal in which peptide self-assembled, it is possible to coat rod-shaped with magnetic core with similar backbone peptide (FF).

CHAPTER SIX

Drug loading and release capacities of spherical core-shell materials

6.1 Introduction

The limited progress in the treatment of cancer has increased the need to explore different approaches for designing multifunctional drug delivery system. The ideal drug delivery systems should control pharmacokinetics of loaded drugs. Moreover, they should have ability to target the effected sites, with lower immunogenicity, higher loading capacity and possiblity to track them at active sites (Saikia et al. 2017; Asadi et al. 2016; Woźniak et al. 2017). Nanotechnology has opened the ways to design the desired materials with these promising properties.

Superparamagnetic iron oxide nanoparticles (SPIONs) can carry the payloads and by applying external magnetic field can be targeted to the affected sites to achieve desired drug efficiencies (schematic depiction in figure 6-1). In addition, SPIONs as contrast agents can be tracked during the release of payloads. The attracting forces of iron oxide and high surface area to volume ratio causes the aggregation of SPIONs, which reduces the superparamagnetic behaviour. The SPIONs were coated with biocompatible peptides to reduce the aggregation in order to be used in drug delivery applications. Doxorubicin (DOX) was used as a model drug, which is an FDA-approved chemotherapeutic antitumor drug with a broad spectrum of effects for the treatment of leukaemia and tumours (Feng & Zhao 2017). The mechanism of action of doxorubicin includes the inhibition of DNA replication and protein translation. It inhibits the topoisomerase II, which involves in the DNA unfolding and replication by intercalating with nucleotide base pairs (Pérez-Arnaiz et al. 2014). The systematic administration of DOX showed

severe cardiac toxicity (Wu et al. 2016). A variety of nanoscale drug delivery systems has been studied as model carriers for DOX delivery to the cancer cells. DOX is anthracycline-based drug, which have intrinsic fluorescence property to track or locate the composite in biodistribution system. DOX possess a net positive charge (pKa 8.6) in neutral environment. Amino and carboxyl groups of FF have pKa values (9.31 and 2.2, respectively). Thus, peptide as zwitterion possess negative and positive charges facilitating the electrostatic interaction of DOX to peptide shell. The hydrophobic interaction of fussed ring of DOX and rings of FF also improves the drug loading of carriers. Drug loading capacity is a key for an ideal formulation for an effective delivery system.

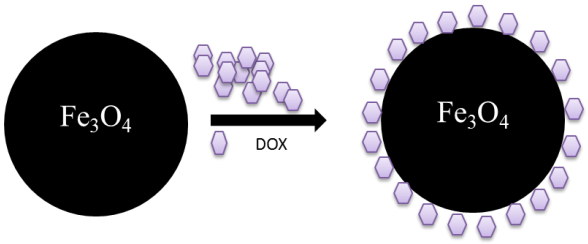

Figure 6-1 Schematic diagram of DOX adsorption on SPIONs

In this chapter, DOX loading and release profile of BOC-SPION-SS *via* adsorption approach will be studied as a potential drug carrier system (figure 6-1). The hydrophobic DOX will be adsorbed on the surface of iron oxide and partitioning into peptide coating. This method is based for magnetically separable drug delivery system without using any toxic surfactant has been designed and applied. The formulated drug delivery system was assessed for drug encapsulation efficiency. The results are discussed in details for drug to nanoparticles/nanocomposites ratios with time-dependant loading and release kinetics.

6.2 Doxorubicin loading profile of spherical bare and coated superparamagnetic iron oxide nanoparticles

6.2.1 Doxorubicin loading profile of spherical bare superparamagnetic iron oxide nanoparticles

The amount of doxorubicin (DOX) was quantified by measuring the absorbance of the free drug at λ_{485} nm after magnetic separation. The free drug was compared to the total drug in a solution of DMSO-water. The quantification was performed from the pre-established standard curves with known concentration of drug in similar DMSO-water (1:1). Standard calibration curves were prepared as 20, 40, 60, 80 and 100 µg.mL^{-1} (figure 6-2).

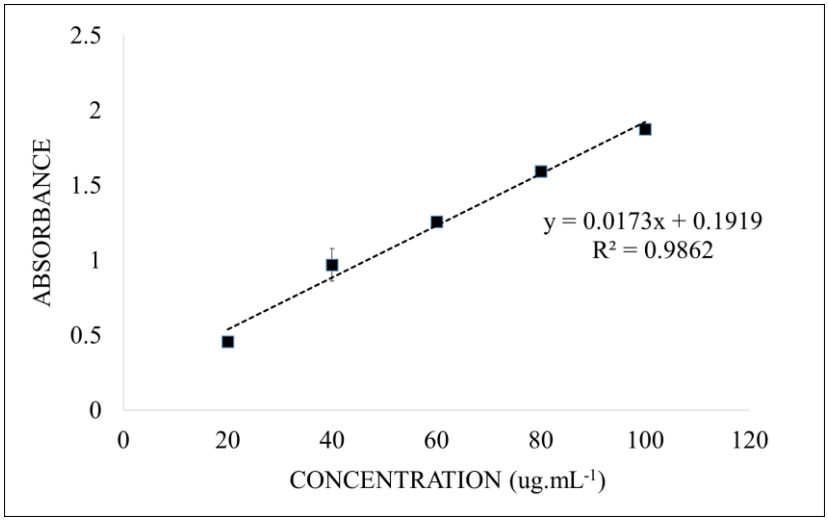

Figure 6-2 Standard calibration curve of DOX in DMSO-water (±SD, no=3)

DOX loading experiment were performed in DMSO-water (1:1) on spherical B-SPION-SS with different nanoparticles concentrations (2.5, 5, 7.5 and 10 mg.mL^{-1}) while, keeping consistent drug amount (100 µg.mL^{-1}) to find the highest loading efficiency. DOX loading capacities for the ratio of DOX to B-SPION-SS 1:25, 1:50, 1:75 and 1:100 were 46%, 81 %, 85 % and 87 %, respectively after incubating at 18 °C for 48 hours

whilst in end-over-end rotation. Figure 6-3 shows the time-dependent drug loading capacity of different ratios.

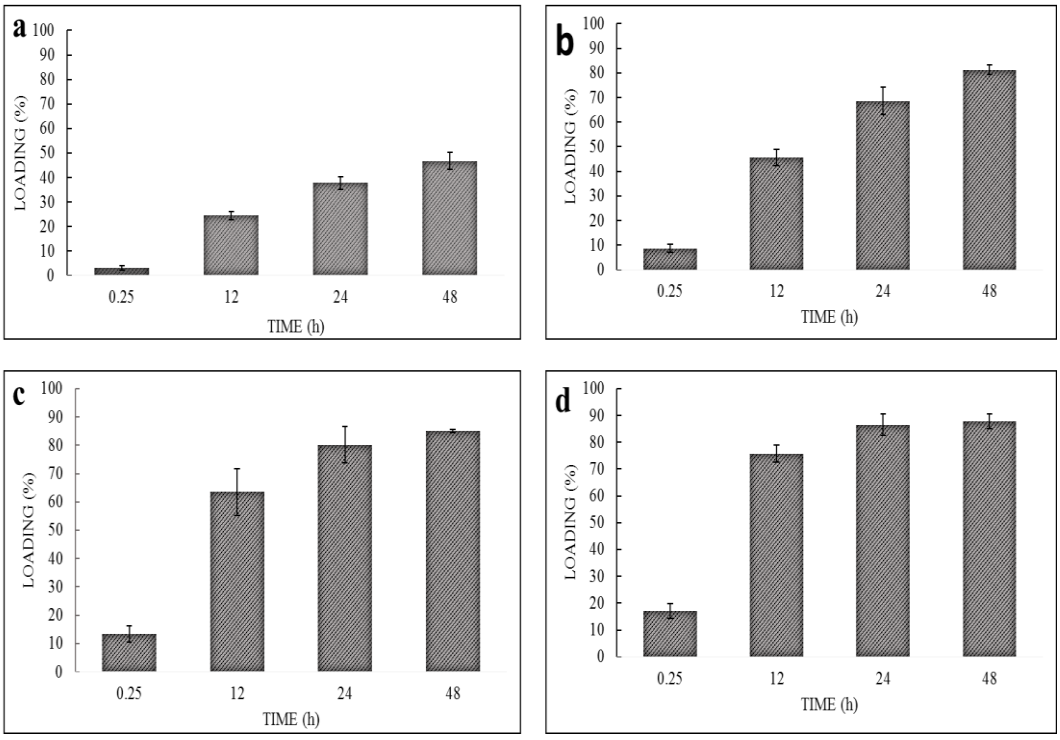

Figure 6-3 DOX loading capacity of B-SPION-SS with reference to incubation time, DOX to B-SPION-SS ratio (a) 1:25 (b) 1:50, (c) 1:75 and (d) 1:100 (±SD, no=3)

Table 6-1 shows the DOX loading content in weight percentage of spherical bare SPIONs of different DOX:B-SPION-SS ratios with time-dependent studies. The lowest DOX content was seen 13 weight percentage for 1:25 at 0 hours formulation. The highest amount of drug was seen in the 1:25 formulation after incubating for 48 hours at 18 °C.

Table 6-1 DOX loading capacity of B-SPION-SS (spheres) (time in hours) (micromole of DOX to milligram of B-SPION-SS)

DOX:B-SPIOPN-SS (mass:mass)	**0.25**	**12**	**24**	**48**
(1:25)	2	18	27	32
(1:50)	3	17	25	30
(1:75)	3	15	20	21
(1:100)	3	14	16	16

DOX loading capacities of (1: 25) formulation were found as 3 %, 24 %, 37 % and 46 % after incubating at 18 °C for 0 hours, 12 hours, 24 hours and 48 hours, respectively. The loading capacities were increasing as SPIONs ratio increased in time-dependent manner (figure 6-3). The loading capacity was almost reached to saturation after 12 hours for the (1:100) formulation. Similarly, 1:75 formulation was also reached its maximum after 24 hours. Increasing the amount of B-SPION-SS, increases the loading amount with relation to time of incubation. The loading capacity in weight percentage of DOX and B-SPION-SS is depicted in Table 6-1.

6.2.2 Doxorubicin loading into spherical mesoporous silica coated superparamagnetic iron oxide nanoparticles

Mesoporous silica offers some advantages on the bare SPIONs over other coating materials. Silica showed good thermal and chemical stability, lower aggregation and lower immunogenicity upon systemic administration (Wang et al. 2013; Graf et al. 2012). Though studies have favoured other polymeric carriers for adequate and controlled release of hydrophilic drugs, porous silica layers have shown great ability to encapsulate the drugs for sustained release. Silica layered particles could overcome the drug stability related limitations over other polymeric particles. In mesoporous silica, mesopores can offer full preservation of drug in pores during the circulation. The method of preparation of mesoporous silica-coated SPIONs was discussed in section 3.3.6. The silica layer thickness was controlled by optimised reaction time and silica source (TEOS).

The percentage DOX loading capacity in Si-SPION-SS was studied by UV absorption measurement at λ_{485} nm of free drug after magnetic separation. The free drug was quantified using pre-established standard calibration curves in DMSO-water. The DOX loading capacity and content were measured at 18 °C, over pre-set time intervals for 48

hours. Figure 6-4 showed the DOX loading capacity of Si-SPION-SS. DOX loading capacity was measured 30 %, 40 %, 55 % and 55 % (for 1:25, 1:50, 1:75 and 1:100 formulations, respectively) at zero hour time after sonication and vortex mixing. The saturation of DOX was achieved from 12 hours for (1:50, 1:75 and 1:100) except the 1:25, where it reached after 48 hours.

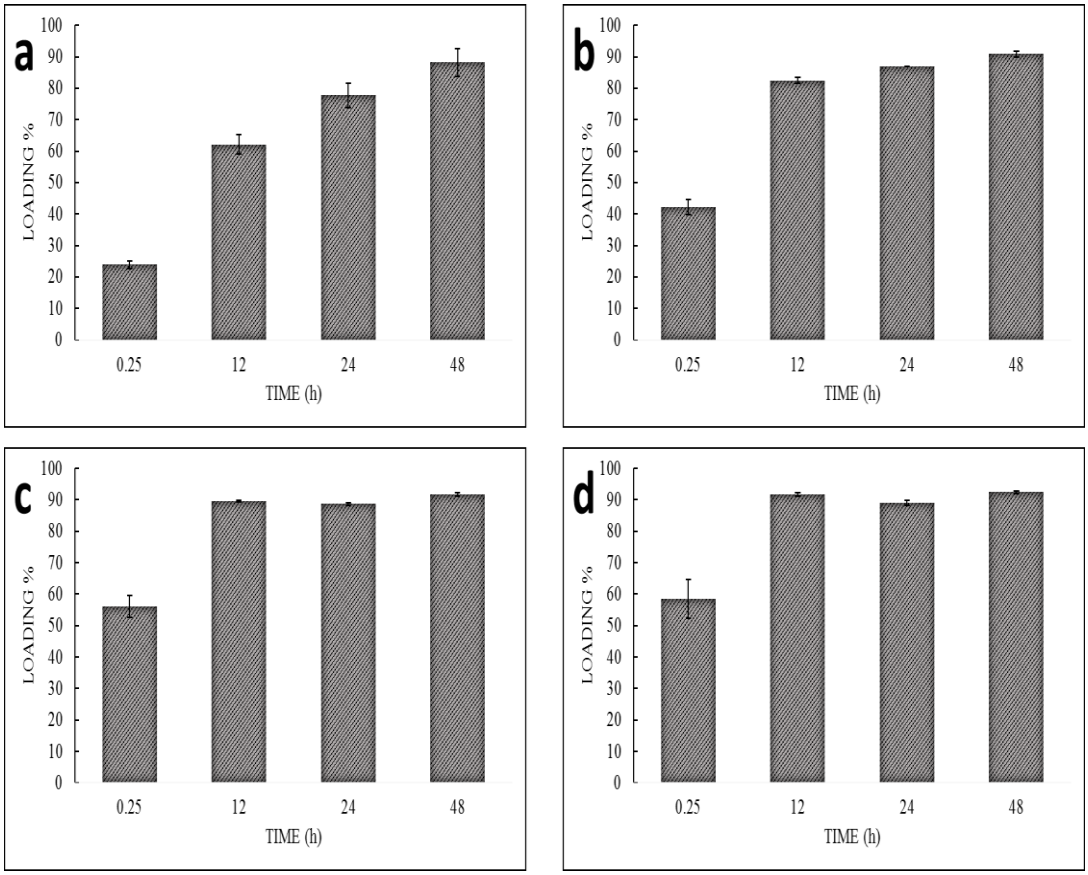

Figure 6-4 DOX loading capacity of Si-SPION-SS with reference to incubation time, DOX to SPIONs ratio at different incubation times (a) 1:25 (b) 1:50, (c) 1:75 and (d) 1:100 (±SD, no=3)

Table 6-2 showed the DOX loading content percentage of different formulation. DOX weight percentage (micromole) content at zero hours was 85 %, 84 %, 75 % and 58 % for formulations (1:25, 1:50, 1:75 and 1:100, respectively). The highest DOX loading content was calculated for 1:25 formulation after 48 hours and lowest was 58 % for (1:100) formulation.

Table 6-2 DOX-loading capacity of spherical core-shell Si-SPION-SS nanocomposites

DOX:Si-PION-SS	**Time of incubation (hours)**			
(micromoles:mg)	0.25	12	24	48
(1:25)	15	42	56	63
(1:50)	15	30	31	33
(1:75)	13	22	21	22
(1:100)	10	17	16	17

6.2.3 Doxorubicin loading into core-shell peptide coated iron oxide nanocomposites

After successful DOX loading into B-SPION-SS and Si-SPION-SS, the experiments were repeated on the peptide-coated SPIONs (BOC-SPION-SS). BOC-SPION-SS composites also showed good magnetic response during the magnetic separation. In addition, by optimising the drug:SPIONs (cores) ratio, the highest DOX loading ratio obtained was used in these experiments. Keeping the DOX:carrier ratio (1:100 weight percentage) consistant, the time-dependent loading studies were performed.

Figure 6-5 shows BOC-SPION-SS maximum DOX loading after 12 hours. It was remained steady until 48 hours. Peptide-coated SPIONs reached to maximum (70 %) over the B-SPION-SS (85 %), which revealed the total 15 % reduction of DOX loading after coating. This was possibly due to the lower SPIONs availability. The magnetic separation assured the attachment of DOX with magnetic nanoparticles. These finding revealed the Si-SPION-SS were found promising carrier for DOX. Figure 6-5 showed time-dependant DOX loading profile of BOC- SPION-SS at 18 °C of incubation. Samples were sonicated for 15 minutes before taking first reading. Readings were recorded after magnetic separation in magnetic Eppendorf tube rack. The time-dependent loading studies showed that 12 hours were maximum time duration to achieve maximum (70 %) DOX loading

into BOC-SPION-SS. Time-dependant studies confirmed the DOX loading with magnetic nanoparticles were consistent from 12 hours to 48 hours.

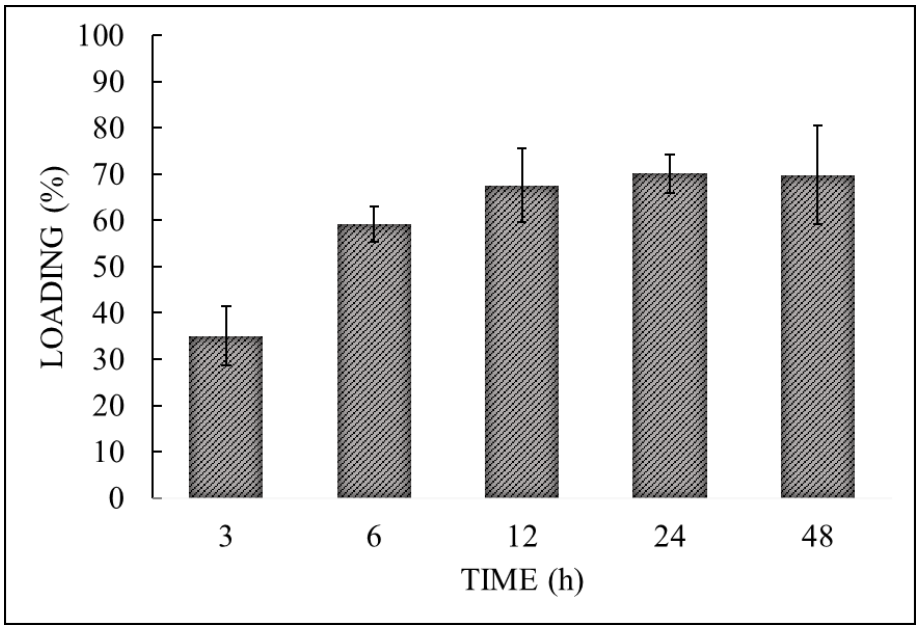

Figure 6-5 DOX loading profile of BOC-SPION-SS at different time intervals (hours) in incubation at 18 °C (1:100) (±SD, no=3)

6.2.4 Doxorubicin loading into the peptide-capped mesoporous silica coated superparamagnetic iron oxide nanoparticles

Mesoporous silica based drug delivery systems were proposed since the beginning of this century (MacLachlan et al. 2000; Hao et al. 2017). In this study, peptide-capped silica-coated particles were studied as potential drug delivery carriers. Peptide capping approach was used to achieve biocompatible and gate keepers to control the release of drug molecules.

DOX loading of Si-SPION-SS was studied using combination of ultrasonication and incubation approach at 18 °C for up to 48 hours using end-over-end rotation, then peptide solution was added to cap the mesopores of silica. The loading capacity and content in weight percentage was performed after magnetic separation of free drug. The

quantification of drug was measured by recording the absorbance of free drug at λ_{485} nm using standard calibration curves.

Figure 6-7 showed the DOX loading profile of BOC-Si-SPION-SS up to 48 hours. Loading capacity was found 88 %. The saturation of drug loading was obtained after 24 hours and remained consistent up to 48 hours. Similar results were obtained in case of silica coated SPIONs.

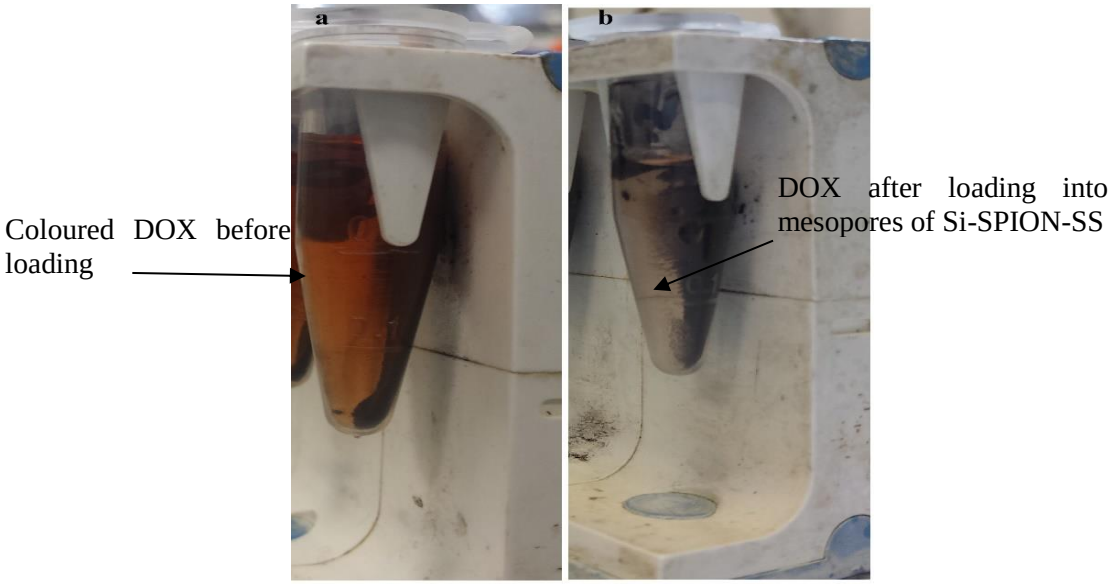

Figure 6-6 Visual image of DOX loaded BOC-Si-SPION-SS (a) magnetic separation before incubation and (b) after incubation for 48 hours

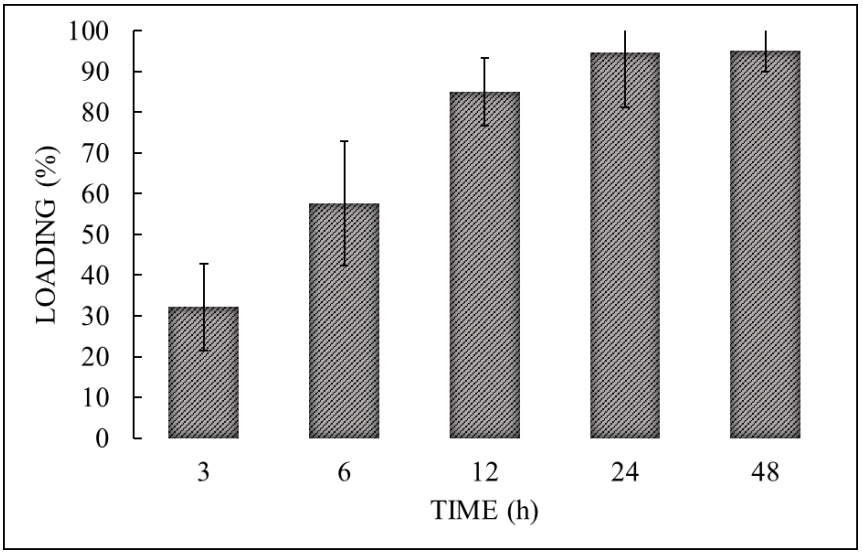

Figure 6-7 DOX loading profile of peptide-capped silica coated SPIONs (BOC-Si-SPION-SS) at different time intervals (hours) in incubation at 18 °C (1:100) (±SD, no=3)

6.3 Doxorubicin release profile of spherical bare and coated iron oxide

Doxorubicin (DOX) loaded B- SPION-SS, Si-SPION-SS, BOC-SPION-SS and BOC-Si-SPION-SS were diluted in 1 mL of PBS at pH 7.4 at 37 °C in incubater whilst rotating up to 48 hours. Free DOX concentration was also diluted in buffer 20 to 100 $\mu g.mL^{-1}$, the absorbance was recorded for further quantification of released drug from carriers (figure 6-8). DOX release profile was studied at pre-set intervals after incubation, the absorbance of free DOX after magnetic separation was recorded at λ_{485} nm. Free DOX release percentage from magnetic carriers was calculated using free DOX standard calibration curve in PBS.

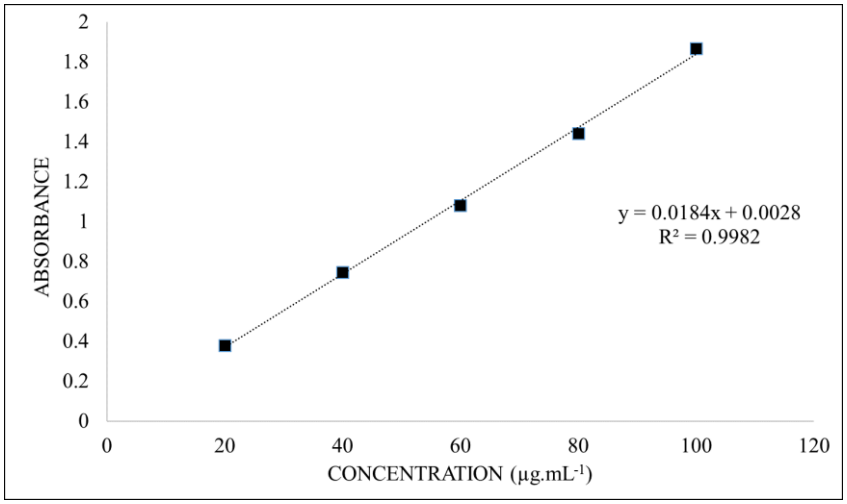

Figure 6-8 DOX standard calibration in PBS for release profile studies (±SD, no=3)

6.3.1 Doxorubicin release from spherical bare magnetite

Doxorubicin release profile of spherical B-SPION-SS *in vitro* was investigated for drug delivery applications. DOX loaded B-SPION-SS were separated using slab magnate at pre-set time intervals of different formulations. Figure 6-9 showed the DOX release profile of B-SPION-SS in PBS buffer at 37 °C. DOX loaded B-SPION-SS release profile revealed the burst release of DOX in first 12 hours. The DOX release plateau was seen after 12 hours. The final drug release after 48 hours was approximately 85 %. The big difference in initial burst release of DOX after 12 hours (70 %) and next 36 hours slow release (15 %) was might be due to the adsorbed DOX on the surface of B-SPION-SS.

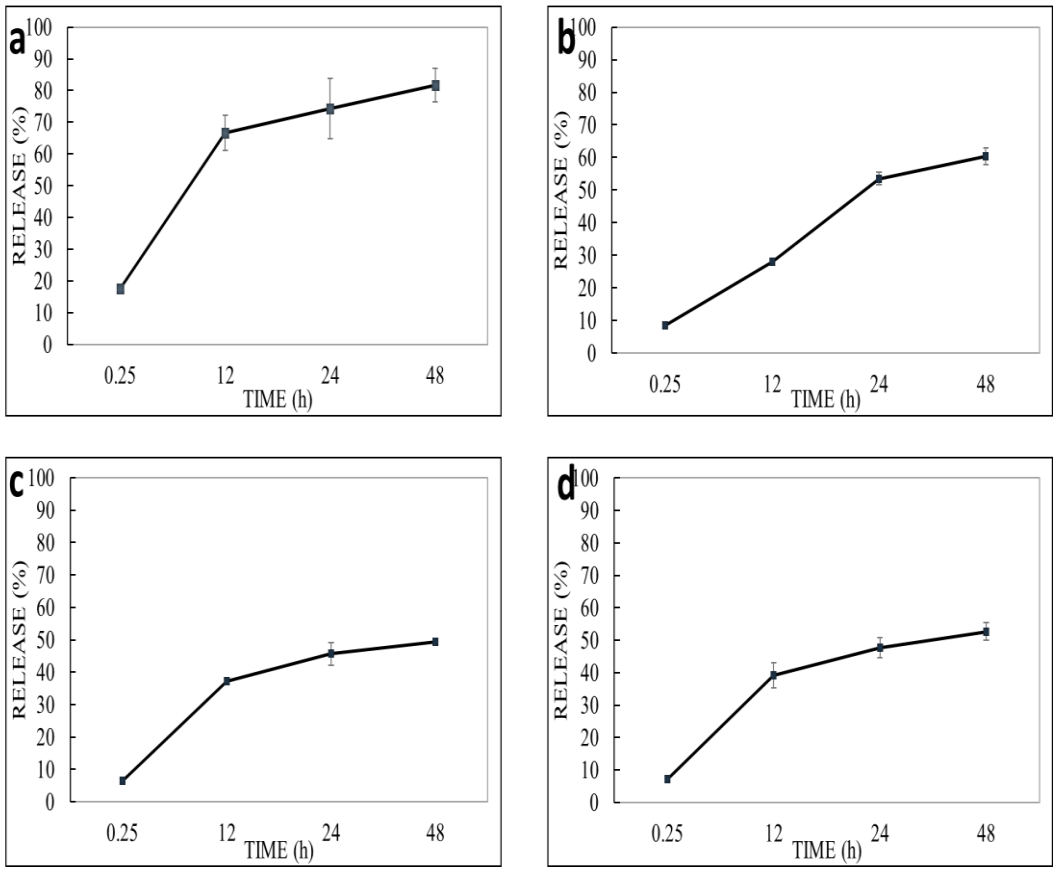

Figure 6-9 DOX release profile of B-SPION-SS with reference to incubation time, (a) DOX to B-SPION-SS ratio 1:25 (b) 1:50, (c) 1:75 and (d) 1:100, respectively (±SD, no=3)

6.3.2 Doxorubicin release profile of spherical mesoporous silica-coated iron oxide

DOX loaded mesoporous Si-SPION-SS showed slow and sustained release. Figure 6-10 showed the sustained release of DOX confirming the DOX incorporation into the mesopores of Si-SPION-SS along successful magnetic separation. The initial absorbance of free drug was continued with time-dependent manner confirming sustained release from mesopores of silica. B-SPION-SS showed the burst release, which appeared due to consequence of non-preferable adsorption to the external surface of particles.

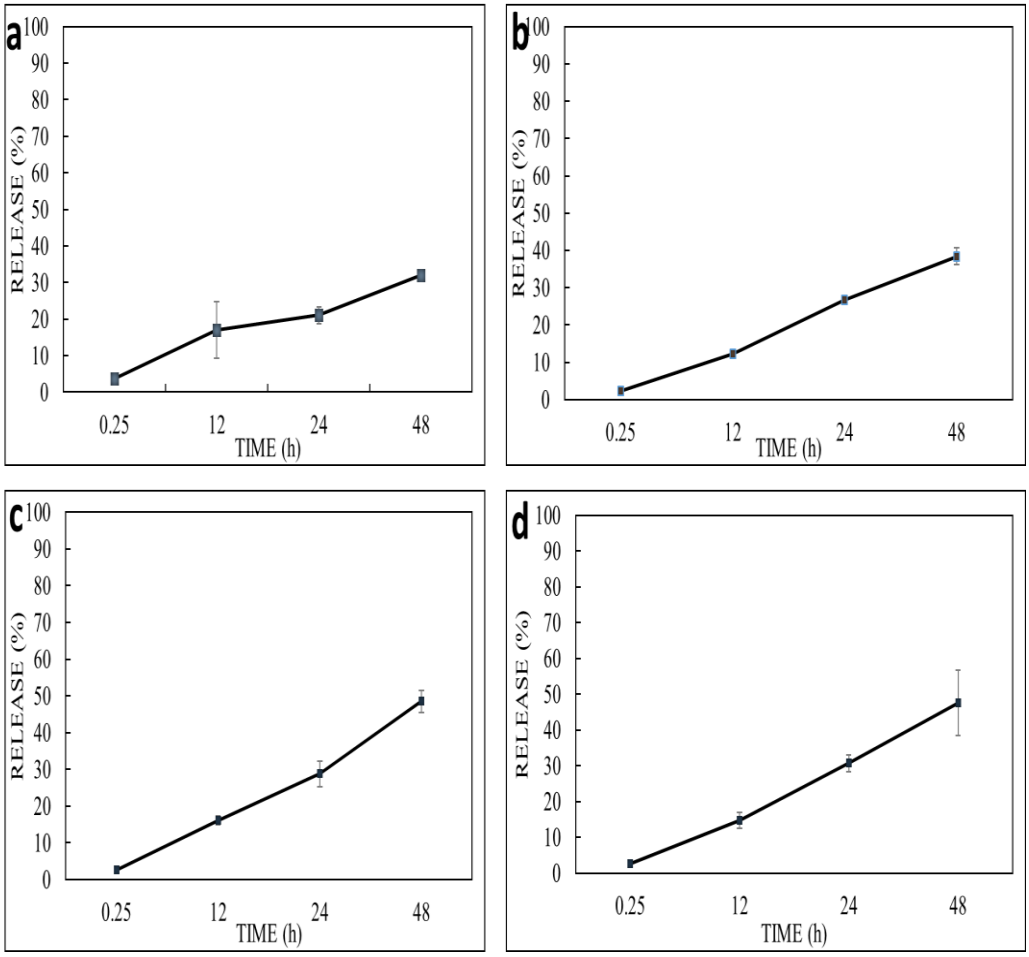

Figure 6-10 DOX release profile of Si-SPION-SS with reference to incubation time, (a) DOX to Si-SPION-SS ratio 1:25 (b) 1:50, (c) 1:75 and (d) 1:100, respectively (±SD, no=3)

This study confirmed the successful incorporation of DOX into mesopores without adsorption on the surface of silica. Figure 6-10 (a) showed the DOX released behaviour, 17 %, 21 % and 31 %, in first 12 hours then 24 and 48 hours, respectively. The total release of DOX from Si-SPION-SS was 31 %, 39 %, 48 % and 47 % for formulations (1:25, 1:50, 1:75 and 1:100, respectively) (figure 6-10).

6.3.3 Doxorubicin release profile of spherical peptide-coated superparamagnetic iron oxide nanoparticles

The peptide coating could work as a barrier for DOX release, thus the DOX diffusivity and solubility within peptide coating is crucial. DOX and peptide interactions can effect

the release profile. If DOX interacts with peptide, it may form hydrophobic micelles, thus the drug release profile can be compromised (Gao et al. 2014). DOX loaded martials were incubated at 37 °C to study the drug release pattern. The release behaviour was monitored for 48 hours and absorbance of free DOX was recorded on pre-set intervals. DOX release was found slower and lower for coated magnetite compared to bare magnetite. It might be due to DOX interactions with the partially charged peptide groups over SPIONs in core-shell structures. There was no burst release effect observed in BOC-SPION-SS (figure 6-11).

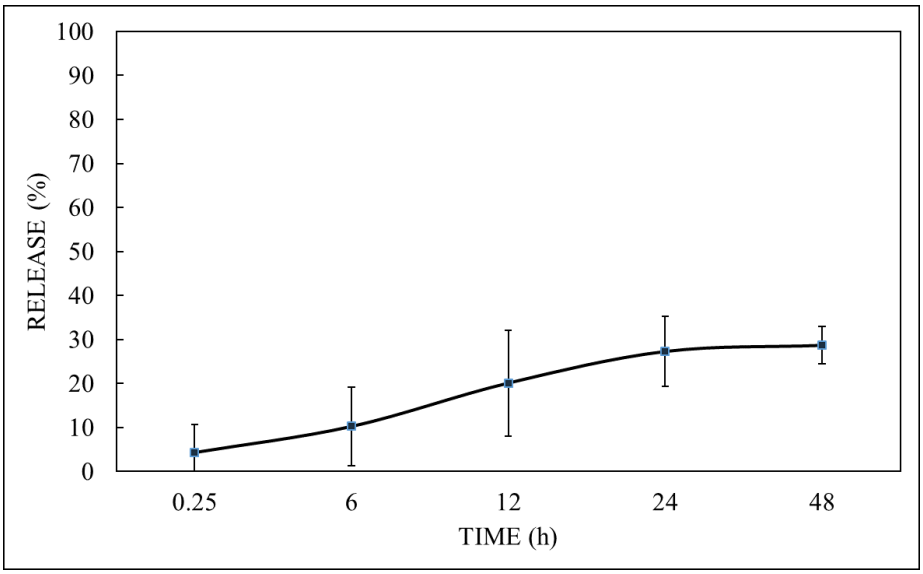

Figure 6-11 DOX release profile of BOC-SPION-SS against different time intervals (±SD, no=3)

As it was expected, the release rate of DOX (figure 6-11) was increasing continuously over time (approximately 4 %, 9 %, 18 %, 27 % and 28 %, respectively). The release profile curve revealed the total DOX release went to plateau after 24 hours. The DOX release was found in sustainable fashion over 48 hours.

6.3.4 DOX release profile of spherical peptide-capped silica-coated superparamagnetic iron oxide materials

The *in vitro* DOX release formulation of BOC-Si-SPION-SS nanocomposites were studied in PBS pH 7.4. The releasing behaviour of DOX in time-dependent manner was in sustainable manner (figure 6-12). The release process was similar to BOC-SPION-SS. Peptide coatings on bare materials has lowered the release rate than the non-coated particles. These results indicated that the peptide was preventing outside diffusion of DOX.

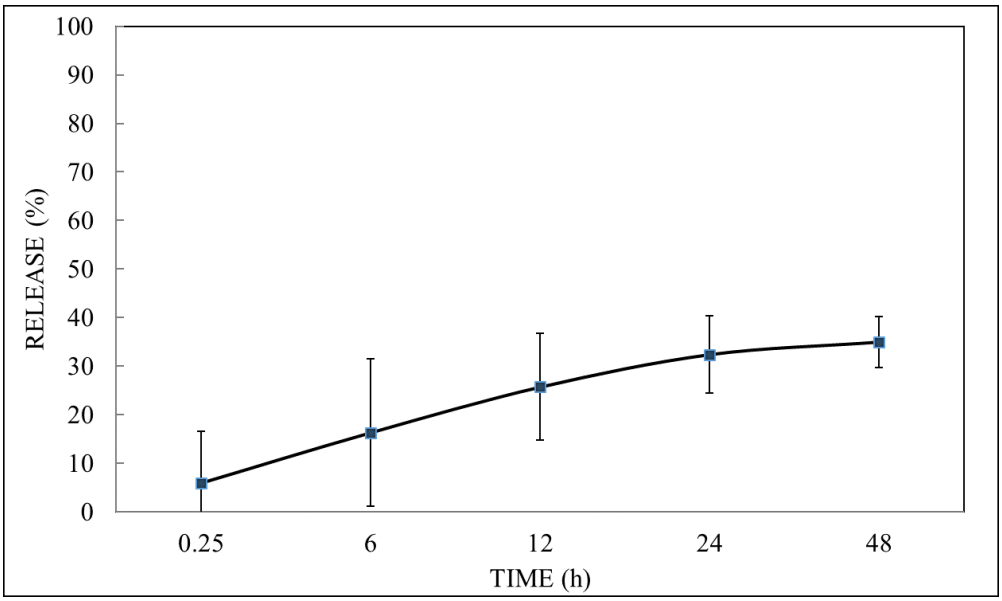

Figure 6-12 DOX release profile of BOC-Si-SPION-SS against different time intervals (±SD, no=3)

Physically adsorbed DOX molecules could be released as burst effect, while layered of peptide-capped SPIONs showed continuous release over 48 hours at 37 °C of incubation in end-over-end rotation. This could be demonstrated as layered incorporated DOX was controlled by diffusion through peptide valves. The DOX release could be attributed to the weakening of hydrophobic and ionic interactions of drug and peptide side chain groups (Pacheco et al. 2016). Thus, loosing of the hydrophobic and ionic interactions was

a slow process that led continuous release of DOX over longer periods. The sustained release of DOX in the affected site can increase the chemotherapeutic effect in anticancer therapy.

6.4 Conclusions

DOX loaded spherical bare and coated SPIONs were prepared to study drug loading and release profile for in vitro applications. Peptide and silica coats around the SPIONs reduced the aggregation and silica pores have facilitated up to 90 % drug loading.

The DOX:SPION of 1:10 showed lowed loading efficiency upto 45 % wheras 1:100 (DOX:SPIONs) showed upto 85 % loading after 48 hours of incubation. The novel drug loaded magnetic nanoparticle over exposure of applied external magnetic field can be directed to targeted sites where can be triggered for cargo release.

DOX release profile revealed burst effect in bare SPIONs and sustained release in coated materials. DOX was almost 70 % released after 12 hours from bare SPIONs, while coated particle showed almost 35 % release capacity even after 48 hours from 1:10 formulation.

These results showed that the novel peptide-coated silica magnetic particles have great potential to be explored as drug delivery system. These magnetic particles can be tracked as contrast agent and directed to targeted site by applying external magnetic field. The magnetic field also triggered the release of loaded drug and increased the temperature to kill the cells, which will be discussed in chapter 08.

CHAPTER SEVEN

Drug loading and release capacities of tubular core-shell nanocomposites

7.1 Introduction

Magnetic nanomaterials have been successfully studied as an effective and promising drug delivery system. A number of studies have been published for designing of magnetic field triggered drug carriers for improved loading, control release and enhanced cellular uptake. A variety of parameters that can influence the particles size, shape and surface chemistry have not been explored thoroughly. More specifically, the magnetic particle shape, which can influence the performance of nanoparticles in biomedical applications was studied in this chapter. Limited data is available so far, which is possibly due to the limited source and availability of strategies controlling shape of nanoparticles from same type of source materials.

The rod-shaped magnetic nanoparticles have been studied compared to spherical shape in biomedical applications. A schematic depiction of DOX loading into FF-FM-ION-RS is given in figure 7-1. The key important for controlling the shape of magnetic nanoparticles includes the reaction condition (time and temperature) and iron source. The formation of different ordered shape could be achieved by changing the iron source (ferrous and ferric and its molar ratio), variable temperatures, use of surfactant and type of solvents (Lu et al. 2007; Lu et al. 2004; Chikazumi et al. 1987). To date, most of FM-ION-RS were synthesised *via* thermal decomposition method, which exploits expensive chemicals including organometallic sources and surfactant. The cobalt and nickel based nanorods were prepared by exploiting the reduction of organio-metals in a high temperature environment (Dumestre et al. 2003; Cordente et al. 2001; Lu et al. 2007). The Fe_2O_3 based

nanorods have been reported in Wang et al. (2004); Cordente et al. (2001); Dumestre et al. (2003), where these were synthesised by inducing magnetic field using the template-assisted method. The controlled-shape synthesises of nanoparticles is a still a big challenge to date. The shape anisotropy of magnetic materials led them promising materials with interesting properties. A small number of different-shaped magnetic nanoparticle have been developed to date, among these, some of the particle either have large size distribution or self-aggregation related properties.

The promising properties of iron oxide based nanoparticles offered various approaches to design a tool for cancer treatment having drug delivery with real-time drug tracking. Magnetic nanoparticles such as γ-Fe_2O_3, α-Fe_2O_3 and Fe_3O_4 have been studied as promising tools for cancer treatment. Magnetic nanoparticles due to the superparamagnetic behaviour not only work as contrast agent but also become a localised heat source upon exposure of applied external magnetic field *via* magnetic hyperthermia phenomenon (Tietze & Alexiou 2017; Stoehr et al. 2011). The heat produced could be utilised as hyperthermia ablation (cooking of cancer cells). Moreover. As nanocarriers, they can be triggered to release the cargo inside. Hence, magnetic nanoparticles can be used as a single tool for imaging, chemotherapy and thermal ablation for the cancer treatment. Thus, they can be named as hyperthermia ablation combined with image-guided chemotherapy.

The superparamagnetic nanoparticle with average size distribution less than 45 nm in diameter as core materials have potential to be used as contrasting agent and drug delivery system. The FM-ION-RS have been studied for their contrasting and magnetic capabilities mostly focusing on biocatalysis, magnetic field triggered drug delivery, bioseparation, gene delivery and as MRI contrast agents (Wei et al. 2015; Wahajuddin &

Arora 2012; Fratila et al. 2015; Mohapatra et al. 2015). The biocompatibility studies of rod-shaped iron oxide showed 70 % cell death at high concentration 250 $\mu g.mL^{-1}$. The biocompatibility studies were largely on time and concentration dependent. These studies were also dependent on the cell type (Lee et al. 2014). The biocompatibility related issued were improved by coating with organic materials, where gold, titanium and silver were coated with lipids, nucleotides, PEG as core-shell materials, respectively (Troiano et al. 2014; Salgueiriño-Maceira et al. 2006; Majdalawieh et al. 2014).

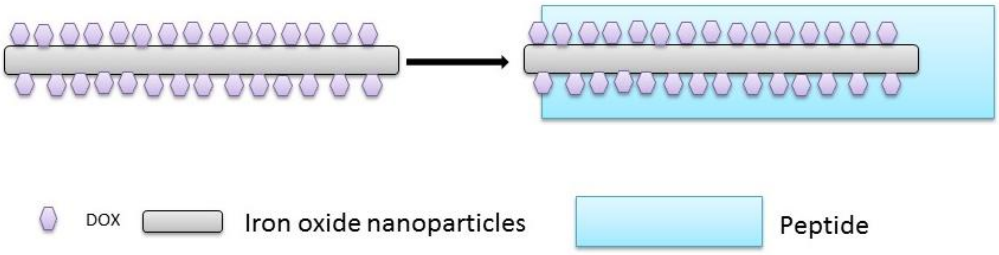

Figure 7-1 Schematic diagram of DOX adsorption on FM-ION-RS nanoparticles and FF-FM-ION-RS nanocomposites

Mai & Meng 2013 studied the safety related limitation of different nanomaterials. Bare Fe_2O_3 showed oxidative DNA damage, when systematically administered (Nemmar et al. 2016). The particles size also played an important role in fate of Fe_2O_3, however small size of bare Fe_2O_3 have shown enhanced permeability and retention effect compared to micron-sized particles (Lee et al. 2014). Cytotoxicity based studies revealed the level of toxicity was dependent on the shape of different nanoparticles. Among these, the dendritic architect of nickel showed higher toxicity compared to spherical structures (Ispas et al. 2009; Choi et al. 2009). Silver nanoparticles during cytotoxicity studies showed higher toxicity with rod-shaped nanoparticles compared to spherical nanoparticles (Stoehr et al. 2011). After the engineering of nanoparticles, the nanoparticles could behave differently compared to the individual constituents of nanoparticles. The shape-dependent bare

magnetic nanoparticles cytotoxicity and drug loading and release studies have not been investigated so far.

In this chapter, drug loading and release profile of bare and coated rod-shaped iron oxide materials will be studied. The drug loading release profile was investigated of different ratios at different time intervals to find the role of shape and their effect on drug loading and release profile.

7.2 Doxorubicin loading profile of bare and peptide coated rod-shaped iron oxide nanoparticles

Doxorubicin (DOX) was used as a model therapeutic agent to study the loading and release profile of rod-shaped bare and peptide coated iron oxide materials. DOX solution was prepared 100 $\mu g.mL^{-1}$ in DMSO-water. Then 1 mL of the drug was added to different ratios of SPIONs (1:25, 1:50, 1:75 and 1:100, respectively). Solution was vortex mixed and sonicated for 15 minutes in the ultrasonic bath. The UV-vis absorbance at λ_{485} nm of free drug was recorded at pre-set time intervals *via* magnetic separation (as discussed in B-SPION-SS). The DOX loading quantification was performed using equation 3-1 and 3-2. The amount of loaded drug was measured from preestablished standard calibration curves in DMSO-water. The calibration curve was prepared of different concentrations (20 [1], 40, 60, 80 and 100 $\mu g.mL^{-1}$).

7.2.1 Doxorubicin loading into rod-shaped bare iron oxide nanoparticles

The loading profile of rod-shaped iron oxide was studied in DMSO-water using different ratios (1:25, 1:50, 1:75 and 1:100 of DOX:FM-ION-RS). DOX loading capacity in weight percentage of rod-shaped iron oxide is shown in Table 7-1. The DOX loading capacity of FM-ION-RS for 1:25 was 34, 26 and 13 (micromole per milligram of FM-ION-RS) at 0

hours, 24 hours and 48 hours, respectively. The highest loading capacity in weight percentage was seen in 1:25 formulation over 48 hours. Similarly, as DOX: iron oxide ratio increased, the weight percentage loading capacity was found decreased with the consistent trend.

Table 7-1 DOX -loading capacity of FM-ION-RS over pre-set time interval

DOX:FM-ION-RS	**Time of incubation (hours) (micromole per milligram)**		
(mass:mass)	**0.25**	**24**	**48**
(1:25)	34	26	13
(1:50)	16	33	21
(1:75)	7	23	21
(1:100)	3	16	15
FF-FM-ION-RS	3	3	5

Figure 7-2 displayed the time-dependent DOX loading efficiency of different formulations. The DOX loading efficiency of (1:25) formulation was nearly 38 % over 48 hours at 18 °C, this reached to maximum after 24 hours, and up to 48 hours DOX started releasing again. This trend was found consistent in all formulations (1:50, 1:75 and 1:100). However, the loading efficiency was increased in all formulations. The loading percentage was reached up to 93 % and 87 % in 1:75 and 1:100 formulations, respectively. The maximum percentage loading was seen after 24 hours for all formulations. Briefly, the percentage loading was achieved initially, as 37 %, 45, 28 % and 20 %, after 24 hours and reached to 47 %, 90 %, 92 % and 87 % and after 48 hours and again decreased to 35 %, 58 %, 86 % and 84 % for 1:25, 1:50, 1:75 and 1:100 formulations, respectively.

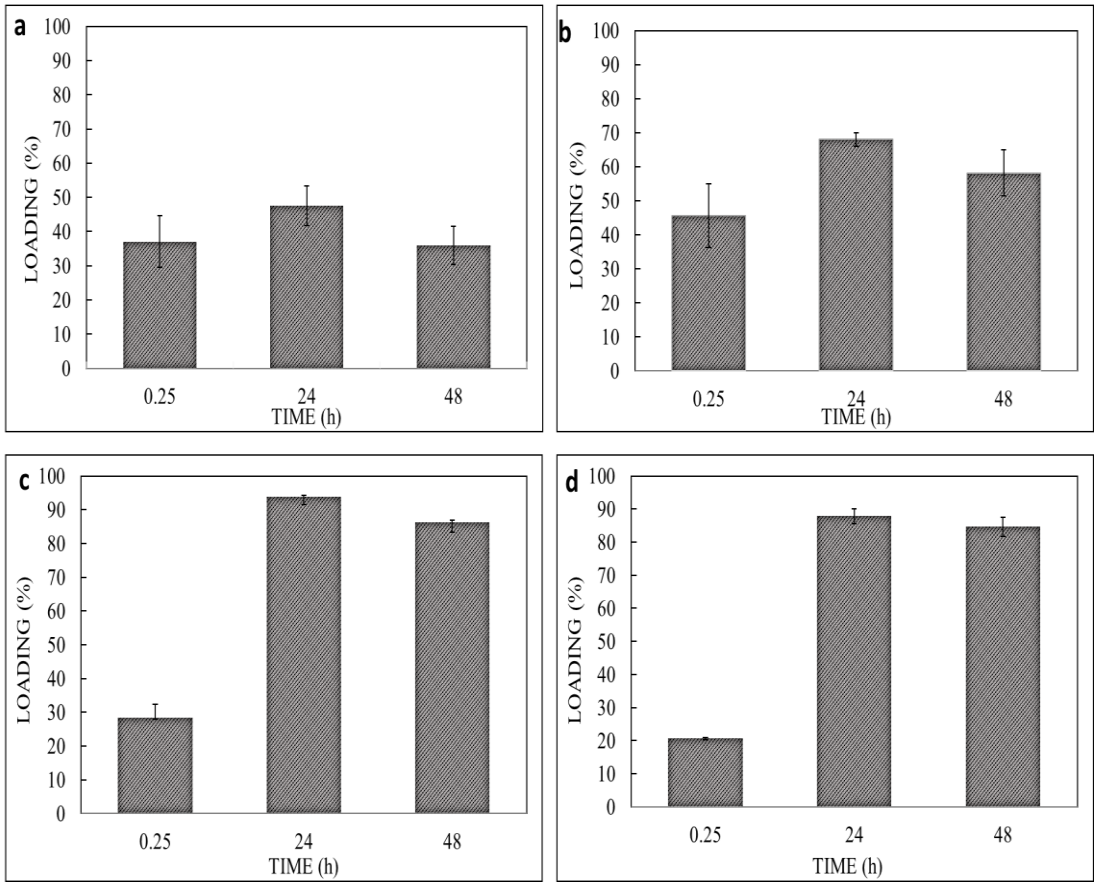

Figure 7-2 DOX loading capacity of bare SPIONs spheres with reference to incubation time, DOX to SPIONs ratio (a) 1:25 (b) 1:50, (c) 1:75 and (d) 1:100 (±SD, no=3)

7.2.2 Doxorubicin loading into peptide-coated rod-shaped iron oxide particles

The FM-ION-RS Fe_2O_3 (maghemite) showed good magnetic separation after coating. The 1:100 formulation was used for drug loading and release experiments. In addition, time-dependent studies were performed as discussed earlier at 18 °C up to 48 hours.

The FF-FM-ION-RS showed 31 % loading after 48 hours at 18 °C. This was followed *via* slowly increasing from 17 % (0 hours) to 30 % (after 24 hours) (figure 7-3). After 24 hours to 48 hours, only 1 % increase was observed. The FF-FM-ION-RS showed lowest DOX loading capacity compared to bare iron oxide nanoparticles 31 % and 87 %, respectively. 56 % decrease in DOX loading was found in FF-FM-ION-RS

nanocomposites. Samples were vortex mixed and sonicated before recording the first reading at 0 hours. The maximum time of DOX loading was 24 hours and 48 hours for FM-ION-RS nanoparticles and FF-FN-ION-RS nanocomposites, respectively.

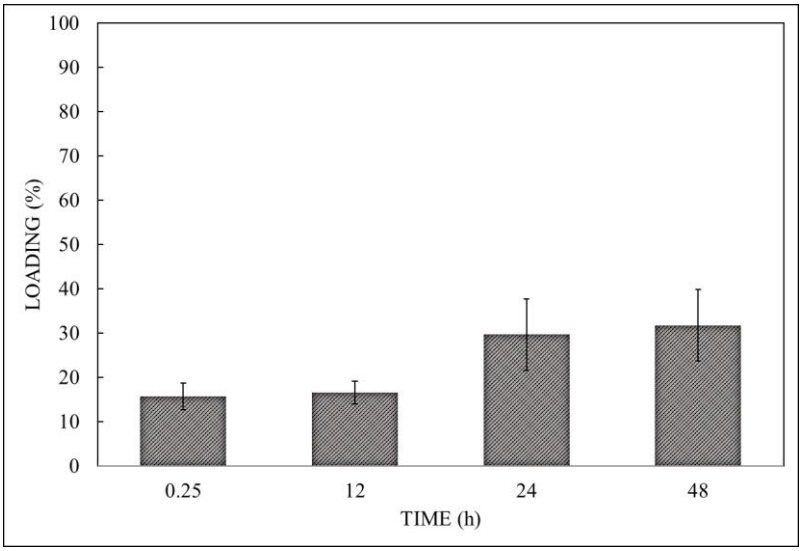

Figure 7-3 DOX loading profile of FF-FM-ION-RS at different time intervals (hours) in incubation at 18 °C (±SD, no=3)

7.3 Doxorubicin release profile of bare and peptide coated rod-shaped iron oxide nanoparticles

FM-ION-RS nanoparticles and FF-FM-ION-RS nanocomposites after incorporating DOX were dispersed in 1 mL of PBS buffer of pH 7.4 at 37 °C in end-over-end rotation in an incubator up to 48 hours. Free DOX solution of different concentrations (20, 40, 60, 80, and 100 $\mu g.mL^{-1}$) was also prepared in PBS for standard calibration curve to quantify the DOX released from particles (figure 7-4). The release behaviour was investigated in a time-dependent manner at 37 °C of incubation. The absorbance of free DOX was recorded at λ_{485} nm.

7.3.1 DOX release behaviour from rod-shaped bare iron oxide nanoparticles

The DOX-loaded FM-ION-RS nanoparticles were magnetically separated from the free drug. The absorbance reading of free drug was recorded at pre-set time intervals of different formulations. Figure 7-4 displayed, the drug release behaviour of the FM-ION-RS nanoparticles at 37 °C up to 48 hours for different formulations (1:25, 1:50, 1:75 and 1:100). DOX-loaded FM-ION-RS nanoparticles showed slow and homogenous release. The total drug was released in 24 hours. Interestingly, The Free DOX was again adsorbed on the surface of magnetite after 24 hours. After 12 hours approximately 90 % of total drug was released from FM-ION-RS nanoparticles. The final DOX release after 48 hours was somewhat similar to the amount of DOX released after 12 hours particularly in 1:25 and 1:50 formulations.

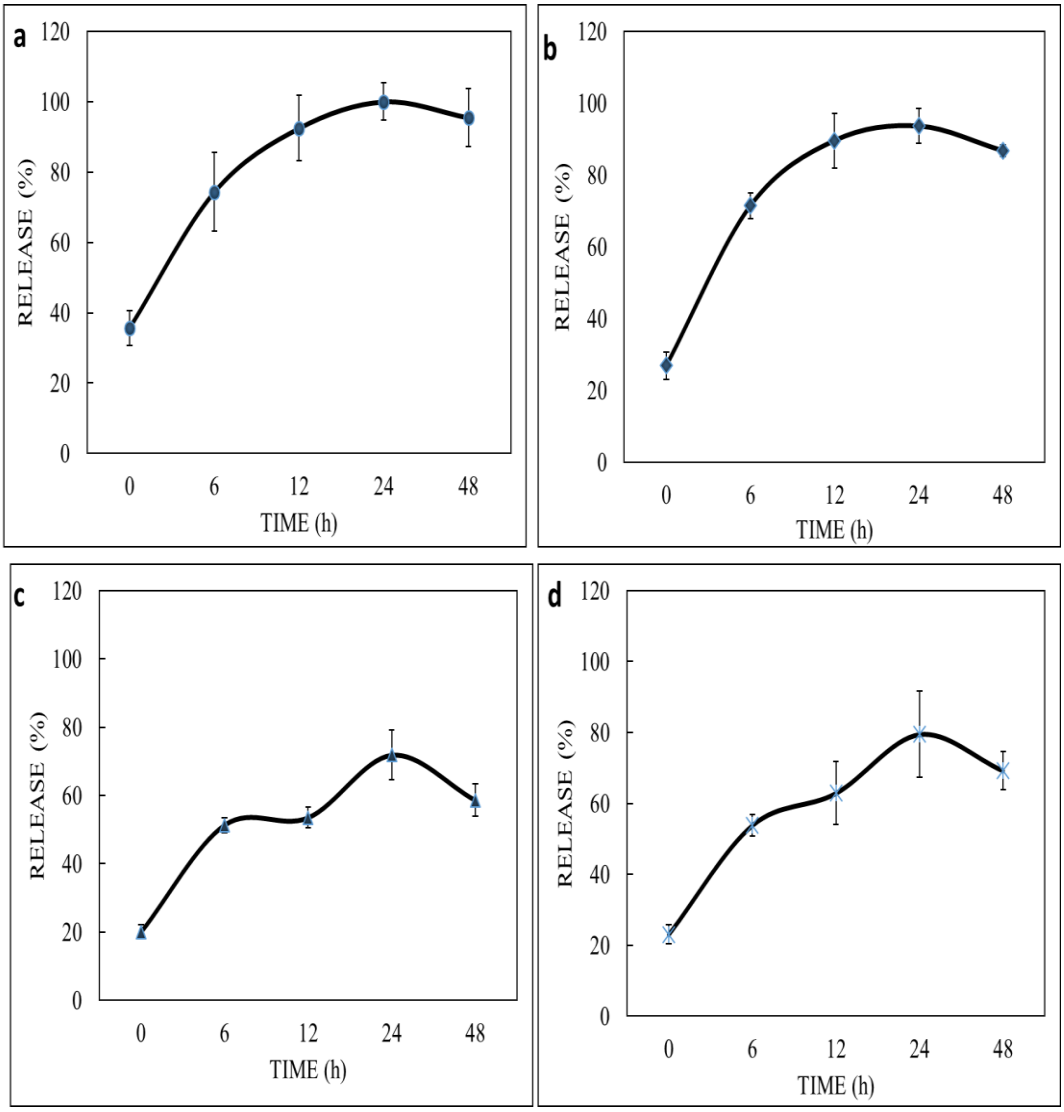

Figure 7-4 DOX release profile of FM-ION-RS with reference to incubation time, DOX to FM-ION-RS ratio (a) 1:25 (b) 1:50, (c) 1:75 and (d) 1:100, respectively (±SD, no=3)

In zero hour time after sonication and vortex mixing, approximately 38 %, 23 %, 20 % and 21 % DOX release (as burst effect) was seen for (1:25, 1:50, 1:75 and 1:100, respectively) formulations. The release trend was consistent up to 6 hours in all formulations. In 1:25 and 1:50 formulations, the maximum release was found after 12 hours of incubation at 37 °C. DOX release was reached at maximum after 6 hours for 1:75 formulations. Similar trend of DOX release was observed in 1:100 formulations. B-SPION-SS showed burst release, which possibly was due to lower loading capacity of

FM-ION-RS nanoparticles. However, the DOX possibly be adsorbed on the surface of rods similarly as in the case of B-SPION-SS.

7.3.2 Doxorubicin release behaviour of rod-shaped peptide-coated iron oxide nanoparticles

Tubular diphenylalanine peptide (FF) was coated to rod-shaped bare iron oxide (FM-ION-RS to enhance the sutained release of DOX, increased biocompatibility and reduced aggregation. The coatings on the FM-ION-RS nanoparticles form a barrier facilitating the slow release of DOX. The shape of particles had significant influence on the releasing behaviour of cargo. DOX-loaded FF-FM-ION-RS nanocomposites were incubated at 37 °C up to 48 hours, to study the release behaviour in PBS (pH 7.4). The time-dependent release behaviour was monitored by recording the UV-vis absorbance at λ_{485} nm at pre-set time intervals during 48 hours of incubation. The slow release pattern was seen in initial 12 hours then in next 12 hours; it reached to a maximum release (100 %) (figure 7-5). This unusual behaviour of DOX release from FF-FM-ION-RS core-shells nanocomposites were found possibly due to the interactions of peptide tubes with DOX. In general, it was clear that FF-FM-ION-RS could be used to slow the burst release effect of DOX after optimising the peptide DOX interactions.

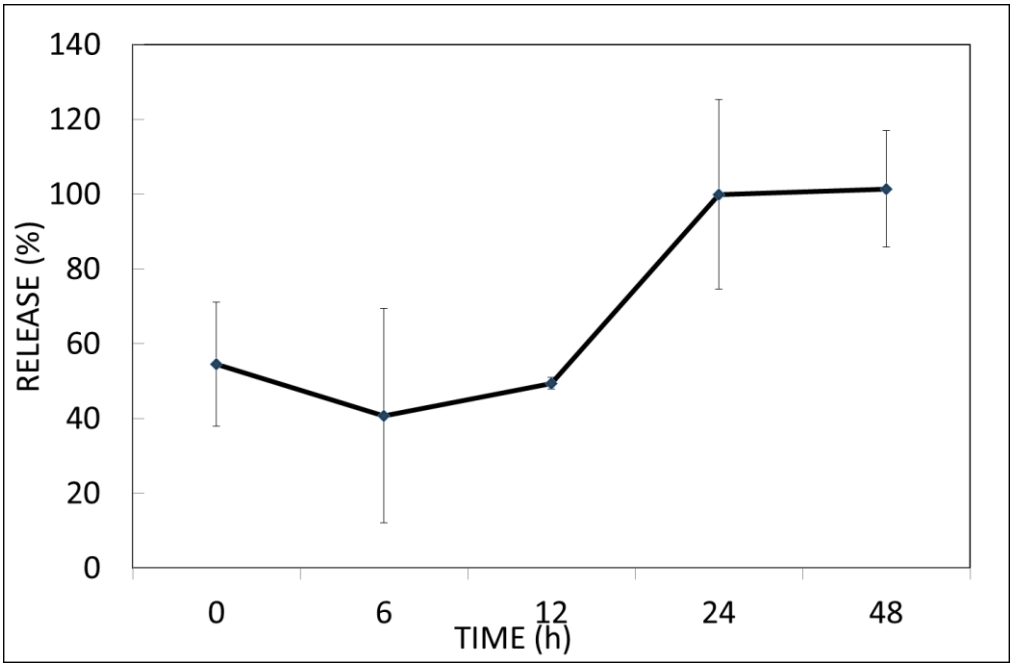

Figure 7-5 DOX release profile of FF-FM-ION-RS nanocomposites at different time intervals (±SD, no=3)

Figure 7-5 showed the release behaviour of FF-FM-ION-RS; the release behaviour was found increasing after 6 hours, 12 hours and 24 hours (40 %, 49 % and 99 %, respectively). The graph curve revealed the total release of DOX went to plateau after 24 hours to 48 hours. The physically adsorbed molecules without layers of coatings could be release in a burst effect; the peptide layer has influenced the burst release by slowing down the pattern of release up to 24 hours. The slow DOX release could be due to the weakening of hydrophobic and ionic interactions of DOX and peptide phenylalanine rings and ionic charge of iron oxide. Hence time in losing of these interactions facilitate the slow release and steady release.

The mechanism of DOX release from its carriers was fundamental to understand how the drug releases from surface or layers of coatings. The binding with the carrier will be too strong to leak drug, however weak binding is not suitable for sustainable release. This study has provided the simple kinetics of loading and release behaviour of DOX to bare,

and peptide coated iron oxide nanoparticles. Studies performed on gold nanorods coated with CTAB layers showed incorporation of small molecules on the gold surface under a thick layer of CTAB (Alkilany et al. 2008). The results suggested that in nM concentration of gold particle could adsorb the μM concentration of drugs. Meanwhile, drug incorporation to gold rods was dependent on length of nanorods. Their data revealed the incorporation of drug molecules in the layer of metallic particles (Alkilany et al. 2008). The studies on releasing behaviour of drugs from the coated magnetic materials are still in initial phase. However, these rod-shaped base materials for drug delivery applications are still in initial phases.

The solvent effect of drug release with similar poly(lactic-co-glycolic acid) sphere was also studied (Huang & Brazel 2001), where they have used double emulsion solvent system using fluorescence tagged drug. The hydrophobic polymer lowered the inner hydrophobic phase volume, which could avoid the uneven distribution of small molecules, causing the burst release. Polymers, where drug distributed non-uniformly in matrices, the release rate could be increased due to the higher diffusion distances that cause the hindrances (Lee 1984; Machín et al. 2013). The non-uniform distributed drug in the polymer matrices improved the sustained release, where higher loading could attribute to the central part of the carriers (Lee 1984). The sustained release could also be improved by increasing the concentration gradient. The researchers also have focused on the designing of non-uniform distribution of drugs to achieve a zero-order release, where they use multi-laminae polymers (Zhao et al. 2015).

7.4 Conclusions

In this work, novel magnetically targeting nanocarriers were prepared with possibilities of improved controlled release mechanism for drug delivery. FM-ION-RS and FF-FM-ION-RS nanocomposites were loaded with DOX.

The ferromagnetic rod-shaped nanoparticles DOX release was found in burst effect manner. Almost 90 % of total DOX loaded was release after 12 hours of incubation in PBS at 37 °C. The peptide-coated materials released the DOX in a sustainable manner, where DOX release was found similar in initial 12 hours of incubation. These rod-shaped core-shell structures showed sustained DOX release and can be used as thermally responsive stimuli material for controlled and magnetic field triggered release.

Though the coated magnetic particles have reduced the burst effect up to 12 hours, the actual mechanism of drug incorporation into core-shells is still unclear. However, in some biomedical applications burst release is ideal as long as burst effect is clearly expected. The complete removal of burst release is possibly a cost prohibitive, but these results could provide the base to enhance the understanding of nanocarriers designs, which precisely predict the sustained and control release pattern of drugs based on shape of magnetic nanoparticles.

Moreover, amino and carboxyl groups of the peptide can open the ways for surface modifications to attach antibodies for active targeting or subcellular signals for enhanced permeability into the targeted cells. The coating could provide better biocompatibility more efficiency for sustained release of drug molecules. These multifunctional materials could be a base to explore the new horizons for magnetic field targeted for drug delivery system to overcome the current limitations.

CHAPTER EIGHT

Magnetic field induced hyperthermia and triggered drug release of magnetic nanoparticles

8.1 Introduction

Iron oxide nanoparticles have been used as MRI contrast enhancers, hyperthermia ablation, drug carriers and targeting materials for diseased tissues using an external magnetic field. Magnetic nanoparticles have been investigated as promising tools for hyperthermia treatment in cancerous tissues *in vitro* studies and animal models. The initials positive results of magnetic nanoparticles induced hyperthermia have provided the impetus for the Phase-I human experiments (Shevtsov & Multhoff 2016). In hyperthermia, body temperature was increased to change the structural characteristics of cellular functions. In localised hyperthermia treatment the temperature may rise up to 42 °C; tumour cells do not resist this temperature with sudden changes compared to normal cells leading to tumour cells destruction (Cavaliere et al. 1967). The change in the temperature alters the structure-function relationship of enzymes and proteins, causing cell apoptosis *via* deregulating the cell growth and differentiation (Sellins & Cohen 1991). Hyperthermia triggered alteration of cell membranes caused changes in the transporting mechanism of membrane permeability. Cellular studies demonstrated the sudden increase in the temperature altered the synthesis and structural conformational of nucleic acids also inhibited DNA repair enzymes (Paolini et al. 2015; Wong et al. 1993). The induction of hyperthermia can be achieved *via* numerous techniques, such as microwave or electromagnetic radiations (Stahl et al. 1995; Sneed et al. 1998), focused high ultrasound waves (Mitsumori et al. 1996) or electrical energy (Wismeth et al. 2010). Even though these techniques generate sufficient heat however they failed to provide uniform

distribution and deep penetration of heat for therapeutic applications in tumours sites. Hence, insufficient or nonhomogeneous distribution of heat in tumour sites causes a temperature rise in only surface sites. Another important factor is excessive and uncontrolled heat induction that causes the peritumoral cell damage. Nanoparticles induced magnetic hyperthermia has somewhat addressed these issues.

Magnetic induced hyperthermia applications were initially reported in Gilchrist et al. (1957). A series of research papers were published for studying the potential application as hyperthermia ablation therapy. However, consistent studies for therapeutic based applications were published after the 1990s. Still fewer studies are available in animal models (Hoopes et al. 2015; Thiesen & Jordan 2008; Attaluri et al. 2015). More studies are needed to adress the limitations, toxicity, selectivity and efficiency for effective and safe treatment of tumours. The mechanism of magnetic hyperthermia involves the systematic administration of magnetic materials. After applied external magnetic field magnetic materials can increase temperature in targeted region (Kashevsky et al. 2015). Currently, magnetic hyperthermia stands for the non-invasive, effective and comparable uniform and deeply penetrating technique for regions where accessibility is limited, specific to targeted regions and have enhanced rate of heat transfer.

Magnetic hyperthermia efficiency depends on the various properties of nanoparticles such as size, shape, saturation magnetisation value and Curie point (*Tc*). Curie point is critical which provides the control of heat transfer to avoid excess heating (Tang et al. 2017). Another important factor for controlling the desired temperature is the tunable strength and frequency of the magnetic field. The efficiency of induced heat of magnetic materials was measured as the specific absorption rate (SAR). SAR reflects the heat transformation from magnetic energy, which is characteristic of Brownian rotation and Nėel relaxation

phenomenon. In Brownian rotation, the particles rotate physically within the dispersion medium. In Nėel relaxation mechanism, particle`s magnetic moment at atomic level rotates within the particles. The Brownian rotation and Nėel rotation processes are revealed as relaxation times (T_B and T_N) respectively. In hyperthermia studies, SAR values are dependent on the particles internal (Nėel) characteristics such as (size, shape, elemental composition, functional modifications and additives) and the external (Brownian) characteristics reflect the strength (H) and frequency of the magnetic field. The following equation can define the SAR:

$$SAR = \frac{c}{M_{\text{mnp}}}\left(\frac{\Delta T}{\Delta t}\right) \qquad \text{Equation 8-1}$$

where c is specific heat capacity of the medium and $\frac{\Delta T}{\Delta t}$ reflects the initial slope of temperature change during the heat induction and M_{mnp} is mass of nanoparticles (mg) (Hervault & Thanh 2014).

The initial study of magnetic hyperthermia based treatment *in vivo* was performed using dextran-coated SPIONs with a core size of approximately 3 nm (Jordan et al. 1997). Dextran coated SPIONs were systematically administered into tumour tissues and subsequently the magnetic field was applied. Applied magnetic fields frequency and strength, tissues selection and conductivity should be taken into consideration to avoid possible harmful effects. The magnetic field frequency of 0.1-1.5 MHz and 0-17 $kA.m^{-1}$ strength is considered safe for *in vivo* application (Schmid 2011). A variety of trials have been conducted by different companies such as MagForce Nanotechnologies (Germany) and NanoTherm (UK), showing the efficiencies of magnetic hyperthermia based treatments of localised solid tumours by reducing the discomfort or harms to normal cells (Maier-Hauff et al. 2011). This treatment involved killing cells using induction heating.

Heating was generated by SPIONs *via* Brownian rotation or Nėel relaxation on subsequent applied magnetic field. This mechanism comprises of different modules; SPIONs, magnetic field and incorporated drugs. Due to the SPIONs ultra-small size and exposure to the applied magnetic field, they are localised inside the tumours and generate concentrated and uniform heat in selected sites (figure 8-1)

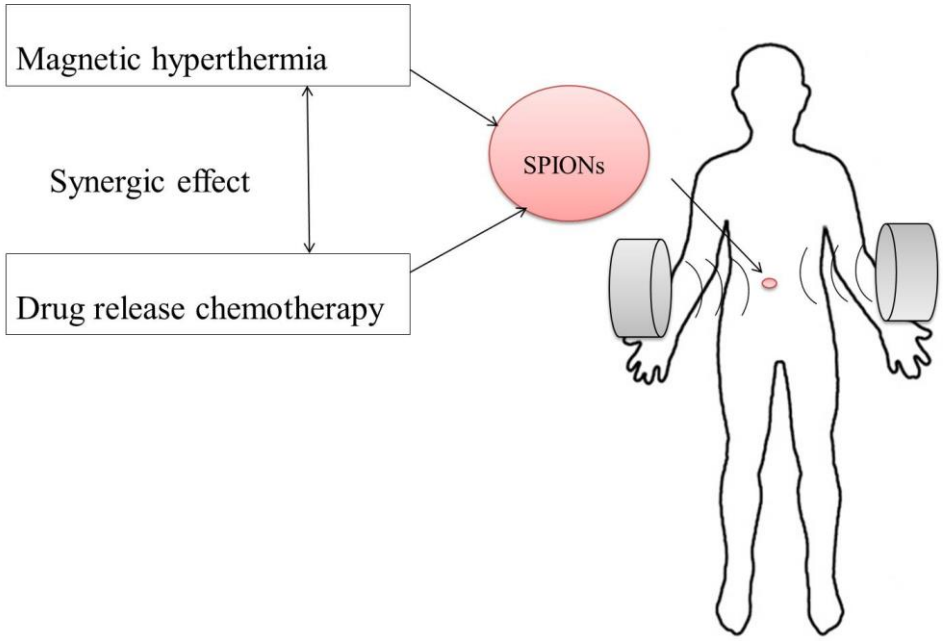

Figure 8-1 Depiction of localised magnetic field triggered nanoparticles thermo-chemotherapy

This research work was derived from the concept of engineering of hyperthermia-responsive peptide coated drug loaded iron oxide nanoparticles, which can increase the internal temperature when exposed to external magnetic field and trigger drug release. This study has investigated the effects of different iron oxide nanoparticle concentration on the hyperthermia of bare and peptide-coated particles. The magnetic field triggered drug release system may provide an ideal system in cancer treatment by simultaneously exploiting both chemotherapy and hyperthermia ablation therapy (figure 8-1).

8.2 Magnetic nanoparticles induced hyperthermia

8.2.1 Magnetic field induced hyperthermia of spherical bare superparamagnetic iron oxide nanoparticles

Spherical iron oxide nanoparticles synthesised *via* co-precipitation method were studied to investigate the concentration effects in water. Four different concentrations (2.5 $mg.mL^{-1}$, 5 $mg.mL^{-1}$, 7.5 $mg.mL^{-1}$ and 10 $mg.mL^{-1}$) were used. Magnetic field with a frequency of 406 kHz and strength of 200 G was kept constant in all of the experiments. Spherical core materials (B-SPION-SS) of different concentrations from 2.5 $mg.mL^{-1}$ to 10 $mg.mL^{-1}$ showed slowest and fastest induced heating rate, respectively upon exposure to the alternate magnetic field (figure 8-2). The results of magnetic field induced hyperthermia were highly concentration dependent. The 2.5 $mg.mL^{-1}$ showed slowest temperature increase and reached 42 °C in 20 minutes of exposure to the AC magnetic field. In the 5 $mg.mL^{-1}$ solution the temperature was increased sharply compared to 2.5 $mg.mL^{-1}$. It reached 50 °C in approximately 10 minutes. Similarly, 7.5 $mg.mL^{-1}$ took only 4 minutes to achieve 50 °C. The fastest heating pattern was seen for 10 $mg.mL^{-1}$ of B-SPION-SS taking only 3.5 minutes to reach 50 °C. These results were consistent with previous studies (Frimpong et al. 2010; Ghosh et al. 2011), where they found a sharp increase in the temperature using constant magnetic field strength and frequency. The mechanism of heat induction from synthesised nanoparticles could be due to the Brownian rotation and Nėel relaxation of Fe_3O_4 nature of the nanoparticles with low conductivity ($\rho = 10^2$ Ω cm, resistivity), hence Eddy current heat induction may be negligible (Ghosh et al. 2011). VSM and XRD data also confirmed the superparamagnetic nature of the nanoparticles, the heat induction from hysteresis loss may also be negligible. The main source of heat induction will only be contributed to the Brownian rotation or Nėel relaxation.

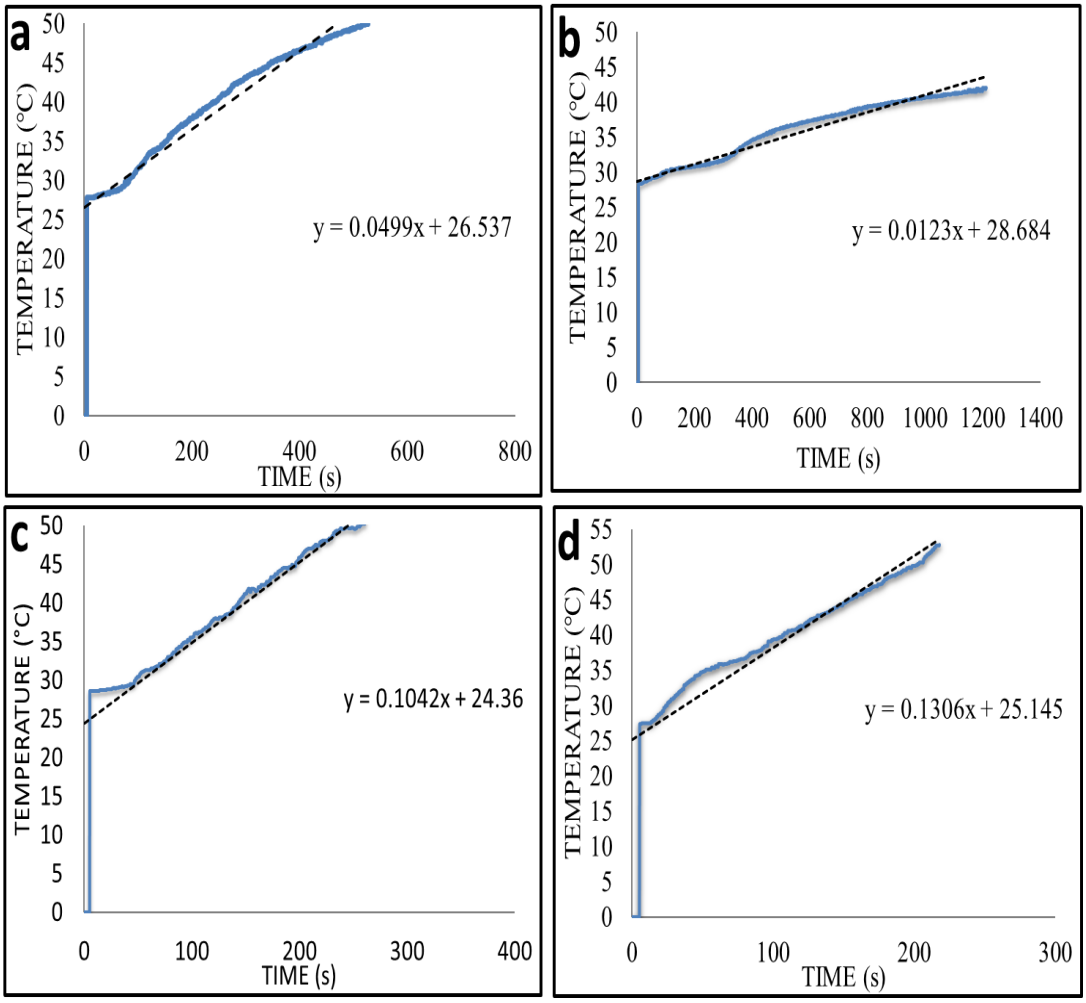

Figure 8-2 B-SPION-SS temperature increase curves after exposure to AC magnetic field on (a) 2.5 mg.mL^{-1}, (b) 5 mg.mL^{-1}, (c) 7.5 mg.mL^{-1} and (d) 10 mg.mL^{-1} (graphs are representative of three independent experiments)

The specific absorption rate (SAR) was measured using equation 8-1. For all studies (figure 8-2 (a –d)), initial slope $\frac{\Delta T}{\Delta t}$ was calculated from first minute of applied magnetic field. The calculated SAR values are shown in table 8-1 for all concentrations. The highest SAR value (63 W.g^{-1}) was found for the 2.5 mg.mL^{-1} with the magnetic field strength and frequency. However, this value was higher compared to previous study (Ma et al. 2004), where the sized dependent effect of SAR calculation was studied. For iron oxide with size of approximately 20 nm, SAR value was 40 W.g^{-1}. In a similar SPIONs size distribution of as this study the SAR value was 63 W.g^{-1}. The minimum SAR value found in this study

was 22 $W.g^{-1}$. These results were consistent with previous studies (Zhang et al. 2007; Müller et al. 2005; Behdadfar et al. 2012; Frimpong et al. 2010).

Table 8-1 Experimental SAR values calculated for spherical iron oxide nanoparticle

Concentration ($mg.mL^{-1}$)	**SAR ($W.g^{-1}$)**
2.5	63
5	36
7.5	30
10	22
BOC-SPION-SS	78

The kinetic studies on the effects of temperature showed a sharp increase for higher concentrations. The SAR values were in reverse in order to the concentration. The highest SAR value was obtained for lowest concentration. The possible reason behind the fast increase of temperature and lower SAR value is the retention of the particles Brownian and relaxation effect in lower concentrations. Higher concentrations of B-SPION-SS facilitated the formation of large aggregates. Other studies confirmed the good dispersions of B-SPION-SS showing higher SAR value *via* better Brownian rotation and Nėel relaxation effects (Rao 2014; Pawar 2013). The 5-10 $mg.mL^{-1}$ of B-SPION-SS were found to be effective and safe for hyperthermia treatment of tumour tissues (Dobson 2003). Figure 8-2 (a-d) showed concentration-dependent heat induction of B-SPION-SS where the temperatures were set in between the minimum of 42 °C and a maximum of 55 °C in water as a medium of dispersion. These results confirmed that the concentration from 2.5 $mg.mL^{-1}$ to 10 $mg.mL^{-1}$ could increase the temperature 42 °C – 55 °C using 406 kHz frequency and 200 G. Table 8-1 shows the SAR values as a function of the concentration of B-SPION-SS. The SAR results obtained in this study are comparable to computer simulated SAR values, where SAR values were found higher in lower

concentration (Salon 2012). This was also common for lower concentration, where particles in suspension were expected as individuals rather than as aggregates after the application of a magnetic field. However, larger aggregates tend to sediment and less exposed to the magnetic field. In a similar study, where SAR was calculated using different volume vials showed lower volume vials have three times higher SAR values than the value obtained with larger volume vials (Salon 2012). This difference may be attributed to exposure of applied magnetic field to individual nanoparticles in a suspension.

8.2.2 Magnetic field induced hyperthermia of silica-coated iron oxide nanoparticles

Figure 8-3 revealed the silica-coated magnetic nanoparticles (Si-SPION-SS) induced heating curves of four concentrations in water of 2.5 $mg.mL^{-1}$, 5 $mg.mL^{-1,}$ 7.5 $mg.mL^{-1}$ and 10 $mg.mL^{-1}$ using a frequency of 406 kHz and a magnetic field strength of 200 G. The higher concentration of silica-coated iron oxide nanoparticles showed a sharp increase and higher maximum temperature compared to lower concentrations. Each formulation reached a plateau temperature within 25 minutes of exposure of magnetic field. In 2.5 $mg.mL^{-1}$, the graph did not display the temperature increase in the first 4-5 minutes. This time possibly indicates a lag phase where Si-SPION-SS heating occurs firstly in the cores and then dissipates to the shell and finally to the medium, where temperature probe was attached. After this time, heating could be seen clearly, requiring 23 minutes to raise 5 °C (figure 8-3 a). In figure 8-3 (c-d) heating curves (5 $mg.mL^{-1}$ – 10 $mg.mL^{-1}$) showed the sharp temperature increase from the first minute of exposure of the magnetic field, however, in first four minutes, the heating trend was somewhat slower than in later time up to 20 or 23 minutes. This trend also confirmed the presence of coating, where initial heat dissipation occurred in shell than it transferred to medium,

where temperature probe was located. 5 $mg.mL^{-1}$ solutions took 23 minutes to raise 9 °C reaching 37 °C (figure 8-3 (b)). Higher concentration of 7.5 $mg.mL^{-1}$ showed an increase in the temperature up to 43 °C by raising 15 °C in 20 minutes (figure 8-3 c). However, the fastest and maximum heat induction was seen for 10 $mg.mL^{-1}$ concentration, where a maximum temperature was observed at 46 °C by raising 18 °C, over exposure of 20 minutes magnetic field (figure 8-3 (d)).

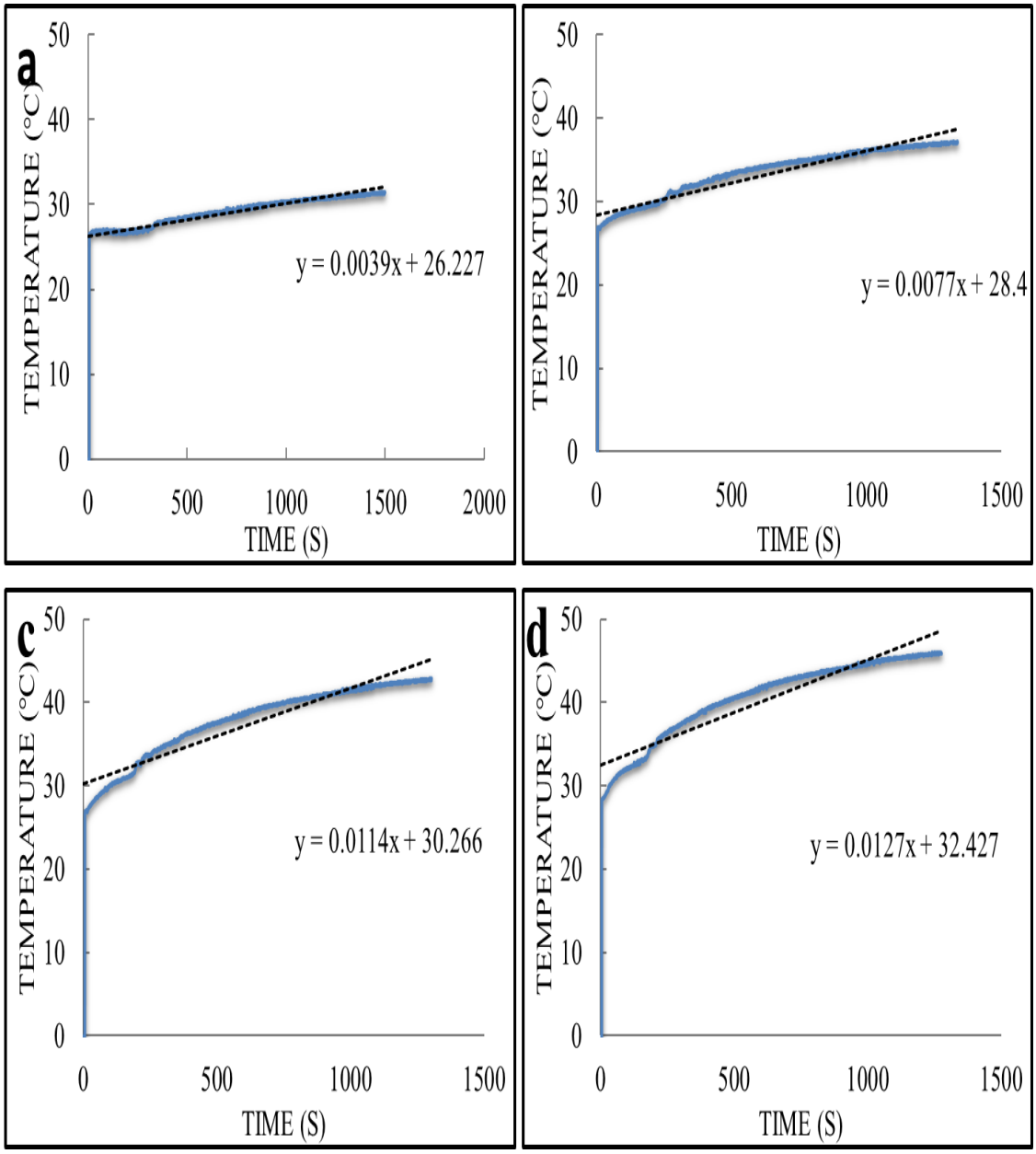

Figure 8-3 Si-SPION-SS hyperthermia effect after exposure to AC magnetic field (a) 2.5 mg.mL^{-1} (b) 5 mg.ml^{-1}, (c) 7.5 mg.mL-1 and (d) 10 mg.mL^{-1} (graphs are representative of three independent experiments)

Table 8-2 Experimental SAR values calculated for spherical silica coated iron oxide nanoparticle

Concentration (mg.mL^{-1})	SAR (W.g^{-1})
2.5	131
5	117
7.5	54
10	30
BOC-Si-SPION-SS	39

8.2.3 Magnetic field induced hyperthermia of peptide-coated iron oxide and peptide-capped silica-coated iron oxide nanoparticles

The experimental heating ability of peptide coated iron oxide nanocomposites (BOC-SPION-SS) and peptide-capped silica-coated iron oxide nanocomposites (BOC-Si-SPION-SS) is shown in figures 8-4 (a) and (b) respectively. Hyperthermia induction graph trend showed that the temperature increased, where peptide coated iron oxide nanoparticles increased the temperature up to 39 °C, over 10 minutes of exposure of magnetic field (figure 8-4 a). BOC-Si-SPION-SS nanocomposites could raise the temperature by 5 °C reaching 32 °C in 20 minutes (figure 8-4 (b)). Pure peptide on exposure to magnetic field curve is shown in figure 8-5. In both formulations, BOC-SPION-SS nanocomposites and BOC-Si-SPION-SS nanocomposites, temperature changes were altered significantly, it is possibly due to the presence of different layers on magnetic cores. This also confirmed the deposition of relatively thick layers on the core magnetite, which affected the Brownian rotation and Nėel relaxation behaviour of SPIONs. This assumption was supported by the size distribution variation of B-SPION-SS, BOC-SPION-SS and BOC-Si-SPION-SS. Hyperthermia induction of SPIONs under magnetic field in composites could also be a consequence of hysteresis loss, physical

rotation *via* Brownian relaxation inside the medium and magnetic moment inside the particles overcoming the energy barrier (Allam et al. 2013).

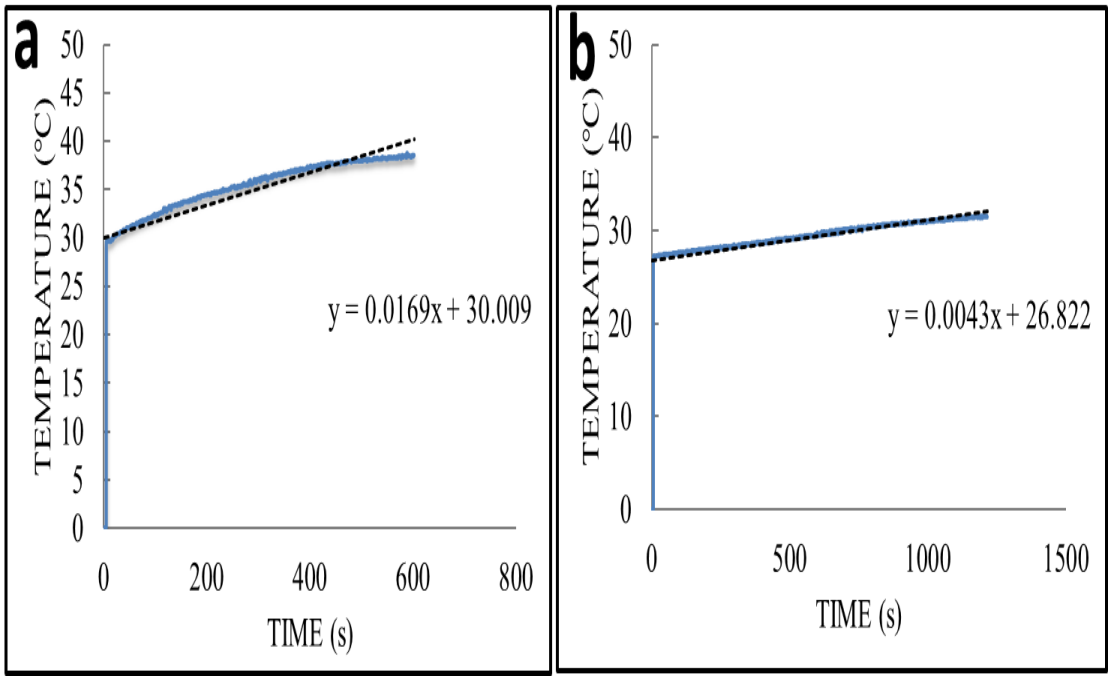

Figure 8-4 Magnetic field induced heating behaviour of (a) BOC-SPION-SS and (b) BOC-Si-SPION-SS nanocomposites (graphs are representative of three independent experiments)

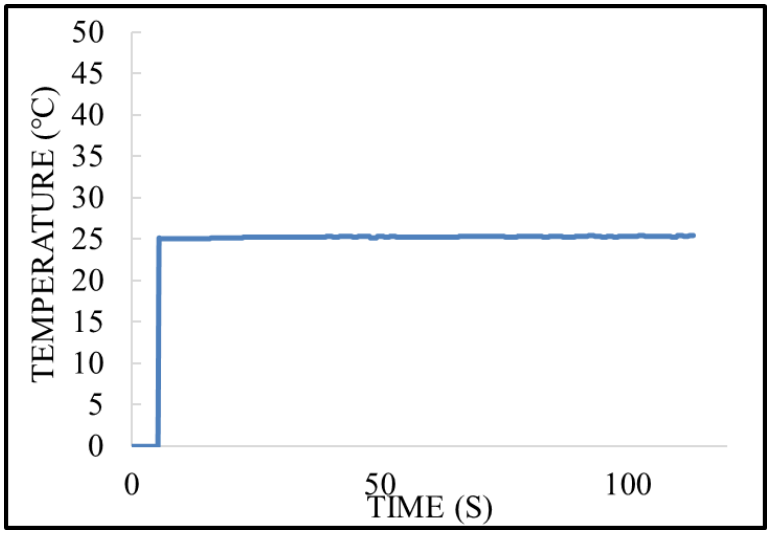

Figure 8-5 Applied magnetic field to BOC-FF spheres (graph is representative of three independent experiments)

8.2.4 Magnetic field induced hyperthermia of bare rod-shaped iron oxide nanoparticles

The shape of SPIONs is an important factor effecting the magnetic capabilities and hyperthermia response. B-SPION-SS were synthesised *via* the co-precipitation of iron (II), and iron (III) method. This method is simpler with less complications and better magnetic capabilities. The Rod-shaped iron oxide nanoparticles (FM-ION-RS) prepared using ferrous sulphate as iron source method showed elongated structures. Magnetic measurement revealed non-superparamagnetic behaviour. Hyperthermia performance was investigated following the similar procedure as discussed earlier. Figure 8-6 showed the heating behaviour at different concentration of FM-ION-RS nanoparticles using consistent magnetic field strength 200 G and frequency 406 kHz. FM-ION-RS nanoparticles showed less heating effect compared to the B-SPION-SS for concentrations studied (2.5 $mg.mL^{-1}$, 5 $mg.mL^{-1}$, 7.5 $mg.mL^{-1}$ and 10 $mg.mL^{-1}$). The maximum and fast heat generation was found in B-SPION-SS when temperature was raised to 50 °C in 2.5 minutes. The FM-ION-RS nanoparticles took 20 minutes to reach 45 °C. The difference in the heating behaviour of both materials may be explained by using the total surface to volume ratio of both shapes since the thermal response represents the unit of heat induction of source (heating materials) and unit of the surface to volume ratio (Taloub et al. 2016). The heat distribution of FM-ION-RS nanoparticles was related to the concentration in dispersion, which is a similar trend seen in the case of spherical SPIONs. The total temperature increase for 2.5 $mg.mL^{-1}$ was nearly 2 °C, over 23 minutes of magnetic field exposure. The similar trend obtained in the case of 5 $mg.mL^{-1}$ and 7.5 $mg.mL^{-1}$, however, temperature change was seen 4 °C and 7 °C, respectively over the same period of exposure to the magnetic field. Rod-shaped morphologies have a lower surface to volume ratio (as discussed in BET section) compared to spherical SPIONs,

which reflects the smaller number of disordered spins with low energy. However, spheres have more ordered spins (Noh et al. 2012). The morphological effect on hyperthermia was further confirmed, when the chemical composition was optimised to develop enhanced hyperthermia effect using zinc iron oxide nanoparticles of cubic and spherical shapes (Bauer et al. 2016).

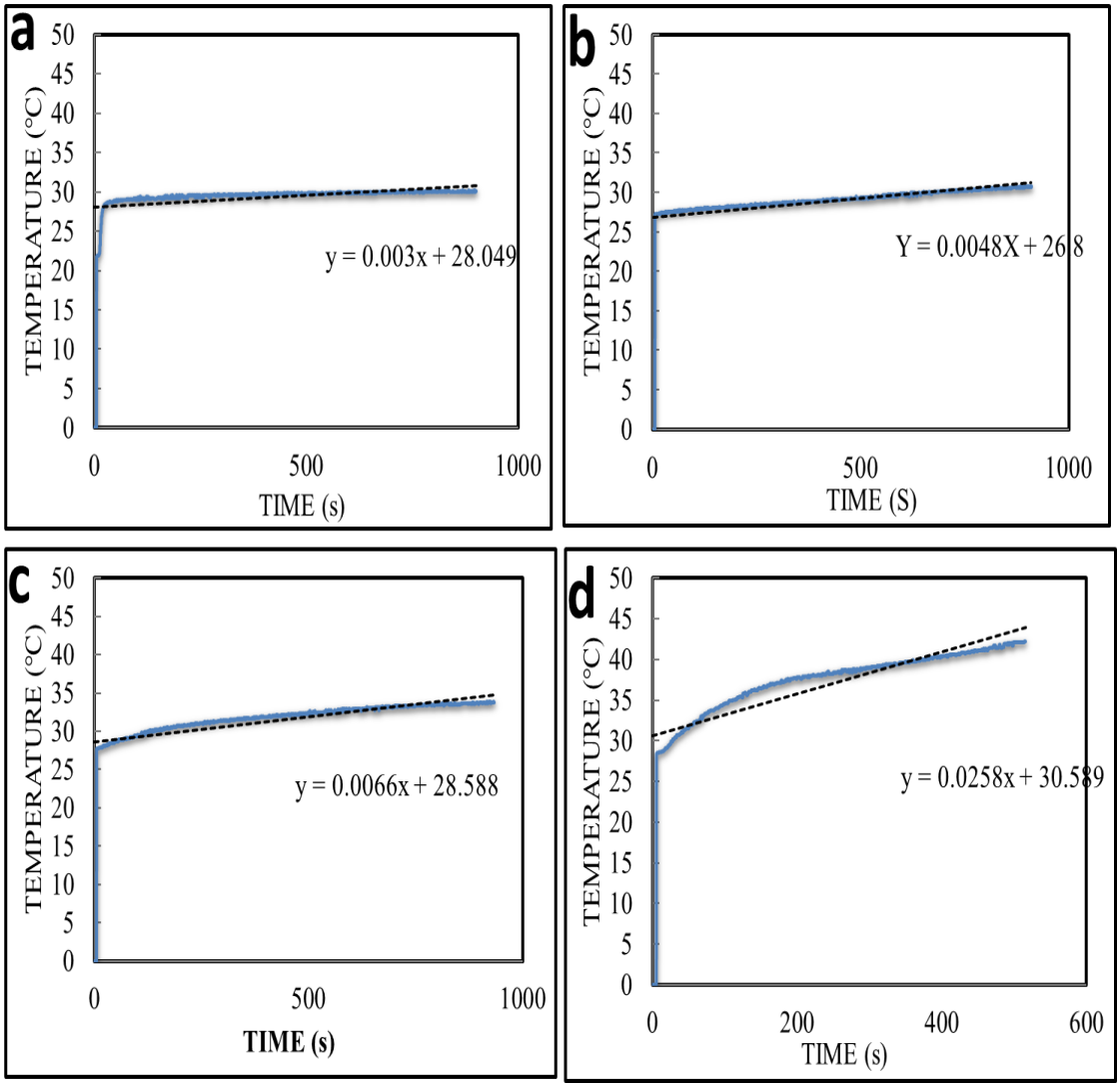

Figure 8-6 FM-ION-RS nanoparticles induced hyperthermia after exposure to applied magnetic field (a) 2.5 mg.mL^{-1} (b) 5 mg.ml^{-1}, (c) 7.5 mg.mL-1 and (d) 10 mg.mL^{-1} (graphs are representative of three independent experiments)

SAR values of rod-shaped iron oxide nanoparticles showed a linear relationship with increasing concentration (Table 8-3). The trend was consistent with spherical morphologies; however, the heating effect was completely different. The heating effect was originating from the Brownian rotation and Nėel relaxation mechanism of nanoparticles. This could be attributed to the changes in the alignment of the domains of easy axis and magnetic field. Both can influence their alignment resulting in different heating performances (Simeonidis et al. 2016). The non-linear heating trend of SAR needs more angular based studies. Generally, in both morphologies heating was common, however the amount and speed of heating were significantly different. Rod-shaped iron oxide has shown hysteresis loss hence they have different magnetisation reversal on exposure of magnetic field compared to spherical. Additionally, the difference in reaching adjacent energy level may be due the energy barrier in hyperthermia induction (Yanes et al. 2007).

Table 8-3 Experimental SAR values calculated for FM-ION-RS nanoparticle

Concentration ($mg.mL^{-1}$)	**SAR ($W.g^{-1}$)**
2.5	10
5	1.15
7.5	2.3
10	2.1

The applied magnetic field strength and frequency were similar in all hyperthermia experiment performed in this study. Hence, the chances for magnetic field strength or frequency could effect on the heating behaviour were negligible. Other factors can trigger the reorientation to a complete reversal should be taken into consideration, however, these are out of the scope of this work.

8.2.5 Magnetic field induced hyperthermia of peptide-coated rod-shaped iron oxide nanoparticles

The peptide coated iron oxide (FF-FM-ION-RS) nanoparticles induced hyperthermia capability was investigated using frequency of 406 kHz and magnetic strength field of 200 G. Briefly, 1 mL of the sample in a vial attached to the temperature probe was placed in designed space between iron cores. The cuvette surrounded the insulating chamber in order to avoid heat transfer. Temperature of the electromagnets was controlled using circulating tap water. Hyperthermia ability of sample was studied for 10 $mg.mL^{-1}$ in ethanol-water. The data was recorded as temperature versus time using applied magnetic field and at regular steps for up to 23 minutes. Figure 8-7 displays the temperature recorded against time of exposure to the external magnetic field for peptide-coated iron oxide rods. Figure 8-7 reflected the zero temperature changes after the coating. The curve was similar to that obtained for the pure peptide (figure 8-5).

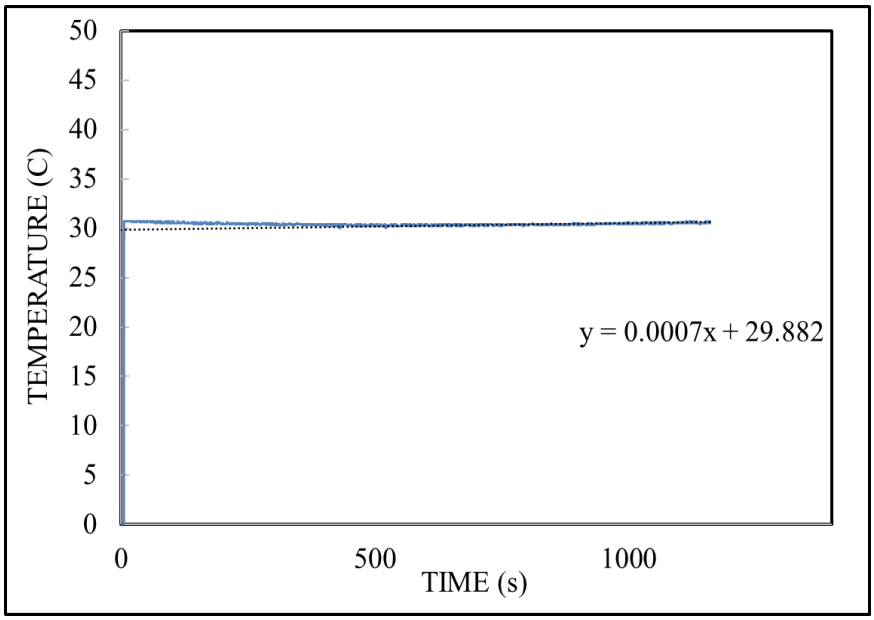

Figure 8-7 Heating behaviour of FF-FM-ION-RS nanocomposites over exposure to AC magnetic field (graph is representative of three independent experiments)

8.3 Magnetic field triggered drug release of spherical magnetic nanoparticles

8.3.1 Bare superparamagnetic iron oxide nanoparticles and peptide-coated superparamagnetic iron oxide nanoparticles

DOX was loaded into the B-SPION-SS to investigate magnetic field triggered release properties. DOX was loaded into B-SPION-SS and BOC-SPION-SS, where SPIONs cores induced hyperthermia *via* Brownian rotation and Nėel relaxation mechanism. DOX-loaded nanoparticles solution was placed in between the magnetic field coils; thermal insulation jacket was used to reduce the effects of the surrounded temperature. Additionally, water circulation was used to control environmental and thermal effect of the coils. The magnetic field strength and frequency were set 200 G and 406 kHz, respectively for all the experiments conducted. The colour of DOX was seen clearly after release experiments as free DOX after exposure of applied magnetic field. Figure 8-8 showed the DOX release behaviour under applied magnetic field and without the magnetic field. The release values were dependent on B-SPION-SS concentration; this was possibly due to the higher heating influence of B-SPION-SS, a similar pattern was also reported in Bi et al. 2016. Figure 8-8 demonstrated different concentrations of 2.5 $mg.mL^{-1}$, 5 $mg.mL^{-1}$, 7.5 $mg.mL^{-1}$ and 10 $mg.mL^{-1}$ used to investigate the release behaviour. In case of BOC-SPION-SS and BOC-Si-SPION-SS, the concentration was kept at 5 $mg.mL^{-1}$. All experiments were repeated at least three times. The release percentage reached up to 60 % for 10 $mg.mL^{-1}$. The presence of greater amount of particles induces more and rapid heat, which ultimately enhances the DOX release. The effect of BOC-SPION-SS displayed relatively lower DOX release compared to B-SPION-SS of the same concentration.

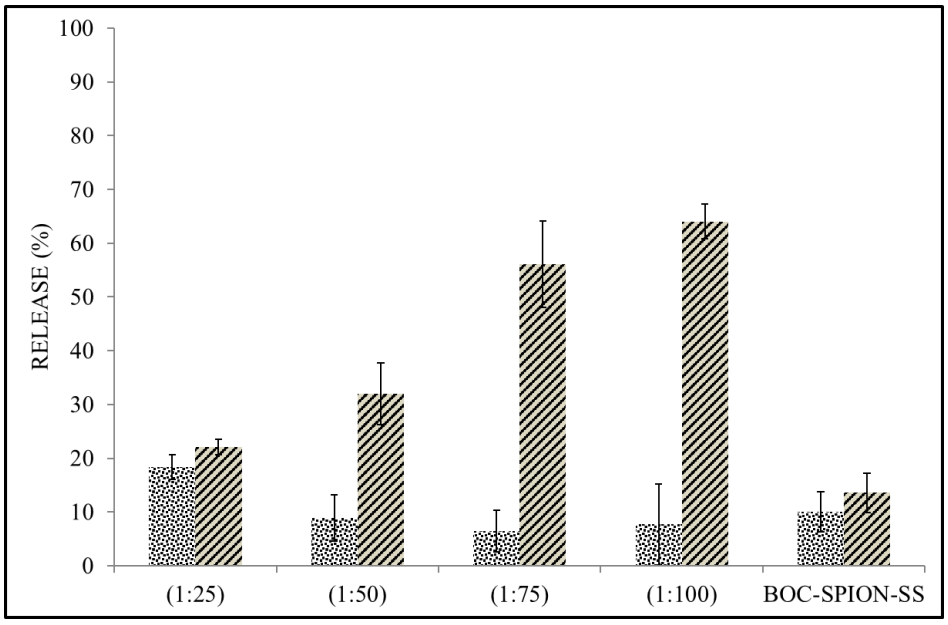

Figure 8-8 Magnetic field triggered drug release from B-SPION-SS without magnetic field exposure (black dots) and applied magnetic field (grey lines) (±SD, no=3)

8.3.2 Silica-coated superparamagnetic iron oxide nanoparticles and peptide-capped silica-coated superparamagnetic iron oxide nanoparticles

Silica-coated SPIONs (Si-SPION-SS) and peptide-capped silica-coated SPIONs (BOC-Si-SPION-SS) DOX release behaviour was investigated in presence and absence of magnetic field. Figure 8-9 showed increase trend of DOX release after exposure of magnetic field in all samples. This release behaviour was in good agreement with previously published studies for poly(trimethylene carbonate) poly(l-glutamate) coated SPIONs (Sanson et al. 2011), , poly(propyl acrylamide) coated SPIONs (Thévenot et al. 2013), PEG-capped silica coated SPIONs (Saint-Cricq et al. 2015) and bare SPIONs (Oliveira et al. 2013). In all of the above studies, different polymer coated SPIONs could increase the drug releasing efficiency up to two-fold on applied magnetic field strength (figure 8-10). As shown in the figure 8-9 in lower concentrations 2.5 $mg.mL^{-1}$, 5 $mg.mL^{-1}$ and 7.5 $mg.mL^{-1}$, the release behaviour was reduced possibly reflecting the sustained release of drug from mesoporous silica shell.

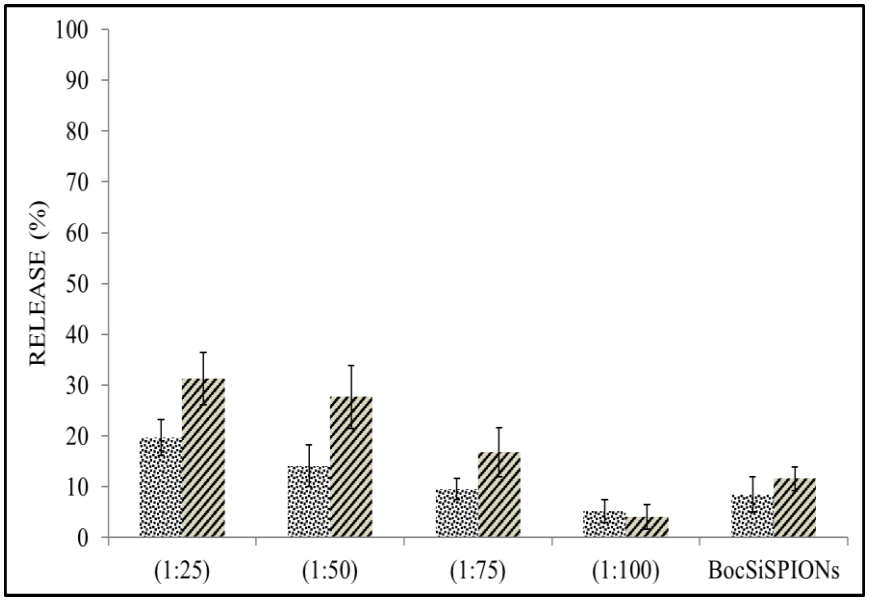

Figure 8-9 Magnetic field triggered drug release Si-SPION-SS (a) 2.5 mg.mL^{-1} (b) 5 mg.mL^{-1}, (c) 7.5 mg.mL^{-1} and (d) 10 mg.mL^{-1} without magnetic field exposure (black) and applied magnetic field (grey) (±SD, no=3)

8.3.3 Magnetic field triggered drug from rod-shaped iron oxide and peptide coated iron oxide nanoparticles

In vitro DOX release from loaded rod-shaped magnetic nanoparticles (FM-ION-RS) was studied using magnetic field strength (200 G) and frequency (406 kHz) depicted in figure 8-10. Low DOX release profile was obtained for all elongated structures compared to spherical samples. Figure 8-10 showed bare rod-shaped iron oxide of 7.5 mg.mL^{-1} and 10 mg.mL^{-1} magnetic field triggered drug release behaviour. However, for lower concentrations 2.5 mg.mL^{-1} and 5 mg.mL^{-1} magnetic field triggered DOX release effect was not found. Similar results were also found for FF-FM-ION-RS, where applied magnetic field could not trigger the DOX release. Taking into consideration of magnetic properties, these materials are multi-domain particles having considerable hysteresis. As a result, their hyperthermia ability was compromised as shown in figure 8-5. Due to lower heat of induction, these materials could not trigger the DOX release.

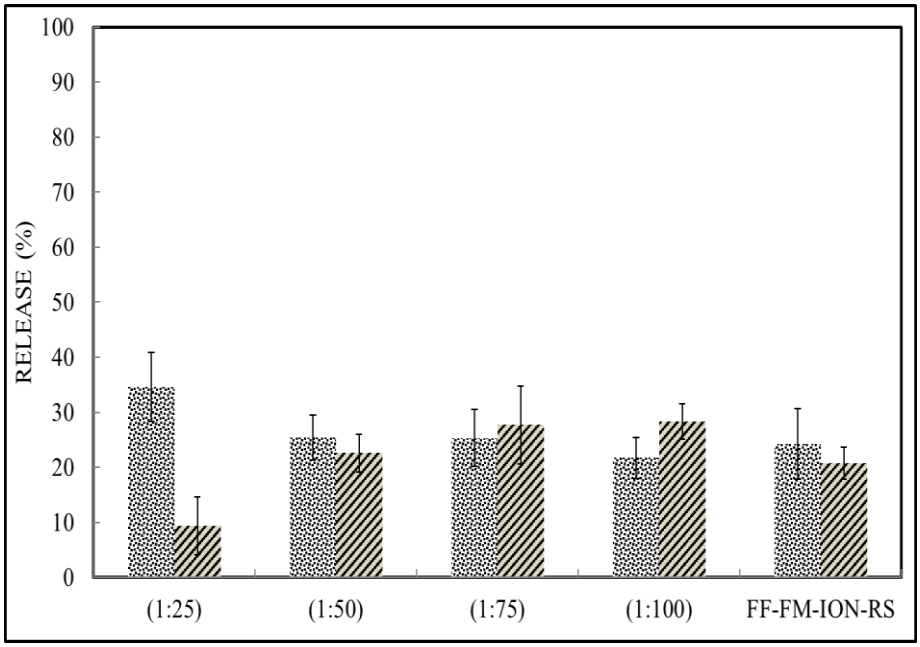

Figure 8-10 Magnetic field triggered drug release from FM-ION-RS without exposure to magnetic field (black dots) and with applied magnetic field (grey lines) (±SD, no=3)

All core-shell structures suspensions were also heated to confirm the breakage of peptide from SPIONs. Simply, 15 mL of particles suspension in a beaker was heated on heating plates. The temperature was checked by coupling thermometer and then supernatant sample, cleaved from magnetic materials was taken for SEM images to confirm the presence of free peptide structures.

To achieve a better response from the magnetic field ideally nanoparticles should have a larger magnetic moment. FM-ION-RS nanoparticles which undergo non-coherent reverse phenomenon could not be an ideal source for hyperthermia (Ivanov et al. 2013). For ideal hyperthermia effect the magnetic materials possess some properties such as single domain magnetic moment, higher surface to volume ratio and coherent reverse path. The B-SPION-SS showed enhanced and sharp heating ability than rods. For rods, wire or elongated materials the energy loss was higher as already reported (Dutz & Hergt 2014). Thus, elongated structures showed lower heating ability whereas spherical structures were found promising for magnetic hyperthermia.

8.4 Conclusions

This study demonstrates the heating abilities of bare spherical SPIONs and rod-shaped iron oxide nanoparticles. Spherical superparamagnetic particles synthesised *via* iron (II) and (III) co-precipitation method have shown good hyperthermia ability on exposure of magnetic field by increasing the temperature up to 50 °C in 3.5 minutes. Rod-shaped iron oxide nanoparticles induce heat up to 42 °C approximately in 23 minutes on exposure to similar magnetic field. This chapter also showed peptide coating on magnetic materials can control the heating of magnetic materials. Currently, the applications of bare magnetic materials are limited, due to their high amount of direct heat induction to targeted sites. This study provides the strategy that DOX-loaded peptide-coated SPIONs can be triggered by applying a magnetic field to achieve better control release. Spherical iron oxide increased the DOX release up to 65 % over exposure of magnetic field where without application magnetic field DOX was 10 % released. In silica-coated SPIONs up to 32 % DOX was released with magnetic field while without magnetic field it was only 19 %. The magnetic field can also be tuned according to the requirement of temperature, location and amount of cargo release. These results suggesting the peptide coated SPIONs could be a better alternative for triggered and controlled release drug delivery system with dual thermos-chemotherapy action along MRI contrast capability.

CHAPTER NINE

Conclusions and future work

9.1 Conclusions

Spherical and rod-shaped shaped core-shell nanocomposites have been synthesised using template-mediated coating of silica and peptide shells. Spherical SPIONs cores (B-SPION-SS) of approximately 10-35 nm were synthesised *via* co-precipitation of iron (II) and iron (III) chloride. A novel method was used to prepare Rod-shape iron oxide nanoparticles cores (FM-ION-RS), which was comparably simple, cost effective from iron (II) sulphate. This method yields nanoparticles with 10 nm in width. Spherical peptide nanoparticles were prepared using BOC-FF in ethanol-water (1:1) with average size up to 1 μm in diameter. Tubular peptide nanoparticles were prepared using FF in ethanol-water (1:1) with 300 nm to 1 μm in width and several micrometres in length. After detailed characterisation of individual components and method optimisation, several fundamental factors influencing the self-assemblies were investigated. These factors included solvent effect, concentration effect, template mediation and one-pot fabrication.

These two shaped magnetic nanostructures were used as cores for further silica and/or peptide shell coating. Encapsulated iron oxide cores in self-assembling peptides were prepared by seeding cores in a peptide solution *via* vortex mixing and ultra-sonication combination. Possibly peptide achieved the encapsulation affinity *via* carboxyl and iron ions interactions on core material where peptide self-assembled around the magnetite cores.

The peptide coated iron oxide (BOC-SPION-SS and FF-FM-ION-RS) nanocomposites were used for drug loading and release studies for controlled release drug delivery system. Several drug delivery systems were known for controlled release in cancer treatment. Some of them could have stimuli-response, while most of them lacked the target specificity. Other delivery systems that can externally directed to targeted sites but had zero release ability. Hence, by firstly coating the spheres using mesoporous silica the drug could be stored up to 90 % in 6 hours of incubation. These could be directed to target sites *via* applied external magnetic field, due to presence of iron oxide cores. This system was capable of triggering the drug release using an applied external magnetic field. Capping with the peptide improved the sustained drug release up to 48 hours. Spherical composite demonstrated the hyperthermia ability by reaching to 40 and 35 °C for BOC-SPION-SS and BOC-SI-SPION-SS, respectively.

FM-ION-RS nanoparticles showed the magnetic response when magnet was applied during separation. This system failed to show the control release behaviour even the exposure of magnetic field. The system could not have control over the cargo release from FM-ION-RS and FF-FM-ION-RS nanomaterials. However, these materials at higher concentration could induce the hyperthermia when magnetic field was applied. The tunable magnetic field strength and frequency could be a valid trigger for hyperthermia and drug release in localised treatment of cancer. The novel approach to coat the metals using short length peptide molecules could serves as promising tools to reduce the aggregation, improve biocompatibility while preserving the native properties of core materials. Peptide coated particles have provided a starting point to overcome the limitations arising in coating of iron oxide nanoparticles of different shapes. The bare iron oxide nanoparticles tend to aggregate; hence, these can be easily eliminated from

body. The coating to nanoparticles had prevented the aggregation, which can improve the biological stability (Tombácz et al. 2016). The novel peptide coated spherical composites system could be a valid step towards magnetic field guided hyperthermia and chemotherapy combination of cancer treatment.

Finally, it could be concluded that the peptide based coatings approach for metallic structure is promising in all fields of nanomedicine. In addition, novel spherical and tubular materials could open new horizon to develop safe, effective, tuneable and low cost drug carriers for improved cancer thermo-chemotherapy along possible MRI imaging.

9.2 Original contribution to research

Magnetic nanoparticles are promising tools for biomedical application. These materials received great attention due to their tunable size and shape properties. However, due to limitations such as aggregation has reduced their performances. The coating of SPIONs with polymers to reduce the aggregation and increased biocompatibility like issues is of huge interest (Laurent et al. 2008). Therefore, two shapes; spherical and rod-shaped iron oxide nanoparticles were prepared using coprecipitation method. The synthesis of rod-shaped iron oxide using ferrous sulphate as iron source is novel method. The suggested method is simple, quick and cost effective compared to already published methods. Both morphologies were then coated with naturally occurring diphenylalanine (Phe-Phe) as in native form and tert-butyloxycarbonyl (BOC) modified BOC-diphenylalanine. This work has focused on synthesis of novel core-shell spherical and tubular structure of peptide shell and SPIONs cores. The core-shell materials were then exploited for novel properties such as for drug loading and release profile, hyperthermia and magnetic field triggered drug release system.

9.3 Future work

The results achieved in this research can lead to further various experiments in different directions. Some of these directions are as follows;

i) Biocompatibility, immunogenicity and enzymatic stability

The limitation of this work includes the unknown immunogenicity of peptide-coated materials. In order to improve this novel drug delivery system, effect of peptide coating content on SPIONs for enzymatic biodegradation and clearance from blood circulation could be investigated. The *in vitro* enzymatic (trypsin) degradation of peptide could be assessed using published method (Gunasekaran et al. 2007). Removal from blood circulation can be studies using method (Genové et al. 2005).

As a novel drug delivery system, the toxicity of peptide coated spherical or tubular structures and peptides as alone need to be more deeply investigated (Teow et al. 2013). The initial studies of our group on iron based spherical nanoparticles showed lower toxicity against SVGP-12 and U87 cell lines (data not published yet). Moreover, further studies in animal model could reveal the organ based cytotoxicity of these materials.

ii) As imaging agent for diagnosis purposes

Magnetic resonance imaging is a non-invasive technique providing the structural details and deep resolution images of tissues. Despite of a huge numbers of contrast agents available for MRI, still there is need for more sensitive compared to radioactive or fluorescence imaging. While, in deep tissue fluorescence imaging could not overcome the MRI resolution. Hence, integration of magnetic resonance and optical fluorescence characteristics as single material can overcome both limitations of individual techniques.

In recent years, several studies have focused on the MRI-FI imaging system for the biomedical applications (Jiang et al. 2016; Li et al. 2016; Chen et al. 2016). The materials developed in this work by coating of magnetic cores and fluorescence shell (silica and presence of DOX) could be used as biocompatible agents for duel MRI-FI imaging. Further studies can reveal the relaxivity, quantum yield and bioavailability of peptide-coated materials.

iii) Active targeting

The target specific drug carrier could improve the bioavailability of loaded drugs to desired sites, while reducing their contact with normal tissues. Generally, tumour associated cells are targeted, alternatively other markers, which are overexpressed on effected cell could be targeted. The ligands such as peptides (RGD) could specifically bind with $\alpha_v\beta_3$ integrin. RGD ligand can be conjugated with free carboxyl group of phenylalanine to amine group of lysine of RGD.

iv) As dual agent for drug delivery and imaging system

The fabrication of mesoporosity of magnetic nanoparticles can be tuned in order to increase the payload and diversity of drugs. The use of surfactant can also key point to achieve better colloidal stability of desired materials. Iron oxide nanoparticles have shown another promising ability to be seen at cellular and molecular level interactions that can be used as contrast agents for MRI, while using them as drug delivery carrier. After coating with peptide and fluorescence loading of DOX, the applicability and efficiency has been improved. In next phase along coating of peptide they need to be studied for their contrast ability according to method published (Kohler et al. 2006).

v) *In vitro* drug delivery system

Degradation kinetics of these novels magnetic materials in water, cellular media and serum based biological systems can be investigated. This study could further reveals the role of coating materials (peptide) on magnetic nanoparticles at normal pH.

The internalisation of coated materials in tumour cells (U87, SVGP12 *etc*) by tagging with fluorescence dye. These experiments could be performed with cytotoxicity studies using MTT or CytoTox-Fluor assays. These results will further reveal the biocompatibility of novel coated magnetic materials by comparing with uncoated once. The biocompatibility of magnetic nanoparticles to red blood cell was found shape-dependent (Yu et al. 2011). Hence, the haemolytic comparison of both spherical and rod-shaped nanostructures would be an important for the potential administration these materials.

From *in vitro* drug release and cytotoxicity studies, the results will also lead to effect of nanoparticles in drug resistant tumours. However, *in vitro* drug release experiments and cytotoxicity results do not always reflects similar to *in vivo* efficiency. In addition, more studies will also assess the *in vivo* drug efficiency in multi-drug resistance tumour models.

References

Adler-Abramovich, L. et al., 2006. Thermal and chemical stability of diphenylalanine peptide nanotubes: implications for nanotechnological applications. *Langmuir*, 22(3), pp.1313–1320.

Adler-Abramovich, L. & Gazit, E., 2008. Controlled patterning of peptide nanotubes and nanospheres using inkjet printing technology. *Journal of Peptide Science*, 14(2), pp.217–223.

Adler-Abramovich, L. et al., 2010. Self-assembled organic nanostructures with metallic-like stiffness. *Angewandte Chemie International Edition*, 49(51), pp.9939–9942.

Aggeli, A. et al., 1997. Responsive gels formed by the spontaneous self-assembly of peptides into polymeric beta-sheet tapes. *Nature*, 386(6622), p.259.

Aggeli, A. et al., 2001. Hierarchical self-assembly of chiral rod-like molecules as a model for peptide β-sheet tapes, ribbons, fibrils, and fibers. *Proceedings of the National Academy of Sciences*, 98(21), pp.11857–11862.

Ahmad, M.Z. et al., 2010. Metallic nanoparticles: technology overview & drug delivery applications in oncology. *Expert Opinion on Drug Delivery*, 7(8), pp.927–942.

Alexis, F. et al., 2008. New frontiers in nanotechnology for cancer treatment. *Urol Oncol*, 26(1), pp.74–85.

Alkilany, A.M. et al., 2008. Gold nanorods as nanoadmicelles: 1-naphthol partitioning into a nanorod-bound surfactant bilayer. *Langmuir*, 24(18), pp.10235–10239.

Allam, A.A. et al., 2013. Stability and magnetically induced heating behavior of lipid-coated Fe_3O_4 nanoparticles. *Nanoscale Research Letters*, 8(1), p.426.

Amara, D. et al., 2009. Synthesis and characterization of Fe and Fe_3O_4 nanoparticles by thermal decomposition of triiron dodecacarbonyl. *Colloids and Surfaces A: Physicochemical and Engineering Aspects*, 339(1), pp.106–110.

Andersen, K.B., 2013. Exploring the properties and possibilities of self-assembling nanotubes and nanoparticles for nano-bio sensors. *Technical University of Denmark*, p.Technical University of Denmark.

Ang, K.L., Venkatraman, S. & Ramanujan, R. V, 2007. Magnetic PNIPA hydrogels for hyperthermia applications in cancer therapy. *Materials Science and Engineering: C*, 27(3), pp.347–351.

Arruebo, M. et al., 2007. Magnetic nanoparticles for drug delivery. *Nano Today*, 2(3), pp.22–32.

Asadi, H., Khoee, S. & Deckers, R., 2016. Polymer-grafted superparamagnetic iron oxide nanoparticles as a potential stable system for magnetic resonance imaging and doxorubicin delivery. *RSC Advances*, 6(87), pp.83963–83972.

Attaluri, A. et al., 2015. Magnetic nanoparticle hyperthermia enhances radiation therapy: A study in mouse models of human prostate cancer. *International Journal of Hyperthermia*, 31(4), pp.359–374.

Baldassarre, M., Bennett, M. & Barth, A., 2016. Simultaneous acquisition of infrared, fluorescence and light scattering spectra of proteins: direct evidence for pre-fibrillar species in amyloid fibril formation. *Analyst*, 141(3), pp.963–973.

Banaei, A. et al., 2015. Synthesis and characterization of new modified silica coated magnetite nanoparticles with bisaldehyde as selective adsorbents of Ag(i) from aqueous samples. *RSC Advances*, 5(101), pp.83304–83313.

Barrett, E.P., Joyner, L.G. & Halenda, P.P., 1951. The determination of pore volume and area distributions in porous substances. I. Computations from nitrogen isotherms. *Journal of the American Chemical society*, 73(1), pp.373–380.

Bauer, L.M. et al., 2016. High-performance iron oxide nanoparticles for magnetic particle imaging–guided hyperthermia (hMPI). *Nanoscale*, 8(24), pp.12162–12169.

Baughman, R.H., Zakhidov, A.A. & de Heer, W.A., 2002. Carbon nanotubes--the route toward applications. *Science*, 297(5582), pp.787–792.

Behdadfar, B. et al., 2012. Synthesis of high intrinsic loss power aqueous ferrofluids of iron oxide nanoparticles by citric acid-assisted hydrothermal-reduction route. *Journal of Solid State Chemistry*, 187, pp.20–26.

Bhirde, A.A. et al., 2009. Targeted killing of cancer cells in vivo and in vitro with EGF-directed carbon nanotube-based drug delivery. *ACS Nano*, 3(2), pp.307–316.

Bi, H. et al., 2016. Magnetically triggered drug release from biocompatible microcapsules for potential cancer therapeutics. *Journal of Materials Chemistry B*, 4(19), pp.3269–3277.

Bianco, A., Kostarelos, K., Partidos, C.D., et al., 2005. Biomedical applications of functionalised carbon nanotubes. *Chem Commun (Camb)*, (5), p.571.

Bianco, A., Kostarelos, K. & Prato, M., 2005. Applications of carbon nanotubes in drug delivery. *Current opinion in chemical biology*, 9(6), pp.674–9.

Boccuzzi, F. et al., 1999. FTIR study of the low-temperature water–gas shift reaction on Au/Fe_2O_3 and Au/TiO_2 catalysts. *Journal of Catalysis*, 188(1), pp.176–185.

Bordbar, A.K. et al., 2014. Characterization of modified magnetite nanoparticles for albumin immobilization. *Biotechnology research international*, 2014.

Le Bourlais, C. et al., 1998. Ophthalmic drug delivery systems—Recent advances. *Progress in Retinal and Eye Research*, 17(1), pp.33–58.

Brown Jr, W.F., 1963. Thermal fluctuations of a single-domain particle. *Physical Review*, 130(5), p.1677.

Bruce, I.J. et al., 2004. Synthesis, characterisation and application of silica-magnetite nanocomposites. *Journal of Magnetism and Magnetic Materials*, 284, pp.145–160.

Bruce, I.J. & Sen, T., 2005. Surface modification of magnetic nanoparticles with alkoxysilanes and their application in magnetic bioseparations. *Langmuir*, 21(15), pp.7029–7035.

Brunauer, S., Emmett, P.H. & Teller, E., 1938. Adsorption of gases in multimolecular layers. *Journal of the American Chemical Society*, 60(2), pp.309–319.

Brusentsov, N.A. et al., 2001. Evaluation of ferromagnetic fluids and suspensions for the site-specific radiofrequency-induced hyperthermia of MX11 sarcoma cells in vitro. *Journal of Magnetism and Magnetic Materials*, 225(1–2), pp.113–117.

Burd, R. et al., 1998. Tumor cell apoptosis, lymphocyte recruitment and tumor vascular changes are induced by low temperature, long duration (fever-like) whole body hyperthermia. *Journal of Cellular Physiology*, 177(1), pp.137–147.

Burton, A.W. et al., 2009. On the estimation of average crystallite size of zeolites from the Scherrer equation: a critical evaluation of its application to zeolites with one-dimensional pore systems. *Microporous and Mesoporous Materials*, 117(1), pp.75–90.

Bushey, M.L., Nguyen, T.-Q. & Nuckolls, C., 2003. Synthesis, Self-assembly, and switching of one-dimensional nanostructures from new crowded aromatics. *Journal of the American Chemical Society*, 125(27), pp.8264–8269.

Byeon, H.J. et al., 2016. Doxorubicin-loaded nanoparticles consisted of cationic-and mannose-modified-albumins for dual-targeting in brain tumors. *Journal of Controlled Release*, 225, pp.301–313.

Cai, H. et al., 2013. Facile hydrothermal synthesis and surface functionalization of polyethyleneimine-coated iron oxide nanoparticles for biomedical applications. *ACS Applied Materials & Interfaces*, 5(5), pp.1722–1731.

Cavaliere, R., Giogatto, B.C. & Giovanella, B.C., 1967. Selective heat sensitivity of cancer cells. *Cancer*, 20(9), pp.1351–1381.

Chatterjee, J., Haik, Y. & Chen, C.-J., 2003. Size dependent magnetic properties of iron oxide nanoparticles. *Journal of Magnetism and Magnetic Materials*, 257(1), pp.113–118.

Chavarria, A.M. et al., 2013. Self-Assembling Peptides. U.S. Patent Application No. 14/655,090.

Chen, H. et al., 2016. Application prospective of nanoprobes with MRI and FI dual-modality imaging on breast cancer stem cells in tumor. *Journal of Nanobiotechnology*, 14(1), p.52.

Chen, S. et al., 2007. Temperature-responsive magnetite/PEO-PPO-PEO block copolymer nanoparticles for controlled drug targeting delivery. *Langmuir*, 23(25), pp.12669–12676.

Chikazumi, S. et al., 1987. Physics of magnetic fluids. *Journal of Magnetism and Magnetic Materials*, 65(2), pp.245–251.

Chirgadze, Y.N., Brazhnikov, E. V & Nevskaya, N.A., 1976. Intramolecular distortion of the α-helical structure of polypeptides. *Journal of molecular biology*, 102(4), pp.781–792.

Cho, K. et al., 2008. Therapeutic nanoparticles for drug delivery in cancer. *Clinical cancer research : an official journal of the American Association for Cancer Research*, 14(5), pp.1310–1316.

Choi, S.-J., Oh, J.-M. & Choy, J.-H., 2009. Toxicological effects of inorganic nanoparticles on human lung cancer A549 cells. *Journal of Inorganic Biochemistry*, 103(3), pp.463–471.

Cihoric, N. et al., 2015. Hyperthermia-related clinical trials on cancer treatment within the clinical trials. gov registry. *International Journal of Hyperthermia*, 31(6), pp.609–614.

Cordente, N. et al., 2001. Synthesis and magnetic properties of nickel nanorods. *Nano Letters*, 1(10), pp.565–568.

Cortes, J. & Saura, C., 2010. Nanoparticle albumin-bound (nab^{TM})-paclitaxel: improving efficacy and tolerability by targeted drug delivery in metastatic breast cancer. *European Journal of Cancer Supplements*, 8(1), pp.1–10.

Craig, G., Allen, P. & Mason, M., 2010. Synthesis, characterization, and functionalization of gold nanoparticles for cancer imaging. In S. R. Grobmyer & B. M. Moudgil, eds. *Cancer Nanotechnology SE - 12*. Methods in Molecular Biology. Humana Press, pp. 177–193.

Cui, D. et al., 2005. Effect of single wall carbon nanotubes on human HEK293 cells. *Toxicology Letters*, 155(1), pp.73–85.

Dalton, A.B. et al., 2004. Hierarchical self-assembly of peptide-coated carbon nanotubes. *Advanced Functional Materials*, 14(12), pp.1147–1151.

Danhier, F., Feron, O. & Préat, V., 2010. To exploit the tumor microenvironment: Passive and active tumor targeting of nanocarriers for anti-cancer drug delivery. *J Control Release*, 148(2), pp.135–146.

Datt, A., El-Maazawi, I. & Larsen, S.C., 2012. Aspirin loading and release from MCM-41 functionalized with aminopropyl groups via co-condensation or postsynthesis modification methods. *The Journal of Physical Chemistry C*, 116(34), pp.18358–18366.

Davis, M.E., Chen, Z.G. & Shin, D.M., 2008. Nanoparticle therapeutics: an emerging treatment modality for cancer. *Nature Reviews Drug Discovery*, 7(9), pp.771–782.

Deng, M. et al., 2014. Fabrication and neuron cytocompatibility of iron oxide nanoparticles coated with silk-fibroin peptides. *Colloids and Surfaces B: Biointerfaces*, 116, pp.465–471.

Diaz, J.A.C. & Çağin, T., 2010. Thermo-mechanical stability and strength of peptide nanostructures from molecular dynamics: self-assembled cyclic peptide nanotubes. *Nanotechnology*, 21(11), p.115703.

Dickey, D.D. & Giangrande, P.H., 2016. Oligonucleotide aptamers: a next-generation technology for the capture and detection of circulating tumor cells. *Methods*, 97, pp.94–103.

Dinesh, B. et al., 2015. Self-assembly of diphenylalanine backbone homologues and their combination with functionalized carbon nanotubes. *Nanoscale*, 7(38), pp.15873–15879.

Dobson, J., 2006. Magnetic nanoparticles for drug delivery. *Drug Development Research*, 67(1), pp.55–60.

Dobson, Q.A.P. and J.C. and S.K.J. and J., 2003. Applications of magnetic nanoparticles in biomedicine. *Journal of Physics D: Applied Physics*, 36(13), p.R167.

Doyle, B.B., Bendit, E.G. & Blout, E.R., 1975. Infrared spectroscopy of collagen and collagen-like polypeptides. *Biopolymers*, 14(5), pp.937–957.

Dumestre, F. et al., 2003. Unprecedented crystalline super-lattices of monodisperse cobalt nanorods. *Angewandte Chemie*, 115(42), pp.5371–5374.

Dutz, S. & Hergt, R., 2014. Magnetic particle hyperthermia—a promising tumour therapy? *Nanotechnology*, 25(45), p.452001.

Eerikäinen, H. & Kauppinen, E.I., 2003. Preparation of polymeric nanoparticles containing corticosteroid by a novel aerosol flow reactor method. *International Journal of Pharmaceutics*, 263(1–2), pp.69–83.

Egodawatte, S. et al., 2015. Chemical insight into the adsorption of chromium (iii) on iron oxide/mesoporous silica nanocomposites. *Langmuir*, 31(27), pp.7553–7562.

Egusquiaguirre, S.P. et al., 2012. Nanoparticle delivery systems for cancer therapy: advances in clinical and preclinical research. *Clinical & translational oncology : official publication of the Federation of Spanish Oncology Societies and of the National Cancer Institute of Mexico*, 14(2), pp.83–93.

Elhissi, A.M. et al., 2012. Carbon nanotubes in cancer therapy and drug delivery. *Journal of Drug Delivery*, 2012, p.837327.

Farokhzad, O.C. & Langer, R., 2006. Nanomedicine: developing smarter therapeutic and diagnostic modalities. *Advanced Drug Delivery Reviews*, 58(14), pp.1456–1459.

Feng, B. et al., 2008. Synthesis of Fe_3O_4/APTES/PEG diacid functionalized magnetic nanoparticles for MR imaging. *Colloids and Surfaces A: Physicochemical and Engineering Aspects*, 328(1), pp.52–59.

Feng, T. & Zhao, Y., 2017. Clinical anticancer drugs for cancer treatment. In *Nanomaterial-Based Drug Delivery Carriers for Cancer Therapy*. Springer, pp. 7–13.

Feynman, R.P., 1960. There's plenty of room at the bottom. *Engineering and Science*, pp.22–36.

Fihri, A. et al., 2012. Nanoroses of nickel oxides: synthesis, electron tomography study, and application in CO oxidation and energy storage. *ChemSusChem*, 5(7), pp.1241–1248.

Fratila, R.M., Rivera-Fernández, S. & Jesús, M., 2015. Shape matters: synthesis and biomedical applications of high aspect ratio magnetic nanomaterials. *Nanoscale*, 7(18), pp.8233–8260.

Frey, N.A. et al., 2009. Magnetic nanoparticles: synthesis, functionalization, and applications in bioimaging and magnetic energy storage. *Chemical Society Reviews*, 38(9), pp.2532–2542.

Frimpong, R.A. et al., 2010. Enhancing remote controlled heating characteristics in hydrophilic magnetite nanoparticles via facile co-precipitation. *Journal of Magnetism and Magnetic Materials*, 322(3), pp.326–331.

Gabizon, A. et al., 2004. Tumor cell targeting of liposome-entrapped drugs with phospholipid-anchored folic acid–PEG conjugates. *Advanced Drug Delivery Reviews*, 56(8), pp.1177–1192.

Gallagher, W., 1997. FTIR analysis of protein structure. *Biochemistry*, (1958), pp.662–666.

Gan, Q. & Wang, T., 2007. Chitosan nanoparticle as protein delivery carrier—Systematic examination of fabrication conditions for efficient loading and release. *Colloids and Surfaces B: Biointerfaces*, 59(1), pp.24–34.

Gao, Y. et al., 2014. Loading and release of amine drugs by ion-exchange fibers: role of amine type. *Journal of pharmaceutical sciences*, 103(4), pp.1095–1103.

Genové, E. et al., 2005. The effect of functionalized self-assembling peptide scaffolds on human aortic endothelial cell function. *Biomaterials*, 26(16), pp.3341–3351.

Ghosh, R. et al., 2011. Induction heating studies of Fe_3O_4 magnetic nanoparticles capped with oleic acid and polyethylene glycol for hyperthermia. *Journal of Materials Chemistry*, 21(35), pp.13388–13398.

Gilchrist, R.K. et al., 1957. Selective inductive heating of lymph nodes. *Annals of surgery*, 146(4), p.596.

Gillies, E.R., Jonsson, T.B. & Fréchet, J.M.J., 2004. Stimuli-responsive supramolecular assemblies of linear-dendritic copolymers. *Journal of the American Chemical Society*, 126(38), pp.11936–11943.

Gillies, E.R. & Fréchet, J.M.J., 2005. Dendrimers and dendritic polymers in drug delivery. *Drug Discovery Today*, 10(1), pp.35–43.

Giri, S. et al., 2005. Stimuli-responsive controlled-release delivery system based on mesoporous silica nanorods capped with magnetic nanoparticles. *Angewandte Chemie International Edition*, 44(32), pp.5038–5044.

Görbitz, C.H. & Gorbitz, C.H., 2006. The structure of nanotubes formed by diphenylalanine, the core recognition motif of Alzheimer's beta-amyloid polypeptide. *Chemical Communications*, (22), pp.2332–4.

Görbitz, C.H., 2007. Microporous organic materials from hydrophobic dipeptides. *Chemistry–A European Journal*, 13(4), pp.1022–1031.

Graczyk, H. et al., 2015. Physicochemical characterization of nebulized superparamagnetic iron oxide nanoparticles (SPIONs). *Journal of Aerosol Medicine and Pulmonary Drug Delivery*, 28(1), pp.43–51.

Graf, C. et al., 2012. Surface functionalization of silica nanoparticles supports colloidal stability in physiological media and facilitates internalization in cells. *Langmuir*, 28(20), pp.7598–7613.

Green, M.R. et al., 2006. Abraxane®, a novel Cremophor®-free, albumin-bound particle form of paclitaxel for the treatment of advanced non-small-cell lung cancer. *Annals of Oncology*, 17(8), pp.1263–1268.

Greene, D. et al., 2014. Synthesis characterization and photocatalytic studies of cobalt ferrite-silica-titania nanocomposites. *Nanomaterials* , 4(2).

Guardia, P. et al., 2012. Water-soluble iron oxide nanocubes with high values of specific absorption rate for cancer cell hyperthermia treatment. *ACS Nano*, 6(4), pp.3080–3091.

Guillaudeu, S.J. et al., 2008. PEGylated dendrimers with core functionality for biological applications. *Bioconjugate Chemistry*, 19(2), pp.461–469.

Gunasekaran, S., Ko, S. & Xiao, L., 2007. Use of whey proteins for encapsulation and controlled delivery applications. *Journal of Food Engineering*, 83(1), pp.31–40.

Guzman, L.A. et al., 1996. Local intraluminal infusion of biodegradable polymeric nanoparticles: a novel approach for prolonged drug delivery after balloon angioplasty. *Circulation*, 94(6), pp.1441–1448.

Hahn, G.M., 1974. Metabolic aspects of the role of hyperthermia in mammalian cell inactivation and their possible relevance to cancer treatment. *Cancer Research*, 34(11), pp.3117–3123.

Hao, N., Li, L. & Tang, F., 2017. Roles of particle size, shape and surface chemistry of mesoporous silica nanomaterials on biological systems. *International Materials Reviews*, 62(2), pp.57–77.

Harris, L.A., 2002. Polymer stabilized magnetite nanoparticles and poly (propylene oxide) modified styrene-dimethacrylate networks.

Hergt, R. et al., 1998. Physical limits of hyperthermia using magnetite fine particles. *IEEE Transactions on Magnetics*, 34(5), pp.3745–3754.

Hervault, A. & Thanh, N.T.K., 2014. Magnetic nanoparticle-based therapeutic agents for thermo-chemotherapy treatment of cancer. *Nanoscale*, 6(20), pp.11553–11573.

Holland, T. & Mikos, A., 2006. Review: Biodegradable polymeric scaffolds. improvements in bone tissue engineering through controlled drug delivery. In K. Lee & D. Kaplan, eds. *Tissue Engineering I*. Springer Berlin Heidelberg, pp. 161–185.

Holmgren, G. et al., 2015. Identification of novel biomarkers for doxorubicin-induced toxicity in human cardiomyocytes derived from pluripotent stem cells. *Toxicology*, 328, pp.102–111.

Holzwarth, U. & Gibson, N., 2011. The Scherrer equation versus the'Debye-Scherrer equation'. *Nature Nanotechnology*, 6(9), p.534.

Hoopes, P.J. et al., 2015. Utility and translatability of mathematical modeling, cell culture and small and large animal models in magnetic nanoparticle hyperthermia cancer treatment research. In *SPIE BiOS*. International Society for Optics and Photonics, p. 932604.

Hopkins, J., Brenner, L. & Tumosa, C.S., 1991. Variation of the amide I and amide II peak absorbance ratio in human hair as measured by Fourier transform infrared spectroscopy. *Forensic Science International*, 50(1), pp.61–65.

Huang, J. et al., 2011. Hematite solid and hollow spindles: Selective synthesis and application in gas sensor and photocatalysis. *Materials Research Bulletin*, 46(8), pp.1211–1218.

Huang, R. et al., 2011. Solvent and surface controlled self-assembly of diphenylalanine peptide: from microtubes to nanofibers. *Soft Matter*, 7(14), p.6418.

Huang, R. et al., 2014. Temperature-induced reversible self-assembly of diphenylalanine peptide and the structural transition from organogel to crystalline nanowires. *Nanoscale Research Letters*, 9(1), p.653.

Huang, X. & Brazel, C.S., 2001. On the importance and mechanisms of burst release in matrix-controlled drug delivery systems. *Journal of Controlled Release*, 73(2–3), pp.121–136.

Hutchings, G., Polshettiwar, V. & Asefa, T., 2013. *Nanocatalysis: Synthesis and Applications*, John Wiley & Sons.

Hyeon, T. et al., 2001. Synthesis of highly crystalline and monodisperse maghemite nanocrystallites without a size-selection process. *Journal of the American Chemical Society*, 123(51), pp.12798–12801.

Ilaria Parisi, O. et al., 2016. Engineered polymer-based nanomaterials for diagnostic, therapeutic and theranostic applications. *Mini Reviews In Medicinal Chemistry*, 16(9), pp.754–761.

Ispas, C. et al., 2009. Toxicity and developmental defects of different sizes and shape nickel nanoparticles in zebrafish. *Environmental Science & Technology*, 43(16), pp.6349–6356.

Ivanov, Y.P., Vázquez, M. & Chubykalo-Fesenko, O., 2013. Magnetic reversal modes in cylindrical nanowires. *Journal of Physics D: Applied Physics*, 46(48), p.485001.

Iyer, A.K. et al., 2006. Exploiting the enhanced permeability and retention effect for tumor targeting. *Drug Discovery Today*, 11(17-18), pp.812–818.

Jain, T.K. et al., 2008. Biodistribution, clearance, and biocompatibility of iron oxide magnetic nanoparticles in rats. *Molecular Pharmaceutics*, 5(2), pp.316–327.

Jain, M. & Jothi, N.S.N., 2015. Structural and magnetic studies of one dimensional hematite (α-Fe_2O_3) nanorods by hydrothermal method. *International Journal on Applied Bioengineering*, 9(2).

Jeon, J., Mills, C.E. & Shell, M.S., 2013. Molecular insights into diphenylalanine nanotube assembly: all-atom simulations of oligomerization. *The Journal of Physical Chemistry B*, 117(15), pp.3935–3943.

Jiang, C. et al., 2016. One-pot aqueous synthesis of gadolinium doped CdTe quantum dots with dual imaging modalities. *Talanta*, 155, pp.14–20.

Jiang, W. et al., 2004. Preparation and properties of superparamagnetic nanoparticles with narrow size distribution and biocompatible. *Journal of Magnetism and Magnetic Materials*, 283(2), pp.210–214.

Jiles, D., 2015. *Introduction to magnetism and magnetic materials*, CRC press.

Johnson, E.K., Adams, D.J. & Cameron, P.J., 2011. Peptide based low molecular weight gelators. *Journal of Materials Chemistry*, 21(7), pp.2024–2027.

Jordan, A. et al., 1997. Effects of magnetic fluid hyperthermia (MFH) on C3H mammary carcinoma in vivo. *International Journal of Hyperthermia*, 13(6), pp.587–605.

Jordan, A. et al., 1999. Magnetic fluid hyperthermia (MFH): Cancer treatment with AC magnetic field induced excitation of biocompatible superparamagnetic nanoparticles. *Journal of Magnetism and Magnetic Materials*, 201(1), pp.413–419.

Kam, N.W.S. et al., 2005. Carbon nanotubes as multifunctional biological transporters and near-infrared agents for selective cancer cell destruction. *Proceedings of the National Academy of Sciences, U S A*, 102(33), pp.11600–11605.

Kampinga, H.H. & Dikomey, E., 2001. Hyperthermic radiosensitization: mode of action and clinical relevance. *International Journal Of Radiation Biology*, 77(4), pp.399–408.

Kampinga, H.H., 2006. Cell biological effects of hyperthermia alone or combined with radiation or drugs: a short introduction to newcomers in the field. *International Journal Of Hyperthermia*, 22(3), pp.191–196.

Kandasamy, G. et al., 2016. Facile synthesis of novel hydrophilic and carboxyl-amine functionalized superparamagnetic iron oxide nanoparticles for biomedical applications. *RSC Advances*, 6(102), pp.99948–99959.

Karanth, H. & Murthy, R.S.R., 2007. pH-sensitive liposomes--principle and application in cancer therapy. *The Journal of Pharmacy and Pharmacology*, 59(4), pp.469–83.

Karim, M.E., 2015. Nanotechnology within the legal and regulatory framework: An introductory overview. *Malayan Law Journal*, 3.

Karimzadeh, I. et al., 2016. A novel method for preparation of bare and poly (vinylpyrrolidone) coated superparamagnetic iron oxide nanoparticles for biomedical applications. *Materials Letters*, 179, pp.5–8.

Kashevsky, B.E. et al., 2015. Magnetic hyperthermia with hard-magnetic nanoparticles. *Journal of Magnetism and Magnetic Materials*, 380, pp.335–340.

Ketebu, O., Gumus, R. & Orodu, O., 2015. The effect of revolution per minute (rpm) on iron oxide nanoparticles (Fe_3O_4NPS) synthesis through direct oxidative alkaline hydrolysis. *International Journal of Academic Research and Reflection*, 3(5), pp.90–98.

Keten, S. et al., 2010. Nanoconfinement controls stiffness, strength and mechanical toughness of β-sheet crystals in silk. *Nature Materials*, 9(4), pp.359–367.

Kim, D., Jeong, Y.Y. & Jon, S., 2010. A Drug-loaded aptamer−gold nanoparticle bioconjugate for combined ct imaging and therapy of prostate cancer. *ACS Nano*, 4(7), pp.3689–3696.

Kim, D.K. et al., 2003. Protective coating of superparamagnetic iron oxide nanoparticles. *Chemistry of Materials*, 15(8), pp.1617–1627.

Kim, E.-S., 2008. Directed Evolution: A historical exploration into an evolutionary experimental system of nanobiotechnology, 1965–2006. *Minerva*, 46(4), pp.463–484.

Kim, K.Y., 2007. Nanotechnology platforms and physiological challenges for cancer therapeutics. *Nanomedicine*, 3(2), pp.103–110.

Kipp, J.E., 2004. The role of solid nanoparticle technology in the parenteral delivery of poorly water-soluble drugs. *International Journal of Pharmaceutics*, 284(1-2), pp.109–122.

Kohler, N. et al., 2006. Methotrexate-immobilized poly(ethylene glycol) magnetic nanoparticles for mr imaging and drug delivery. *Small*, 2(6), pp.785–792.

Koley, P., Sakurai, M. & Aono, M., 2015. Tunable morphology from 2D to 3D in the formation of hierarchical architectures from a self-assembling dipeptide: thermal-induced morphological transition to 1D nanostructures. *Journal of Materials Science*, 50(8), pp.3139–3148.

Kong, J. & Yu, S., 2007. Fourier transform infrared spectroscopic analysis of protein secondary structures. *Acta Biochimica Et Biophysica Sinica*, 39(8), pp.549–559.

Kumar, C.S.S.R. & Mohammad, F., 2011. Magnetic nanomaterials for hyperthermia-based therapy and controlled drug delivery. *Advanced Drug Delivery Reviews*, 63(9), pp.789–808.

Lam, C.-W. et al., 2004. Pulmonary Toxicity of Single-Wall Carbon Nanotubes in Mice 7 and 90 Days After Intratracheal Instillation. *Toxicological Sciences*, 77(1), pp.126–134.

Laurent, S. et al., 2008. Magnetic iron oxide nanoparticles: synthesis, stabilization, vectorization, physicochemical characterizations, and biological applications. *Chemical reviews*, 108(6), pp.2064–2110.

Laurent, S. et al., 2017. Superparamagnetic iron oxide nanoparticles. In *MRI Contrast Agents*. Springer, pp. 55–109.

Lee, C.C. et al., 2006. A single dose of doxorubicin-functionalized bow-tie dendrimer cures mice bearing C-26 colon carcinomas. *Proceedings of the National Academy of Sciences, USA*, 103(45), pp.16649–16654.

Lee, J.H. et al., 2014. Rod-shaped iron oxide nanoparticles are more toxic than sphere-shaped nanoparticles to murine macrophage cells. *Environmental Toxicology and Chemistry*, 33(12), pp.2759–2766.

Lee, P.I., 1984. Effect of non-uniform initial drug concentration distribution on the kinetics of drug release from glassy hydrogel matrices. *Polymer*, 25(7), pp.973–978.

Lele, P.P., 1990. Electronically-controlled variable focus ultrasound hyperthermia system.

Lepock, J.R., 2004. Role of nuclear protein denaturation and aggregation in thermal radiosensitization. *International Journal of Hyperthermia*, 20(2), pp.115–130.

Levin, A. et al., 2014. Ostwald's rule of stages governs structural transitions and morphology of dipeptide supramolecular polymers. *Nature Communications*, 5, p.5219.

Li, C., 2014. A targeted approach to cancer imaging and therapy. *Nature Materials*, 13(2), pp.110–115.

Li, C. et al., 2016. Synthesis of a UCNPs@ SiO_2@ gadofullerene nanocomposite and its application in UCL/MR bimodal imaging. *RSC Advances*, 6(101), pp.98968–98974.

Li, D. et al., 2016. Functionalized magnetic mesoporous silica nanoparticles for U removal from low and high pH groundwater. *Journal of Hazardous Materials*, 317, pp.494–502.

Li, M. et al., 2013. Self-assembled peptide–polyoxometalate hybrid nanospheres: two in one enhances targeted inhibition of amyloid β-peptide aggregation associated with alzheimer's disease. *Small*, 9(20), pp.3455–3461.

Li, Q. et al., 2015. Facile fabrication of diphenylalanine peptide hollow spheres using ultrasound-assisted emulsion templates. *Chemical Communications*, 51(33), pp.7219–7221.

Li, S. et al., 2016. Catalytic reduction of hexavalent chromium by a novel nitrogen-functionalized magnetic ordered mesoporous carbon doped with Pd nanoparticles. *Environmental Science and Pollution Research*, pp.1–10.

Ling, D. & Hyeon, T., 2013. Chemical design of biocompatible iron oxide nanoparticles for medical applications. *Small*, 9(9-10), pp.1450–1466.

Ling, D., Lee, N. & Hyeon, T., 2015. Chemical synthesis and assembly of uniformly sized iron oxide nanoparticles for medical applications. *Accounts of chemical research*, 48(5), pp.1276–1285.

Liu, D. & Auguste, D.T., 2015. Cancer targeted therapeutics: from molecules to drug delivery vehicles. *Journal of Controlled Release*, 219, pp.632–643.

Lowrie, W., 1990. Identification of ferromagnetic minerals in a rock by coercivity and unblocking temperature properties. *Geophysical Research Letters*, 17(2), pp.159–162.

Lu, A.-H. et al., 2004. Nanoengineering of a magnetically separable hydrogenation catalyst. *Angewandte Chemie*, 116(33), pp.4403–4406.

Lu, A.-H., Salabas, E.L. & Schüth, F., 2007. Magnetic nanoparticles: synthesis, protection, functionalization, and application. *Angewandte Chemie (International ed. in English)*, 46(8), pp.1222–44.

Ma, M. et al., 2004. Size dependence of specific power absorption of Fe_3O_4 particles in AC magnetic field. *Journal of Magnetism and Magnetic Materials*, 268(1), pp.33–39.

Maaz, K. et al., 2016. Fabrication and size dependent magnetic studies of Ni x Mn 1− x Fe_2O_4 (x= 0.2) cubic nanoplates. *Journal of Alloys and Compounds*.

Machín, R., Isasi, J.R. & Vélaz, I., 2013. Hydrogel matrices containing single and mixed natural cyclodextrins. Mechanisms of drug release. *European Polymer Journal*, 49(12), pp.3912–3920.

MacLachlan, M.J. et al., 2000. Superparamagnetic ceramic nanocomposites: Synthesis and pyrolysis of ring-opened poly (ferrocenylsilanes) inside periodic mesoporous silica. *Journal of the American Chemical Society*, 122(16), pp.3878–3891.

Maeda, H., Bharate, G.Y. & Daruwala, J., 2009. Polymeric drugs for efficient tumor-targeted drug delivery based on EPR-effect. *European Journal of Pharmaceutics and Biopharmaceutics*, 71(3), pp.409–419.

Mahdavi, M. et al., 2013. Synthesis, surface modification and characterisation of biocompatible magnetic iron oxide nanoparticles for biomedical applications. *Molecules*, 18(7).

Mahler, A. et al., 2006. Rigid, self-Assembled hydrogel composed of a modified aromatic dipeptide. *Advanced Materials*, 18(11), pp.1365–1370.

Mahmoudi, M. et al., 2011. Superparamagnetic iron oxide nanoparticles (SPIONs): Development, surface modification and applications in chemotherapy. *Advanced Drug Delivery Reviews*, 63(1–2), pp.24–46.

Mai, W.X. & Meng, H., 2013. Mesoporous silica nanoparticles: a multifunctional nano therapeutic system. *Integrative Biology*, 5(1), pp.19–28.

Maier-Hauff, K. et al., 2011. Efficacy and safety of intratumoral thermotherapy using magnetic iron-oxide nanoparticles combined with external beam radiotherapy on patients with recurrent glioblastoma multiforme. *Journal of Neuro-Oncology*, 103(2), pp.317–324.

Maity, D. et al., 2009. Studies of magnetite nanoparticles synthesized by thermal decomposition of iron (III) acetylacetonate in tri (ethylene glycol). *Journal of Magnetism and Magnetic Materials*, 321(19), pp.3093–3098.

Maity, S. et al., 2011. Fabrication of hollow self-assembled peptide microvesicles and transition from sphere-to-rod structure. *Langmuir*, 27(7), pp.3835–3841.

Maity, S., Nir, S. & Reches, M., 2014. Co-assembly of aromatic dipeptides into spherical structures that are similar in morphology to red and white blood cells. *Journal of Materials Chemistry B*, 2(17), pp.2583–2591.

Majdalawieh, A. et al., 2014. Recent advances in gold and silver nanoparticles: synthesis and applications. *Journal of Nanoscience and Nanotechnology*, 14(7), pp.4757–4780.

Majeed, J. et al., 2014. Enhanced specific absorption rate in silanol functionalized Fe_3O_4 core–shell nanoparticles: Study of Fe leaching in Fe_3O_4 and hyperthermia in L929 and HeLa cells. *Colloids and Surfaces B: Biointerfaces*, 122, pp.396–403.

Majoros, I.J. et al., 2006. PAMAM Dendrimer-based multifunctional conjugate for cancer therapy: synthesis, characterization, and functionality. *Biomacromolecules*, 7(2), pp.572–579.

Makin, O.S., Sikorski, P. & Serpell, L.C., 2006. Diffraction to study protein and peptide assemblies. *Current Opinion in Chemical Biology*, 10(5), pp.417–422.

Malekigorji, M., Curtis, ADM., Hoskins, C., 2014. The Use of iron oxide nanoparticles for pancreatic cancer therapy. *Journal of Nanomedicine Research*, 1(1), pp.04-12.

Marchesan, S. et al., 2015. Higher and lower supramolecular orders for the design of self-assembled heterochiral tripeptide hydrogel biomaterials. *Journal of Materials Chemistry B*, 3(41), pp.8123–8132.

Marsh, H., 1987. Adsorption methods to study microporosity in coals and carbons—a critique. *Carbon*, 25(1), pp.49–58.

Mart, R.J. et al., 2006. Peptide-based stimuli-responsive biomaterials. *Soft Matter*, 2(10), pp.822–835.

Martinez, G. & Millhauser, G., 1995. FTIR spectroscopy of alanine-based peptides: assignment of the amide I' modes for random coil and helix. *Journal of Structural Biology*, 114(1), pp.23–27.

Martinez-Boubeta, C. et al., 2013. Learning from nature to improve the heat generation of iron-oxide nanoparticles for magnetic hyperthermia applications. *Scientific Reports*, 3.

Matsumura, Y. & Maeda, H., 1986. A new concept for macromolecular therapeutics in cancer chemotherapy: mechanism of tumoritropic accumulation of proteins and the antitumor agent smancs. *Cancer Research*, 46(12 Part 1), pp.6387–6392.

El Mendili, Y. et al., 2016. Structural behavior of laser-irradiated γ-Fe_2O_3 nanocrystals dispersed in porous silica matrix : γ-Fe_2O_3 to α-Fe_2O_3 phase transition and formation of ε-Fe_2O_3. *Science and Technology of Advanced Materials*, 17(1), pp.597–609.

Metselaar, J.M. et al., 2003. A novel family of l-amino acid-based biodegradable polymer−lipid conjugates for the development of long-circulating liposomes with effective drug-targeting capacity. *Bioconjugate Chemistry*, 14(6), pp.1156–1164.

Misra, R., Acharya, S. & Sahoo, S.K., 2010. Cancer nanotechnology: application of nanotechnology in cancer therapy. *Drug Discovery Today*, 15(19-20), pp.842–850.

Mitsumori, M. et al., 1996. A phase I and II clinical trial of a newly developed ultrasound hyperthermia system with an improved planar transducer. *International Journal of Radiation Oncology* Biology* Physics*, 36(5), pp.1169–1175.

Mohapatra, J. et al., 2015. Iron oxide nanorods as high-performance magnetic resonance imaging contrast agents. *Nanoscale*, 7(20), pp.9174–9184.

Monshi, A., Foroughi, M.R. & Monshi, M.R., 2012. Modified Scherrer equation to estimate more accurately nano-crystallite size using XRD. *World Journal of Nano Science and Engineering*, 2(03), p.154.

Mornet, S. et al., 2004. Magnetic nanoparticle design for medical diagnosis and therapy. *Journal of Materials Chemistry*, 14(14), pp.2161–2175.

Müller, R. et al., 2005. Preparation of magnetic nanoparticles with large specific loss power for heating applications. *Journal of Magnetism and Magnetic Materials*, 289, pp.13–16.

Nakamura, K. et al., 2013. Self-heating temperature and AC hysteresis of magnetic iron oxide nanoparticles and their dependence on secondary particle size. *IEEE Transactions on Magnetics*, 49(1), pp.240–243.

Nemmar, A. et al., 2016. Ultrasmall superparamagnetic iron oxide nanoparticles acutely promote thrombosis and cardiac oxidative stress and DNA damage in mice. *Particle and Fibre Toxicology*, 13(1), p.22.

Neuberger, T. et al., 2005. Superparamagnetic nanoparticles for biomedical applications: possibilities and limitations of a new drug delivery system. *Journal of Magnetism and Magnetic Materials*, 293(1), pp.483–496.

Nikam, D.S. et al., 2014. Study of AC magnetic heating characteristics of Co 0.5 Zn 0.5 Fe 2 O 4 nanoparticles for magnetic hyperthermia therapy. *Journal of Magnetism and Magnetic Materials*, 349, pp.208–213.

Nishita, M. et al., 1998. Nuclear translocation and increased expression of Bax and disturbance in cell cycle progression without prominent apoptosis induced by hyperthermia. *Experimental Cell Research*, 244(1), pp.357–366.

Noh, S. et al., 2012. Nanoscale magnetism control via surface and exchange anisotropy for optimized ferrimagnetic hysteresis. *Nano Letters*, 12(7), pp.3716–3721.

Nordmeyer, D. et al., 2014. Iron oxide nanoparticles stabilized with dendritic polyglycerols as selective MRI contrast agents. *Nanoscale*, 6(16), pp.9646–9654.

Nyman, D.W. et al., 2005. Phase I and pharmacokinetics trial of abi-007, a novel nanoparticle formulation of paclitaxel in patients with advanced nonhematologic malignancies. *Journal of Clinical Oncology*, 23(31), pp.7785–7793.

O'Brien, M.E.R. et al., 2004. Reduced cardiotoxicity and comparable efficacy in a phase III trial of pegylated liposomal doxorubicin HCl (CAELYX™/Doxil®) versus conventional doxorubicin for first-line treatment of metastatic breast cancer. *Annals of Oncology*, 15(3), pp.440–449.

Oliveira, H. et al., 2013. Magnetic field triggered drug release from polymersomes for cancer therapeutics. *Journal of Controlled Release*, 169(3), pp.165–170.

Ozdemir, A., Ekiz, M.S., Dilli, A., Guler, M.O. and Tekinay, A.B., 2016. Amphiphilic peptide coated superparamagnetic iron oxide nanoparticles for in vivo MR tumor imaging. *RSC Advances*, 6(51), pp.45135-45146

Pacheco, S. et al., 2016. Formulation of hydrophobic therapeutics with self-assembling peptide and amino acid: A new platform for intravenous drug delivery. *Journal of Controlled Release*, 239, pp.211–222.

Paolini, A. et al., 2015. Rhamnose-coated superparamagnetic iron-oxide nanoparticles: an evaluation of their in vitro cytotoxicity, genotoxicity and carcinogenicity. *Journal of Applied Toxicology*.

Thorat, N. D., et al., 2013. Surface functionalized LSMO nanoparticles with improved colloidal stability for hyperthermia applications. *Journal of Physics D: Applied Physics* 46.10 (2013): 105003.

Pérez-Arnaiz, C. et al., 2014. New insights into the mechanism of the DNA/doxorubicin interaction. *The Journal of Physical Chemistry B*, 118(5), pp.1288–1295.

Petitjean, A. et al., 2002. Cation-promoted hierarchical formation of supramolecular assemblies of self-organized helical molecular components. *Angewandte Chemie*, 41(7), pp.1195–1198.

Petros, R.A. & DeSimone, J.M., 2010. Strategies in the design of nanoparticles for therapeutic applications. *Nature Reviews Drug Discovery*, 9(8), pp.615–627.

Pettigrew, R.T. et al., 1974. Clinical effects of whole-body hyperthermia in advanced malignancy. *British Medical Journal*, 4(5946), pp.679–682.

Ping, Z.H. et al., 2001. States of water in different hydrophilic polymers—DSC and FTIR studies. *Polymer*, 42(20), pp.8461–8467.

Van der Poll, D.G. et al., 2010. Design, synthesis, and biological evaluation of a robust, biodegradable dendrimer. *Bioconjugate Chemistry*, 21(4), pp.764–773.

Polshettiwar, V., Baruwati, B. & Varma, R.S., 2009. Self-assembly of metal oxides into three-dimensional nanostructures: synthesis and application in catalysis. *Acs Nano*, 3(3), pp.728–736.

Putnam, D. & Kopeček, J., 1995. Polymer conjugates with anticancer activity. In N. Peppas & R. Langer, eds. *Biopolymers II*. Springer Berlin Heidelberg, pp. 55–123.

Qu, L. & Tie, S., 2009. Mesoporous silica-coated superparamagnetic magnetite functionalized with CuO and its application as a desulfurizer. *Microporous and Mesoporous Materials*, 117(1), pp.402–405.

Quinto, C.A. et al., 2015. Multifunctional superparamagnetic iron oxide nanoparticles for combined chemotherapy and hyperthermia cancer treatment. *Nanoscale*, 7(29), pp.12728–12736.

Rad-Malekshahi, M. et al., 2015. Biomedical applications of self-assembling peptides. *Bioconjugate Chemistry*, 27(1), pp.3–18.

Rajabi, F., Kakeshpour, T. & Saidi, M.R., 2013. Supported iron oxide nanoparticles: Recoverable and efficient catalyst for oxidative SS coupling of thiols to disulfides. *Catalysis Communications*, 40, pp.13–17.

Rao, M.K.S. and R.D. and M.S.R., 2014. Realization of highest specific absorption rate near superparamagnetic limit of $CoFe_2O_4$ colloids for magnetic hyperthermia applications. *Materials Research Express*, 1(2), p.26107.

Ray, S. et al., 2006. A short water-soluble self-assembling peptide forms amyloid-like fibrils. *Chemical Communications*, (40), pp.4230–4232.

Reches, M. & Gazit, E., 2003. Casting metal nanowires within discrete self-assembled peptide nanotubes. *Science*, 300(5619), pp.625–627.

Reches, M. & Gazit, E., 2005. Self-assembly of peptide nanotubes and amyloid-like structures by charged-termini-capped diphenylalanine peptide analogues. *Israel journal of chemistry*, 45(3), pp.363–371.

Richard, S., Boucher, M., Lalatonne, Y., Mériaux, S. and Motte, L., 2017. Iron oxide nanoparticle surface decorated with cRGD peptides for magnetic resonance imaging of brain tumors. *Biochimica et Biophysica Acta*, 1861(6), pp.1515-1520.

Riley, J.M. et al., 2009. Bioproduction and characterization of a pH responsive self-assembling peptide. *Biotechnology and Bioengineering*, 103(2), pp.241–251.

Ringler, P. & Schulz, G.E., 2003. Self-assembly of proteins into designed networks. *Science*, 302(5642), pp.106–109.

Rutgers, A.J. & De Smet, M., 1947. Electrosmosis, streaming potentials and surface conductance. *Transactions of the Faraday Society*, 43, pp.102–111.

Šafařík, I. & Šafaříková, M., 2002. Magnetic nanoparticles and biosciences. *Monatshefte für Chemie/Chemical Monthly*, 133(6), pp.737–759.

Saha, R.N. et al., 2010. Nanoparticulate drug delivery systems for cancer chemotherapy. *Molecular Membrane Biology*, 27(7), pp.215–231.

Saikia, C. et al., 2017. Evaluation of folic acid tagged aminated starch/ZnO coated iron oxide nanoparticles as targeted curcumin delivery system. *Carbohydrate Polymers*, 157, pp.391–399.

Saint-Cricq, P. et al., 2015. Magnetic field activated drug delivery using thermodegradable azo-functionalised PEG-coated core–shell mesoporous silica nanoparticles. *Nanoscale*, 7(31), pp.13168–13172.

Sakulkhu, U. et al., 2014. Protein corona composition of superparamagnetic iron oxide nanoparticles with various physico-chemical properties and coatings. *Scientific reports*, 4, p.5020.

Sakurai, M., Koley, P. & Aono, M., 2014. A new approach to molecular self-assembly through formation of dipeptide-based unique architectures by artificial supersaturation. *Chemical Communications*, 50(83), pp.12556–12559.

Salgueiriño-Maceira, V. et al., 2006. Bifunctional gold-coated magnetic silica spheres. *Chemistry of Materials*, 18(11), pp.2701–2706.

Salim, M. et al., 2014. Amphiphilic designer nano-carriers for controlled release: from drug delivery to diagnostics. *MedChemComm*, 5(11), pp.1602–1618.

Salon, S.H. and S.-Y.W. and A.G. and D.-A.B.-T. and S.J., 2012. On the measurement technique for specific absorption rate of nanoparticles in an alternating electromagnetic field. *Measurement Science and Technology*, 23(3), p.35701.

Sanson, C. et al., 2011. Doxorubicin loaded magnetic polymersomes: theranostic nanocarriers for MR imaging and magneto-chemotherapy. *ACS Nano*, 5(2), pp.1122–1140.

Santhosh, P.B. & Ulrih, N.P., 2013. Multifunctional superparamagnetic iron oxide nanoparticles: promising tools in cancer theranostics. *Cancer Letters*, 336(1), pp.8–17.

Santra, S. et al., 2001. Synthesis and characterization of silica-coated iron oxide nanoparticles in microemulsion: the effect of nonionic surfactants. *Langmuir*, 17(10), pp.2900–2906.

Sarawade, P. et al., 2014. Size-and shape-controlled synthesis of hexagonal bipyramidal crystals and hollow self-assembled al-mof spheres. *ChemSusChem*, 7(2), pp.529–535.

Sayed, F.N. & Polshettiwar, V., 2015. Facile and sustainable synthesis of shaped iron oxide nanoparticles: effect of iron precursor salts on the shapes of iron oxides. *Scientific Reports*, 5.

Schmid, G., 2011. *Nanoparticles: from theory to application*, John Wiley & Sons.

Seip, C.T. & O'Connor, C.J., 1999. The fabrication and organization of self-assembled metallic nanoparticles formed in reverse micelles. *Nanostructured Materials*, 12(1), pp.183–186.

Sellins, K.S. & Cohen, J.J., 1991. Hyperthermia induces apoptosis in thymocytes. *Radiation Research*, 126(1), pp.88–95.

Sen, T., 2016. Meet the nanomachines that could drive a medical revolution. *The Conversation*.

Sen, T. et al., 2012. Simple one-pot fabrication of ultra-stable core-shell superparamagnetic nanoparticles for potential application in drug delivery. *RSC Advances*, 2(12), p.5221.

Sen, T. & Bruce, I.J., 2009. Mesoporous silica–magnetite nanocomposites: Fabrication, characterisation and applications in biosciences. *Microporous and Mesoporous Materials*, 120(3), pp.246–251.

Sen, T., Sebastianelli, A. & Bruce, I.J., 2006. Mesoporous silica−magnetite nanocomposite: fabrication and applications in magnetic bioseparations. *Journal of the American Chemical Society*, 128(22), pp.7130–7131.

Shao, H. & Parquette, J.R., 2009. Controllable peptide–dendron self-assembly: interconversion of nanotubes and fibrillar nanostructures. *Angewandte Chemie*, 48(14), pp.2525–2528.

Sharifabad, M.E. et al., 2014. Enzyme immobilised novel core-shell superparamagnetic nanocomposites for enantioselective formation of 4-(R)-hydroxycyclopent-2-en-1-(S)-acetate. *Chemical Communications*, 50(76), pp.11185–11187.

Shen, R.-N. et al., 1994. Influence of elevated temperature on natural killer cell activity, lymphokine-activated killer cell activity and lectin-dependent cytotoxicity of human umbilical cord blood and adult blood cells. *International Journal of Radiation Oncology* Biology* Physics*, 29(4), pp.821–826.

Shevtsov, M. & Multhoff, G., 2016. Recent developments of magnetic nanoparticles for theranostics of brain tumor. *Current Drug Metabolism*, 17(8), pp.737–744.

Simeonidis, K. et al., 2013. Fe-based nanoparticles as tunable magnetic particle hyperthermia agents. *Journal of Applied Physics*, 114(10), p.103904.

Simeonidis, K. et al., 2016. In-situ particles reorientation during magnetic hyperthermia application: Shape matters twice. *Scientific Reports*, 6.

Simões, S. et al., 2004. On the formulation of pH-sensitive liposomes with long circulation times. *Advanced Drug Delivery Reviews*, 56(7), pp.947–965.

Sneed, P.K. et al., 1998. Survival benefit of hyperthermia in a prospective randomized trial of brachytherapy boost±hyperthermia for glioblastoma multiforme. *International Journal of Radiation Oncology* Biology* Physics*, 40(2), pp.287–295.

Song, Y. et al., 2004. Synthesis of peptide-nanotube platinum-nanoparticle composites. *Chemical Communications*, (9), pp.1044–1045.

Stahl, H. et al., 1995. The use of an early postoperative interstitial-hyperthermia combination therapy in malignant gliomas. *Strahlentherapie und Onkologie: Organ der Deutschen Rontgengesellschaft...[et al]*, 171(9), pp.510–524.

Stoehr, L.C. et al., 2011. Shape matters: effects of silver nanospheres and wires on human alveolar epithelial cells. *Particle and Fibre Toxicology*, 8(1), p.36.

Strable, E. et al., 2001. Synthesis and characterization of soluble iron oxide-dendrimer composites. *Chemistry of Materials*, 13(6), pp.2201–2209.

Strebhardt, K. & Ullrich, A., 2008. Paul Ehrlich's magic bullet concept: 100 years of progress. *Nature Reviews Cancer*, 8(6), pp.473–480.

Sukhanova, A. et al., 2016. Nanosized fluorescent diagnostic probes consisting of single-domain antibodies conjugated with quantum dots. *Materials Today: Proceedings*, 3(2), pp.518–522.

Sun, C., Lee, J.S.H. & Zhang, M., 2008. Magnetic nanoparticles in MR imaging and drug delivery. *Advanced drug delivery reviews*, 60(11), pp.1252–1265.

Świerniak, A. et al., 2016. Cell cycle as an object of control. In *System Engineering Approach to Planning Anticancer Therapies*. Springer, pp. 9–54.

Takeuchi, H. et al., 2001. Evaluation of circulation profiles of liposomes coated with hydrophilic polymers having different molecular weights in rats. *Journal of Controlled Release*, 75(1–2), pp.83–91.

Talelli, M. et al., 2009. Superparamagnetic iron oxide nanoparticles encapsulated in biodegradable thermosensitive polymeric micelles: Toward a targeted nanomedicine suitable for image-guided drug delivery. *Langmuir*, 25(4), pp.2060–2067.

Taloub, S. et al., 2016. FEM Investigation of coated magnetic nanoparticles for hyperthermia. *Nanoscience and Nanotechnology*, 6(1A), pp.55–61.

Tang, Y., Flesch, R.C.C. & Jin, T., 2017. A method for increasing the homogeneity of the temperature distribution during magnetic fluid hyperthermia with a Fe-Cr-Nb-B alloy in the presence of blood vessels. *Journal of Magnetism and Magnetic Materials*, 432, pp.330–335.

Teow, H.M. et al., 2013. Delivery of paclitaxel across cellular barriers using a dendrimer-based nanocarrier. *International Journal of Pharmaceutics*, 441(1–2), pp.701–711.

Thévenot, J. et al., 2013. Magnetic responsive polymer composite materials. *Chemical Society Reviews*, 42(17), pp.7099–7116.

Thiesen, B. & Jordan, A., 2008. Clinical applications of magnetic nanoparticles for hyperthermia. *International Journal of Hyperthermia*, 24(6), pp.467–474.

Tietze, R. & Alexiou, C., 2017. Improving cancer imaging with magnetic nanoparticles: where are we now?. *Furure Medicines*

Tolcher, A.W. et al., 1999. Randomized Phase II study of br96-doxorubicin conjugate in patients with metastatic breast cancer. *Journal of Clinical Oncology*, 17(2), p.478.

Tombácz, E. et al., 2016. Polyelectrolyte coating on superparamagnetic iron oxide nanoparticles as interface between magnetic core and biorelevant media. *Interface Focus*, 6(6).

Torchilin, V.P. et al., 2001. Amphiphilic poly-N-vinylpyrrolidones:: synthesis, properties and liposome surface modification. *Biomaterials*, 22(22), pp.3035–3044.

Troiano, J.M. et al., 2014. Direct probes of 4 nm diameter gold nanoparticles interacting with supported lipid bilayers. *The Journal of Physical Chemistry C*, 119(1), pp.534–546.

Ulbrich, K. et al., 2016. Targeted drug delivery with polymers and magnetic nanoparticles: covalent and noncovalent approaches, release control, and clinical studies. *Chemical reviews*, 116(9), pp.5338–5431.

Unsoy, G. et al., 2014. Synthesis of Doxorubicin loaded magnetic chitosan nanoparticles for pH responsive targeted drug delivery. *European Journal of Pharmaceutical Sciences*, 62, pp.243–250.

Valéry, C. et al., 2003. Biomimetic organization: Octapeptide self-assembly into nanotubes of viral capsid-like dimension. *Proceedings of the National Academy of Sciences, USA*.100(18), pp.10258–10262.

Varon, J. & Acosta, P., 2008. Therapeutic hypothermia: past, present, and future. *Chest Journal*, 133(5), pp.1267–1274.

Vaupel, P., Kallinowski, F. & Okunieff, P., 1989. Blood flow, oxygen and nutrient supply, and metabolic microenvironment of human tumors: a review. *Cancer Research*, 49(23), pp.6449–6465.

Vayssieres, L. et al., 2005. One-dimensional quantum-confinement effect in α-Fe_2O_3 ultrafine nanorod arrays. *Advanced Materials*, 17(19), pp.2320–2323.

Wahajuddin & Arora, S., 2012. Superparamagnetic iron oxide nanoparticles: magnetic nanoplatforms as drug carriers. *International Journal of Nanomedicine*, 7, pp.3445–3471.

Wang, J. et al., 2004. Magnetic-field-induced growth of single-crystalline Fe_3O_4 nanowires. *Advanced Materials*, 16(2), pp.137–140.

Wang, K., Keasling, J.D. & Muller, S.J., 2005. Effects of the sequence and size of non-polar residues on self-assembly of amphiphilic peptides. *International Journal of Biological Macromolecules*, 36(4), pp.232–240.

Wang, S. et al., 2003. Peptides with selective affinity for carbon nanotubes. *Nature Materials*, 2(3), pp.196–200.

Wang, X. et al., 2008. Application of nanotechnology in cancer therapy and imaging. *CA: A Cancer Journal For Clinicians*, 58(2), pp.97–110.

Wang, X. et al., 2013. Particle-size-dependent toxicity and immunogenic activity of mesoporous silica-based adjuvants for tumor immunotherapy. *Acta Biomaterialia*, 9(7), pp.7480–7489.

Wang, Y.D. et al., 2007. Synthesis and room temperature photoluminescence of ZnO/CTAB ordered layered nanocomposite with flake-like architecture. *Journal of luminescence*, 126(2), pp.661–664.

Wei, X. et al., 2015. Polymorphous transformation of rod-shaped iron oxides and their catalytic properties in selective reduction of NO by NH3. *RSC Advances*, 5(81), pp.66141–66146.

Whiteman, K.R. et al., 2001. POly(Hpma)-Coated Liposomes Demonstrate Prolonged Circulation in Mice. *Journal of Liposome Research*, 11(2-3), pp.153–164.

Wilcoxon, J.P. & Provencio, P.P., 1999. Use of surfactant micelles to control the structural phase of nanosize iron clusters. *The Journal of Physical Chemistry B*, 103(45), pp.9809–9812.

Wismeth, C. et al., 2010. Transcranial electro-hyperthermia combined with alkylating chemotherapy in patients with relapsed high-grade gliomas: phase I clinical results. *Journal of Neuro-Oncology*, 98(3), pp.395–405.

Wong, R.S.L. et al., 1993. Critical steps for induction of chromosomal aberrations in CHO cells heated in S phase. *Radiation Research*, 133(1), pp.52–59.

Woo, K. et al., 2003. Sol–gel mediated synthesis of Fe_2O_3 nanorods. *Advanced Materials*, 15(20), pp.1761–1764.

Woźniak, E. et al., 2017. Stabilization of aqueous dispersions of poly (methacrylic acid)-coated iron oxide nanoparticles by double hydrophilic block polyelectrolyte poly (ethylene oxide)-block-poly (N-methyl-2-vinylpyridinium iodide). *Colloids and Surfaces A: Physicochemical and Engineering Aspects*, 514, pp.32–37.

Wu, M. et al., 2011. Release of hydrophobic anticancer drug from a newly designed self-assembling peptide. *Mol Biosyst*, 7(6), pp.2040–2047.

Wu, R. et al., 2016. Doxorubicin toxicity changes myocardial energy metabolism in rats. *Chemico-Biological Interactions*, 244, pp.149–158.

Wu, W. et al., 2005. Targeted delivery of amphotericin b to cells by using functionalized carbon nanotubes. *Angewandte Chemie International Edition*, 44(39), pp.6358–6362.

Wu, W., He, Q. & Jiang, C., 2008. Magnetic iron oxide nanoparticles: synthesis and surface functionalization strategies. *Nanoscale Research Letters*, 3(11), pp.397–415.

Wust, P. et al., 2002. Hyperthermia in combined treatment of cancer. *The Lancet Oncology*, 3(8), pp.487–497.

Xie, X. et al., 2009. Low-temperature oxidation of CO catalysed by Co_3O_4 nanorods. *Nature*, 458(7239), pp.746–749.

Xu, C. et al., 2004. Nitrilotriacetic acid-modified magnetic nanoparticles as a general agent to bind histidine-tagged proteins. *Journal of the American Chemical Society*, 126(11), pp.3392–3393.

XU, K., 2011. *Characterization and Utilization of Self-Assembled Diphenylalanine Nanotubes*. Diss. University of Nottingham

Xu, T. et al., 2011. Subnanometer porous thin films by the co-assembly of nanotube subunits and block copolymers. *ACS Nano*, 5(2), pp.1376–1384.

Xu, Z.Z. et al., 2004. Encapsulation of nanosized magnetic iron oxide by polyacrylamide via inverse miniemulsion polymerization. *Journal of Magnetism and Magnetic Materials*, 277(1), pp.136–143.

Yan, X. et al., 2007. Transition of cationic dipeptide nanotubes into vesicles and oligonucleotide delivery. *Angewandte Chemie*, 119(14), pp.2483–2486.

Yan, X., Zhu, P., Fei, J., et al., 2010. Self-assembly of peptide-inorganic hybrid spheres for adaptive encapsulation of guests. *Advanced Materials*, 22(11), pp.1283–1287.

Yan, X., Zhu, P. & Li, J., 2010a. Self-assembly and application of diphenylalanine-based nanostructures. *Chemical Society Reviews*, 39(6), pp.1877–1890.

Yanes, R. et al., 2007. Effective anisotropies and energy barriers of magnetic nanoparticles with Néel surface anisotropy. *Physical Review B*, 76(6), p.64416.

Yang, Y. et al., 2008. Preparation of polymer-coated mesoporous silica nanoparticles used for cellular imaging by a “graft-from” method. *Journal of Materials Chemistry*, 18(47), pp.5731–5737.

Yatvin, M.B. et al., 1980. pH-sensitive liposomes: possible clinical implications. *Science*, 210(4475), pp.1253–1255.

Yu, T., Malugin, A. & Ghandehari, H., 2011. Impact of silica nanoparticle design on cellular toxicity and hemolytic activity. *ACS Nano*, 5(7), pp.5717–5728.

Zhang, L., He, R. & Gu, H.-C., 2006. Oleic acid coating on the monodisperse magnetite nanoparticles. *Applied Surface Science*, 253(5), pp.2611–2617.

Zhang, L.-Y., Gu, H.-C. & Wang, X.-M., 2007. Magnetite ferrofluid with high specific absorption rate for application in hyperthermia. *Journal of Magnetism and Magnetic Materials*, 311(1), pp.228–233.

Zhao, Y. et al., 2015. Dynamic layer-by-layer films: a platform for zero-order release. *Biomacromolecules*, 16(7), pp.2032–2039.

Zheng, C. et al., 2013. Environmentally compatible synthesis of superparamagnetic magnetite (fe3o4) nanoparticles with prehydrolysate from corn stover, *BioResources* 9(1), pp.589-601

Web References

Bachem, 2016. Boc-diphenylalanine. MSDS. Available at: http://msds.bachem.com/A-3205.pdf [Accessed January 31, 2016].

SubsTech

SubsTech, 2016. Knowledge Source on Materials Engineering. Available at: http://www.substech.com/dokuwiki/doku.php?id=scanning_electron_microscope [Accessed August 1, 2016].

Horiba, 2016. Measurement Techniques. Available at: http://www.horiba.com/scientific/products/particle-characterization/particle-size-analysis/details/sz-100-7245/ [Accessed August 1, 2016].

Appendices

Appendix A

Zeta potential of boc-diphenylalanine in water (black) and ethanol-water (1:1) mixture (grey)

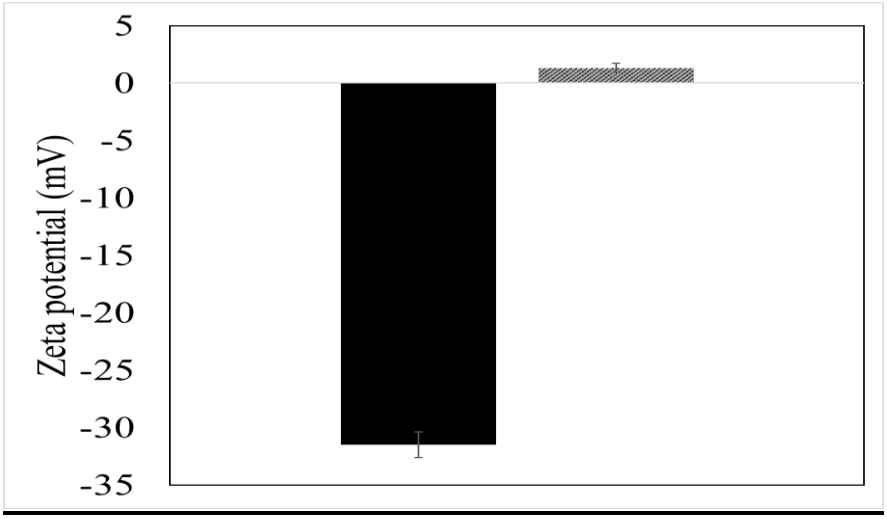

Zeta potential of diphenylalanine in water (black) and ethanol-water (1:1) mixture (grey)

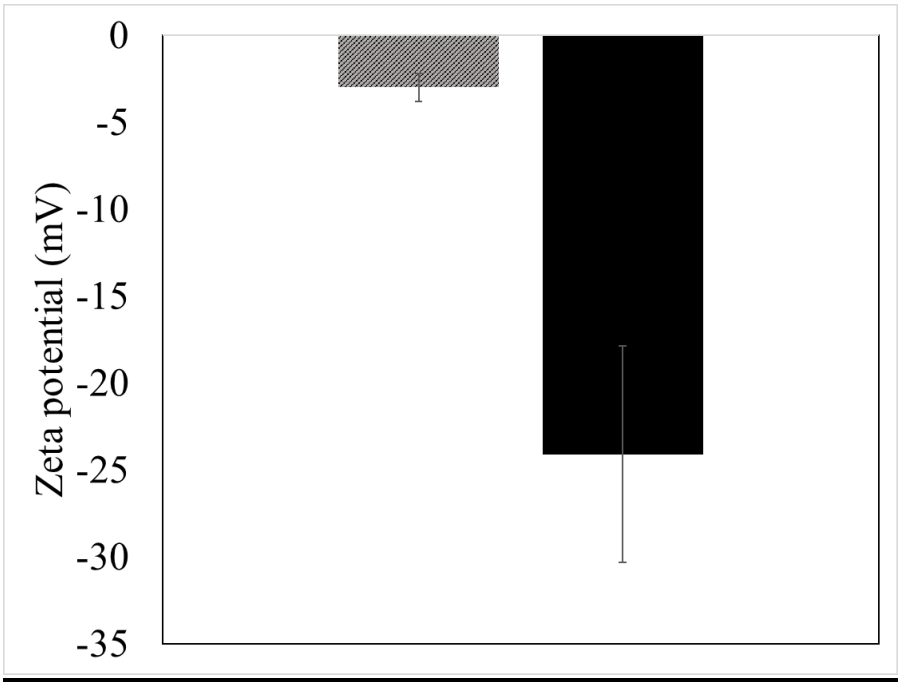

Appendix B

Commercially available boc-diphenylalanine

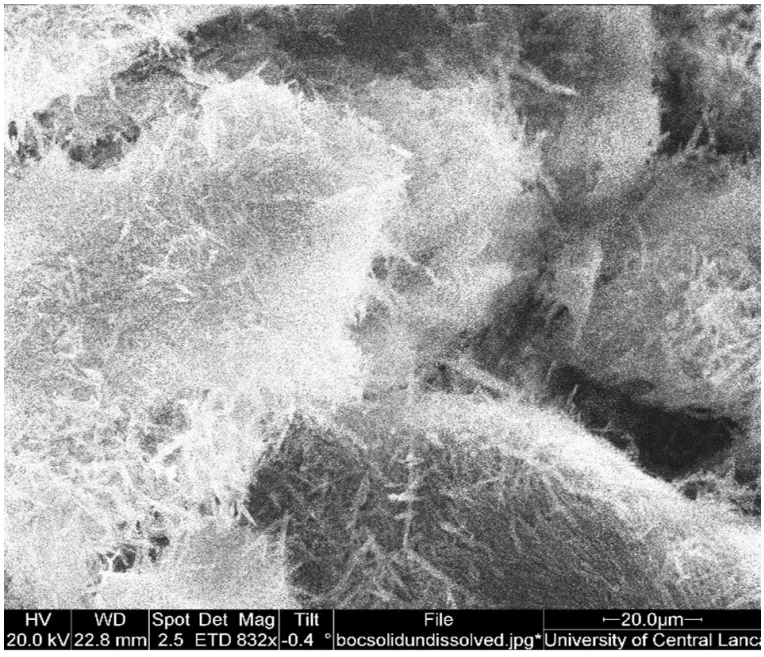

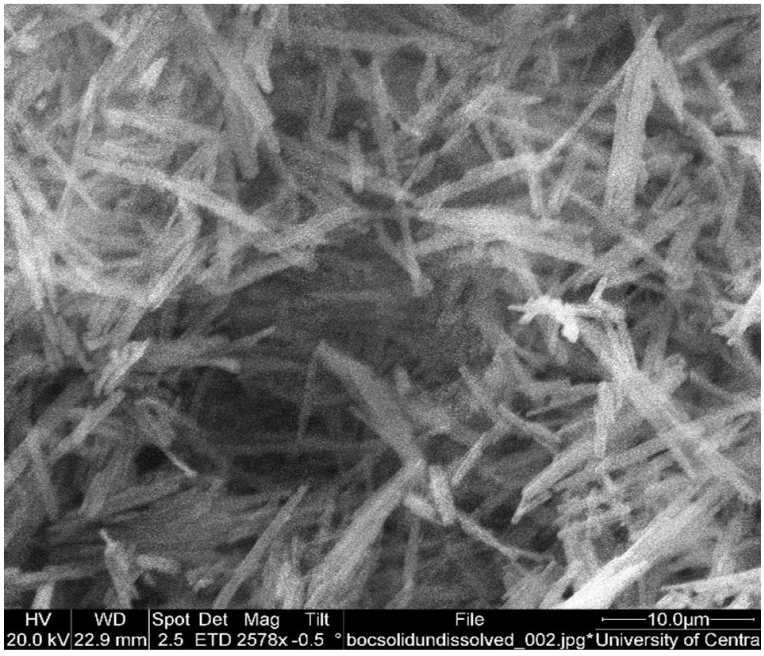

Appendix C

UCLan Functional Nanomaterials in Industrial Applications: Academic-Industry Meet 2016-Poster

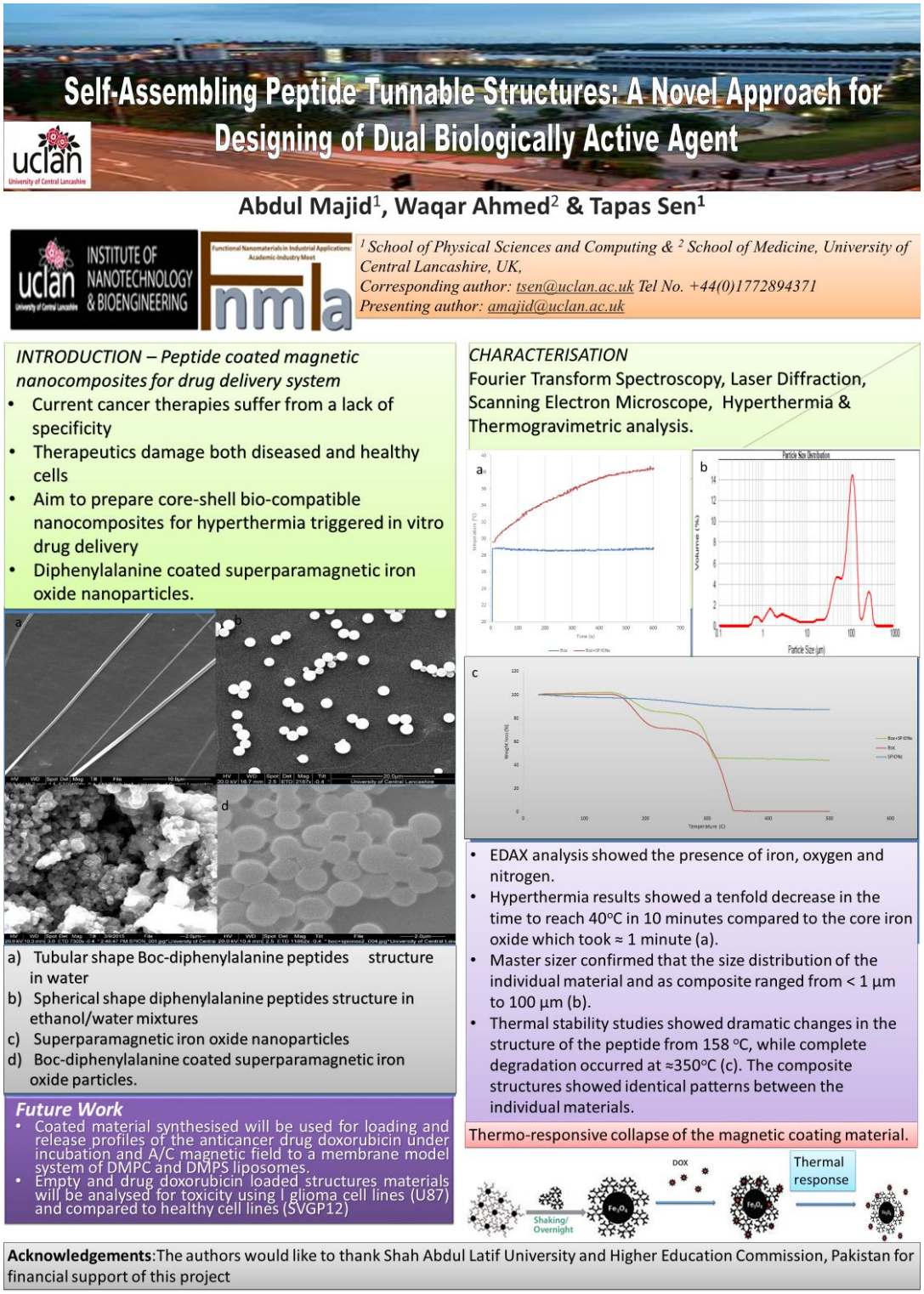

Available online at www.sciencedirect.com

ScienceDirect

Materials Today: Proceedings 4 (2017) 32–40

materialstoday: PROCEEDINGS

www.materialstoday.com/proceedings

Functional nanomaterials in Industrial Applications: Academic - Industry

Tunable Self-Assembled Peptide Structure: A Novel Approach to Design Dual-Use Biological Agents

Abdul Majid[a], Yogita Patil-Sen[a*], Waqar Ahmed[b], Tapas Sen[a]*

[a]*School of Physical Sciences and Computing, University of Central Lancashire, Preston, PR1 2HE, UK.*
[b]*School of Medicine, University of Central Lancashire, Preston, PR1 2HE, UK.*

Abstract

Micro/nanostructures based naturally occurring building blocks have attracted much attention as potential materials in the field of bio-nanotechnology. In this context, peptides are ideal naturally occurring materials for tissue regeneration, scaffolding, and drug delivery. Herein we report an initial study of fabrication of spherical and tubular structures by self-assembly process using butoxy carbonyl (Boc)-diphenylalanine as a naturally occurring peptides under different solvent conditions in the presence and absence of superparamagnetic iron oxide (SPIONs) core. The novel nanocomposites have been characterized using Scanning Electron Microscopy (SEM), Fourier Transform Infrared Spectroscopy (FTIR), Dynamic Light Scattering (DLS) Thermogravimetric Analysis (TGA) and Magnetic Hyperthermia under Alternating Magnetic Field (AMF).

Selection and Peer-review under responsibility of the Conference Committee Members of Functional Nanomaterials in Industrial Applications.

Keywords: Self-assembling peptides; Superparamagnetic iron oxide; core-shell nanoparticles.

1. Introduction

The molecular self-assembly is an attractive approach to engineer the nanostructures in various applications of nanoscience such as in the bioelectronics as sensor devices, drug delivery system, scaffolds, micro/nano fluidics and

* Corresponding author. Tel.: +44(0)1772894371.
E-mail address: tsen@uclan.ac.uk.or YPatil-sen@uclan.ac.uk